Silicon and Germanium Nanowires Anode Materials for Lithium and Sodium-ion Batteries

by

Alireza Kohandehghan

A thesis submitted in partial fulfillment of the requirements for the degree of

Doctor of Philosophy
in
Materials Engineering

Department of Chemical and Materials Engineering
University of Alberta

Abstract

This thesis is focused on the silicon-based anode materials for lithium-ion batteries (LIBs) as well as germanium-based electrode materials for sodium-ion batteries (NIBs). In our first attempt we studied electrochemical cycling stability and degradation mechanisms of silicon nanowires (SiNWs) coated with Mg and Mg_2Si for LIB anodes. Compared to SiNWs, both Mg-and Mg_2Si-coated materials show significant improvement in coulombic efficiency (CE) during cycling, with pure Mg coating being slightly superior by ~ 1% in each cycle. XPS measurements on cycled nanowire forests showed lower Li_2CO_3 and higher polyethylene oxide content for coated nanowires, thus revealing a passivating effect towards electrolyte decomposition. The formation of large voids between the nanowire assembly and the substrate during cycling, causing the nanowires to lose electrical contact with the substrate, is identified as an important degradation mechanism.

In our second attempt we demonstrated that nanometer-scale TiN coatings deposited by atomic layer deposition (ALD), and to a lesser extent by magnetron sputtering, will significantly improve the electrochemical cycling performance of SiNWs LIB anodes. A 5 nm thick ALD coating resulted in optimum cycling capacity retention (55% vs. 30% for SiNWs, after 100 cycles) and CE (98% vs. 95%, at 50 cycles), also more than doubling the high rate capacity retention (e.g. 740 vs. 330 mAh/g at 5C). The conformal 5 nm TiN remains sufficiently intact to limit the growth of the solid electrolyte interphase (SEI), which in turn both improves the overall CE and reduces the life-ending delamination of the nanowire assemblies from the underlying current collector.

Our third attempt was demonstrating cycling performance improvement for SiNWs LIB anodes by a thin partially dewetted coating of Sn. The optimum architecture 3Sn/SiNWs (i.e. a

Sn layer with an average film thickness of a 3 nm covering the nanowire) maintained a reversible capacity of 1865 mAh/g after 100 cycles at a rate of 0.1C. This is almost double of the SiNWs, where the reversible capacity after 100 cycles was 1046 mAh/g (~ 78% improvement). The 1Sn/SiNWs and 3Sn/SiNWs electrodes demonstrated much improved cycling CE, with > 99% vs. 94 - 98% for SiNWs. At a high current density of 5C, these nanocomposite offered 2X the capacity retention of bare SiNWs (~ 20 vs. ~ 10% of 0.1C capacity). It is demonstrated that the Sn coating both lithiates and delithiates at a higher voltage than Si and thus imparts a compressive stress around the nanowires. This confines their radial expansion in favor of longitudinal, and reduces the well-known failure mode by lithiation-induced nanowire stranding and fracture. TOF-SIMS analysis on the post-cycled delithiated specimens shows enhanced Li signal near the current collector due to accelerated SEI formation at the interface. FIB demonstrates concurrent en-masse delamination of SEI agglomerated sections of the nanowires from the current collector. Both of these deleterious effects are lessened by the presence of the Sn coatings.

Germanium is a promising sodium ion battery (NIB, NAB, SIB) anode material that is held back by its extremely sluggish kinetics and poor cyclability. In our last attempt we demonstrated for the first time that activation by a single lithiation - delithiation cycle leads to a dramatic improvement in practically achievable capacity, in rate capability and in cycling stability of Ge nanowires (GeNWs) and Ge thin films (GeTF). TEM and TOF-SIMS analysis shows that without activation, the initially single crystal GeNWs are effectively Na inactive, while the 100 nm amorphous GeTF sodiate to only less than half their thickness. Activation with Li induces amorphization (in GeNWs) reducing the barrier for nucleation of the Na_xGe phase(s), while introducing a dense distribution of nanopores that reduce the Na solid-state diffusion distances

and buffer the sodiation stresses. The resultant sodiation kinetics are promising: Tested at 0.15C (1C = 369 mA/g, i.e. Na:Ge 1:1) for 50 cycles the GeNWs and GeTFs maintain a reversible (desodiation) capacity of 346 mAh/g and 418 mAh/g. The nanowires and films demonstrate a capacity of 355 and 360 mAh/g at 1C and 284 and 310 mAh/g at 4C, respectively. Even at a very high rate of 10C the GeTF delivers over 169 mAh/g.

Preface

Chapter 2 of this thesis has been published as Kohandehghan, Alireza, Peter Kalisvaart, Martin Kupsta, Beniamin Zahiri, Babak Shalchi Amirkhiz, Zhipeng Li, Elmira L. Memarzadeh, Leonid A. Bendersky, and David Mitlin. "Magnesium and magnesium-silicide coated silicon nanowire composite anodes for lithium-ion batteries." J. Mater. Chem. A 1, (2013): 1600-1612.

Chapter 3 of this thesis has been published as Kohandehghan, Alireza, Peter Kalisvaart, Kai Cui, Martin Kupsta, Elmira Memarzadeh, and David Mitlin. "Silicon nanowire lithium-ion battery anodes with ALD deposited TiN coatings demonstrate a major improvement in cycling performance." J. Mater. Chem. A 1, (2013): 12850-12861.

Chapter 4 of this thesis has been published as Kohandehghan, Alireza, Kai Cui, Martin Kupsta, Elmira Memarzadeh, Peter Kalisvaart, and David Mitlin. "Nanometer-scale Sn Coatings Improve the Performance of Silicon Nanowire LIB Anodes." J. Mater. Chem. A 2, (2014): 11261-11279.

Chapter 5 of this thesis has been published as Kohandehghan, Alireza, Kai Cui, Martin Kupsta, Jia Ding, Elmira Memarzadeh, Peter Kalisvaart, and David Mitlin. "Activation with Li Enables Facile Sodium Storage in Germanium." Nano Lett., 2014, 14 (10), pp 5873–5882.

I was responsible for the data collection and analysis as well as the manuscript composition. Dr. David Mitlin was the supervisory author and was involved with concept formation and manuscript composition.

Dedication

To my lovely Mom, my supportive Dad, my sister Maryam, and my brother Mohammadreza.

Acknowledgment

First I offer my utmost gratitude to my supervisor, Dr. David Mitlin, who has supported me throughout this research with his knowledge and patience, and also for giving me the freedom and resources I required. It was such a great honor for me to be guided by him.

I am also very grateful to my colleagues for their invaluable and unconditional help. Many thanks go to Peter Kalisvaart, Tyler Stephenson, Brian Olsen, Li Zhang, Babak Shalchi-Amirkhiz, Beniamin Zahiri, Elmira Memarzadeh, Xuehai Tan, Mike Hazelton, Jia Ding, Huanlei Wang, Zhi Li, Mohsen Danaie, Zhanwei Xu, Chris Holt, Behdokht Farbod, Erik Luber, and Yashar Behnamian. It is a pleasure to thank those who made this thesis possible, Martin Kupsta for assistance with the FIB/SEM and his helpful and friendly advices, Kai Cui and Greg Popowich for TEM assistance, and Dimitre Karpuzov for XPS assistance. Finally, thanks to all the technicians and staff members of the Chemical and Materials Engineering (CME) Department, National Institute for Nanotechnology (NINT), Alberta Centre for Surface Engineering and Science (ACSES), and Cross-Cancer Institute at University of Alberta.

I also thank all my other fiends for their unequivocal supports. My last and sincere acknowledge goes to my family for all the support and encouragement given to me during the tough times through all years of my studies and giving me a foundation to always be able to fall back on.

Table of Contents

List of Tables

List of Figures

Chapter 1: Introduction and Background

Continuous increase in oil consumption and depletion of non-renewable resources threaten the fossil fuel energy economy. Besides, due to CO_2 emissions resulting in a rise in global temperature with dramatic climate changes, the demand for the green renewable energy has become more imperative. Investments for the exploitation of renewable energy resources have been concentrated on wind and solar power energy plants, which require high efficiency energy storage systems. Indeed you probably could not imagine today world without stored energy. The air pollution issue in urban areas may be solved by replacing the conventional combustion engines with fully electric vehicles or plug-in hybrid electric vehicles. Electrochemical energy storage with generally number of desirable features such as pollution free operation, flexible power and energy density characteristics, and long cycle life, play a crucial role in this field. Electrochemical energy storage approaches can be distinguished by the storage mechanism. Energy in form of electricity can be stored in either supercapacitors or batteries. Batteries, in general, store energy within the electrode structure through charge transfer reactions in some sort of chemical manner, with high volumetric energy density. Supercapacitors, however, offer different storage mechanism via a capacitive process originating from electrochemical double layer at the electrode – electrolyte interface, resulting in rather low volumetric energy density. This type of energy storage systems provides higher power density and longer cycle life than that of batteries, although researchers try to improve its energy density as well. Lithium-ion batteries (LIB)s typically store between 100 – 200 W/kg while electrochemical capacitors store 1 – 10 Wh/kg in less than 1 minute. In general, batteries are used when portable power is necessary for periods of hours. Supercapacitors are used for applications that require fast delivery or uptake of electrical energy. Plug-in hybrid electric vehicles development focuses great attention on batteries as power source. [1] A reliable power source for these vehicles should have high capacity and offer long cycle life while it has to be safe and capable of working in large temperature range.

1.1 Batteries

A battery is composed of several electrochemical cells to provide the required voltage (in series) and/or for the required capacity (in parallel). Each cell consists of two electrodes at which the redox reactions take place. The electrodes are separated physically and electronically by an electronically insulating but ionically conducting electrolyte, which is usually a solution of dissociated salt in a solvent. A separator is also used for mechanical separation of two electrodes to prevent electronic short circuits. The ion transfer occurs through the electrolyte between two electrodes and the electrons travel through the external circuit connecting two electrodes so that the chemical reactions proceed at both electrodes. There are two main types of batteries: primary batteries or non-rechargeable batteries and secondary/rechargeable batteries. The major difference is the redox (reduction and oxidation) reactions and structural changes which can be reversed for the rechargeable batteries, allowing the discharged secondary batteries to be charged again. Since the secondary batteries are the most commonly used battery today, we focus only on this type of battery in this thesis.

Driving force to accept or give away electrons between two electrodes is the difference in oxidation or reduction potential. The electrode that is more reducing or has stronger reducing driving force to give up electrons, i.e. become oxidized, is the negative electrode and the positive electrode will accept the electrons from the negative side and become reduced. In fact, anode is the side of a battery releasing electrons (oxidation occurs) and cathode is the electrode accepting electrons (reduction occurs) during discharge. The electrons exchanging between electrode materials are made to travel through the external circuit so that one can utilize the energy from the electron transfer process. Upon discharge, the negative electrode is oxidized and the positive material is reduced. Voltage difference between positive and negative poles reduces during discharge, i.e. electrons travel from negative to positive side until the voltage difference becomes too low, i.e. zero (fully discharged battery). Charging, during which at the positive side of the cell oxidation and at the negative pole reduction occurs, requires external energy because we oxidize the material that tends to reduce and reduce the electrode material which is likely to oxidize. Indeed we store electrical energy in the form of chemical energy in the battery electrode materials during charge process. The transfer of electrons through the circuit is balanced by the

transfer of ions in the electrolyte. The cations are adsorbed onto the inert materials' surface, while are inserted into the active materials' structure via different mechanisms.

1.1.1 Voltage

Driving force for any chemical reaction is the difference between the standard Gibbs free energy of formation of the products and the reactants of the reaction (Eq. 1-1). Since ΔG represents the useful energy from a reaction, the available electrical energy from a reaction in a cell is given by Eq. 1-2.

$$\Delta G^{\circ} = \sum \Delta G_f^{\circ}(products) - \sum \Delta G_f^{\circ}(reactants) \quad 1\text{-}1$$

$$\Delta G^{\circ} = -nFE \quad 1\text{-}2$$

Where E is the voltage difference between the electrodes or voltage of the cell with the specific chemical reaction, in other words, E is the electromotive force (emf) of the cell reaction, n is the stoichiometric number of electrons exchanged in the reaction, and F is the Faraday constant (96485 A.sec/mol). Spontaneous processes have a negative free energy and a positive emf with the reaction written in a reversible fashion going in the forward direction. The voltage of a Li-ion battery is related to the difference in chemical potential of Li in each electrode material. The open circuit voltage of a cell, which is not yet discharged, can be obtained from Eq. 1-3.

$$V_{OCP} = \frac{-(\mu_{Li}^{+} - \mu_{Li}^{-})}{nF} \quad 1\text{-}3$$

Where μ_{Li}^{+} and μ_{Li}^{-} is chemical potential of Li in the cathode and anode, respectively. For a fully charged Li cell, $\mu_{Li}^{-} > \mu_{Li}^{+}$, the Li cell voltage is a positive value. As it starts to discharge the voltage of the cell begins to drop since Li ions transfer from higher chemical potential (anode) to the lower chemical potential (cathode). Equation 1-4 below describes the change in chemical potential of Li in each electrode during discharge.

$$\mu_i = \mu_i^{\circ} + RTlna_i \quad 1\text{-}4$$

Where μ_i° is the chemical potential of species i in its standard state, a_i is the activity of species i, R is the ideal gas constant, and T is absolute temperature. As the activity of specie i is

indeed its concentration, chemical potential and hence voltage changes as a function of Li concentration. This voltage change is usually reported as a function of time.

Gibbs phase rule helps us to understand the potential profiles obtained from galvanostatic electrochemical examinations. [2,3] F is the freedom degree of the system, i.e. the number of thermodynamic parameters (chemical potential, voltage, temperature, and pressure) can be changed freely. If there is a compound, A, reacting with lithium and form Li_xA based on the following electrochemical reaction:

$$A + xLi^+ + x\bar{e} \rightarrow Li_xA$$

In the reaction there are two elements, $C = 2$. If the A and Li form a solid solution (corresponding to sloped region in potential profile) there is only one phase, $P = 1$, thereby F would be three. It means that temperature, pressure, and chemical potential of lithium can change freely. Typical electrochemical reactions are being conducted at constant temperature and pressure, thereby lithium chemical potential can change freely. Change in chemical potential means voltage change over time, appearing as sloped region in potential curve.

If a new phase nucleated and formed an alloy with lithium, it would result in two degrees of freedom. Assuming conducting the redox reactions at constant temperature and pressure, there is no other thermodynamic parameters to vary over time. Therefore, chemical potential of lithium would be constant and it means the voltage is constant over time during this reaction. Accordingly, a flat plateau within this potential range appears. In a word, plateau in voltage profile indicates coexistence of two phases.

1.1.2 Capacity

Capacity of an active material is the amount of charge, i.e. energy, which can be stored in its structure. In LIBs, it could be expressed as the amount of stored lithium. It represents in gravimetric or volumetric specific capacities where the amount of stored charge per unit mass or volume of the active material is presented, respectively. Ampere equals coulomb/sec. Thus, milliampere hour (mAh) is another way to present charge in coulomb.

If the stoichiometric of the lithiated compound is known, according to the point that for every Li^+ only one electron transferred, one can calculate the gravimetric specific capacity (mAh/g) by using the below equation:

$$C_W = \frac{1000 \times \mathrm{F} \times x}{3600 \times M_W} \quad \text{1-5}$$

Here, x is the mole fraction of lithium in the lithiated compound, Li_xA, M_w is the molecular weight of A, and F is the Faraday constant (96485 A.sec/mol). The volumetric specific capacity is defined as $C_V = \rho C_W$, where ρ is the density of the host material. The total capacity of a battery may generally be expressed in terms of capacities of its anode and cathode materials as below:

$$\frac{1}{C_{Total}} = \frac{1}{C_A} + \frac{1}{C_C} + \frac{1}{Q_M} \quad \text{1-6}$$

Where, C_A and C_C is the capacity of anode and cathode materials, respectively. $1/Q_M$ (g/mAh) is the specific mass of other components of the cell including electrolyte, separator, current collectors, case, and etc. Q_M for the Sony 18650G8 cell is about 130 mAh/g. Having a specific capacity of 372 mAh/g for graphite and 135 mAh/g for $LiCoO_2$, a total specific capacity of ~ 56 mAh/g can be calculated for the commercial Sony Li-ion battery (2550 mAh, 46 g). [4]

The amount of energy that a battery is able to deliver is a function of the cell voltage (V) and capacity (Ah/kg). It is expressed either per unit of weight (Wh/kg) or per unit of volume (Wh/L). It is always important to consider both voltage and specific capacity of the electrode material to maximize the energy density when looking at possible new electrode materials. The total energy stored (E) is an integral function of the overall capacity (C) and voltage (V).

$$E = \int C dV \quad \text{1-7}$$

1.1.3 Coulombic efficiency

Coulombic efficiency (CE) is the ratio of delithiation capacity over the lithiation one. Indeed, it reflects how reversible the lithiation reactions are. In other words, it expresses the amount of irreversible consumption of lithium through the electrochemical reactions in a Li cell. CE lower than 100% means some lithium ions and electrons, thereby energy, consumed

irreversibly. For electrode materials, it has been correlated to formation of a porous amorphous not electrical conductive layer on the active materials' surface called solid electrolyte interphase (SEI). The reason that the first CE is usually lower than that of the subsequent cycles for all the materials might be irreversible SEI formation at the freshly exposed surface of active materials to the electrolyte. Afterwards, this passivating SEI layer would protect the active materials from participation in side reactions with electrolyte. Thus, in following cycles CE is larger than that of first cycle.

1.1.4 Power

Thermodynamics describe reactions at equilibrium like the equilibrium voltage (open circuit voltage, E_{OCV}). However, the voltage drops off when current is drawn from the battery due to kinetic limitations of reactions and processes that must occur to produce current flow. This is in fact electrode polarization or overpotential. The battery electrode reactions involve a number of chemical, physical, and electrochemical steps. The rate of each of these steps determines the kinetics of the electrode and of course the whole cell. Three different kinetics effects for polarization need to be considered: activation polarization, ohmic polarization, and concentration polarization. The polarization, η, is defined by Eq. 1-8 as following:

$$\eta = E_{OCV} - E_T \qquad 1\text{-}8$$

Where E_T is the cell voltage with current flowing and E_{OCV} is the cell voltage at open circuit. Activation polarization is associated with the redox reactions at the interface of electrode/electrolyte. Ohmic polarization originates from the resistance due to contact problems between cell components and most importantly the charge transfer in the electrolyte. Concentration polarization is related to mass transport limitations for example limited diffusion of active species to and from the electrode surface. [5]

The power a battery can supply is related to the amount of current drained during specific amount of time in discharge. The polarization effects become more important when larger current is associated with the redox reactions in the battery. This might cause problems with phase transformations and solid-state diffusion in the electrode materials, affecting the voltage

profile during discharge/charge and also resulting in lower capacity and voltage the battery can deliver. In order to evaluate the cycling performance of batteries, they are typically examined at different current densities. For galvanostatic (constant current) cycling evaluations, battery researchers defined a standard rate as "C". 1C is defined as the amount of current needed to fully charge or discharge a battery in one hour. So 0.1C and 2C is the current required to charge or discharge a battery in 10 and 0.5 hours.

1.2 Lithium ion Batteries

With the continual miniaturization of electric devices such as cell phones and labtops, the challenges of powering them become more important. Furthermore, as plug-in hybrid electric vehicles and fully electroc vehicles have been developed, much attention has been focused on batteries as a reliable power source. [6-8] Today we have many different types of batteries like lead-acid batteries, nickel-cadmium batteries, nickel-manganese, nickel-metal hydride, and the modern lithium-ion batteries. In comparison with other batteries (Figure 1-1), LIBs have some major advantages that it comes to energy density (both gravimetric and volumetric), power density, and cycling performance. In terms of design they are the most efficient batteries in the market right now. A reliable power source should have high capacity and offer long cycle life while it has to be safe and capable of working in large temperature range, which are all potential features of LIBs. [9]

Secondary lithium batteries have a higher energy density than most of other rechargeable batteries because lithium has the lowest reduction potential (-3.04 V vs. SHE) and possesses high specific capacity (3862 mAh/g). More importantly, it is the lightest electrochemically active metal, the third lightest element, (0.53 g/cm^3), which means that for their size or weight they can store more energy than other secondary batteries. Because LIBs use non-aqueous electrolyte (usually organic solvents), they can operate in a large voltage range, resulting in a higher energy density. The specific energy density of LIBs with a voltage in the order of 4 V is ranging between 100 and 150 Wh/kg. Moreover, LIBs exhibit a lower self-discharge rate (the rate at which a fully charged battery loses its capacity only by sitting on shelf without being cycled) than other types of rechargeable battery. [2,10] These advantages could be enough drives in order to

be the most commonly used rechargeable batteries for different applications. However, there are few drawbacks with LIBs such as capacity loss and poor cyclability, which are caused by interactions between the electrode material and the electrolyte at their interface. Therefore, substantial improvements in terms of performance, cost, and safety are required to employ LIBs in future practical applications such as plug-in hybrid and electric vehicles. [11]

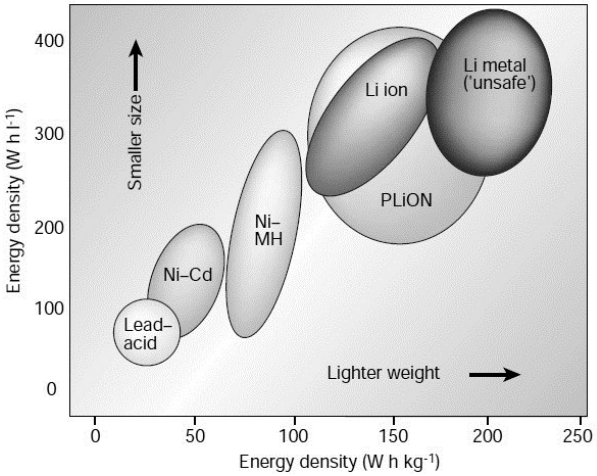

Figure 1-1: Comparison of different battery technologies in terms of volumetric and gravimetric energy density. Reproduced from 12

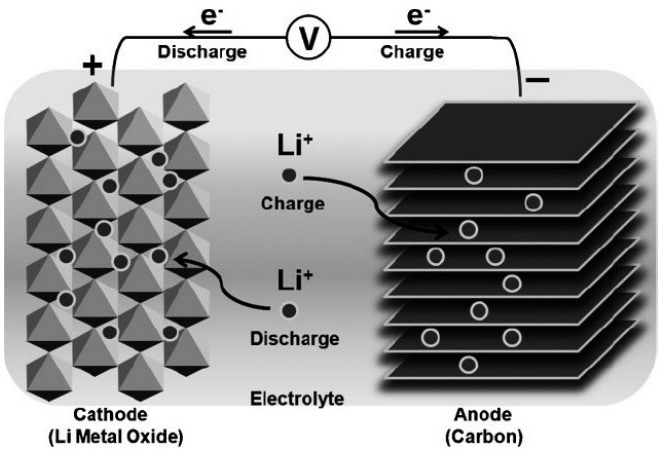

Figure 1-2: A schematic illustration of the working principles of a lithium-ion cell. Reproduced from 9

Frist commercial lithium-ion battery which was introduced by Sony Corporation in the early 1990s consisted of graphite anode and $LiCoO_2$ cathode, at which lithium ions intercalate within the free spaces of the host structure, immersed into EC organic solvent with $LiPF_6$ lithium salt. The advantage of utilizing these two electrode materials is that they result in a high cell voltage of 3.6 V and an energy density of approximately 120 – 150 Wh/kg. The reactions during the energy storage (charging) stage are:

Positive Electrode: $LiCoO_2 <=> Li_{1-x}CoO_2 + xLi^+ + x\bar{e}$ 1-9

Negative Electrode: $C + xLi^+ + x\bar{e} <=> Li_xC$ 1-10

Overall: $LiCoO_2 + C <=> Li_{1-x}CoO_2 + Li_xC$ 1-11

Commercial lithium-ion batteries are regarded for approximately 500 charge/discharge cycles. [13] During charge and discharge, lithium ions shuttle reversibly between two host structures (Figure 1-2).

1.2.1 Anode Materials

Increasing the specific energy of lithium cells requires electrode materials with higher capacity and/or cell voltage. To this end, several approaches are being adopted in attempts to enhance the performance of the state-of-the-art LIBs. With improvement in the practical electrochemical capacity of cathode materials from the commercialized systems (layered $LiMO_2$, M = Co, Ni, Mn, being 140 – 160 mAh/g)[14] to new cathode systems such as olivine $LiFePO_4$, defective Li-Mn-O spinels, $Li[Ni_xCo_{(1-2x)}Mn_x]O_2$ with a capacity in a range of 160 – 180 mAh/g, [4] 5 – 10% (C_a = 372 mAh/g and Q_M = 130 mAh/g) increase in total capacity of commercial LIBs can be obtained (Eq. 1-6). On the other hand, transition from conventional anode material with capacity of 372 mAh/g to novel anode systems with a capacity of 1000 – 3500 mAh/g leads to about 11 – 16% increase in total capacity of a LIB (C_c = 150 mAh/g and Q_M = 130 mAh/g). As finding fit cathode materials with higher capacities has been a difficult task, higher performance LIBs will require anode materials with higher specific capacities than those of commercial anodes with of course long stable cycling performance.

Commercial graphite anode is abundant, inexpensive, and exhibits a quite stable cyclability over prolonged charge/discharge cycles. The weak bonding of Li with carbon, structural stability of graphite, and small volume change (10%) upon cycling are other advantages of graphite. Li insertion/extraction reaction of graphite occurs at around 0.1 V vs. Li/Li^+, well above the critical voltage at which Li plating occurs and is still low enough to provide a high cell voltage. However, it has a modest specific capacity of 372 mAh/g upon intercalation of 1 lithium per 6 carbon (LiC_6). [15-18] Therefore it cannot meet the requirements for high energy power source demands. Most of the charge storage in graphite occurs between 0.1 and 0.2 V vs. Li/Li^+, and at high rates lithium plating may occur which presents a serious safety issue. One decade ago carbon materials were state-of-the-art in commercialized LIBs, while nowadays battery applications require much more energy than the amount of charge that carbonous material can provide. Therefore, considerable effort has been made toward discovering a new anode material with good cyclability performance and high capacity for LIB applications.

In theory, anode material could be pure lithium with specific capacity of 3862 mAh/g and volumetric capacity of 2062 mAh/cm^3, but in practice some safety problems would be necessary to be considered. Once Li metal piece is used as anode, lithium redeposition upon charging will lead to dendrite formation. The Li ions tend to plate out at locations that already had deposition rather than redepositing at the location where they originated, resulting in dendrite formation. These dendrites grow long enough to penetrate through the separator and would cause a short circuit in case making contact with the other side of the battery. Since large amount of current passes through those dendrites with small cross sections, ohmic heating occurs in presence of flammable organic electrolyte, leading to thermal runaway and fire/explosions. [19,20] Explosion occurs as more CO_2 is produced upon side reactions of organic solvent at high temperatures.

Table 1-1: Comparison of electrochemical properties of different LIB anodes. Reproduced from 21

Material	Density (g/cm^3)	Theoretical gravimetric capacity (mAh/g)	Theoretical volumetric capacity (mAh/cm^3)	Volume change (%)	Lithiation potential vs. Li/Li$^+$ (V)
Graphite	2.25	372	837	10	0.05
Li	0.53	3862	2062	100	0
$Li_4Ti_5O_{12}$	3.5	175	613	1	1.6
Si	2.33	3590	8365	280	0.37
Ge	5.5	1600	8800	270	0.5
Sn	7.29	994	7246	260	0.6
Al	2.7	993	2681	~ 100	0.3
Sb	6.7	660	4422	200	0.9
Bi	9.78	385	3765	215	0.8
Mg	1.3	3350	4355	100	0.1

The key parameters for electrode materials may be pointed out as: reversible Li ion insertion/extraction reactions; large capacity and light weight to offer high energy density; high ionic and electrical conductivity; minimum volume change during Li insertion/extraction; not too reactive with the electrolyte; environmentally benign; ease of manufacture; low cost. Since charge carrier in LIBs is lithium ions, higher capacity materials should be capable to store more lithium in their structure. Thus elements that are able to alloy with lithium could be very promising candidates for anode material applications in terms of capacity and energy. Every element with the capability to alloy with Li electrochemically could be employed as LIB anode including silicon (Si), aluminum (Al), antimony (Sb), germanium (Ge), lead (Pb), zinc (Zn),

cadmium (Cd), magnesium (Mg), gold (Au), platinum (Pt), and tin (Sn). Another merit of alloy anodes is their moderate operation voltage versus lithium, considering both safety concerns of lithium deposition and energy penalty of battery cells. Table 1-1 compares the electrochemical properties of different anode materials.

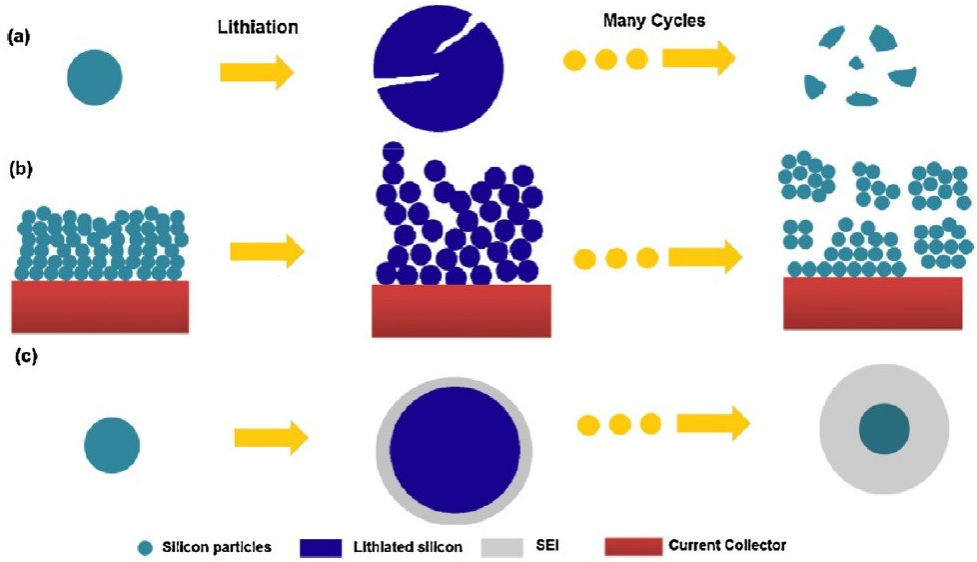

Figure 1-3: Schematic electrode failure mechanisms for alloy anode materials: (a) material pulverization, (b) morphology and volume change of the entire electrode, and (c) continuous SEI growth. Reproduced from 22

Li alloying (lithiation) is a different Li storage mechanism from Li intercalation in a layered material such as $LiCoO_2$ or graphite because Li alloying generally induces significant changes in the host material as a new phase with different properties and crystal structure will form. [23] In spite of achieving higher specific capacity and safer operation, there are many issues around employing alloy anode materials in a lithium cell. The unfortunate fact about these active materials is that they suffer from large volume changes during lithium insertion/extraction. Volume change is about 10% for lithium intercalation into graphite structure between graphene sheets, while it could go as high as 280% for alloy anodes. [2,21] Huge structure expansion/contraction in lithiation/delithiation causes some mechanical disintegration and structural degradation because of nonuniform distribution of mechanical stresses. Then crack initiation and propagation are expected by cycling, which finally leads to mechanical failure of

the material. This is the main issue of using alloy anode materials for Li battery application. Hence, poor cyclability would occur due to integrity loss of active parts of the battery cell and/or losing electronic contact between active material and conductive network or active material and current collector. [24-27] Generally there are three fundamental challenges to using alloy anodes as a viable battery electrode material (Figure 1-3); material pulverization, morphology and volume change of the whole electrode, and overgrowth of SEI layer.

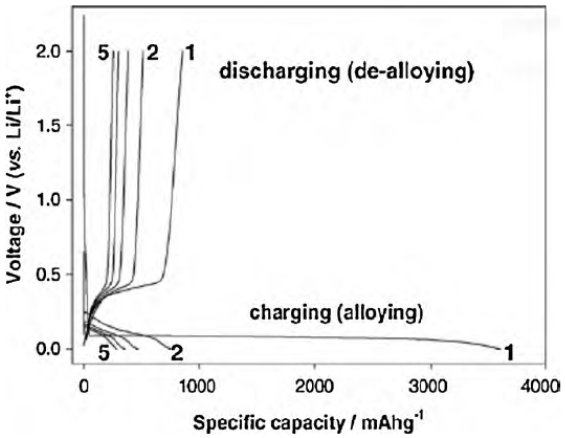

Figure 1-4: Galvanostatic lithiation – delithiation voltage profiles of Si anode with an average powder size of 10 µm at cycle 1, 2, and 5. Reproduced from 21

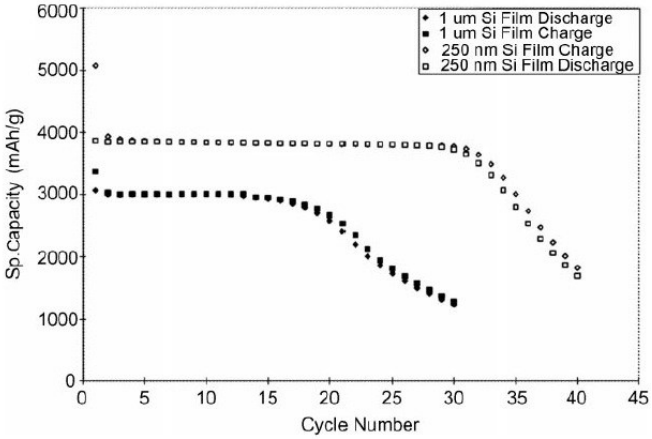

Figure 1-5: LIB cycling performance of Si thin films with thicknesses of 1 µm and 250 nm. Reproduced from 9

1.2.2 Nanostructuring Anode Materials

Numerous approaches have been applied on these high capacity alloy anode materials to exhibit better cycling performance and have more stable structure during battery operation. One of the decent solutions is nanostructuring. Figure 1-4 shows an example of the charge/discharge curves of Si anode with an average powder size of 10 µm, which clearly demonstrates poor cycling performance of Si anode, i.e. large initial irreversible capacity, low coulombic efficiency, and rapid capacity loss. More obviously Figure 1-5 illustrates the difference in cycling performance of micron sized and nanometer sized Si thin films. Recently nanomaterials have been extensively developed for enhanced properties. Research has revealed that reducing active material size down to nano scale enhances fracture resistance of materials and also boosts

lithiation/delithiation rates. In other words, nanomaterials can accommodate large strain and stress better and more efficiently than the bulk structures, therefore large volume changes during cycling would not necessarily cause crack formation and pulverization of material. This directly results in more stable cycling performance. Indeed, smaller size structures provide better volume change accommodation in which cracking and fracture could be postponed due to small imposed stress magnitudes compared with the strength of the active material. [28]

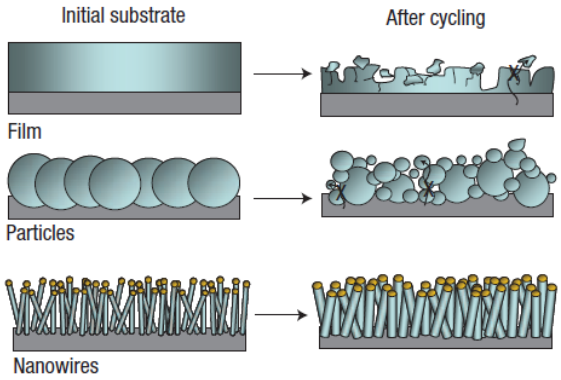

Figure 1-6: Schematic of structural changes that occur for different morphologies of materials (films, particles, and wires) during electrochemical cycling against Li. Reproduced from 28

The key advantages of utilizing nanomaterials for energy storage can be increasing charge/discharge rates due to shorter solid-state diffusion distances for Li, enhanced electron transport, and high contact area with electrolyte enabling high Li flux into the materials' structure. Disadvantages associated with nanomaterials application for electrochemical energy storage systems could be difficulty to synthesize and/or control the shape and size, significant side reactions with electrolyte due to high contact with electrolyte (high surface area), and low volumetric energy density due to high porosity. [29] Volumetric energy density is significantly important for mobile applications. Larger surface area of nanomaterials offers more electrolyte decomposition on active materials surface and SEI formation through which Li is consumed irreversibly and leads to irreversible capacity loss. Most of SEI formation occurs at first cycle when a fresh active materials surface exposes to organic solvents of electrolyte at voltages below 0.9 V vs. Li/Li^+. Therefore, most of irreversible capacity loss during first cycle originates from SEI formation. Besides, continuous breakage and reformation of SEI on subsequent cycles

increases internal battery impedance due to thickening such a nonconductive film on active materials surface. Thin films, [30-33] nanoparticles, [34-38] mesoporous nanomaterials, [39-43] nanotubes, [44-48] and nanowires [49-55] are nanostructure morphologies, which have been tried as LIB anode material. Among nanostructure morphologies, one-dimensional oriented nanostructures have attained the most attention because of promising electrochemical cycling performance (Figure 1-6). One-dimensional structures have become a more favorable configuration for anode active material and studies on nanowires and nanotubes are increasing in the last few years. [28,44,56-69]

1.2.3 Silicon Anodes

Silicon with volume expansion of about 280% corresponding to $Li_{15}Si_4$ phase upon lithiation is the most challenging anode material for LIB applications because this huge volume change can lead to mechanical and structural disintegration of anode material in the form of cracking and fracture, consequently results in rapid capacity loss over the course of cycling. However, despite its mechanical instability upon (de)alloying with Li, Si remains a very interesting material for LIB anodes since it provides the highest known specific capacity for room temperature electrochemical lithiation (~ 3590 mAh/g), one order of magnitude larger than that of graphite. As well, Si has a low delithiation potential, around 0.37 V vs. Li/Li^+, so that high battery voltages, thereby high energy density, can still be reached with the classical oxide- or phosphate-based cathodes. Si is an environment-friendly material and it is the second most abundant material in the Earth crust, which guarantees availability at low cost for future commercial use. Because of these attributes, a great deal of attention has been given to using silicon as Li-ion cell anode material. To overcome the large volume change issue and thus obtain better capacity retention and cycle life, various approaches have been applied to Si anodes. Of all, nanostructuring is the most promising method, although it is still far from practical application for long lasting batteries. Therefore combination of strategies (nano-sized Si and dispersing Si in either active or inactive matrixes) have been suggested and tried for improvement in Li cycling performance of Si anode.

An inactive matrix acts as a cushion and accommodates the volume change in the Si active material, thereby prevents pulverization of Si. The host matrix must possess good ionic and

electronic conductivities and suitable mechanical strength. [21] Also, the inactive matrix must be able to sustain a high stress with a large elastic deformation (ideally superelastic material) when the active materials expand so that the active particles are under high compressive residual stress during Li insertion. This compressive stress effectively prevents particles from cracking as cracking occurs under tensile stress. [70,71] Therefore, a matrix with high strength, low ductility, and a low elastic modulus may reduce the tendency for active material cracking. Ball milling electrochemically inert metallic compounds such as TiB_2, [72] SiC, [73] and TiC [74] with Si nanoparticles resulted in improvement in cycling performance of Si in LIB. Carbon coating was also applied onto the Si-TiN [75] and Si-TiB_2 [76] nanocomposite anodes and showed an improved performance. When there is an active matrix in anode nanocomposite, both the active and the host material are electrochemically reactive towards Li. The idea here is to have one component lithiated while the other acts as a buffer to alleviate the volume change as they react with Li at different onset potentials. Sb-Sn, [77] Mg-Si, [78] Sb-Al, [79] Sn-Ag [80] are the examples.

Silicon thin film is one of the simplest nanostructures that can be prepared and used for lithium cycling. They can be synthesized through physical vapor deposition (PVD) and chemical vapor deposition (CVD). An increase in film thickness of amorphous Si thin films prepared using CVD on stainless steel substrate from 250 nm to 1350 nm results in lower capacity of 370 mAh/g (vs. 1100 mAh/g) after 100 cycles at 0.175 mA/cm^2. [81] For alloy anode thin films, thickness plays a critical role as thinner films always show more stable cycling performance. Ultra thin Si films down to 50 nm have been reported for antipulverization and no capacity fade over 2000 cycles. [82] Such a thin Si film is not a practical solution for commercial LIBs as the active material mass loading in this case would be so low, thereby the absolute measured capacity would be low. Very interesting approaches have been applied to Si thin film anodes for longer cycling stability. Yu et al. [83] proposed a new strategy of stress relaxation for Si films using an elastometer susbtrate and an anode design for more efficient ion and electron transport (Figure 1-7). In another study, authors introduced a small amount of oxygen (> 20 at.%) during synthesis of Si thin films, resulted in improvement in cycling performance as LIB anode. [31]

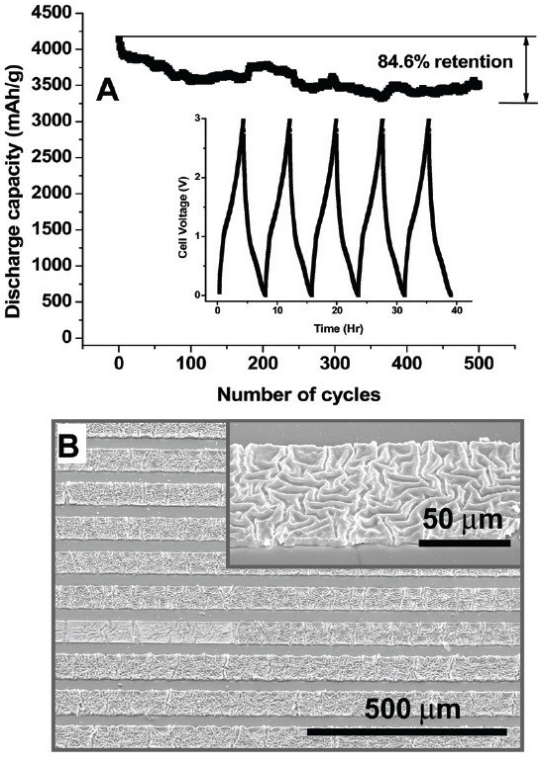

Figure 1-7: (A) Long cycle stability of the battery cell up to the 500th cycle with nearly 85% capacity retention. The inset is a typical charge/discharge profile from the 13th cycle to the 18th cycle. (B) SEM images show the buckled Si after lithiation, after six cycles charge/discharge under the charge rate of 1C. Reproduced from 83

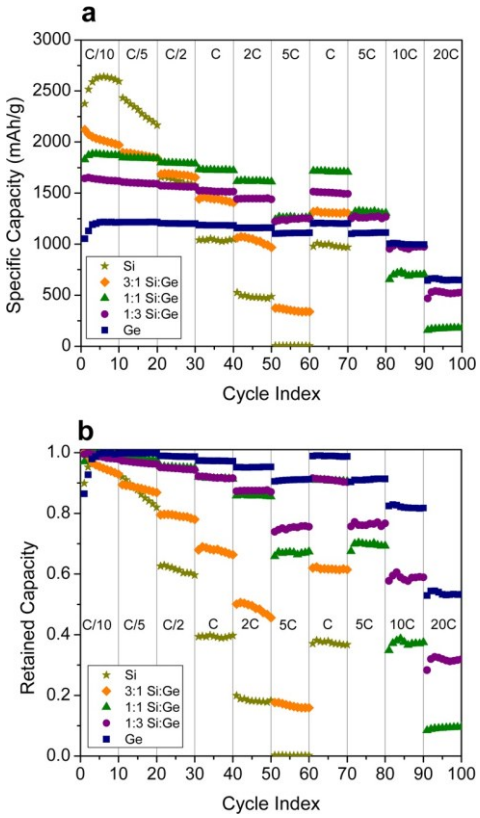

Figure 1-8: Cycling data of $Si_{(1-x)}Ge_x$ films. (a) Specific capacity, (b) retained capacity. Reproduced from 84

A high capacity of 2200 mAh/g with no capacity loss for the first 120 cycles and about 0.15% loss per cycle for cycles 150 – 300 and 80% retention after 300 cycles was obtained using this strategy combined with low-temperature annealing in air. Abel et al. [84] investigated the Li electrochemical cycling performance of Si thin film with different amount of incorporated Ge (25, 50, 75, and 100 at.%). The idea behind this is the fact that silicon has high Li storage capacity (high energy density) while germanium is a superior electronic and ionic conductor (high power density). At 5C, Si film retains almost zero capacity, Ge film retains about 90%, $Si_{25}Ge_{75}$ retains 75%, and $Si_{50}Ge_{50}$ retains 68% their initial capacity. Adjusting the composition in the $Si_{(1-x)}Ge_x$ system demonstrates a trade-off between rate capability and specific capacity.

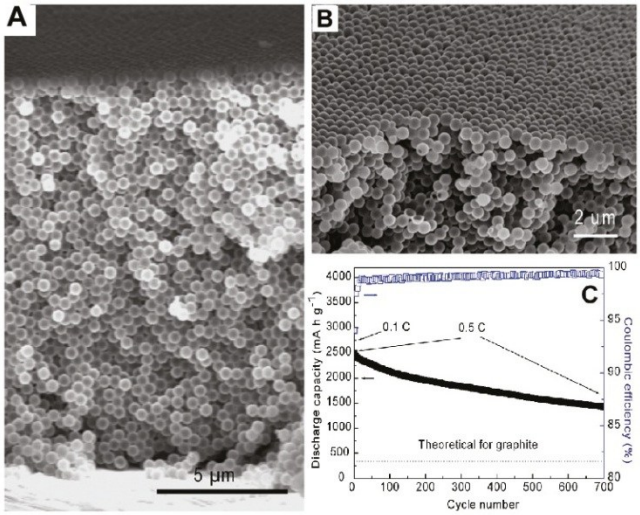

Figure 1-9: (A) Typical cross-sectional SEM image of hollow Si nanospheres. (B) SEM side view (45° tilt) of the same sample of hollow Si nanospheres. (C) Reversible Li discharge capacity and Coulombic efficiency of the hollow Si nanospheres versus cycle number in comparison with the theoretical capacity of graphite. Reproduced from 85

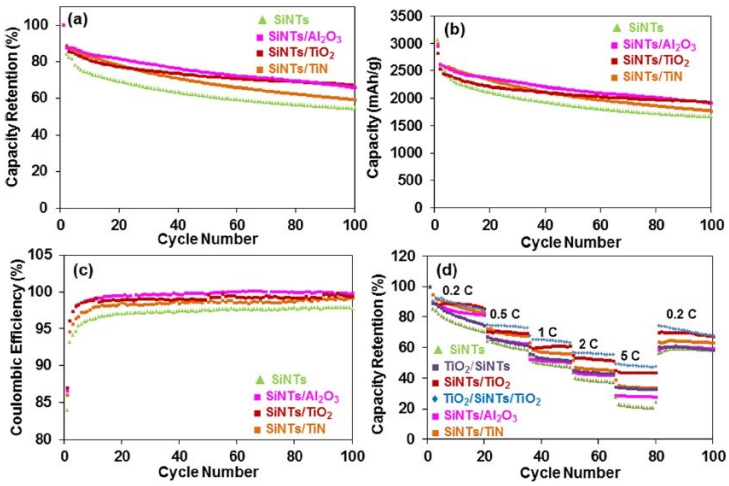

Figure 1-10: (a) and (b) Capacity retention vs. cycle number for SiNT's coated with 3 nm of Al_2O_3, TiN, and TiO_2 on their outer surface, tested at 0.2C rate; (c) corresponding coulombic efficiency; and (d) rate dependence of capacity retention as a percentage of capacity at 0.2C. Reproduced from 65

Hollow Si structures are also interesting candidates for future LIB anode materials. They provide empty space for the volume expansion. This offers lower diffusion-induced stresses, which could be 5 times lower than that in a solid structure with an equal volume. [38] This means that the hollow structures will show more stable structure as they fracture less during alloying/dealloying with Li and correspondingly show better cycling performance. Hollow Si nanospheres with an initial reversible capacity of 2725 mAh/g and only 8% capacity loss after 100 cycles during 700 total cycles demonstrate good electrochemical stability of hollow nanostructures (Figure 1-9). [85] The Li electrochemical performance of hollow Si nanotubes has been also examined and a good performance was exhibited. The use of Si nanotubes increases the accessible surface area of the active material to the electrolyte, so Li ions can incorporate into the Si more easily. Reversible capacity of 3200 mAh/g with retention of 89% after 200 cycles at 1C was reported for Si nanotubes. [66] A recent study on Si nanotubes from our group showed further improvement in cycling performance and more importantly on coulombic efficiency by coating them with ALD TiN, TiO_2, and Al_2O_3. [65] Substantial improvements were achieved in the

capacity retention (1700 mAh/g vs. 1287 mAh/g for the uncoated baseline, after 200 cycles at 0.2C), steady-state coulombic efficiency (100% vs. 97–98%), and high rate capability (capacity retention of 50% vs. 20%, going from 0.2C to 5C) (Figure 1-10).

Table 1-2: Characteristics of Lithium and Sodium. Reproduced from 90

Parameter	Lithium	Sodium
Ion radius (Å)	0.76	1.06
Atomic weight (g/mol)	6.9	23
E° (V vs. Li/Li^{+})	0	0.3
Cost for their carbonate ($/ton)	5000	150
Capacity (mAh/g)	3829	1165

1.3 Sodium ion Batteries

LIBs gained wide popularity due to their high energy density and have been commonly used in portable devices nowadays. This rechargeable battery has attracted a great deal of interest for plug-in hybrid and electrical vehicles in the last decade. However, the LIB industry (first commercialized in 1991) has faced an increasing concern on the cost and scarcity of lithium resources since recently. [86,87,88,89] Other factors such as geographical limitations on the lithium resources are also in charge here. Sodium is an intriguing alternative for lithium because of the lower cost (90 – 95% cheaper sodium precursors than lithium carbonate), its far more natural abundance, i.e. the 6th most abundant element in the earth's crust (~ 2.64 wt.% for Na vs. 0.006 wt.% on earth for Li), and its widespread terrestrial reserves of sodium mineral salts (Table 1-2). [90,91,92] Lower gravimetric and volumetric density of sodium-ion batteries (NIBs, NABs, or SIBs) in comparison with LIBs makes it an appropriate choice for stationary energy storage systems for electric grids. Na-ion technology is indeed a promising low-cost alternative for current Li-ion system, where the most significant cost benefit originates from the fact that Al shows no activity toward Na, allows it to be employed as anode current collector rather than more expensive and heavier Cu current collectors, which are necessary for LIBs. [93]

1.3.1 Anode Materials

With the aim of accomplishing reasonable energy densities in NIBs with optimal cycling performance similar to what have been explored for LIBs in the last two decades, significant amount of scientific research is being conducted on discovery and optimization of new materials for secondary Na batteries. The Na insertion/extraction in a host material is much more challenging than that of Li due to the size matter. Areas of NIB research that need to be addressed include cathode, anode, electrolyte, and separators. Tremendous effort has been dedicated to develop new cathode materials resulted in diversification of the cathode structures from $Na_2FeP_2O_7$, [94] $NaCrO_2$, [95] $Na[Ni_{0.25}Fe_{0.5}Mn_{0.25}]O_2$, [96] $Na_{0.67}Mn_{0.95}Mg_{0.05}O_2$, [97] to low cost sodium manganese hexacyanoferrates, [98] carbon-coated $Na_3V_2(PO_4)_3$ embedded in porous carbon matrix, [99] porous graphite nanoplatelets, [100] and indigo carmine, [101] whereas much less work has been focused on the anode side.

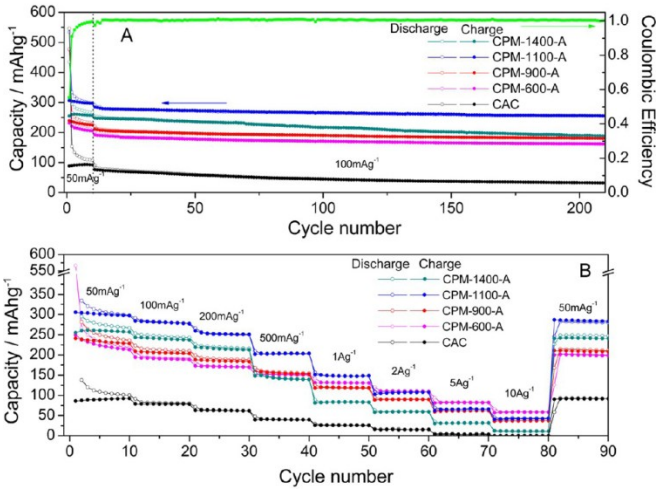

Figure 1-11: (a) Cycling performance and (b) rate performance of carbonized peat moss (CPM) with carbonization temperatures of 600, 900, 1100, 1400 °C and with activation along with commercial activated carbon (CAC). Reproduced from 112

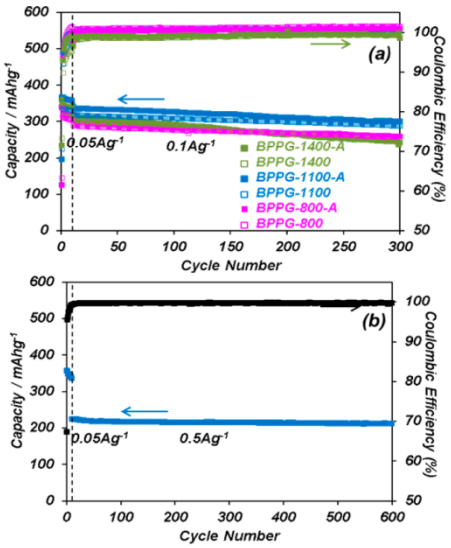

Figure 1-12: Cycling performance of banana peel pseudographite (BPPG) with carbonization temperature of 800, 1100, 1400 °C and with activation. Reproduced from 113

Similar to Li, metallic Na (with theoretical specific capacity of 1165 mAh/g and volumetric capacity of 1130 mAh/cm^3) [102] suffers from the safety issue of dendritic formation. Besides, low

melting point of Na (98 °C vs. Li with 181 °C) would raise more doubts concerning its safety. [87,90,103,104,105] After successful implementation of graphite as common anode for commercial LIBs, the majority of anode research has been devoted to carbon-based materials. Carbon is abundant, chemically inert, and is one of the most versatile elements in the periodic table. It can take on many structures and morphologies, ranging from diamond to graphite and everything in between. The sodiation of graphite is thermodynamically unfavorable at room temperature and it is widely known as an electrochemically inactive material in Na electrolyte. [106] Non-graphitic carbons, e.g. hard carbons, have attracted significant attention instead. [92,107,108] Several other type of carbonous materials have been suggested as NIB anode such as a highly disordered carbon composite with a reversible capacity of 225 mAh/g at 100 mA/g, [109] carbon nanofibers derived from cellulose exhibiting reversible capacity of 176 mAh/g at 200 mA/g, [110] hollow carbon nanospheres, [111] the one derived from peat moss giving a capacity of 298 mAh/g at 50 mA/g and 203 mAh/g at 500 mA/g (Figure 1-11), [112] and the one derived from banana peel offering superb functionality for NIB, charge capacity of 221 mAh/g at 500 mA/g is degraded by 7% after 600 cycles and a capacity of 336 mAh/g at 100 mA/g is degraded by 11% after 300 cycles with about 100% coulombic efficiency (Figure 1-12). [113]

Anatase TiO_2 with reasonably small volume change of 4%, [114,115,116] TiO_2 with the hollandite structure, [117] $Na_2Ti_3O_7$, [118] and $Li_4Ti_5O_{12}$ [119] have also been attempted and are appealing due to their cost and environmental friendliness advantages. Several different nanocomposite anodes showed respectable performance against Na including sandwich-like porous carbon/graphene composite, [120] acid-exfoliated MoS_2 nanoflakes in a reduced graphene oxide matrix, [121] nanocomposite of MoO_3 nanobelts coated with conductive polypyrrole polymer, [122] nano-Se-impregnated mesoporous carbon composite, [123] and low cost Fe_2O_3 nanocrystals anchored onto graphene nanosheets. [124] The amount of efforts conducted on development of sodium battery electrode materials in the past few years indeed shows the importance of NIBs implementation for the next generation of energy storage systems.

The interest of sodium battery research on metallic anode materials has been intensified recently. Na can alloy with several metallic elements including Sn, Sb, Pb, P, and Bi with theoretical specific capacities of 847 ($Na_{15}Sn_4$), 660 (Na_3Sb), 484 ($Na_{15}Pb_4$), 2596 (Na_3P), and 385 mAh/g (Na_3Bi), respectively. However, there is a large volume change associated with the

Na alloying/dealloying reaction of these materials, ~ 410% for $Na_{15}Sn_4$, [125,126] 290% for Na_3Sb, [127,128] 365% for $Na_{15}Pb_4$, [102,129] 308% for Na_3P, [130] and 250% for Na_3Bi. [129] Repeated volume expansion/contraction induces tremendous microstructural damage to the electrode materials, leading to severe pulverization and electric contact loss, subsequently results in capacity loss over time.

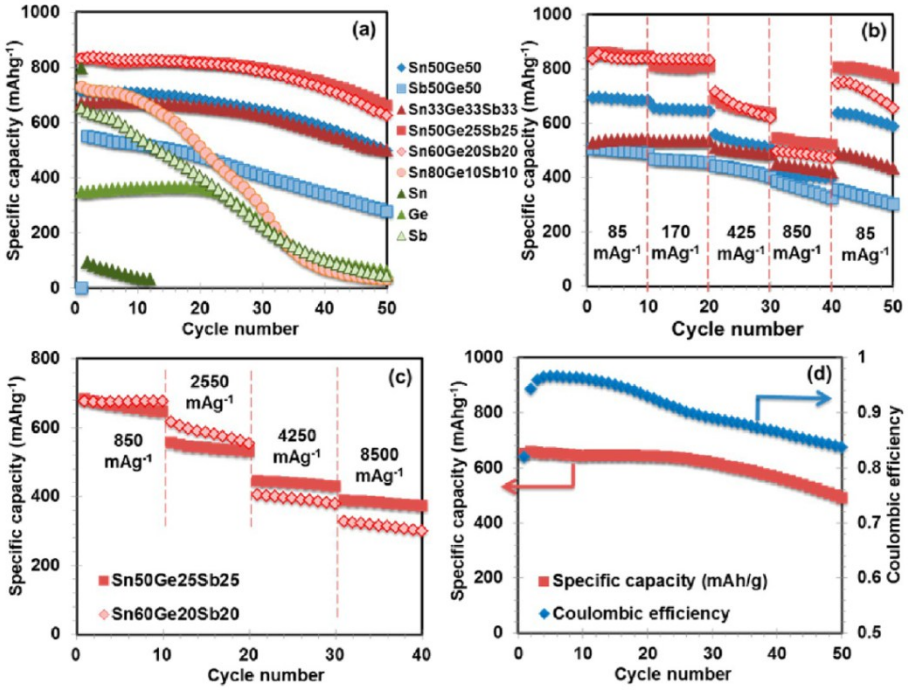

Figure 1-13: (a) Cycling of the various SnGeSb mixed alloys along with comparisons to the bulk pure metals at a current rate of 85 mA/g. (b) Power performance of the mixed metal alloys. (c) High power performance of the Sn50Ge25Sb25 and Sn60Ge20Sb20 alloys. (d) Long term cycling at 425 mA/g. Reproduced from 138

From the valuable lessons with LIB materials, several different nanostructuring approaches can be applied to resolve the abovementioned issues. For instance, using hybrid nanostructures is an effective method to accommodate the volume change produced by the alloy material, which is dispersed in an either active or inactive matrix. SnO_2@MWCNT nanocomposite with 72% capacity retention (604 mAh/g) over 50 cycles at 0.1C, [131] layered-structured SnS_2-reduced graphene oxide nanocomposite showing a capacity of 630 mAh/g at 200 mA/g, [132] Sn_4P_3/C nanocomposite with a reversible capacity of 850 mAh/g, [133] commercial microsized red

phosphorous and CNTs composite delivering initial reversible capacity of 1675 mAh/g and 76.6% retention over 10 cycles, [134] amorphous phosphorous/carbon nanocomposite retaining about 1000 mAh/g reversible capacity after 80 cycles at 250 mA/g, [135] Sb nanoparticles embedded in the carbon nanofibers with reversible capacity of 568 mAh/g at C/15 after 400 cycles, [136] and Sb_2S_3 coated graphene giving a capacity of 636 mAh/g after 50 cycles at 50 mA/g, [137] are some examples. A novel microstructure engineering in Sn50Ge25Sb25 thin film, a nanocomposite consisting of 10 – 15 nm Sn and SnGe nanocrystallites densely dispersed within an amorphous matrix, also led to a high initial reversible capacity of 833 mAh/g and retention of 662 mAh/g after 50 cycles at 85 mA/g with excellent rate capability of holding 381 mAh/g at 8500 mA/g (Figure 1-13). [138]

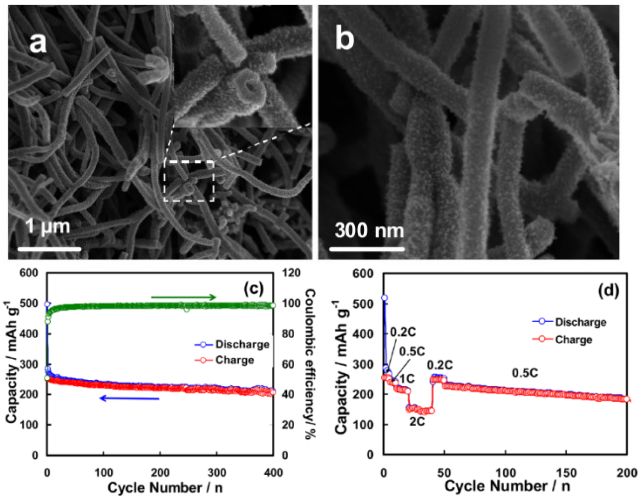

Figure 1-14: (a,b) SEM micrographs of Hollow carbon nanowires (HCNWs). (c) Cycling performance of the HCNWs electrode at a current density of 50 mA/g (0.2C). (d) Discharge capacity of the HCNWs electrode as a function of cycle number at different current densities. Reproduced from 142

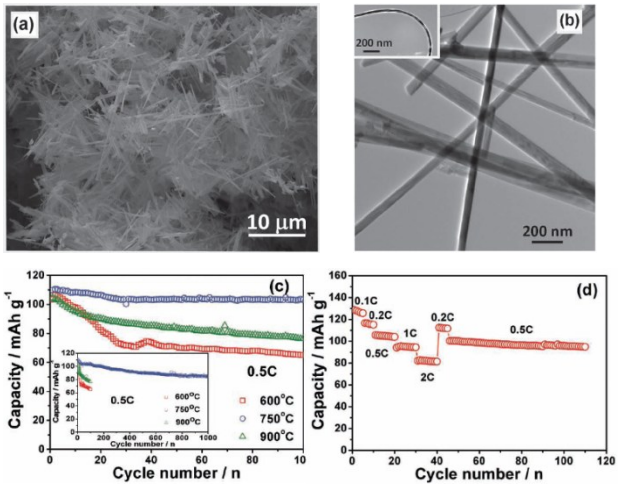

Figure 1-15: (a) SEM and (b) TEM micrograph of $Na_4Mn_9O_{18}$ calcined at 750 °C. (c) Cycle performance of $Na_4Mn_9O_{18}$ samples calcined at different temperatures at a current density of 60 mA/g (0.5C). (d) Discharge capacity of $Na_4Mn_9O_{18}$ nanowires calcined at 750 °C at different current densities. Reproduced from 144

Superb cycling performance of one-dimensional nanostructures in Li-ion batteries has drawn significant attention of Na battery researchers to consider 1D nanostructure materials as potential anodes for NIBs. [139,140,141] The key advance is the capability of the nanowire structure to overcome the problems associated with the large volume change upon cycling. They also offer

short diffusion distance, good electrical conductivity along their length, larger surface area in contact with the electrolyte, and more importantly, the ability to be grown directly on conductive substrates without any binder or additive. Examples of intriguing performances of 1D nanostructure anodes for NIBs could be carbon-coated anatase TiO_2 nanorods structure showing good high-rate capability with a capacity of 53 mAh/g at rate of 33 A/g, [116] hollow carbon nanowires (Figure 1-14) with excellent cycling stability (82.2% retention over 400 cycles and delivering 149 mAh/g at 500 mA/g), [142] 3D nanoforest of C/Sn/Ni/TMV1cys retaining 405 mAh/g_{Sn} capacity after 150 cycles at 50 mA/g, [143] and also $Na_4Mn_9O_{18}$ nanowires exhibiting 77% retention after 1000 cycles at 0.5C (Figure 1-15). [144]

1.3.2 Germanium Anodes

Ge can also electrochemically alloy with Na up to 1:1 ratio, NaGe phase with theoretical capacity of 369 mAh/g, [145,146,147] Na_3Ge and $NaGe_4$ are other equilibrium phases present in the Ge – Na phase diagram. [148] An early effort to cycle Ge powder versus Na was unsuccessful though. [149] The theoretical results show that the Na diffusion along the surface of Ge is more facile than that in the bulk. [146,147] Hence implementation of Ge nanostructures anodes for Na battery application is necessary, as the large surface area to volume shortens the bulk diffusion distances. Very recently, Baggetto et al. [146] and Abel et al. [147] reported application of Ge nanostructures as sodium-ion anode material, which are, to the best of our knowledge, the only studies examining Ge as anode for NIBs. The electrochemical performances of Ge thin film and Ge nanocolumnar structures are certainly promising, although more improvements are required for practical application. Dense evaporated Ge thin film showed a significant capacity loss after only 15 cycles. [147] Our study on thin film anodes also demonstrated that pure Ge film's capacity starts to decay after few initial cycles. [138] Thorough characterization of cycled anodes revealed that a sharp Na segregation developed through the film thickness after only two cycles, considered as major contributor to electrical contact loss. High cost is the main drawback of Ge, although its price can be reduced since it is abundant on the earth's crust. [150]

1.4 Motivation and Scope of this Thesis

Since current LIB systems are still far from reaching the demands of the high energy density on electric vehicles and hybrid electric vehicles and they cannot match the high charge/discharge current requirements of the next generation of batteries, this doctoral thesis aims to improve the long-term electrochemical cycling performance of LIB and NIB anode materials by designing nanomaterials and also investigate the degradation mechanisms of electrode materials. In fact, the ultimate goal here is to enhance battery cycle life as well as capacity of anode structures via design and synthesis of promising materials for mobile and stationary applications, with particular attention to one-dimensional nanostructure (nanowires) materials and surface coating strategy.

Chapter 2 presents the results of our study on the effect of Mg and Mg_2Si coating materials with different thicknesses on the electrochemical cycling performance of SiNWs LIB anode materials. The cycling performance of the coated and baseline SiNWs are compared and we show that how the coating materials affect the coulombic efficiency of the bare SiNWs anode through comprehensive surface analysis. The role of the coating materials on the mechanical integrity of the nanowires is also revealed by electron microscopy analysis. We also discuss how the SiNWs-based anode material degrades upon cycling in Li-ion cell and propose the major degradation mechanism for the SiNWs-based anodes with the nanowires being directly grown on the substrate.

In chapter 3 we demonstrate significant improvement in the electrochemical performance of SiNWs by using inactive, conductive, and adherent titanium nitride (TiN) coating films. We explore the TiN coating effects through characterization of as-synthesized and cycled samples. Effect of coating deposition method (reactive sputtering and ALD) and temperature as well as TiN coating thickness is evaluated. We also optimize the anode materials performance by tuning the parameters regarding materials synthesis. TEM analysis shows that thinner or thicker than a certain coating thickness may not be as effective for mechanical integrity of the wires.

We propose a SiNWs-based anode system with Sn coating deposited via magnetron sputtering for LIBs in chapter 4. In order to obtain the optimum electrochemical performance from the anode material, different Sn coating thicknesses are also evaluated. Our results clearly

determine the optimum conditions for the best performing anode material. Detailed analysis of as-synthesized, cycled, and partially cycled anode materials are also included and explain why sputtered Sn coating can effectively promote the cycling performance of SiNWs LIB anode. Partially lithiated/delithiated anodes are also characterized to further support our hypothesis.

In Chapter 5, we propose an approach based on pre-cycling against Li through which the challenge of poor sodiation/desodiation kinetics of Ge NIB anode can be tackled and enabled us to examine the electrochemical cycling performance of GeNWs against Na for the first time. As well, we demonstrate that such an approach leads to improve the cycling performance of Ge thin film anodes. Comprehensive analysis and characterization of GeNWs and Ge thin film NIB anodes are also presented with the aim to help understanding why pre lithiation – delithiation could make such difference.

1.5 References

1 J. M. Tarascon, and M. Armand, Nature, 2001, 414, 359-367.

2 W. J. Zhang, J. Power Sources, 2011, 196, 877-885.

3 A. Anani, and R. A. Huggins, J. Power Sources, 1992, 38, 351-362.

4 U. Kasavajjula, C. Wang, and A. J. Appleby, J. Power Sources, 2007, 163, 1003-1039.

5 M. Winter, and R. J. Brodd, Chem. Rev., 2004, 104, 4245-4270.

6 D. Linden, and T. B. Reddy, Handbook of Batteries, 3rd Ed., McGraw-Hill, New York, 2002.

7 M. R. Palacín, Chem. Soc. Rev., 2009, 38, 2565-2575.

8 A. Manthiram, J. Phys. Chem. Lett., 2011, 2, 176-184.

9 R. Teki, M. K. Datta, R. Krishnan, T. C. Parker, T.-M. Lu, P. N. Kumta, and N. Koratkar, Small, 2009, 5, 2236-2242.

10 W. Xu, Silicon Nanowire Anode for Lithium-Ion Batteries: Fabrication, Characterization and Solid Electrolyte Interphase, PhD thesis, Louisiana State University, 2011.

11 J. Wen, Y. Yu, and C. Chen, Mater. Express, 2012, 2, 197-212.

12 J. M. Tarascon, and M. Armand, Nature, 2001, 414, 359-367.

13 C. A. Vincent, and B. Scrosati, Modern Batteries: An Introduction to Electrochemical Power Sources. E. Arnold, 1997, Ed. 2.

14 M. M. Thackeray, C. Wolverton, and E. D. Isaacs, Energy Environ. Sci., 2012, 5, 7854-7863.

15 B. Scrosati, Electrochim. Acta, 2000, 45, 2461-2466.

16 E. Peled, C. Menachem, D. Bar-Tow, and A. Melman, J. Electrochem. Soc., 1996, 143, L4-L7.

17 M. Yoshio, H. Wang, and K. Fukuda, Angew. Chem., 2003, 115, 4335-4338.

18 M. Yoshio, H. Wang, K. Fukuda, Y. Hara, and Y. Adachi, J. Electrochem. Soc., 2000, 147, 1245-1250.

19 Q. Wang, P. Ping, X. Zhao, G. Chu, J. Sun, and C. Chen, J. Power Sources, 2012, 208, 210-224.

20 Y. Chen, and J. W. Evans, J. Electrochem. Soc., 1996, 143, 2708-2712.

21 W. J. Zhang, J. Power Sources, 2011, 196, 13-24.

22 H. Wu, and Y. Cui, Nano Today, 2012, 7, 414-429.

23 M. R. Zamfir, H. T. Nguyen, E. Moyen, Y. H. Lee, and D. Pribat, J. Mater. Chem. A, 2013, 1, 9566-9586.

24 J. YangáLee, J. Mater. Chem., 2011, 21, 9819-9824.

25 Y. Oumellal, N. Delpuech, D. Mazouzi, N. Dupre, J. Gaubicher, P. Moreau, P. Soudan, B. Lestriez, and D. Guyomard, J. Mater. Chem., 2011, 21, 6201-6208.

26 C. R. Becker, K. E. Strawhecker, Q. P. McAllister, and C. A. Lundgren, ACS Nano, 2013, 7, 9173-9182.

27 M. N. Obrovac, and L. Christensen, Electrochem. Solid-State Lett., 2004, 7, A93-A96.

28 C. K. Chan, H. Peng, G. Liu, K. McIlwrath, X. F. Zhang, R. A. Huggins, and Y. Cui, Nat. Nanotechnol., 2007, 3, 31-35.

29 P. G. Bruce, B. Scrosati, and J. -M. Tarascon, Angew. Chem., Int. Ed., 2008, 47, 2930-2946.

30 M. K. Datta, J. Maranchi, S. J. Chung, R. Epur, K. Kadakia, P. Jampani, P. N. Kumta, Electrochim. Acta, 2011, 56, 4717-4723.

31 P. R. Abel, Y. M. Lin, H. Celio, A. Heller, and C. B. Mullins, ACS Nano, 2012, 6, 2506-2516.

32 H. C. Liu, and S. K. Yen, J. Power Sources, 2007, 166, 478-484.

33 J. P. Maranchi, A. F. Hepp, and P. N. Kumta, Electrochem. Solid-State Lett., 2003, 6, A198-A201.

34 Z. S. Wu, W. Ren, L. Wen, L. Gao, J. Zhao, Z. Chen, G. Zhou, F. Li, and H. M. Cheng, ACS Nano, 2010, 4, 3187-3194.

35 J. Z. Wang, C. Zhong, D. Wexler, N. H. Idris, Z. X. Wang, L. Q. Chen, and H. K. Liu, Chemistry-A European Journal, 2011, 17, 661-667.

36 C. He, S. Wu, N. Zhao, C. Shi, E. Liu, and J. Li, ACS Nano, 2013, 7, 4459-4469.

37 J. Luo, X. Zhao, J. Wu, H. D. Jang, H. H. Kung, J. Huang, J. Phys. Chem. Lett., 2012, 3, 1824-1829.

38 H. Wu, G. Zheng, N. Liu, T. J. Carney, Y. Yang, and Y. Cui, Nano letters, 2012, 12, 904-909.

39 A. Xing, S. Tian, H. Tang, D. Losic, and Z. Bao, RSC Adv., 2012, 3, 10145-10149.

40 J. Li, S. Xiong, Y. Liu, Z. Ju, and Y. Qian, ACS Appl. Mater. Interfaces, 2013, 5, 981-988.

41 J. Li, P. Wu, F. Lou, P. Zhang, Y. Tang, Y. Zhou, and T. Lu, Electrochim. Acta, 2013, 111, 862-868.

42 E. Kim, D. Son, T. G. Kim, J. Cho, B. Park, K. S. Ryu, and S. H. Chang, Angew. Chem., 2004, 116, 6113-6116.

43 Z. Wen, Q. Wang, Q. Zhang, and J. Li, Adv. Funct. Mater., 2007, 17, 2772-2778.

44 T. Song, J. Xia, J. H. Lee, D. H. Lee, M. S. Kwon, J. M. Choi, J. Wu, S. K. Doo, H. Chang, W. I. Park, D. S. Zang, H. Kim, Y. Huang, K. C. Hwang, J. A. Rogers, and U. Paik, Nano Lett., 2010, 10, 1710–1716.

45 Z. Wen, G. Lu, S. Mao, H. Kim, S. Cui, K. Yu, X. Huang, P. T. Hurley, O. Mao, and J. Chen, Electrochem. Commun., 2013, 29 67-70.

46 J. Wang, N. Du, H. Zhang, J. Yu, and D. Yang, J. Phys. Chem. C, 2011, 115, 11302-11305.

47 H. Wu, G. Chan, J. W. Choi, Y. Yao, M. T. McDowell, S. W. Lee, A. Jackson, Y. Yang, L. Hu, Y. Cui, Nat. Nanotechnol., 2012, 7, 310-315.

48 C. de las Casas, and W. Li, J. Power Sources, 2012, 208, 74-85.

49 H. Wu, M. Xu, Y. Wang, and G. Zheng, Nano Res., 2013, 6, 167-173.

50 L. P. Tan, Z. Lu, H. T. Tan, J. Zhu, X. Rui, Q. Yan, and H. H. Hng, J. Power Sources, 2012, 206, 253-258.

51 J. Chen, X. H. Xia, J. P. Tu, Q. Q. Xiong, Y. X. Yu, X. L. Wang, and C. D. Gu, J. Mater. Chem., 2012, 22, 15056-15061.

52 J. Y. Huang, L. Zhong, C. M. Wang, J. P. Sullivan, W. Xu, L. Q. Zhang, S. X. Mao, N. S. Hudak, X. H. Liu, A. Subramanian, H. Fan, L. Qi, A. Kushima, and J. Li, Science, 2010, 330, 1515-1520.

53 P. Meduri, E. Clark, J. H. Kim, E. Dayalan, G. U. Sumanasekera, M. K. Sunkara, Nano Lett., 2012, 12, 1784-1788.

54 N. Liu, L. Hu, M. T. McDowell, A. Jackson, and Y. Cui, Y. ACS Nano, 2011, 5, 6487-6493.

55 B. Liu, J. Zhang, X. Wang, G. Chen, D. Chen, C. Zhou, and G. Shen, Nano Lett., 2012, 12, 3005-3011.

56 H. Kim, and J. Cho, Nano Lett., 2008, 8, 3688-3691.

57 K. T. Nam, D. W. Kim, P. J. Yoo, C. Y. Chiang, N. Meethong, P. T. Hammond, Y. M. Chiang, and A. M. Belcher, Science, 2006, 312, 885-888.

58 M. S. Park, G. X. Wang, Y. M. Kang, D. Wexler, S. X. Dou, and H. K. Liu, Angew. Chem., 2007, 119, 764-767.

59 H. Ma, S. Zhang, W. Ji, Z. Tao, and J. Chen, J. Am. Chem. Soc., 2008, 130, 5361-5367.

60 A. Débart, A. J. Paterson, J. Bao, and P. G. Bruce, Angew. Chem., 2008, 120, 4597-4600.

61 Y. Li, B. Tan, and Y. Wu, Nano Lett., 2008, 8, 265-270.

62 K. Peng, J. Jie, W. Zhang, and S. T. Lee, Appl. Phys. Lett., 2008, 93, 033105.

63 L. F. Cui, Y. Yang, C. M. Hsu, and Y. Cui, Nano Lett., 2009, 9, 3370-3374.

64 H. Kim, and J. Cho, J. Mater. Chem., 2008, 18, 771-775.

65 E. M. Lotfabad, P. Kalisvaart, A. Kohandehghan, K. Cui, M. Kupsta, B. Farbod, and D. Mitlin. J. Mater. Chem. A, 2014, 2, 2504-2516.

66 M. H. Park, M. G. Kim, J. Joo, K. Kim, J. Kim, S. Ahn, Y. Cui, and J. Cho, Nano Lett., 2009, 9, 3844-3847.

67 J. Xu, C. Jia, B. Cao, and W. F. Zhang, Electrochim. Acta, 2007, 52, 8044-8047.

68 X. W. Lou, D. Deng, J. Y. Lee, J. Feng, and L. A. Archer, Adv. Mater., 2008, 20, 258-262.

69 A. L. M. Reddy, M. M. Shaijumon, S. R. Gowda, and P. M. Ajayan, Nano Lett., 2009, 9, 1002-1006.

70 J. H. Ryu, J. W. Kim, Y. E. Sung, and S. M. Oh, Electrochem. Solid-State Lett., 2004, 7, A306-A309.

71 E. L. Memarzadeh, W. P. Kalisvaart, A. Kohandehghan, B. Zahiri, C. M. Holt, and D. Mitlin, J. Mater. Chem., 2012, 22, 6655-6668.

72 I. S. Kim, G. E. Blomgren, and P. N. Kumta, Electrochem. Solid-State Lett., 2003, 6, A157-A161.

73 I. S. Kim, G. E. Blomgren, and P. N. Kumta, J. Power Sources, 2004, 130, 275-280.

74 Z. Y. Zeng, J. P. Tu, Y. Z. Yang, J. Y. Xiang, X. H. Huang, F. Mao, and M. Ma, Electrochim. Acta, 2008, 53, 2724-2728.

75 Y. Liu, K. Hanai, T. Matsumura, N. Imanishi, A. Hirano, and Y. Takeda, Electrochem. Solid-State Lett., 2004, 7, A492-A495.

76 K. Hanai, Y. Liu, N. Imanishi, A. Hirano, M. Matsumura, T. Ichikawa, and Y. Takeda, J. Power Sources, 2005, 146, 156-160.

77 H. Mukaibo, T. Osaka, P. Reale, S. Panero, B. Scrosati, and M. Wachtler, J. Power Sources, 2004, 132, 225-228.

78 H. Kim, J. Choi, H. J. Sohn, and T. Kang, J. Electrochem. Soc., 1999, 146, 4401-4405.

79 M. Stjerndahl, H. Bryngelsson, T. Gustafsson, J. T. Vaughey, M. M. Thackeray, and K. Edström, Electrochim. Acta, 2007, 52, 4947-4955.

80 J. Yin, M. Wada, S. Yoshida, K. Ishihara, S. Tanase, and T. Sakai, J. Electrochem. Soc., 2003, 150, A1129-A1135.

81 T. L. Kulova, A. M. Skundin, Y. V. Pleskov, E. I. Terukov, and O. I. Kon'Kov, J. Electroanal. Chem., 2007, 600, 217-225.

82 T. Takamura, S. Ohara, M. Uehara, J. Suzuki, and K. Sekine, J. Power Sources, 2004, 129, 96-100.

83 C. Yu, X. Li, T. Ma, J. Rong, R. Zhang, J. Shaffer, Y. An, Q. Liu, B. Wei, and H. Jiang, Adv. Energy Mater., 2012, 2, 68-73.

84 P. R. Abel, A. M. Chockla, Y.-M. Lin, V. C. Holmberg, J. T. Harris, B. A. Korgel, A. Heller, and C. B. Mullins, ACS Nano, 2013, 7, 2249-2257.

85 Y. Yao, M. T. McDowell, I. Ryu, H. Wu, N. Liu, L. Hu, W. D. Nix, and Y. Cui, Nano Lett., 2011, 11, 2949-2954.

86 B. L. Ellis, and L. F. Nazar, Curr. Opin. Solid State Mater. Sci., 2012, 16, 168-177.

87 V. Palomares, P. Serras, I. Villaluenga, K. B. Hueso, J. Carretero-González, and T. Rojo, Energy Environ. Sci., 2012, 5, 5884-5901.

88 K. B. Hueso, M. Armand, and T. Rojo, Energy Environ. Sci., 2013, 6, 734-749.

89 J. M. Tarascon, Phil. Trans. R. Soc. A, 2010, 368, 3227-3241.

90 M. D. Slater, D. Kim, E. Lee, and C. S. Johnson, Adv. Funct. Mater., 2013, 23, 947-958.

91 D. Buchholz, A. Moretti, R. Kloepsch, S. Nowak, V. Siozios, M. Winter, and S. Passerini, Chem. Mater., 2013, 25, 142-148.

92 S. W. Kim, D.-H. Seo, X. Ma, G. Ceder, and K. Kang, Adv. Energy Mater., 2012, 2, 710-721.

93 J. L. Murray, Bull. Alloy Phase Diagrams, 1983, 4, 407-410.

94 C. Y. Chen, K. Matsumoto, T. Nohira, C. Ding, T. Yamamoto, and R. Hagiwara, Electrochim. Acta, 2014, 133, 583-588.

95 X. Xia, and J. R. Dahn, Electrochem. Solid-State Lett., 2012, 15, A1-A4.

96 S. M. Oh, S. T. Myung, C. S. Yoon, J. Lu, J. Hassoun, B. Scrosati, K. Amine, and Y. K. Sun, Nano Lett., 2014, 14, 1620-1626.

97 J. Billaud, G. Singh, A. R. Armstrong, E. Gonzalo, V. Roddatis, M. Armand, T. Rojo, and P. G. Bruce. Energy Environ. Sci., 2014, 7, 1387-1391.

98 L. Wang, Y. Lu, J. Liu, M. Xu, J. Cheng, D. Zhang, and J. B. Goodenough, Angew. Chem., Int. Ed., 2013, 52, 1964 –1967.

99 C. Zhu, K. Song, P. A. van Aken, Y. Yu, and J. Maier, Nano Lett., 2014, 14, 2175–2180.

100 H. Kim, Y. U. Park, K. Y. Park, H. D. Lim, J. Hong, and K. Kang, Nano Energy, 2014, 4, 97-104.

101 M. Yao, K. Kuratani, T. Kojima, N. Takeichi, H. Senoh, and T. Kiyobayashi, Sci. Rep., 2014, 4.

102 T. R. Jow, and L. W. Shacklette, J. Electrochem. Soc., 1989, 136, 1-6.

103 S. Y. Hong, Y. Kim, Y. Park, A. Choi, N. S. Choi, and K. T. Lee, Energy Environ. Sci., 2013, 6, 2067-2081.

104 Y. Shao, J. Xiao, W. Wang, M. Engelhard, X. Chen, Z. Nie, M. Gu, L. V. Saraf, G. Exarhos, J. G. Zhang, and J. Liu, Nano Lett., 2013, 13, 3909–3914.

105 T. T. Tran, and M. N. Obrovac, J. Electrochem. Soc., 2011, 158, A1411-A1416.

106 A. Metrot, D. Guérard, D. Billaud, and A. Hérold, Synth. Met., 1980, 1, 363-369.

107 D. A. Stevens, and J. R. Dahn, J. Electrochem. Soc., 2000, 147, 1271-1273.

108 S. Komaba, W. Murata, T. Ishikawa, N. Yabuuchi, T. Ozeki, T. Nakayama, A. Ogata, K. Gotoh, and K. Fujiwara, Adv. Funct. Mater., 2011, 21, 3859-3867.

109 X. Zhou, and Y.-G. Guo, ChemElectroChem, 2014, 1, 83-86.

110 W. Luo, J. Schardt, C. Bommier, B. Wang, J. Razink, J. Simonsen, and X. Ji, J. Mater. Chem. A, 2013, 1, 10662-10666.

111 K. Tang, L. Fu, R. J. White, L. Yu, M.-M. Titirici, M. Antonietti, and J. Maier, Adv, Energy Mater., 2012, 2, 873–877.

112 J. Ding, H. Wang, Z. Li, A. Kohandehghan, K. Cui, Z. Xu, B. Zahiri, X. Tan, E. Memarzadeh Lotfabad, B. C. Olsen, and D. Mitlin, ACS Nano, 2013, 7, 11004-11015.

113 E. Memarzadeh Lotfabad, J. Ding, K. Cui, A. Kohandehghan, W. P. Kalisvaart, M. Hazelton, and D. Mitlin, ACS Nano, 2014, 8, 7115–7129.

114 Y. Xu, E. Memarzadeh Lotfabad, H. Wang, B. Farbod, Z. Xu, A. Kohandehghan, and D. Mitlin, Chem. Commun., 2013, 49, 8973-8975.

115 L. Wu, D. Buchholz, D. Bresser, L. G. Chagas, and S. Passerini, J. Power Sources, 2014, 251, 379-385.

116 K. T. Kim, G. Ali, K. Y. Chung, H. Yashiro, Y. K. Sun, J. Lu, K. Amine, and S. T. Myung, Nano Lett., 2014, 14, 416–422.

117 J. C. P. Flores, C. Baehtz, A. Kuhn, and F. G. Alvarado, J. Mater. Chem. A, 2014, 2, 1825-1833.

118 G. Rousse, M. E. A. Y. De Dompablo, P. Senguttuvan, A. Ponrouch, J. M. Tarascon, and M. R. Palacín, Chem. Mater., 2013, 25, 4946-4956.

119 X. Yu, H. Pan, W. Wan, C. Ma, J. Bai, Q. Meng, S. N. Ehrlich, Y. S. Hu, and X. Q. Yang, Nano Lett., 2013, 13, 4721-4727.

120 Y. Yan, Y. X. Yin, Y. G. Guo, and L. J. Wan, Adv. Energy Mater., 2014.

121 L. David, R. Bhandavat, and G. Singh, ACS Nano, 2014, 8, 1759–1770.

122 Y. Liu, B. H. Zhang, S. Y. Xiao, L. L. Liu, Z. B. Wen, and Y. P. Wu, Electrochi. Acta, 2014, 116, 512–517.

123 C. Luo, Y. Xu, Y. Zhu, Y. Liu, S. Zheng, Y. Liu, A. Langrock, and C. Wang, ACS Nano, 2013, 9, 8003–8010.

124 Z. Jian, B. Zhao, P. Liu, F. Li, M. Zheng, M. Chen, Y. Shi, and H. Zhou, Chem. Commun., 2014, 50, 1215-1217.

125 H. Zhu, Z. Jia, Y. Chen, N. Weadock, J. Wan, O. Vaaland, X. Han, T. Li, and L. Hu, Nano Lett., 2013, 13, 3093–3100.

126 K. Dai, H. Zhao, Z. Wang, V. Battaglia, and G. Liu, J. Power Sources, 2014, 263, 276-279.

127 L. Baggetto, H. Y. Hah, C. E. Johnson, C. A. Bridges, J. A. Johnson, and G. M. Veith, Phys. Chem. Chem. Phys., 2014, 16, 9538-9545.

128 M. He, K. V. Kravchyk, M. Walter, and M. V. Kovalenko, Nano Lett., 2014, 14, 1255–1262.

129 L. D. Ellis, B. N. Wilkes, T. D. Hatchard, and M. N. Obrovac, J. Electrochem. Soc., 2014, 161, A416-A421.

130 Y. Kim, Y. Park, A. Choi, N.-S. Choi, J. Kim, J. Lee, J. H. Ryu, S. M. Oh, and K. T. Lee, Adv. Mater., 2013, 25, 3045-3049.

131 Y. Wang, D. Su, C. Wang, and G. Wang, Electrochem. Commun., 2013, 29, 8-11.

132 B. Qu, C. Ma, G. Ji, C. Xu, J. Xu, Y. S. Meng, T. Wang, and J. Y. Lee, Adv. Mater., 2014.

133 J. Qian, Y. Xiong, Y. Cao, X. Ai, and H. Yang, Nano Lett., 2014, 14, 1865–1869.

134 W. J. Li, S. L. Chou, J. Z. Wang, H. K. Liu, and S. X. Dou, Nano Lett., 2013, 13, 5480-5484.

135 J. Qian, X. Wu, Y. Cao, X. Ai, and H. Yang, Angew. Chem., 2013, 125, 4731-4734.

136 L. Wu, X. Hu, J. Qian, F. Pei, F. Wu, R. Mao, X. Ai, H. Yang, and Y. Cao, Energy Environ. Sci., 2014, 7, 323-328.

137 Y. W. Denis, P. V. Prikhodchenko, C. W. Mason, S. K. Batabyal, J. Gun, S. Sladkevich, A. G. Medvedev, and O. Lev, Nat. Commun., 2013, 4.

138 B. Farbod, K. Cui, W. P. Kalisvaart, M. Kupsta, B. Zahiri, A. Kohandehghan, E. Memarzadeh, Z. Li, E. J. Luber, and D. Mitlin, ACS Nano, 2014, 8, 4415–4429.

139 M. H. Seo, M. Park, K. T. Lee, K. Kim, J. Kim, and J. Cho. Energy Environ. Sci., 2011, 4, 425-428.

140 C. K. Chan, X. F. Zhang, and Y. Cui, Nano Lett., 2008, 8, 307–309.

141 T. Kennedy, E. Mullane, H. Geaney, M. Osiak, C. O'Dwyer, and K. M. Ryan, Nano Lett., 2014, 14, 716–723.

142 Y. Cao, L. Xiao, M. L. Sushko, W. Wang, B. Schwenzer, J. Xiao, Z. Nie, L. V. Saraf, Z. Yang, and J. Liu, Nano Lett., 2012, 12, 3783-3787.

143 Y. Liu, Y. Xu, Y. Zhu, J. N. Culver, C. A. Lundgren, K. Xu, and C. Wang, ACS Nano, 2013, 7, 3627-3634.

144 Y. Cao, L. Xiao, W. Wang, D. Choi, Z. Nie, J. Yu, L. V. Saraf, Z. Yang, and J. Liu, Adv. Mater., 2011, 23, 3155-3160.

145 V. L. Chevrier, and G. Ceder, J. Electrochem. Soc., 2011, 158, A1011-A1014.

146 L. Baggetto, J. K. Keum, J. F. Browning, and G. M. Veith, Electrochem. Commun., 2013, 34, 41-44.

147 P. R. Abel, Y. M. Lin, T. de Souza, C. Y. Chou, A. Gupta, J. B. Goodenough, G. S. Hwang, A. Heller, and C. B. Mullins, J. Phys. Chem. C, 2013, 117, 18885-18890.

148 J. Sangster, and A. D. Pelton, J. Phase Equilib., 1997, 18, 295-297.

149 S. Komaba, Y. Matsuura, T. Ishikawa, N. Yabuuchi, W. Murata, and S. Kuze, Electrochem. Commun., 2012, 21, 65-68.

150 J. Graetz, C. C. Ahn, R. Yazami, and B. Fultz, J. Electrochem. Soc., 2004, 151, A698-A702.

Chapter 2: Magnesium and Magnesium-Silicide coated Silicon Nanowire composite Anodes for Lithium-ion Batteries

Material in this chapter has been published in:

Kohandehghan, Alireza, Peter Kalisvaart, Martin Kupsta, Beniamin Zahiri, Babak Shalchi Amirkhiz, Zhipeng Li, Elmira L. Memarzadeh, Leonid A. Bendersky, and David Mitlin. "Magnesium and magnesium-silicide coated silicon nanowire composite anodes for lithium-ion batteries." J. Mater. Chem. A 1, (2013): 1600-1612.

2.1 Introduction

Lithium-ion batteries (LIBs) are rechargeable batteries offering higher energy density than other secondary batteries such as Nickel-Cadmium or Nickel-Metal Hydride. LIBs are the most promising candidates for plug-in hybrid electric vehicles due to their high operating voltage, high power density, high energy-to-weight ratio, and no memory effect. [1-3] Conventional graphite anodes have only 372 mAh/g specific capacity, which is much less than the required energy for high-power demands. [4] Also in terms of capacity per volume, 843 mAh/cm^3 for graphite, there is still a lot of potential for improvement by changing the anode active material.

After lithium, silicon exhibits the highest theoretical gravimetric specific capacity, 3590 mAh/g corresponding to formation of $Li_{15}Si_4$, and is therefore considered the most promising replacement for graphite in commercial LIBs. [5,6] However, there are major practical difficulties associated with the application of silicon in a rechargeable lithium-ion battery. The most important issue is the very large volume change of Si upon Li insertion and extraction. Whereas graphite expands by only ~ 10% upon lithiation to LiC_6, Si expands 280% upon lithiation. [7-12] This huge repeated expansion (shrinkage) during lithium alloying (dealloying) leads to poor cyclability due to disintegration of active materials, leading to electronic contact loss with either the conductive additive or the current collector. [13-15] The volumetric capacity of Si, even taking the high expansion into account, is 2172 mAh/cm^3 and thereby exceeds that of graphite by a

factor of 2.6 and even tops that of Li metal (2066 mAh/cm^3). Thus, major efforts to improve the cycling stability of Si-based Li-ion battery anodes are certainly justified from an application point of view.

The abovementioned problems can potentially be overcome by using nanostructured Si anodes in the form of thin films, nanocomposite powders with carbon or Si particles anchored to carbon nanostructures. [12,16-18] However, these have the disadvantage of incorporating a lot of 'dead weight' in the form of substrates (thin films) or inactive carbon fillers and templates. In 2008, the idea that Silicon nanowires (SiNWs) might have superior cycling stability over Si (nano)powders as LIB anodes was first published. [19] The rationale was that the nanowire morphology would allow for easy accommodation of volume expansion and short diffusion distances in the radial direction and fast electron transport in the axial direction. With the SiNWs directly anchored to a conductive substrate, the need for conductive additives and binders would also be eliminated. Cycling stability of the SiNWs was indeed superior to Si powder electrodes, but was not reported beyond 10 cycles. [19] Subsequent studies on SiNWs by the same authors showed approximately 40% capacity loss in the first 50 cycles which is still far from satisfactory for practical applications. [20]

Although their performance is superior to Si powders, SiNWs are still vulnerable to fracture and pulverization during galvanostatic cycling. [21,22] Thus, one of the required modifications in SiNWs electrodes is structural stability improvements to avoid disintegration of nanowires. To this end, coatings might be beneficial to prevent SiNWs from decrepitation. [23-27] Indeed, the coating could play a physical support role for improved structural integrity of the core active material. A proof of this principle was demonstrated by in-situ TEM studies on SnO_2 nanowires, where carbon or aluminum coating completely inhibited radial expansion of the nanowire in favor of the longitudinal direction, thus maintaining the mechanical integrity of the material. [27] More recently, a study on anchored arrays of SiNWs on TiN showed that Al coating can modify the expansion of silicon as well and also demonstrated a significant improvement in the cycling stability for 3-8 wt.% Al coating, although degradation was only delayed, not prevented. [28] Therefore, the question remains as to what selection rules can be formulated for coatings on SiNWs. Al is also active towards Li, whereas Cu, reported on by Chen et al. [29], is inactive. Both

showed some benefits to the cycling stability, although active Al appeared superior. However, there are likely to be more confounding factors in terms of nanowire diameter and length. [30]

Magnesium as a coating material for SiNWs is similar to copper in the sense that it is reactive with Si, can improve conductivity and only accommodates Li as a solid solution, [31] but it is much lighter. Furthermore, a simple heat treatment step after synthesis of the Mg-SiNW composite can react the Mg to the ordered Mg_2Si intermetallic phase which is reactive towards Li, thus allowing a comparison between 'inactive-active' and 'active-active' composite that are synthesized in identical ways. Upon reaction with Li, Mg_2Si undergoes a displacement reaction upon lithiation to Li_2MgSi and Mg. The total measured capacity of 1363 mAh/g is, however, much higher than 2 Li/Mg_2Si (= 699 mAh/g), although it is not entirely clear where the remaining Li is accommodated. [32,33] It was also reported Mg_2Si reacts at similar potentials to Si, which means both the Si core and Mg_2Si shell start to expand at the same time. [34,35] Therefore, Mg_2Si may be an interesting intermetallic compound as a lightweight coating for SiNW arrays.

The large surface area due to their high aspect ratio of SiNWs is both an advantage and a disadvantage. Although high active area is crucial for lithiation and delithiation at higher rates, it results in more solid-electrolyte interphase (SEI) formation. SEI has been proven as one of the main sources of initial capacity loss and low coulombic efficiency since it consumes lithium ions and electrons irreversibly. Nevertheless, a stable SEI layer helps avoid further capacity loss on the subsequent cycles. [36-38] Previous studies on etched and surface-functionalized and carbon-coated SiNWs showed that the reactivity of the nanowires with the organic electrolyte is influenced significantly by changes in the surface chemistry of the material. [39-41] It is therefore reasonable to assume that a (inter)metallic coating can also modify the SEI layer and, possibly, positively influence the coulombic efficiency.

Here we present a microstructural, and electrochemical characterization study of Mg-and Mg_2Si-coated SiNWs core-shell composites. The objective of the current work is to evaluate whether the coatings have any advantageous effects in terms of cycling stability and/or coulombic efficiency when the nanowires are utilized as Li-ion battery anodes. We compare the galvanostatic charge-discharge performance of the synthesized nanocomposites having various Mg and Mg_2Si thicknesses with a bare SiNWs anode as a baseline. In addition, TEM and SEM

microstructural studies on the as-synthesized and post cycled nanocomposites are presented with particular focus on degradation mechanisms. The compositions of the SEI layers on Mg-and Mg_2Si-coated SiNWs will be compared using XPS analysis to investigate possible correlations with cycling stability and/or coulombic efficiency.

2.2 Experimental procedures

316 stainless steel spacer disks (MTI Corporation), 15.8 mm in diameter and 0.5 mm thick served as the substrate for SiNW growth. The spacers were polished using SiC sandpaper with progressively smaller grit size down to 5 μm (Allied High Tech Products, Inc.) followed by polishing with 1.0 and 0.05 μm alumina paste (Buehler). After the polishing steps, the substrates were cleaned by sonication in acetone, iso-propanol, and Milli-Q water and were then dried.

Prior to all deposition experiments, the maximum base pressure of the sputtering chamber was 5×10^{-8} Torr. Sputtering of Ti and Au was performed in Ar gas of 5N purity at a pressure of 4 mTorr. A mixture of Ar and N_2 (20:1) was used for sputtering of titanium nitride (TiN) during which the substrates were held at 250 ºC. We deposited a 200 nm thick TiN layer with a 50 nm Ti film as an adhesion layer underneath the nitride film on the polished spacers. Deposition was performed by DC-magnetron sputtering (AJA International, Inc.) of a titanium target (Plasmaterials, 99.995% purity) with a deposition rate of ~ 0.4 Å/sec. Deposition of the adhesion layer and of the TiN film were performed sequentially with continuous substrate rotation. Subsequently, a 10 nm Au film deposited by radio frequency (RF) magnetron sputtering with ~ 0.35 Å/sec deposition rate to catalyze subsequent nanowire growth.

SiNWs arrays were synthesized by vapor-liquid-solid (VLS) mechanism in a commercial low-pressure chemical-vapor deposition (LP-CVD) tube furnace (Tystar, Inc.). First, the samples were loaded into the reactor at 300 ºC. Then the furnace is purged with Ar gas and heated up to the growth temperature of 525 ºC at 10 ºC/min under a flow of Ar and H_2, and held at this temperature for 30 minutes prior to nanowire growth in order to dewet the gold film. SiNWs were grown at 525 ºC using a SiH_4:H_2 ratio of 1:4. The total pressure during growth was set at 100 Torr and the growth time was set to 2 minutes.

The magnesium coating was deposited onto the SiNWs by RF magnetron sputtering at an Ar pressure of 4 mTorr at a rate of ~ 0.15 Å/sec. The Mg thicknesses used are 10, 20, and 50 nm based on a planar geometry. In order to react the Mg to Mg_2Si, some of the Mg-coated SiNWs samples were annealed at 400 ºC for 30 minutes in a high vacuum (10^{-9} Torr) environment. After sample preparation, spacers were weighed with a high accuracy Mettler Toledo MX5 (1 μg resolution) microbalance. The resulting mass-loading of silicon on a single substrate is ~ 0.3 mg or 0.15 mg/cm^2, on average.

Electrochemical tests were carried out using a coin cell configuration, CR2032, with diameter and thickness of 20 mm and 3.2 mm, respectively, which had been assembled in an argon-filled glove box in which oxygen and moisture concentrations were kept below 0.1 ppm. Lithium metal foil used as counter electrode was separated from the working electrode with Polyethene separator (MTI Corporation, porosity of 36-44% and mainly 0.03 μm pore size) with 19 mm diameter. The electrolyte is 1 M lithium hexafluorophosphate ($LiPF_6$) salt in ethylene carbonate (EC), dimethyl carbonate (DMC), and diethylcarbonate (DEC) solution with a 1:1:1 volumetric ratio. [42]

To elucidate long-term cyclability of the composite, galvanostatic charge-discharge experiments were performed on a BT2000 Arbin potentiostat with the cutoff potentials set to of 0.01 and 2 V vs. Li/Li$^+$. Constant current (CC) cycling was performed at 0.1C rate. Cyclic voltammetry (CV) and electrochemical impedance spectroscopy (EIS) measurements were conducted on a Solartron 1470 Multistat system with Corrware data acquisition software. For CV experiments, the potential was scanned in a range of 0.01-2 V vs. Li/Li$^+$ with a scan rate of 1 mV/s for 10 cycles. All electrochemical tests were conducted at room temperature.

Samples for post-cycling characterization of their microstructure were obtained by disassembling coin cells in an Ar-filled glove box. Subsequently, the cycled electrodes were rinsed in acetonitrile to remove excess electrolyte and kept in the glovebox overnight to dry. The nanocomposites were analyzed with scanning electron microscopy (SEM) on a Hitachi FESEM S-4800 and Hitachi FESEM S-5500, the latter of which is capable of energy-dispersive x-ray (EDX) spectroscopy to perform elemental mapping. Transmission electron microscopy (TEM) was performed on a JEOL 2200FS, 2100, and 2010 at 200 kV accelerating voltage. Electron

diffraction patterns were simulated via the commercial software Desktop Microscopist, with the input of known space group information of the relevant phases. Cross-sectional samples of cycled materials were obtained by using a Hitachi NB5000 dual beam FIB/SEM. From the bulk of the sample, a suitable area was located using the SEM, the selected volume was isolated, lifted out, and placed on a Cu 5-post grid using the FIB and micro-sample manipulator.

X-ray photoelectron spectroscopy (XPS) measurements were performed on an ULTRA (Kratos Analytical) spectrometer using monochromatic Al-K_α radiation (hv=1486.6 eV) run at 210 W. Data collection was conducted under ultrahigh vacuum (10^{-9} Torr) from analyzed area of 300×700 μm^2. Spectra were collected with an energy window of 20 eV. A charge neutralizer was used to compensate charging effects. The binding energy scale was calibrated from the universal hydrocarbon contamination using the C1s peak at 284.8 eV. The XPS data were analyzed using CasaXPS software. Background subtraction was done using a nonlinear Shirley-type background model.

2.3 Results and discussion

2.3.1 Characterization of as-made composites

Both cross-sectional and planar-view SEM images of as-made bare SiNWs and Mg-coated SiNWs both before and after annealing are included as Figure 2-1. The nanowires are, on average, approximately 12 micrometers long and 114 nm thick. From the average diameter and length, the density of silicon (2.3 g/cm^3), and the average silicon mass loading of 0.3 mg on a stainless steel spacer with 1.96 cm^2 surface area, one can calculate the number nanowires on each substrate and the surface area-enhancement, which is approximately a factor of ~ 23 based on these numbers. In principle, this would result in sub-nanometer thickness for the coatings if coverage were perfectly uniform. However, since the nanowires are not aligned with one another, nor perfectly perpendicular to the substrate and strongly interconnected, coverage by sputtering will not be uniform. Therefore, for simplicity, we will from here on refer to each sample material by the *geometric* thickness of the coating. After annealing, the resulting Mg_2Si thickness will be ~ 1.4 times that of Mg, assuming all Mg is transformed into Mg_2Si. Thus, the

materials described from here on will be referred to 10, 20, 50Mg/SiNWs and 14, 28, 70Mg_2Si/SiNWs.

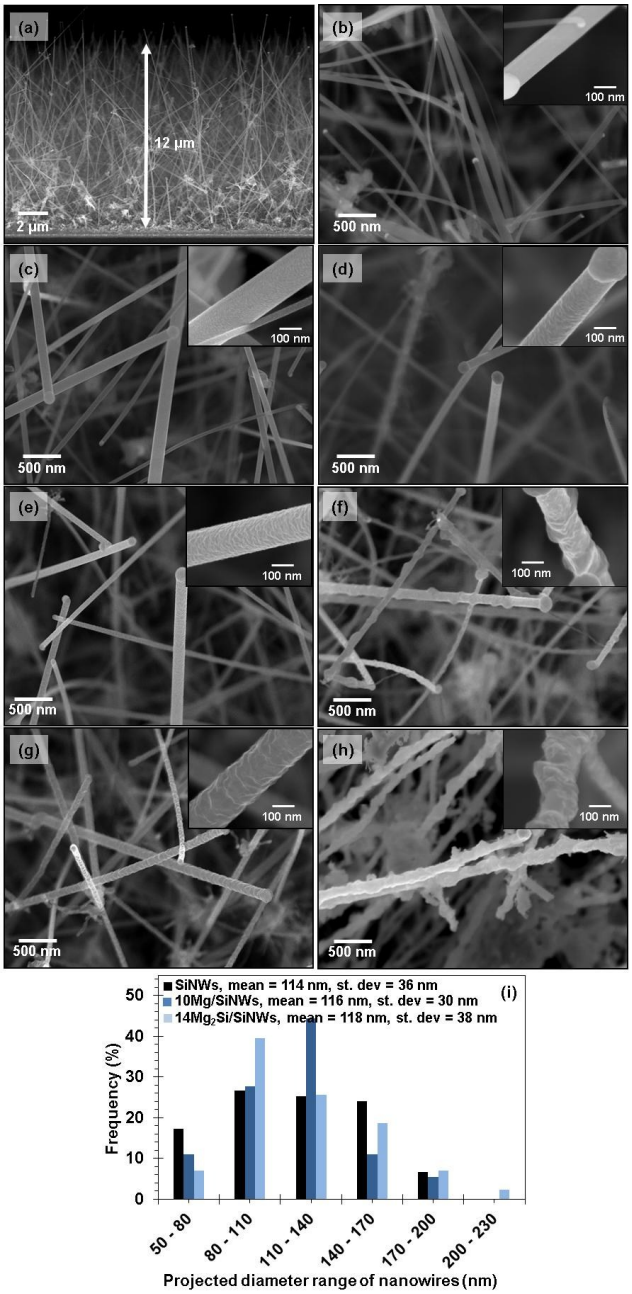

Figure 2-1: (a) cross-sectional view SEM micrograph of SiNWs forest grown on Si wafer/Ti/TiN, in-plane view SEM micrographs for (b) bare SiNWs, (c) 10Mg/SiNWs, (d) 14Mg_2Si/SiNWs, (e) 20Mg/SiNWs, (f) 28Mg_2Si/SiNWs, (g) 50Mg/SiNWs, and (h) 70Mg_2Si/SiNWs nanocomposite anode materials. A series of representative images like (b)-(h) were used to obtain the diameter distribution in (i).

Figure 2-2(a-d) show bright-and dark-field TEM micrographs, the corresponding SAD pattern, and a high-resolution image of an uncoated silicon nanowire. The electron diffraction pattern indicates that pure Si nanowires are single-crystalline, consistent with results on other VLS-grown SiNWs with Au catalyst. [43] The dark-field micrograph was taken from the 022 reflection of the silicon lattice.

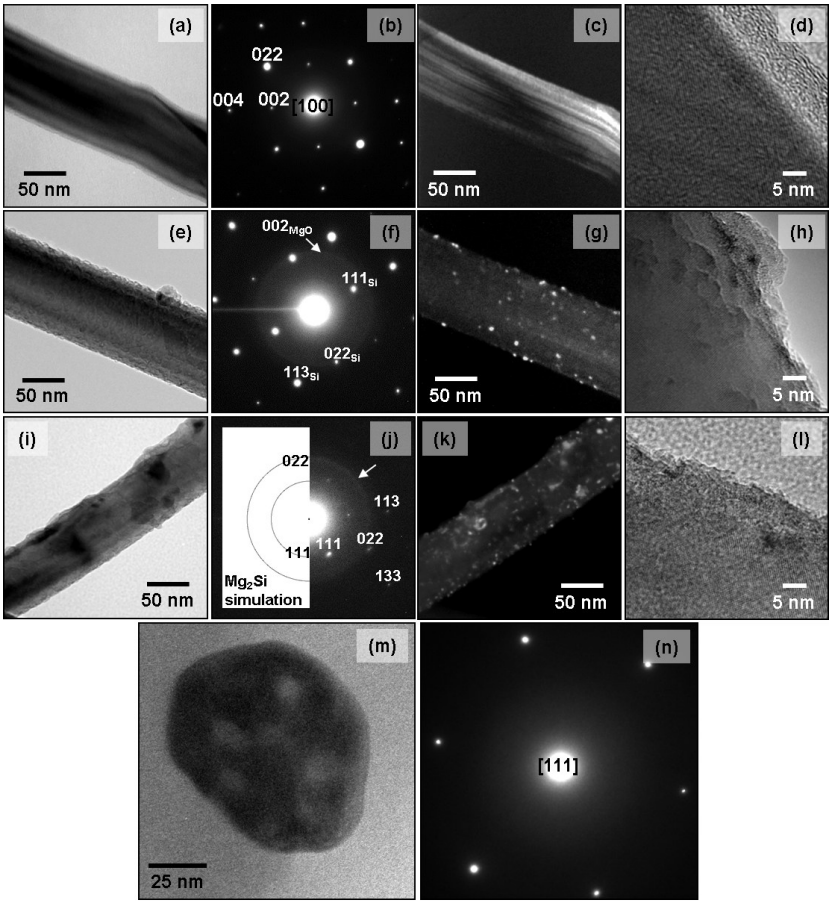

Figure 2-2: (a-d) TEM micrographs of as-grown pure SiNWs; (b) corresponding indexed SAD pattern of the nanowire oriented near the 100 zone axis, the extra weak spots are observed as a result of double diffraction, (c) Dark-field micrograph obtained using $g=022_{Si}$ reflection, (d) HRTEM image of the SiNW structure. (e-h) As-prepared 10Mg/SiNWs; (e) bright-field TEM image with (f) corresponding indexed SAD pattern, (g) dark-field TEM micrograph, obtained using $g=002_{MgO}$ reflection, (h) HRTEM image of the nanowire shown in (e). (i-l) As-synthesized 14Mg_2Si/SiNWs; (i) bright-field micrograph and (j) corresponding indexed SAD pattern with Mg_2Si ring pattern simulation, (k) dark-field image, obtained using part of the 022 diffraction ring of Mg_2Si, (l) HRTEM micrograph of the material in (i). (m,n) Cross-section bright-field TEM micrograph of a silicon nanowire and corresponding SAD pattern showing that the imaged SiNW is oriented near the 111 zone axis.

The particular SiNW imaged in Figure 2-2(a-d) is near the [100] zone axis. There is an extra set of diffraction spots appearing where the forbidden (002) reflection would be that most likely arises from double diffraction. From Figure 2-2(d) it can be seen that an approximately 5 nm thick amorphous layer is present on the nanowire surface, which could be due to a combination of amorphous silicon from the growth step and amorphous SiO_2 resulting from exposure to air. A *cross-sectional* TEM image of a SiNW, included as Figure 2-2(m,n), shows its shape is actually roughly hexagonal, a feature not immediately obvious from the images in Figure 2-2(a-d).

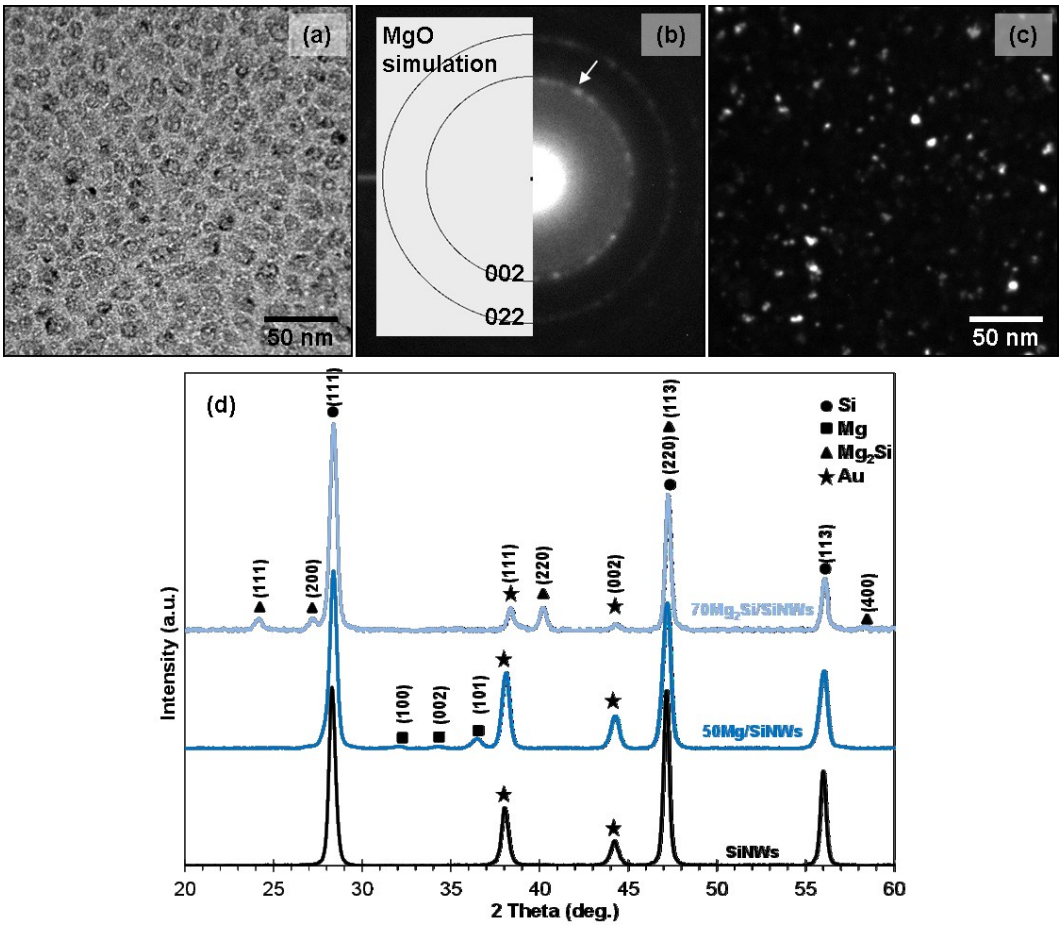

Figure 2-3: TEM images of sputtered 10 nm Mg onto a TEM grid (on the Cu side) at room temperature, (a) bright-field, (b) corresponding SAD pattern with MgO ring pattern simulation, and (c) dark-field TEM micrograph, obtained using part of 002_{MgO} diffracted ring. This thin Mg layer appears mostly oxidized, as it did on the composite. (d) XRD patterns of bare SiNWs, 50Mg/SiNWs and 70Mg_2Si/SiNWs made by annealing 50Mg/SiNWs at 400 °C for 30 minutes.

Figure 2-2(e-h) and (i-l) present TEM micrographs of 10Mg/SiNWs and 14Mg_2Si/SiNWs anode materials, respectively. For the 10Mg/SiNWs, the Mg coating seems to be completely oxidized as only a diffraction ring of MgO (002) could be detected. The same result is obtained for a planar 10 nm Mg film on a TEM grid (see Figure 2-3). However, metallic Mg could be detected in as-made composites with thicker Mg coating. An XRD pattern of 50Mg/SiNWs is included in Figure 2-3(d) clearly showing the (100), (002) and (101) reflections of Mg. When the Mg coated nanowires are annealed under high vacuum in the sputter system, the Mg coating reacts with Si to form Mg_2Si. The (022) reflection ring of Mg_2Si was detected as indicated by the arrow. From the dark-field image taken from the (022) reflection of Mg_2Si in Figure 2-2, Mg_2Si appears quite homogeneously distributed over the surface of the nanowire.

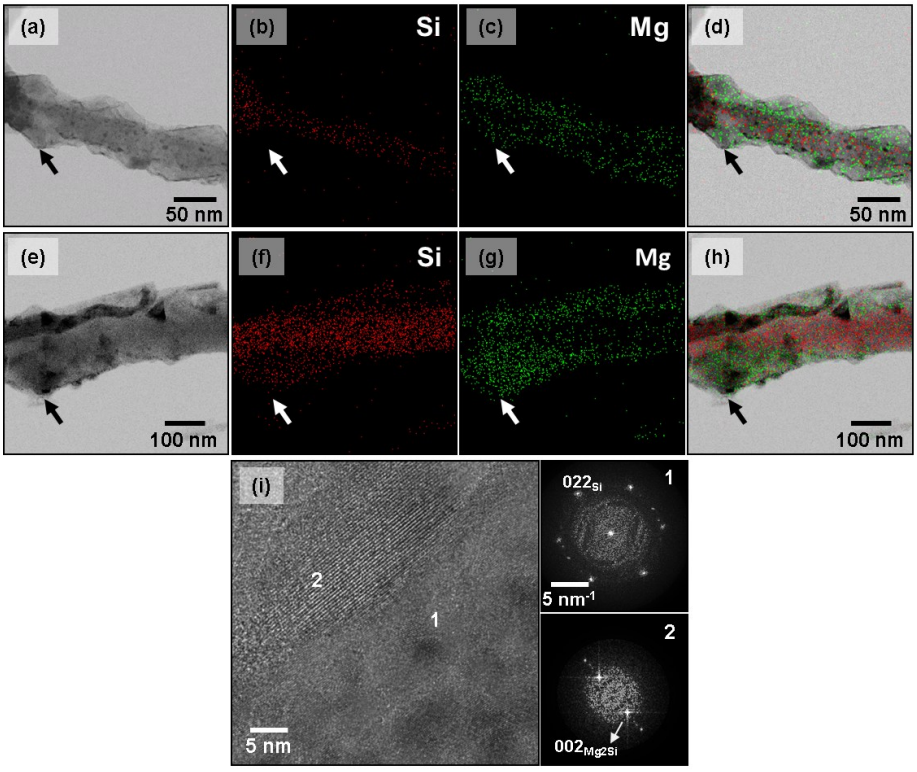

Figure 2-4: (a-d) As-synthesized 50Mg/SiNWs, (a) bright-field micrograph and corresponding EDX elemental mappings of Si and Mg, (b) and (c), (d) the corresponding overlay map of both Si and Mg in red and green, respectively. (e-h) As-synthesized 70Mg_2Si/SiNWs, (e) bright-field image of as-made 70Mg_2Si/SiNWs and corresponding EDX elemental maps of Si and Mg, (f) and (g), (h) the overlay map with Si in red and Mg in green. Areas where Mg and Si are not intermixed for the 50Mg/SiNWs and are in the 70Mg_2Si/SiNWs are indicated by the arrows. (i) HRTEM micrograph of 70Mg_2Si/SiNWs and corresponding FFT pattern of (1) interior parts of coated nanowire and (2) outer shell of nanowire, which is covered with Mg_2Si.

Figure 2-4 shows bright-field TEM micrographs and Si and Mg EDX elemental mappings for 50Mg/SiNWs, (a-d), and 70Mg_2Si/SiNWs, (e-h), which are of equivalent Mg thickness before and after annealing, respectively. The 50Mg/SiNWs show a very clear core-shell structure where the region where Si is detected is clearly narrower than the area where Mg is found. The arrows in the images indicate the outer edge of both the nanowire and the area where Mg is detected. Before annealing, the areas near the arrow in Figure 2-4(c) are clearly free of Si, whereas a considerable amount of Mg is detected. After annealing, there is a clear overlap between the Si and Mg maps, showing the Si and Mg have formed the Mg_2Si alloy. XRD patterns of bare and Mg_2Si-coated SiNWs also confirm this. A HRTEM image of a region near the Mg_2Si/SiNW interface is shown in Figure 2-4(i), together with FFTs of the nanowire core and the coating. From the FFT patterns, the *d*-spacings of $(220)_{Si}$ and $(200)_{Mg2Si}$ can be extracted as being 1.92 and 3.17 Å, respectively, once again showing the reaction of the Mg coating with the SiNW.

2.3.2 Electrochemical performance

Figure 2-5 shows the first 10 CV curves of bare and Mg-and Mg_2Si-coated SiNWs for different coating thicknesses. The CVs of bare SiNWs show two characteristic peaks at 0.3 and 0.5 V in the oxidation branch that are typically found for any Si-based anode. The large, broad peak at ~ 0.1 V in the reduction branch is also commonly observed for Si electrodes. [28] Over the course of the first 10 cycles, the peak current at 0.5-0.6 V increases by a factor of 5, likely due to reduction and/or break-up of the native oxide on the surface of the nanowires. For SiNWs coated with pure Mg, as shown in Figure 2-5(b) and (d), the picture is quite different. For 10Mg/SiNWs the peak currents at E ~ 0.5 V are considerably lower than even for bare SiNWs and increase by less than a factor of 4 in the first 10 cycles. Thus, thin Mg coating seems to be detrimental to the reaction kinetics towards Li insertion/extraction of the nanowires, consistent with the detection of a considerable amount of native oxide in the electron diffraction pattern and dark-field TEM image. Increasing the thickness of Mg to 50 nm, the first 10 CVs are virtually identical,

indicating that thicker Mg coatings are not fully oxidized and the oxide shell can be readily broken during cycling.

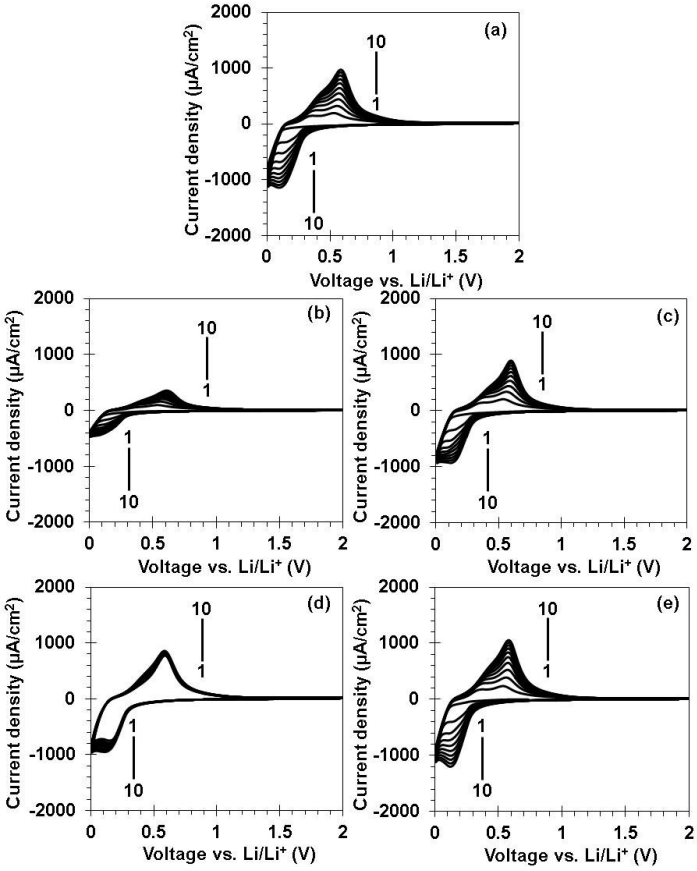

Figure 2-5: Cyclic voltammograms of (a) bare SiNWs, (b) and (c) 10Mg/SiNWs and 14Mg_2Si/SiNWs, (d) and (e) 50Mg/SiNWs and 70Mg_2Si/SiNWs at a scan rate of 1 mV/s between 0.01 and 2 V vs. Li/Li^+.

As can be seen in Figure 2-5(c) and (e), the Mg_2Si coating does not alter the general features of the CV curves with respect to bare SiNWs. There is no consistent trend to the maximum peak current densities that are achieved with increasing coating thickness, which indicates that Mg_2Si neither improves nor deteriorates the reaction kinetics. The fact that the CV curves of bare and Mg_2Si-coated nanowires are so similar in the activation behavior they show, also indicates that the native oxide on both can be reduced by lithium. Indeed, SiO_2 is thermodynamically less stable than Li_2O. It should be noted here that this is not true for MgO, which is more stable than both SiO_2 and Li_2O and will therefore not react with Li at all. [44] This could explain the low

currents and slow activation behavior found for 10Mg/SiNWs in Figure 2-5(b). Beside similar peak current densities, the composite also shows no additional peaks due to the Mg_2Si coating.

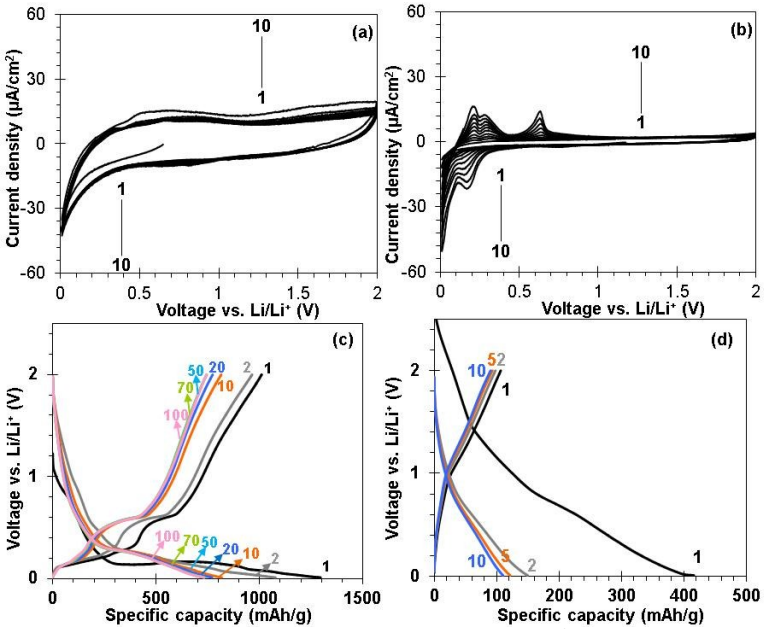

Figure 2-6: (a) and (b) CV curves between 0.01 and 2 V vs. Li/Li^+ for a planar 100 nm Mg_2Si layer at 1 and 0.2 mV/s, respectively, (c) Galvanostatic cycling at 0.1C rate of the same over the same potential window. (d) Constant current measurement on 100 nm planar Mg film at 1 μA current.

CV curves of a planar 100 nm thick Mg_2Si film are included in Figure 2-6(a-c). At 1 mV/s, the CV curves are featureless and a visible contribution from Mg_2Si would therefore not be expected at this scan rate. At 0.2 mV/s, however, current peaks at ~ 0.2 and towards 0 V and at 0.2, 0.25, and 0.61 V vs. Li/Li^+ are visible in the anodic and cathodic branch, respectively. Given that the scan rate had to be lowered from 1 to 0.2 mV/s to see any distinct features, the reaction kinetics of the Mg_2Si phase seem to be slow.

Figure 2-7 shows the voltage profiles of the nanocomposites during charge and discharge in a voltage window of 0.01-2 V vs. Li/Li^+ at a rate of 0.1C. The potential curves for the coated and uncoated SiNWs electrodes are quite similar. The measured initial discharge (lithiation) specific capacity, first-cycle discharge capacity loss, initial irreversible capacity, and coulombic efficiency (CE), defined as CE=delithiation capacity/lithiation capacity, as taken from the galvanostatic potential curves for bare SiNWs and nanocomposites are listed in Table 2-1.

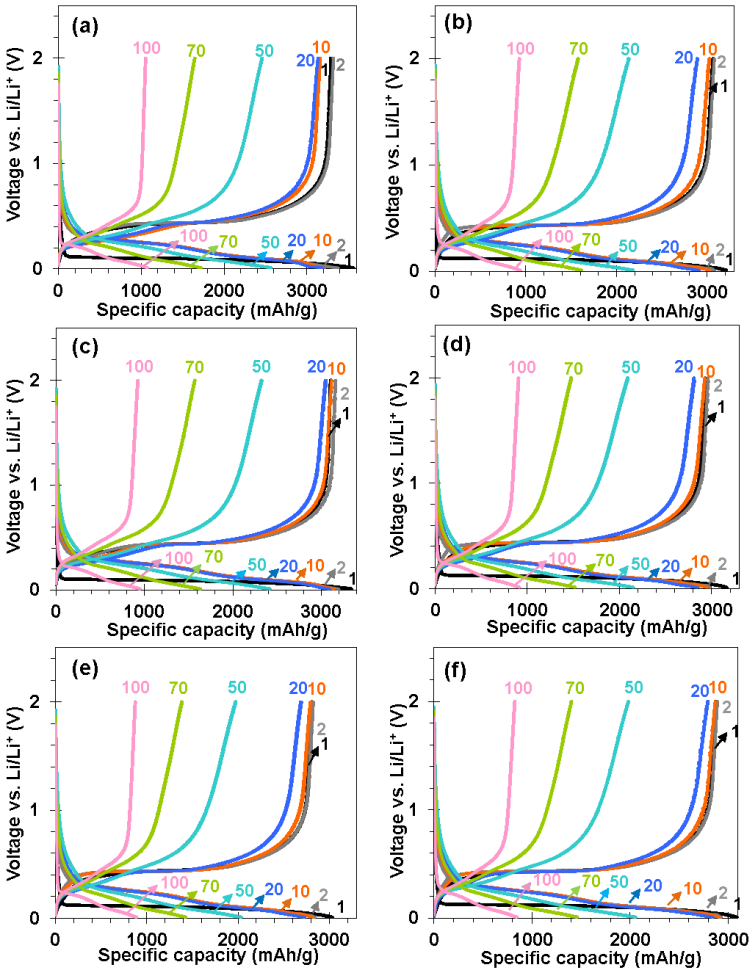

Figure 2-7: Charge-discharge profiles of (a) bare SiNWs, (b) 10Mg/SiNWs, (c) 14Mg_2Si/SiNWs, (d) 20Mg/SiNWs, (e) 50Mg/SiNWs, and (f) 70Mg_2Si/SiNWs nanocomposite anode materials cycled in the potential window of 0.01-2 V vs. Li/Li^+ at a rate of 0.1C.

Analogous to what was found for Al-coated SiNWs, the coating has no consistent, significant influence on the coulombic efficiency or capacity loss in the first cycle. For all the electrodes, initial Li alloying exhibits a long flat plateau at ~ 0.1 V, which corresponds to phase transformation of crystalline Si to amorphous Li_xSi phase. [45,46] During subsequent cycles, rather than a single flat plateau, several sloping plateaus are observed, corresponding to multiple transitions between (amorphous) Li-Si phases with different Li/Si ratios. As expected, the total capacity decreases for thicker Mg_2Si coatings, because the capacity of Mg_2Si is much smaller than that of Si (1300 vs. 3590 mAh/g). The results for Mg-coated SiNWs are very similar to

those for Mg_2Si coating, although in the case of Mg, the electrode with the thinnest Mg coating has clearly the highest CE and lowest initial capacity losses.

Table 2-1: Galvanostatic constant-current electrochemical results obtained for the bare SiNWs, the Mg_2Si, and the Mg coated Si nanowires nanocomposites at 0.1C cycle rate.

Electrode	Measured first discharge specific capacity (mAh/g)	First discharge capacity loss (mAh/g)	Initial irreversible capacity (mAh/g)	Initial Coulombic efficiency (%)
SiNWs	3576	184	280	92.0
10Mg/SiNWs	3209	132	134	95.8
14Mg_2Si/SiNWs	3338	141	234	93.0
20Mg/SiNWs	3165	180	205	93.5
50Mg/SiNWs	3030	190	205	93.2
70Mg_2Si/SiNWs	3089	172	213	93.1

Upon delithiation, there is a single flat plateau at ~ 0.4 V during the first 10-20 cycles, followed by an upward sloping region in all delithiation profiles. It is known that at potentials around 20 mV vs. Li/Li^+, crystallization of $Li_{15}Si_4$ can occur during lithiation. During subsequent delithiation, there will be a two-phase co-existence region between this crystalline phase and an amorphous Si-Li solid solution. [9] At higher cycle numbers, the shape of the delithiation curve changes. When the capacity decreases and the absolute current is kept constant, the 'effective' C-rate will increase. This increases the overpotential during lithiation and decreases the time that the potential is below 20 mV and crystallization of $Li_{15}Si_4$ may no longer occur or to a smaller extent. Thus, the plateau at 0.4 V becomes much narrower during cycling. See, for instance, the 20^{th} delithiation curve for 14Mg_2Si/SiNWs in Figure 2-7(c), where the length of the plateau around 0.4 V is less than half of that in cycle 1, although total capacity loss is still only 7%. For the Mg-coated SiNWs (Figure 2-7(b), (d), and (e)), the picture is basically the same. The voltage profiles have the same shape as for the Mg_2Si/SiNWs, both for lithiation and delithiation.

The similarities between bare and Mg/Mg_2Si-coated SiNWs are illustrated further in Figure 2-8(a) and (c), where the capacity retention expressed as % of the first cycle is plotted vs. cycle number for both Mg-and Mg_2Si-coated SiNWs in comparison with bare SiNWs. Both Mg and Mg_2Si coating materials have no noticeable effect on the cycling stability at 0.1C rate, contrary to e.g. Al coating which was found to have favorable influence between 3 and 8 wt.% Al. [28]

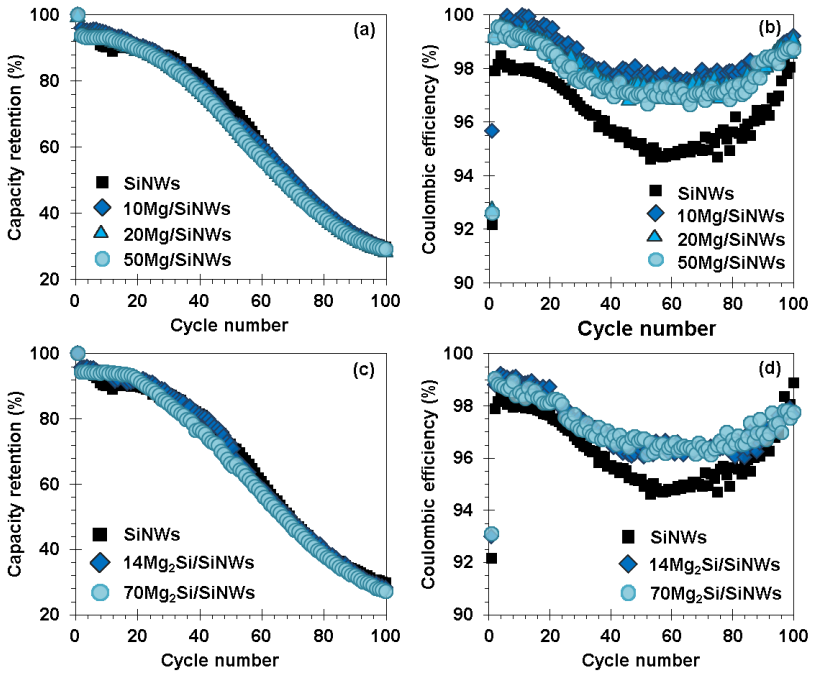

Figure 2-8: (a) % capacity retention vs. cycle number for different Mg thicknesses, (b) Coulombic efficiency, (c) % capacity retention vs. cycle number for Mg_2Si/SiNWs nanocomposites, (d) Corresponding coulombic efficiency. Note that all results are from cycling at charging rate of 0.1C over 0.01-2 V vs. Li/Li^+ voltage window.

All materials show gradual capacity decay in the first 20-30 cycles and considerably faster degradation beyond that. Approximately 30% of the initial capacity is left after 100 cycles in every case corresponding to 850-1000 mAh/g. The coulombic efficiency as a function of cycle number is plotted in Figure 2-8(b) and (d) for Mg and Mg_2Si/SiNWs, respectively. The cycles where the coulombic efficiency is lowest coincide with those where the capacity decays most rapidly. For the bare SiNWs, the CE varies from ~ 98% in the earliest and latest stages of cycling to < 95% around cycle 50. Interestingly, all coated materials have significantly and consistently higher coulombic efficiency than the bare nanowires. Both for Mg-and Mg_2Si-coated SiNWs, the coulombic efficiency is close to 100% at the start of cycling in some cases and never below 97 and 96% for Mg/SiNWs and Mg_2Si/SiNWs, respectively. So even though the capacity retention is not influenced by the coatings, side reactions such as electrolyte decomposition to Li_2CO_3, which consume electrons and is thus a factor in reduced CE, appear to be inhibited to some extent by the coatings.

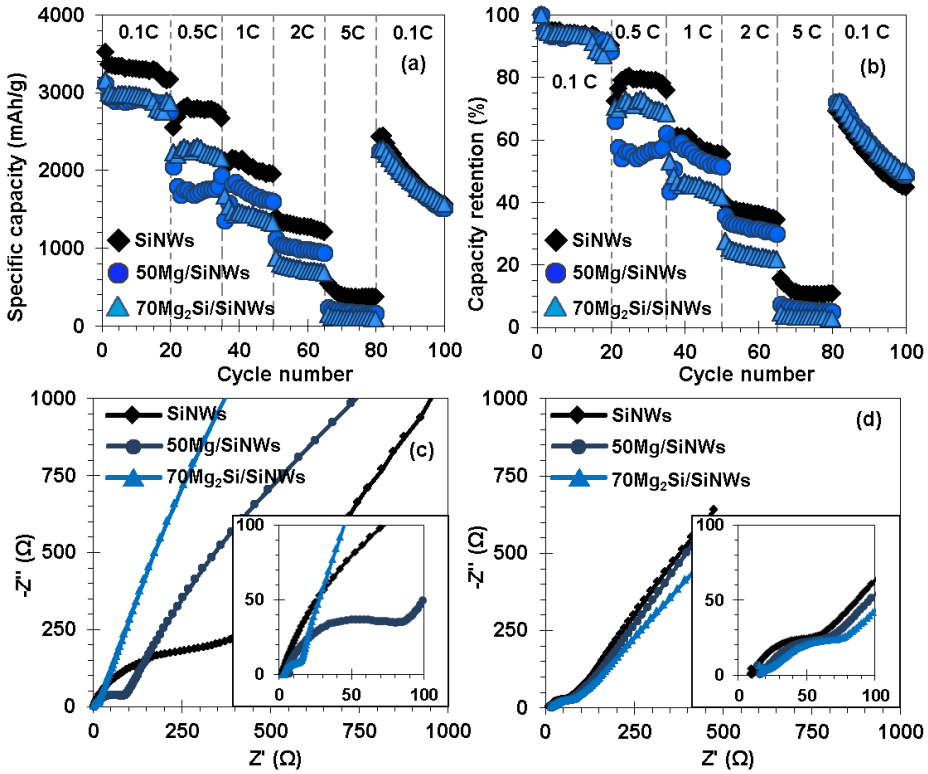

Figure 2-9: Comparison of the rate capability of bare SiNWs, 50Mg, and 70Mg_2Si/SiNWs expressed in mAh/g (a) and % of initial capacity (b). (c) Impedance spectra in as-made state and (d) impedance spectra after 100 cycles.

Because Si is a semiconductor, a metallic Mg coating could help improve conductivity in the composite material and help improve the charge and discharge capacity at higher rates. A comparison between bare SiNWs, 50Mg-and 70Mg_2Si/SiNWs is shown in Figure 2-9. Each electrode was first cycled 20 times at 0.1C and the current was then increased stepwise up to a maximum of 5C for 15 cycles at each step and eventually decreased back to 0.1C up to cycle 100. The results basically confirm the picture previously obtained from the CV curves. Even though Mg might be expected to enhance conductivity and thus improve the kinetics, 50Mg and 70Mg_2Si/SiNWs' capability to cycle at high rates is actually worse than for bare SiNWs. At 0.1C rate, the total capacity of the bare SiNWs is higher than that of the composites due to the added weight, and lower capacity compared to Si, of Mg and Mg_2Si. At 0.5C rate and higher, the difference becomes even more pronounced. Remarkably, the capacity of 50Mg/SiNWs is nearly identical at 0.5 and 1C rates and from that moment onwards, the rate capability of 50Mg/SiNWs

is superior to that of 70Mg_2Si/SiNWs. This may be indicative of the superior conductivity of Mg metal compared to Mg_2Si after the native oxide has been sufficiently broken up after a certain number of charge/discharge cycles. The fact that the capacities of all three electrodes virtually coincide again when the rate is decreased back to 0.1C further supports this.

Figure 2-9(c) and (d) show impedance spectra for the as-made and 100 times cycled states, respectively. Here too, the influence of native oxide can be clearly seen both for bare SiNWs and 50Mg/SiNWs. The diameter of the semicircle at higher frequencies, indicative of the charge transfer resistance, is several hundred ohms for bare SiNWs. Remarkably, the charge transfer resistance for Mg_2Si coated SiNWs appears to be much smaller, indicating that a native oxide on Mg_2Si either does not form or is very thin compared to a native oxide on either pure Si or pure Mg. After 100 charge/discharge cycles, the charge transfer resistance is approximately equal for all three electrodes, as would be expected based on their (nearly) identical capacities in cycles 80-100.

2.3.3 Post-cycling SEM and TEM characterization

Figure 2-10 shows SEM images of bare SiNWs (a-c), 50Mg/SiNWs (d-e), and 70Mg_2Si/SiNWs (f-g) after the 1st (left), 10th (middle), and 100th (right) cycles. As can be seen in parts (a) and (b), disintegration of bare SiNWs sets in early. Already after 10 cycles, a substantial number of nanowires are in the process of breaking up. Interestingly, rather than fracturing, the nanowires that are in the process of breaking up in Figure 2-10(b) have turned into a loose agglomeration of thin filaments. This is consistent with the morphology observed in in-situ TEM studies on the lithiation of SiNWs where a dumbbell-shaped morphology was observed during lithiation to the point of splitting the nanowire down the middle. [21] Similar phenomena have been observed for Si particles, [12] where pore formation inside the particles was found to occur upon delithiation, creating similar structural vulnerabilities to those observed for nanowires during lithiation cycling. Our observations here indicate that this process repeats itself during subsequent cycles (See Figure 2-10(c), (f), and (i)). The Mg-and Mg_2Si coating seems to inhibit this process to some extent, similar to what was observed for Al-coated SiNWs.

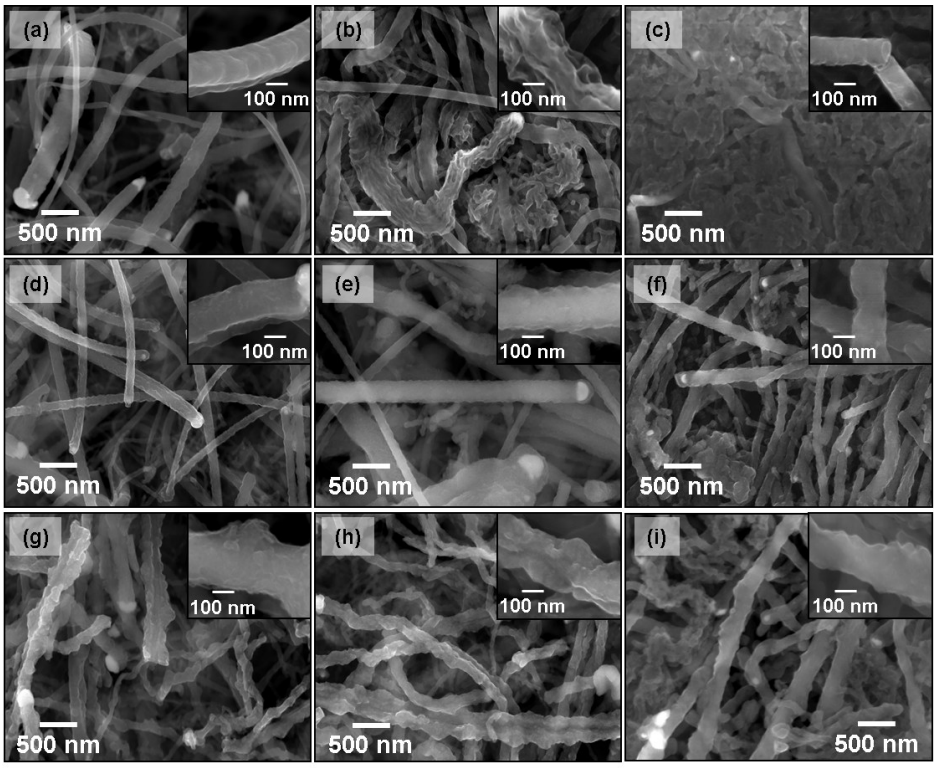

Figure 2-10: SEM micrographs and high magnification close-up inserts of (a-c) bare SiNWs, (d-f) 50Mg/SiNWs, and (g-i) 70Mg_2Si/SiNWs after 1st (left), 10th (middle), and 100th (right) cycles at 0.1C rate in delithiated state.

Figure 2-11 shows FIB cross-section SEM images and elemental mappings of bare SiNWs (top), 50Mg/SiNWs (middle), and 70Mg_2Si/SiNWs (bottom) after 100 cycles. The spaces between the nanowires are seen to have completely filled up with SEI from the substrate all the way to the tips of the nanowires. It is clear from the Mg elemental maps for 50Mg/SiNWs and 70Mg_2Si/SiNWs that despite the strong directionality of sputter deposition, Mg penetrates deep into the nanowire forest, all the way to the TiN/SS substrate. In all three cases, large voids between the bottom of the nanowire forests and the substrates are observed. From the elemental mappings it can be seen that, especially for the bare SiNWs, large deposits of electrolyte decomposition products seem to have formed near these voids, as evidenced by the strong signal in the carbon mapping in particular.

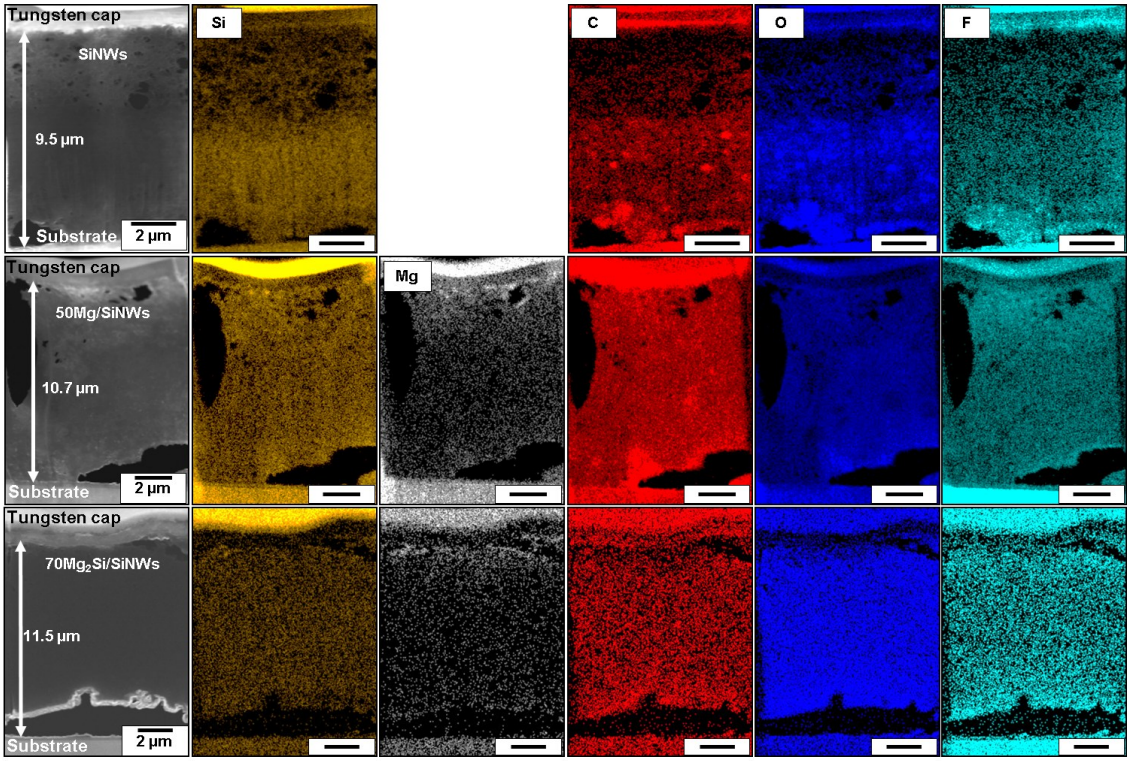

Figure 2-11: FIB cross-section SEM images of bare SiNWs, 50Mg/SiNWs, and 70Mg_2Si/SiNWs together with elemental mappings of Silicon, Magnesium, Carbon, Oxygen, and Fluorine after 100 cycles at rate of 0.1C over 0.01-2 V vs. Li/Li^+ voltage window. Note that heavier elements in the steel substrate and the W in the cap have a very large number of emission lines that overlap with any of the lighter elements and thus appear bright in all of the maps.

The same is true for the oxygen and fluorine mappings as well as the carbon map for 50Mg/SiNWs. The formation of these large voids provides direct evidence that loss of electrical contact between the nanowire forest and the substrate is an important degradation mechanism, as we proposed before based on impedance measurements. [28] We also observe that the TiN interlayer stays in contact with the stainless steel substrate even after 100 cycles at the rate of 0.1C and that all the contact loss occurs between the nanowires and the TiN layer. This illustrates the excellent Li diffusion barrier properties of TiN. [47] After 100 cycles, the electrode materials are approximately 10 micrometers thick. Initially (see Figure 2-1(a)), the average length of the nanowires was slightly taller at 12-15 µm. Furthermore, the top part of the cross-section of especially the bare SiNWs seems to have a large fraction of voids.

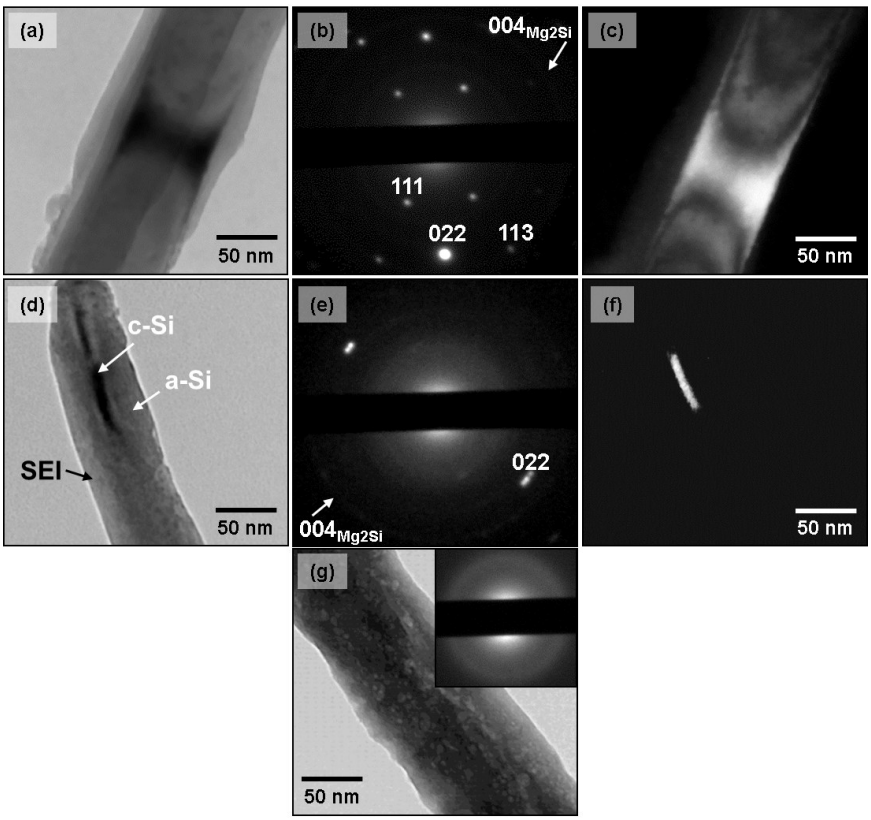

Figure 2-12: TEM micrographs of cycled $14Mg_2Si$/SiNWs anode material after 100 cycles at the rate of 0.1C in delithiated state. (a-c) A SiNW with a thick crystalline core, (b) corresponding indexed SAD pattern, (c) dark-field image of silicon, obtained using $g=022_{Si}$. (d-f) A crystalline core-amorphous shell SiNW, (d) bright-field of the nanowire with mentioned crystalline and amorphous areas, (e) corresponding indexed SAD pattern, (f) dark-field micrograph, obtained using $g=022_{Si}$. (g) Bright-field with corresponding SAD pattern of a completely amorphous SiNW.

This suggests that the major part of the nanowire forest has agglomerated to a thick, solid mass of Si near the substrate. This phenomenon of electrochemically-induced agglomeration has often been observed. It was found by Karki et al. [48] that silicon nanowires that cross each other become 'welded' together after lithiation/delithiation. This provides a mechanism through which agglomeration of nanowires can occur. Similarly, lithiation-induced 'contact flattering' has been reported by Gu et al. [12] for lithiation of Si nano*particles* embedded in, or attached to, a carbon matrix. The coated nanowire forests are slightly higher after cycling, suggesting some benefit to the mechanical strength of the nanowires from the coatings, although the difference is less than 25%. This provides an explanation for the observed void formation as thick Si films are known to delaminate in early stages of cycling. [15]

Figure 2-12 shows TEM micrographs of 14Mg_2Si/SiNWs after being cycled 100 times at a rate of 0.1C in the delithiated state. It demonstrates three different SiNWs with different degrees of crystallinity. The SiNW shown in Figure 2-12(a-c) is mostly single crystalline with weak diffuse rings, showing there likely is a small amount of amorphous material as well. In Figure 2-12(d-f), one can see a nanowire that is for the most part amorphous, but has a partly crystalline core, which is confirmed by the dark-field micrograph obtained from 022 reflection of silicon. Finally, Figure 2-12(g) shows a TEM micrograph of a completely amorphous SiNW, confirmed by the diffuse rings in the SAD pattern. These observations may be explained as follows. As-made nanowires are rigid and brittle and some may break, or almost break off, during coin cell assembly. Only these nanowires would remain completely, or almost completely, single-crystalline, as the nanowires are completely amorphisized after the first cycle. [28] Nanowires that survive for multiple cycles will therefore end up with a larger amorphous fraction. These nanowires may become detached from the substrate due to the void formation that was observed in Figure 2-11. Depending on the cycle number at which nanowires lose their electrical connections with the current collector or the rest of the nanowire forest, they will have different crystalline-to-amorphous ratios.

The mechanical integrity of the nanowires themselves will also play a role. Bare SiNWs are subject to disintegration, as was most obvious from the inset in the SEM image of Figure 2-10(b). Similar to Al, the coatings seem to improve the mechanical integrity of the nanowires, as comparison of Figure 2-10(a-c) with (d-f) and (g-i) shows. Despite the improved mechanical integrity, the cycling stability is not improved, contrary to Al-coated SiNWs. Comparing the Mg/Mg_2Si coating on the one hand and Al on the other, there are a number of important differences. Al can alloy with Li up to a 1:1 ratio and will itself undergo considerable expansion. Some reports on Mg metal give its maximum capacity as > 3000 mAh/g corresponding to $MgLi_3$, [49] others suggest that Li merely deposits onto Mg without forming new phases. [50] Mg metal can dissolve up to 17 at.% Li, corresponding to 226 mAh/g (see also Figure 2-6(d)), without undergoing phase transformation and will not expand very much. A similar argument can be made for Mg_2Si. CC measurements on a planar Mg_2Si film (see Figure 2-6(a-c)) did show the capacity to be approximately equal to the aforementioned study by Kim et al. [32], which should induce considerable expansion in the coating as well. However, the CV curves showed

that the reaction kinetics of the Mg_2Si phase is slower than those of Si, delaying expansion relative to the Si nanowire. This can make the coatings more prone to delamination, again leading to more agglomeration of the nanowires compared to an active coating such as Al.

2.3.4 XPS measurements

The coulombic efficiency during extended cycling was consistently higher for both Mg-and Mg_2Si-coated nanowires as compared to bare SiNWs (see Figure 2-8). The reasons for this difference may be deduced form a more detailed compositional analysis of the SEI layer during cycling. To this end, X-ray photoelectron spectroscopy (XPS) was performed on as-made and cycled electrodes. Figure 2-13 shows C 1s, O 1s, F 1s, Si 2p, Li 1s/Mg 2p, and P 2p XPS spectra for bare SiNWs as well as both Mg-and Mg_2Si-coated materials in the as-made state and after 1, 10, and 100 cycles in delithiated state. All XPS spectra shown in Figure 2-13 were obtained from the top surface of the (cycled) nanowire forests. In all three cases, the presence of a native oxide is detected in the as-made material. The MgO signal disappears for both 50Mg and 70Mg_2Si/SiNWs after cycle 1, which indicates that the oxide is either reduced, as is possible for SiO_2, or simply covered by the SEI layer. For bare SiNWs, the peak assigned to SiO_2 has strong overlap with other signals in the O 1s spectra, but the Si 2p spectra show that the native oxide is clearly present in the as-grown state. After the first cycle, there is no Si signal in the XPS spectra. For bare SiNWs, a small amount of LiF is detected only after 10 cycles. After 100 cycles, the signal is barely detectable anymore. For both 50Mg and 70Mg_2Si/SiNWs, the LiF signal keeps increasing during cycling and for 70Mg_2Si/SiNWs the signal is by far the strongest.

Both in the C 1s and F 1s spectra, a small shoulder is visible beside the hydrocarbon and LiF peaks at 286.7 eV and 686.9 eV, respectively. The second peak in the F 1s spectra is most likely due to the presence of a mixed Li-P-O-F salt as reported by Nadimpalli et al.. [51] The peak at 290 eV in the C 1s spectra is consistent with the presence of free carbonate (CO_3^{2-}) ions as in Li_2CO_3. [52] The shoulder next to the main hydrocarbon peak in the C 1s spectra can also be assigned to C-O or C=O groups for the coated SiNWs.

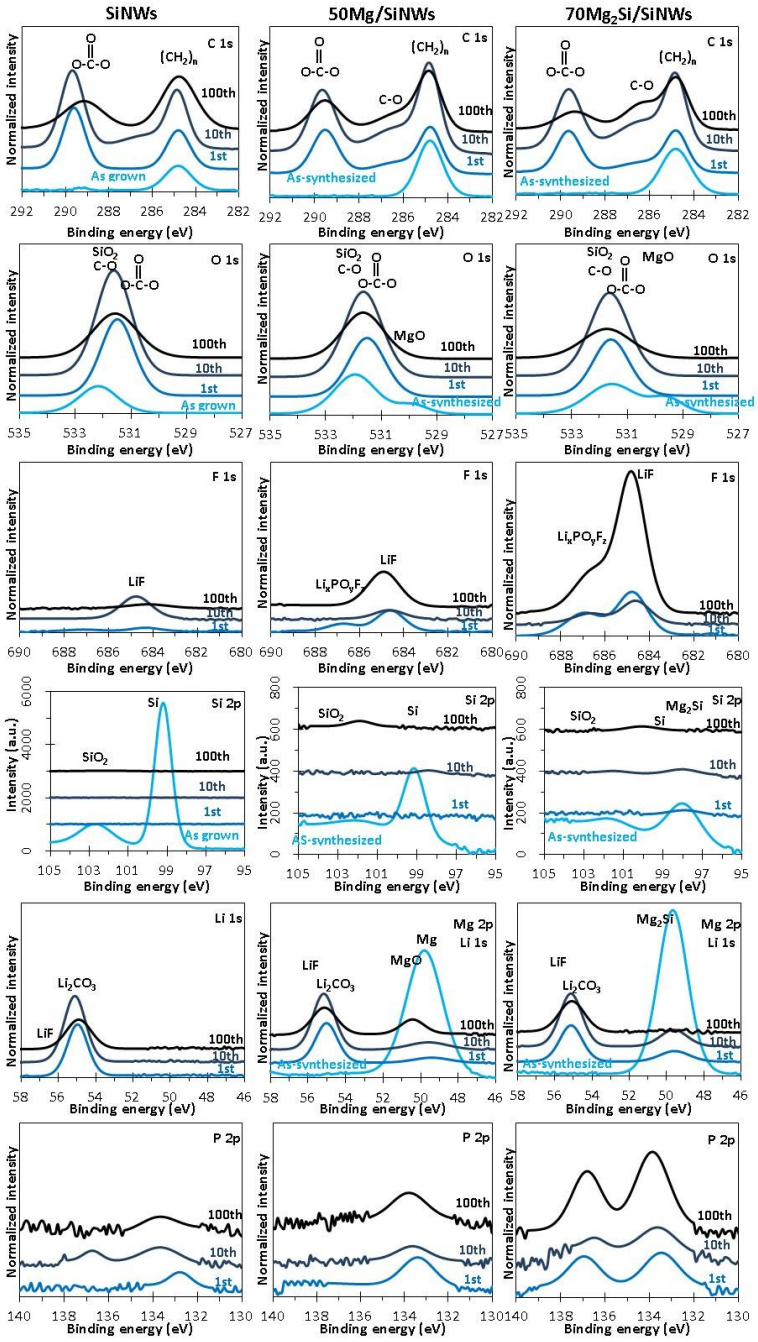

Figure 2-13: C 1s, O 1s, F 1s, Si 2p, Li 1s/Mg 2p, and P 2p high resolution XPS spectra of bare SiNWs, 50Mg/SiNWs, and 70Mg_2Si/SiNWs from the top surface of as-synthesized structures and the film formed on top of structure after 1st, 10th, and 100th cycles in delithiated state.

The main peak in the O 1s spectra is near to where it is expected for Li_2CO_3 although the maximum is at slightly higher binding energies. This is also consistent with carbonate groups

that are still attached to a hydrocarbon group on at least one side, [51,52] or with oxygen atoms as part of ether linkages. [52] From the XPS spectra, the elemental composition of the samples' surface was determined and the results, in atomic percentage, are listed in Table 2-2. For all electrodes, irrespective of cycle number, except the as-made material, a large amount of Li is detected, which may be in the form of Li_2CO_3, lithium alkylcarbonates or LiF, all of which are decomposition products of the electrolyte. [53] The SEI layers on the bare and coated nanowires show some clear differences in composition. Especially the Li content is significantly lower for the Mg-coated SiNWs as compared to the bare SiNWs. The same is true for the oxygen content, which suggests the Mg coating induces formation of electrolyte decomposition products other than Li_2CO_3. A significant amount of Mg also remains detectable throughout the course of cycling when measured from the top of the nanowire forest.

Table 2-2: Atomic composition (in percentage) as derived from the XPS spectra in Figure 2-13.

Electrode	**SiNWs**				**50Mg/SiNWs**				**70Mg$_2$Si/SiNWs**			
State	**As-grown**	**1st**	**10th**	**100th**	**As-synthesized**	**1st**	**10th**	**100th**	**As-synthesized**	**1st**	**10th**	**100th**
C 1s	11.5	24.3	26.3	35.5	9.1	27.4	31.3	31.6	8.6	24.4	29.7	31.7
O 1s	24.7	38.2	38.2	33.7	12.6	32.8	32.2	29.5	12.7	30.6	31.3	24.3
Si 2p	62.9	-	-	0.4	1.5	-	0.1	0.2	1.2	0.2	0.2	0.2
Li 1s	-	37.0	34.2	29.9	-	31.0	28.5	24.0	-	29.1	26.8	31.6
F 1s	-	0.3	0.9	0.3	-	1.5	0.3	2.1	-	3.7	1.0	10.7
Mg 2p	-	-	-	-	76.8	6.8	7.1	12.3	77.5	11.2	10.3	-
Other	0.9 (Au)	0.2	0.4	0.2	-	0.5	0.5	0.3	-	0.8	0.7	1.5 (P)

The $LiPF_6$ salt in the electrolyte is always in a chemical equilibrium with its decomposition products LiF and PF_5. [53] However, a significant amount of fluorine is detected only in the Mg- and Mg_2Si-coated SiNWs but mostly in Mg_2Si/SiNWs. PF_5 is highly reactive and may also be reduced further to PF_3 combining with 2 Li ions and 2 electrons to form more LiF and also reducing the coulombic efficiency. Both a slightly lower CE and a higher amount of LiF were found for Mg_2Si/SiNW as compared to Mg/SiNWs, indicating that this reaction was more prevalent for the Mg_2Si-coated SiNWs. Furthermore, PF_5 is a strong Lewis acid and can initiate a ring-opening polymerization reaction of ethylene carbonate. [54,55] The resulting polymer, depending on the exact conditions, will consist of polycarbonate and polyethylene oxide (PEO)

blocks where the carbonate units may evolve CO_2 gas, eventually resulting in a polyethylene-oxide polymer on the surface of the active material. [55] Based on these observations, the amount of LiF and C-O-C linkages should be correlated, which was indeed observed for the coated nanowires. The decomposition of $LiPF_6$ to PF_5 and LiF is an electro*less* process and would not contribute to lower the coulombic efficiency. The polymerization of EC, except for possible initial formation of an anionic end-group, also proceeds without electron transfer. The formation of significant amounts of LiF and PEO on coated SiNWs and the absence of the same on bare SiNWs could therefore explain the differences in coulombic efficiency. PEO, contrary to lithium alkylcarbonates resulting from electrolytic reduction of electrolyte solvents contains no ionic groups and would therefore act as a passivating layer with relatively poor Li ionic conductivity. This may explain our observation that bare SiNWs have superior rate capability over Mg_2Si/SiNWs (see Figure 2-9).

We have elucidated a number of important degradation mechanisms that occur simultaneously during electrochemical cycling of SiNWs. From the cross-sections in Figure 2-11, it is obvious that detachment of the nanowires from the substrate/current collector is an important factor in determining the cycling stability of the electrodes. A build-up of electrolyte decomposition products such as those detected by the XPS measurements can exert additional mechanical pressure leading to detachment of the active material from the substrate. The high concentrations of carbon, oxygen, and fluorine found near the large voids in the bare SiNW and 50Mg/SiNW electrodes in Figure 2-11 seem to support this. It should be noted that coulombic efficiency is a very important parameter in practical operation of a battery. For all our electrodes, the coulombic efficiency was considerably lower than 100%, which is due to a combination of Li consumption by SEI formation and immobilization of Li in nanowires that detach from the substrate or fracture before they are fully delithiated. In our coin cell configuration, the Li foil provides a virtually inexhaustible reservoir of Li/Li^+, so that Li that is trapped in the SEI layer can be replenished. However, in a Li-ion battery all the Li is initially contained in the $LiCoO_2$ electrode. Immobilization of Li in the SEI layer will immediately lead to a decrease in the capacity of the battery. So while the intrinsic capacity degradation due to loss of active material appears to be roughly the same for all of our electrodes, the improvement of the coulombic efficiency for the coated materials is definitely an important finding.

In order to bring SiNWs closer to application, the weight of the substrate should be reduced or eliminated. Using TiN diffusion barriers, it should be possible to use Cu foil as substrate/current collector instead of stainless steel disks. Furthermore, since the formation of voids and detachment of the nanowire assembly from the substrate seems to be an important degradation mechanism, further improvements could be achieved by using the nanowires in 'powder' form, either by detaching them from the substrate prior to electrochemical testing or synthesizing them by wet-chemical methods and mixing them with binders and conductive additives. Stable capacity of up to 2000 mAh/g Si over 50 cycles was recently achieved in this manner. [56] Based on our results, further improvements could be achieved by conformal coating of the nanowires to improve coulombic efficiency and reduce nanowire agglomeration during cycling.

2.4 Conclusions

The electrochemical properties and microstructural evolution of bare silicon nanowires and nanowires coated with Mg and Mg_2Si were studied and compared. Compared to bare SiNWs, the coulombic efficiency was significantly higher for the coated materials, most significantly so for the Mg-coated material. XPS analysis showed clear differences in the composition of the SEI between bare and coated nanowires and evidence for a passivating polyethyleneoxide layer was found in the latter case. For both the Mg-and Mg_2Si-coated materials more decomposition product from the electrolyte salt in the form of LiF and Li-P-O-F compound was found compared to bare SiNWs. SEM showed a beneficial effect of the coatings on the mechanical integrity of the nanowires during early-stage cycling. FIB cross-sectional SEM identified the formation of large voids between the bottom of the nanowire forests and the TiN substrate as possibly the most important capacity degradation mechanism in SiNW electrodes. This diminishes electrical contact between the substrate and active material, leading to capacity degradation in all the materials studied. Agglomeration of the nanowires upon repeated lithiation/delithiation cycling into a microns-thick Si layer is a possible driving force for the observed delamination. Future efforts should therefore concentrate on improving adhesion between the nanowires and the substrate and use of deposition methods that can produce

conformal coatings that fully cover the nanowires such as atomic layer deposition to avoid nanowire agglomeration.

2.5 References

1 M. Roberts, P. Johns, J. Owen, D. Brandell, K. Edstrom, G. El Enany, C. Guery, D. Golodnitsky, M. Lacey, C. Lecoeur, H. Mazor, E. Peled, E. Perre, M. M. Shaijumon, P. Simon, and P. L. Taberna, J. Mater. Chem., 2011, 21, 9876.

2 R. Marom, S. F. Amalraj, N. Leifer, D. Jacob, and D. Aurbach, J. Mater. Chem., 2011, 21, 9938.

3 M. R. Palacin, Chem. Soc. Rev., 2009, 38, 2565.

4 M. Liang, and L. Zhi, J. Mater. Chem., 2009, 19, 5871.

5 H. K. Liu, Z. P. Guo, J. Z. Wang, and K. Konstantinov, J. Mater. Chem., 2010, 20, 10055.

6 V. L. Chevrier, J. W. Zwanziger, and J. R. Dahn, Can. J. Phys., 2009, 87, 625.

7 J. Li, and J. R. Dahn, J. Electrochem. Soc., 2007, 154, A156.

8 S. D. Beattie, D. Larcher, M. Morcrette, B. Simon, and J. M. Tarascon, J. Electrochem. Soc., 2008, 155, A158.

9 T. D. Hatchard, and J. R. Dahn, J. Electrochem. Soc., 2004, 151, A838.

10 V. L. Chevrier, and J. R. Dahn, J. Electrochem. Soc., 2010, 157, A392.

11 J. L. G. Cámer, J. Morales, and L. Sánchez, J. Mater. Chem., 2011, 21, 811.

12 M. Gu, Y. Li, X. Li, S. Hu, X. Zhang, W. Xu, S. Thevuthasan, D. R. Baer, J. G. Zhang, J. Liu, and C. Wang, ACS Nano, 2012, 6, 8439.

13 Y. Oumellal, N. Delpuech, D. Mazouzi, N. Dupre, J. Gaubicher, P. Moreau, P. Soudan, B. Lestriez, and D. Guyomard, J. Mater. Chem., 2011, 21, 6201.

14 L. Y. Beaulieu, T. D. Hatchard, A. Bonakdarpour, M. D. Fleischauer, and J. R. Dahn, J. Electrochem. Soc., 2003, 150, A1457.

15 H. Haftbaradaran, and H. Gao, Appl. Phys. Lett., 2012, 100, 121907.

16 U. Kasavajjula, C. Wang, and A.J. Appleby, J. Power Sources, 2007, 163, 1003.

17 J. Cho, J. Mater. Chem., 2010, 20, 4009.

18 A. Gohier, B. Laïk, K. H. Kim, J. L. Maurice, J. P. Pereira-Ramos, C. S. Cojocaru, and P. T. Van, Adv. Mater., 2012, 24, 2592.

19 C. K. Chan, H. Peng, J. Liu, K. McIlwrath, X. F. Zhang, R. A. Huggins, and Y. Cui, Nat. Nanotechnol., 2008, 3, 31.

20 C. K. Chan, R. Ruffo, S. S. Hong, R. A. Huggins, and Y. Cui, J. Power Sources, 2009, 189, 34.

21 X. H. Liu, H. Zheng, L. Zhong, S. Huang, K. Karki, L. Q. Zhang, Y. Liu, A. Kushima, W. T. Liang, J. W. Wang, J. H. Cho, E. Epstein, S. A. Dayeh, S. T. Picraux, T. Zhu, J. Li, J. P. Sullivan, J. Cumings, C. Wang, S. X. Mao, Z. Z. Ye, S. Zhang, and J. Y. Huang, Nano Lett., 2011, 11, 3312.

22 J. W. Choi, J. McDonough, S. Jeong, J. S. Yoo, C. K. Chan, and Y. Cui, Nano Lett., 2010, 10, 1409.

23 G. P. Yin, Y. H. Xu, Y. L. Ma, P. J. Zuo, and X. Q. Cheng, J. Mater. Chem., 2010, 20, 3216.

24 H. Jung, Y. U. Kim, M. S. Sung, Y. Hwa, G. Jeong, G. B. Kim, and H. J. Sohn, J. Mater. Chem., 2011, 21, 11213.

25 C. Du, M. Chen, L. Wang, and G. Yin, J. Mater. Chem., 2011, 21, 15692.

26 Z. Chen, Y. Qin, K. Amine, and Y. K. Sun, J. Mater. Chem., 2010, 20, 7606.

27 L. Q. Zhang, X. H. Liu, Y. Liu, S. Huang, T. Zhu, L. Gui, S. X. Mao, Z. Z. Ye, C. M. Wang, J. P. Sullivan, and J. Y. Huang, ACS Nano, 2011, 5, 4800 and references therein.

28 E. L. Memarzadeh, W. P. Kalisvaart, A. Kohandehghan, B. Zahiri, C. M. B. Holt, and D. Mitlin, J. Mater. Chem., 2012, 22, 6655.

29 H. Chen, Y. Xiao, L. Wang, and Y. Yang, , J. Power Sources, 2011, 196, 6657.

30 I. Ryu, J. W. Choi, Y. Cui and W. D. Nix, J. Mech. Phys. Solid, 2011, 59, 1717.

31 H. Okamoto, Desk Handbook “Phase Diagrams for Binary Alloys”, ASM International, 2000, p. 527.

32 H. Kim, J. Choi, H. J. Sohn, and T. Kang, J. Electrochem. Soc., 1999, 146, 4401.

33 T. Moriga, J. Solid State Chem., 2000, 153, 386.

34 G. A. Roberts, E. J. Cairns, and J. A. Reimer, J. Power Sources, 2002, 110, 424.

35 S. W. Song, K. A. Striebel, X. Song, and E. J. Cairns, J. Power Sources, 2003, 119-121, 110.

36 G. Ji, Y. Ma, and J. Y. Lee, J. Mater. Chem., 2011, 21, 9819.

37 K. Xu, and A. von Cresce, J. Mater. Chem., 2011, 21, 9849.

38 A. J. Smith, J. C. Burns, X. Zhao, D. Xiong, and J. R. Dahn, J. Electrochem. Soc., 2011, 158, A447.

39 C. K. Chan, R. Ruffo, S. S. Hong, and Y. Cui, J. Power Sources, 2009, 189, 1132.

40 Y. C. Yen, S. C. Chao, H. C. Wu, and N. L. Wu, J. Electrochem. Soc., 2009, 156, A95.

41 W. Xu, S. S. S. Vegunta, and J. C. Flake, ECS Transactions, 2011, 33, 55.

42 http://www.mtixtl.com/ElectrolyteLiPF6forLiCoO2Lithium-ionbatteryRandD1KginaSafeStainle.aspx

43 G. S. Doerk, N. Ferralis, C. Carraro, and R. Maboudian, J. Mater. Chem., 2008, 18, 5376.

44 L. Brewer, Chem. Rev., 1953, 52, 1.

45 B. Key, R. Bhattacharyya, M. Morcrette, V. Seznec, J. M. Tarascon, and C. P. Grey, J. Am. Chem. Soc., 2009, 131, 9239.

46 V. L. Chevrier, J. W. Zwanziger, and J. R. Dahn, J. Alloy Compd., 2010, 496, 25.

47 H. C. M. Knoops, L. Baggetto, E. Langereis, M. C. M. van de Sanden, J. H. Klottwijk, F. Roozeboom, R. A. H. Niessen, P. H. L. Notten, and W. M. M. Kessels, J. Electrochem. Soc., 2008, 155, G287.

48 K. Karki, E. Epstein, J. H. Cho, Z. Jia, T. Li, S. T. Picraux, C. Wang, and J. Cumings, Nano Lett., 2012, 12, 1392.

49 W. J. Zhang, J. Power Sources, 2011, 196, 13.

50 J. Morales, R. Trócoli, and J. Santos-Peña, Electrochem. Solid St. Lett., 2009, 12, A145.

51 S. P. V. Nadimpalli, V. A. Sethuraman, S. Dalave, B. Lucht, M. J. Chon, V. B. Shenoy, and P. R. Guduru, J. Power Sources, 2012, 215, 145.

52 NIST XPS database at http://srdata.nist.gov/xps/Default.aspx

53 K. Xu, Chem. Rev., 2004, 104, 4303.

54 T. Kawamura, A. Kimura, M. Egashira, S. Okada, and J. I. Yamaki, J. Power Sources, 2002, 104, 260.

55 J. C. Lee, and M. H. Litt, Macromolecules, 2000, 33, 1618.

56 A. M. Chockla, T. D. Bogart, C. M. Hessel, K. C. Klavetter, C. B. Mullins, and B. A. Korgel, J. Phys. Chem. C, 2012, 116, 18079.

Chapter 3: Silicon Nanowire Lithium-ion Battery Anodes with ALD Deposited TiN Coatings Demonstrate a Major Improvement in Cycling Performance

Material in this chapter has been published in:

Kohandehghan, Alireza, Peter Kalisvaart, Kai Cui, Martin Kupsta, Elmira Memarzadeh, and David Mitlin. "Silicon nanowire lithium-ion battery anodes with ALD deposited TiN coatings demonstrate a major improvement in cycling performance." J. Mater. Chem. A 1, (2013): 12850-12861.

3.1 Introduction

Lithium-ion batteries (LIBs) offer several advantages such as high gravimetric and volumetric energy density, high power density, and low self-discharge rate. Since the first commercial announcement of LIBs, tremendous effort has been made in material development which has resulted in diversification of the cathode materials from $LiCoO_2$ to other Li-transition metal oxides such as spinel $LiMn_2O_4$ and Li-transition metal phosphates, especially $LiFePO_4$, as well as improved and safer electrolyte chemistries. [1] On the other hand, for anodes, graphite is still the primary material in commercial Li-ion batteries having been this way since their introduction. [2] However, since the theoretical gravimetric and volumetric capacities of graphite are limited to ~372 mAh/g and 837 mAh/cm^3, respectively, research into higher energy density anodes is ongoing and has been intensifying over the past decade. [3]

Graphene-based carbon nanostructures generally have higher capacity than graphite combined with good rate capability. [4,5] However, the group 14 elements other than carbon, Sn, Ge and Si, can theoretically be alloyed with up to 3.75 Li atoms per atom of the host material and are all being investigated as anode materials with even higher capacities. [6-8] Because of its high abundance, low toxicity, and largest specific capacity per weight (~ 3590 mAh/g) after lithium (3862 mAh/g), Si is the most attractive alternative to graphite. [9-14] It also has a high

volumetric capacity of about 8257 mAh/cm^3. In fact, even after taking the high volume expansion after full lithiation up to $Li_{15}Si_4$ (280%) [15,16] into account, the volumetric capacity is still higher than that of Li metal; 2170 vs. 2066 mAh/cm^3. However, it is this same high volume expansion that has hindered practical application of silicon as a LIB anode material. Repeated volume expansion and contraction upon cycling results in severe decrepitation, breakdown of the electronic contact within the electrode, and rapid capacity fading to, in some cases, nearly zero. [17,18]

A variety of silicon nanostructures have shown improved performance in LIBs as anode in terms of capacity and cyclability, [19-30] e.g. by making porous [26] or hollow spherical and tubular structures [27-30] part of the volume expansion can be accommodated internally. Silicon nanowires (SiNWs) grown on a conductive substrate can potentially eliminate the need for binders and conductive additives and have attracted the most attention during the past five years. [19,22-25,31-41] Their small diameter keeps Li diffusion distances short and enables accommodation of the strain in the radial direction. Most early studies on SiNWs presented nanowires performance over few initial cycles during which cycling stability of SiNWs is always superior to powder. After 30-40 cycles, SiNWs anode starts to lose its capacity rapidly. For instance, about 70% capacity loss after 100 cycles within 0.01-2 V vs. Li/Li^+ at 0.1C, [24] and ~ 63% loss after 80 cycles over a similar potential window at 0.2C have been observed. [32] This failure is known to be due to fracture of the individual nanowires, as well as due to solid electrolyte interface (SEI) driven nanowire agglomeration and *en-masse* delamination. [33]

In order to modify materials expansion and SEI amount and composition and thereby improve the electrochemical cycling stability, some surface coatings have been shown to be effective. [24,33,36-40] For example, enhanced cyclability was achieved for Al-coated SiNWs. [24] This was attributed to an electrical conductivity improvement due to the metallic coating, which also buffered the induced volume change. Radial expansion has been shown to be greatly reduced by coatings. [42] Furthermore, below a nanowire diameter of ~ 50 nm, a thin layer of SiO_2 has been observed to even prevent expansion altogether. [43] Thermodynamic calculations showed that although the maximum Li content in Si is influenced by stress, [43,44] up to 80% of the theoretical capacity of free-standing Si can be achieved with only 25% volume expansion. [43] Therefore, it is

expected that applying a conformal coating to SiNWs will have a strong positive influence on their electrochemical cycling stability.

Transition metal nitrides have many applications in energy storage and conversion [45] including but not limited to LIBs, supercapacitors, electrocatalysis and oxygen reduction catalysts for fuel cells [46] or Li-air batteries. [47] For TiN in particular, its high electrical conductivity (resistivity of 25 μΩ.cm) [48] is one of its most important attributes. As a conductive additive in the form of nanoparticles, it has been widely applied in both supercapacitors [49,50] and Li-ion batteries to enhance the performance of cathodes [51] as well as anodes [52-54] as a way to increase the rate capability of the electrodes. Combined with Si, either by ball-milling [55] or chemical synthesis, [56] TiN has also proved useful to enhance electrical conductivity and hence rate capability in a composite material. However, all aforementioned studies use TiN in the form of (nano)particles, either as a homogeneous mixture or in the form of a core-shell composite, although in the latter case, the coating would be highly defective.

Atomic layer deposition (ALD) has been proven able to conformally coat structures with high aspect ratios [21,57,58] and can be expected to achieve uniform and conformal coating with arrays of SiNWs as well. TiN can be deposited using ALD and has been used in this form to enhance the performance of lithium titanate spinel powder electrodes by increasing electrical conductivity. [59] Since it is also quite tough and unreactive towards Li, it can potentially fulfill a dual role in SiNW electrodes. It is expected to increase rate performance through its high electrical conductivity, and in addition act as a structural support/passivation layer for SiNWs and increase their cycle life. While a relatively thick (> 50 nm) layer of TiN is actually an effective barrier layer to prevent Li penetration, [60] it is expected that for truly nanocrystalline TiN, several nm-thick coatings there would be sufficient Li diffusion through the boundaries to enable lithiation in the first cycle. Moreover, Li would diffuse through any local nanoscale cracks that were to form on the TiN surface, even if the coating layer were to be macroscopically intact.

3.2 Experimental

We prepared the SiNW electrodes by using a gold-catalyzed, vapour–liquid–solid (VLS) growth on 316L stainless steel spacers (∅ 15.5 mm, 1.89 cm^2). In order to prevent penetration of Au into stainless steel at elevated temperatures, a Ti/TiN diffusion barrier with layer thicknesses of 50 nm/200 nm was magnetron sputtered (AJA International, ATC Orion 8) onto the polished spacers. The base pressure in the sputtering chamber was always below 5×10^{-8} Torr. For reactive sputtering of TiN, a N_2:Ar ratio of 1:20 was used and the deposition temperature raised to 250 °C. A 10 nm Au catalyst layer was deposited after cooling the substrate down to room temperature. SiNWs were grown in a commercial Tystar CVD furnace using a SiH_4:H_2 ratio of 1:4 at a pressure of 100 Torr. The resulting mass loading of SiNWs grown under these conditions on each electrode is approximately 0.32 mg. TiN was coated onto SiNWs structures by means of both reactive sputtering under the same conditions as for the barrier layer and by ALD. ALD deposition was performed using an Oxford FlexAL ALD instrument with $TiCl_4$ and N_2 as the Ti and nitrogen sources, respectively. TiN coatings were deposited at 120 ºC for different cycle numbers to control the thickness, with the average deposition rate of 0.2 Å/cycle.

CR2032 button half-cells with SiNW working electrodes and Li counter electrodes were assembled in an Ar glovebox with less than 0.2 ppm oxygen and moisture contamination. A polyethylene (MTI technologies) separator (porosity of 36–44% and 0.03 mm pore size) soaked with a liquid electrolyte of 1 M $LiPF_6$ dissolved in a 1:1:1 volume ratio of ethylene carbonate (EC): dimethyl carbonate (DMC): diethyl carbonate (DEC) organic solvents was placed between the electrode and the lithium in the cell. The cells were galvanostatically charged and discharged on a computer controlled BT2000 Arbin potentiostat between 0.01 and 2 V (vs. Li/Li^+) at various current densities. Capacities and C-rates were calculated based on the combined mass of the TiN coatings and the SiNWs. Cyclic voltammetry (CV) was carried out using Versa STAT 3 potentiostat in potential range of 0.01-2 V vs. Li/Li^+, at 1 mV/s scan rate. Electrochemical impedance spectroscopy (EIS) measurements were performed in a frequency range from 1000 Hz to 100 mHz with a perturbation amplitude of 10 mV. All electrochemical measurements were run at room temperature.

For post-cycling characterization, the coin cells were disassembled in an Ar-filled glovebox. The electrodes were rinsed with acetonitrile to ensure removal of excess electrolyte. Subsequently, the cycled materials were vacuum dried overnight at room temperature. The morphology of as-synthesized and cycled electrodes was observed using a field-emission scanning electron microscope (FESEM, Hitachi S-4800). Cross sectional SEM images of the bulk cycled materials were acquired by using a Hitachi NB5000 dual beam FIB/SEM. Conventional transmission electron microscopy (TEM) was performed using a JEOL JEM-2100. Selected area diffraction (SAD) patterns were processed using an open source software package that was developed in-house (Diffraction-Ring-Profiler). Electron energy loss spectroscopy (EELS) measurements were conducted using a JEOL 2200FS TEM operated at 200 kV in a scanning mode (STEM) with a nominal analytical beam size of 0.5 nm. High angle annular dark field (HAADF) images were recorded simultaneously with the EELS analysis. EELS analysis for compositional mapping were achieved with an in-column Ω filter in the microscope. The software employed for signal collection and data extraction from EELS spectra was Digital Micrograph (Gatan, Inc.). The data extraction was performed by following the standard procedure of pre-edge background subtraction and integration on the edge. [61] For each elemental map, a thickness map was also calculated from low-loss EELS spectra recorded for the same region to check for possible artifacts arising from large variation in thickness. We mapped Si, C, N, Ti, and O elements by integrating over core-loss edges of Si L, C K, N K, Ti L, and O K-edge, respectively. [62] Lithium maps for cycled materials were collected by integrating over low-loss edge of Li K-edge.

Surface composition of electrode materials is characterized via X-ray photoelectron spectroscopy (XPS) using an ULTRA (Kratos Analytical) spectrometer with Al K_α X-ray source (hv=1486.6 eV) run at 210 W. The main XPS chamber has a base pressure of less than 10^{-9} Torr. The beam was rastered over an area of 300×700 μm^2. All XPS spectra were calibrated according to universal C 1s binding energy at 284.8 eV. We used CasaXPS software for the peak fitting, background removal, and also atomic concentration calculation. Background subtraction was done using a nonlinear Shirley-type model.

3.3 Results and Discussion

3.3.1 As-synthesized Microstructures

We will employ a shorthand designation to label the various SiNW specimens, based on the synthesis method employed and the TiN thickness. For instance, 5 nm ALD TiN synthesized is termed ALD5TiN/SiNWs. From the mass increase of the electrode after ALD TiN deposition, the surface area enhancement can be estimated as approximately a factor 12, as the added weight (0.0593 mg) was equivalent to a planar film of ~ 60 nm. This same nominal thickness deposited by sputtering would also result in 5 nm thick TiN coating on the nanowires if the sputter flux were able to penetrate all the way to the nanowire base and will be designated Sp5TiN/SiNWs. TEM analysis confirms a highly uniform coating thickness for the case of ALD, but a relatively heterogeneous coating for the case of sputtering due to shadowing of the sputter flux. The smaller improvement with sputtering as compared to ALD is very likely due to the processes' intrinsically less conformal character where shadowing prevents atomic penetration near the base of the electrodes.

Figure 3-1 presents TEM micrographs of the as-synthesized Sp5TiN/SiNWs (a-c), ALD1TiN/SiNWs (d-f), ALD5TiN/SiNWs (g-i), ALD15TiN/SiNWs (j-l), and Sp15TiN/SiNWs (m-o). In the selected area diffraction (SAD) patterns shown in Fig. 1 (middle column), the rings of various sharpness correspond to the crystalline TiN with a cubic structure ($Fm\bar{3}m$), matching the simulation shown on the left side of the micrographs. The individual spot pattern corresponds to the SiNWs, which are either single crystal or twinned. It was straightforward to perform dark-field imaging of the TiN coatings while leaving out the Si spots. As Figure 3-1(a) indicates, the magnetron sputtered TiN coatings cover the SiNW core in a non-uniform manner. The coating is thicker on the right side of the nanowire compared to its left side, demonstrating the effect of flux shadowing during sputtering. Moreover, a comparison of the bright-field images of the sputtered coating with the ALD coating, demonstrates that the former contains much coarser TiN crystallites. Figure 3-1(b-c) highlight the substantially coarser crystallites in the sputtered TiN coatings: The TiN SAD pattern in Figure 3-1(b) is actually discontinuous, with the individual TiN crystallites being readily imaged in dark-field using a portion of this pattern. Figure 3-1(d-f) show the TEM micrographs of ALD1TiN/SiNWs in the as-synthesized state.

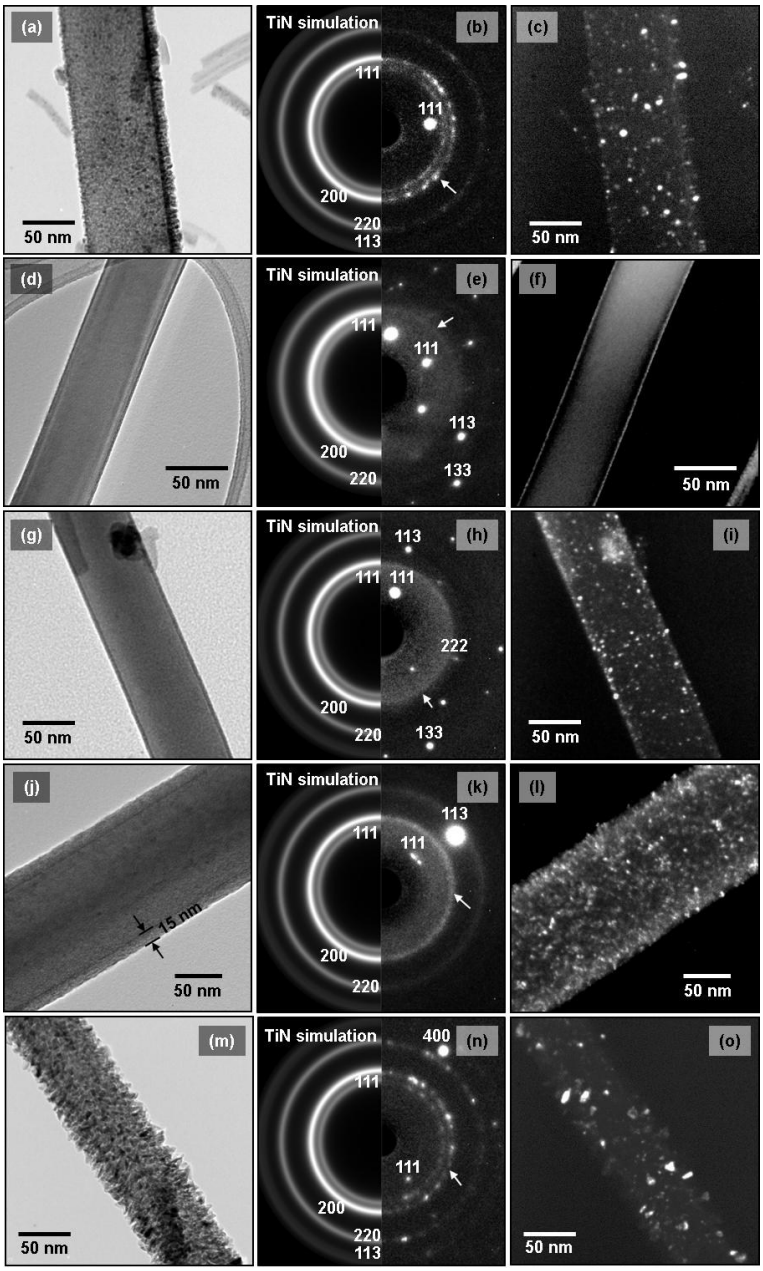

Figure 3-1: (a-c) TEM micrographs of as-synthesized Sp5TiN/SiNWs; (a) bright-field micrograph, (b) corresponding selected area diffraction (SAD) pattern with TiN ring pattern simulation, and (c) dark-field micrograph, obtained by using a portion of the 200_{TiN} ring pattern. (d-f) ALD1TiN/SiNWs; (d) bright-field micrograph, (e) SAD pattern with simulation, (f) dark-field micrograph obtained using the arrowed portion of the diffuse ring pattern. (g-i) ALD5TiN/SiNWs; (g) bright-field micrograph, (h) SAD pattern with simulation, and (i) dark-field micrograph obtained using the arrowed portion of TiN ring pattern. (j-l) ALD15TiN/SiNWs; (j) bright-field micrograph (k) SAD pattern with simulation, (l) dark-field micrograph taken using the arrowed portion of g=200_{TiN} reflection. (m-o) TEM micrographs of Sp15TiN/SiNWs, (m) bright-field micrograph, (n) corresponding indexed SAD pattern with TiN simulation, and (o) dark-field micrograph taken using portion of 200TiN ring.

The washed out ring in the SAD pattern fits with the 200_{TiN} from the simulation. Increasing the TiN thickness to 5 nm results in sharper and more clearly defined TiN rings. While it is very difficult to discern the TiN crystallites from the dark-field micrographs of the 1 nm thick coatings (Figure 3-1(f)), when the layer is 5 nm thick the individual grains may be readily imaged (Figure 3-1(i)). The TiN grain size further increases when the coating is 15 nm thick. Direct analysis of the dark-field micrographs yielded an average TiN grain size of 4 nm for the ALD5TiN/SiNWs, 7 nm for the ALD15TiN/SiNWs and 9 nm for Sp5TiN/SiNWs, with the sputtered microstructure having an overall much wider crystallite size distribution. This is even more obvious for the Sp15TiN/SiNWs depicted in Figure 3-1(m-o).

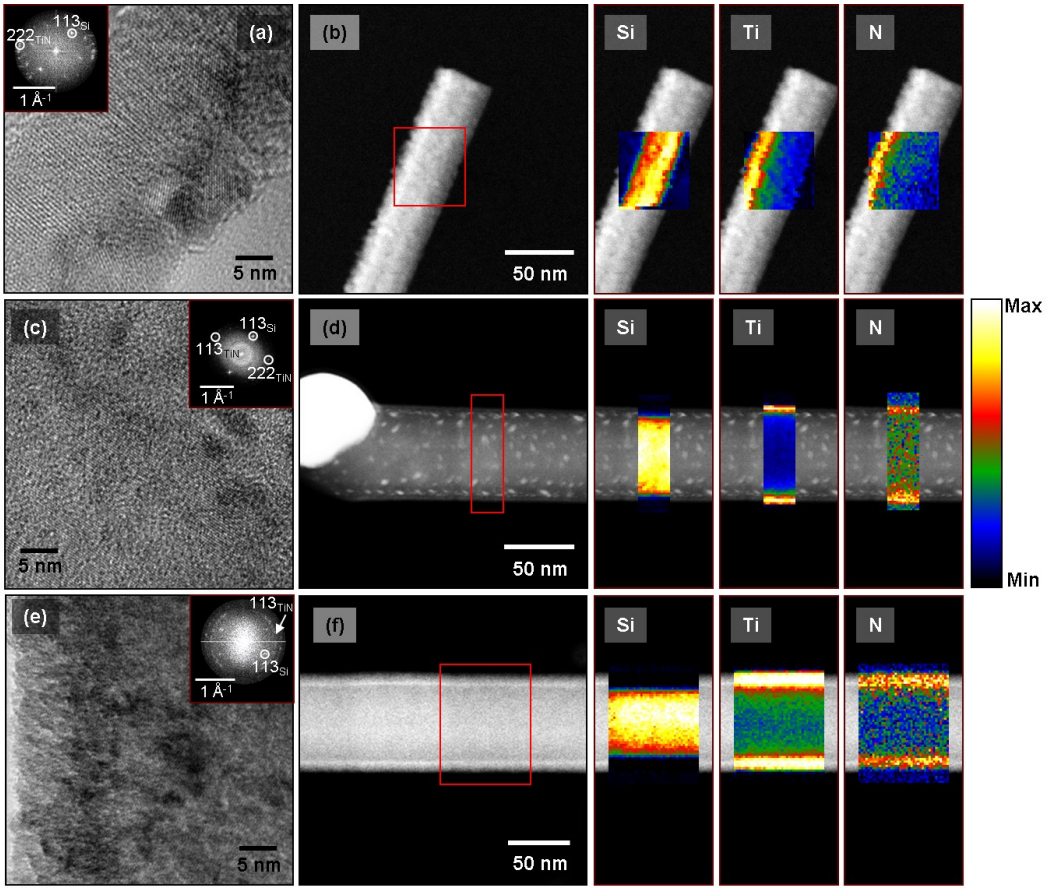

Figure 3-2: High-resolution TEM (HRTEM) micrograph with the corresponding Fast Fourier Transform (FFT) pattern insert, High Angle Annular Dark Field (HAADF) micrographs, and EELS elemental maps of Si, N, and Ti for (a-b) Sp5TiN/SiNWs, (c-d) ALD5TiN/SiNWs, and (e-f) ALD15TiN/SiNWs.

Figure 3-2(a) shows a high resolution TEM (HRTEM) micrograph of the TiN coating in Sp5TiN/SiNWs, confirming its relatively coarse polycrystalline morphology. From the Fast Fourier Transform (FFT) it is confirmed that the fringes are associated with 222_{TiN} and 220_{Si} planes. EELS analysis shown in Figure 3-2(b) shows a typical thickness of the sputtered TiN coating, which is actually substantially thicker (~ 8-9 nm) than the mean value of 5 nm. Conversely, HRTEM and EELS results for the ALD5TiN/SiNWs and ALD15TiN/SiNWs demonstrate a much more uniform coating morphology, finer TiN crystallite sizes, and coating thicknesses exactly in line with what was expected from the number of ALD deposition cycles.

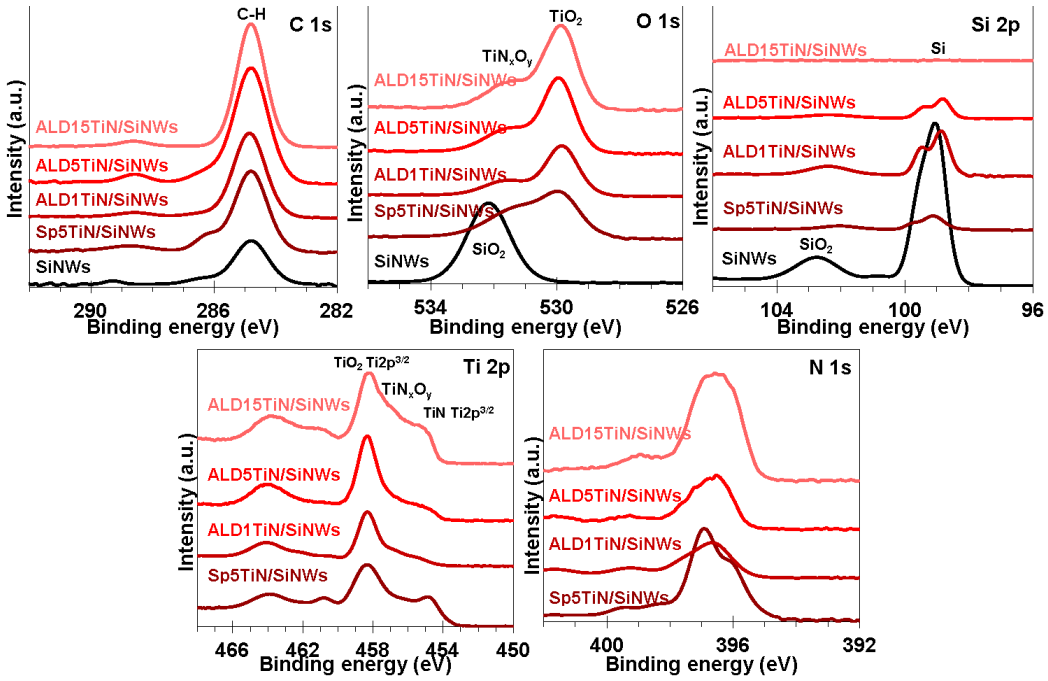

Figure 3-3: XPS spectra of SiNWs, Sp5TiN/SiNWs, ALD1TiN/SiNWs, ALD5TiN/SiNWs, and ALD15TiN/SiNWs materials in as-synthesized state.

Figure 3-3 shows the XPS spectra of the as-synthesized bare SiNWs and of the ALD and sputter TiN coated ones and the atomic compositions are listed in **Error! Reference source not found.**. The large universal hydrocarbon peak at 284.8 eV was used to calibrate the energy scale in the measured spectra. The spectra show that the outer surface of the TiN is partially oxidized to TiO_2 though even in the case of the 1 nm ALD layer the TiN signal is still present. Since the

standard enthalpy of TiO_2 formation (-946 kJ/mol Ti) [63] is greater than that of TiN (-337 kJ/mol Ti), [64] this result is expected. The peak positions in the Ti 2p and N 1s spectra are at roughly the same binding energies as those reported before for planar TiN films with a native oxide film. [65]

3.3.2 Electrochemical Performance

Figure 3-4(a), (c), and (e) show cyclic voltammetry (CV) profiles of bare SiNWs, ALD5TiN/SiNWs, and Sp5TiN/SiNWs measured at a rate of 1 mV/s. Fig. 3(b), (d), and (f) show the constant-current (CC) voltage profiles for the same electrodes at a rate of 0.1C. The CC and CV curves for ALD1TiN/SiNWs and ALD15TiN/SiNWs are included in Figure 3-4(g-h) and (i-j), respectively. For all three electrodes, a peak at ~ 150 mV appears in the reduction branch of cycle 2-10, which we commonly observe for SiNW electrodes. [24,33] Only in the first cycle, where Li is inserted into the pristine, crystalline SiNWs, this feature is not seen. In the oxidation branch, two broad peaks are observed at 300-350 and 500-550 mV that correspond to Li-Si de-alloying, forming amorphous Si. Over the course of cycling, all peak currents increase and the spacing between the two oxidation peaks becomes smaller, most clearly for Sp5TiN/SiNWs. The increase in the peak currents is a result of more Si becoming activated in the course of CV cycling. The partial merging of the two oxidation peaks can be ascribed to progressively more material crystallizing into $Li_{15}Si_4$ at low potentials (< 50 mV) upon discharge. Upon subsequent lithium extraction this would lead to a single sharp oxidation peak when this phase dissolved. [66]

As can be seen from Figure 3-4, thicker ALD coatings lead to slower activation and the sputter-coated electrode activates the fastest. This reflects the Li barrier properties of thick TiN layers and the conformal coverage by ALD as opposed to sputtering. The latter is not likely to fully penetrate to the nanowire base resulting in less than 100% coverage, but could still form a percolated network between the nanowire base and tip. This would result in an overall improvement in the electronic conductivity, resulting in the fastest activation and highest peak currents observed here. The same features can be seen in the CC profiles where a long plateau is observed in the first cycle at approximately 100 mV, which is indicative of Li insertion into crystalline Si. After one full cycle, Si is usually found to be fully amorphisized [24] and as a result, all later cycles show two sloping plateaus at ~ 250 and 100 mV. The delithiation profiles show a

long plateau at 0.4 V, which is indicative of a transition between crystalline $Li_{15}Si_4$ and amorphous Li_xSi.

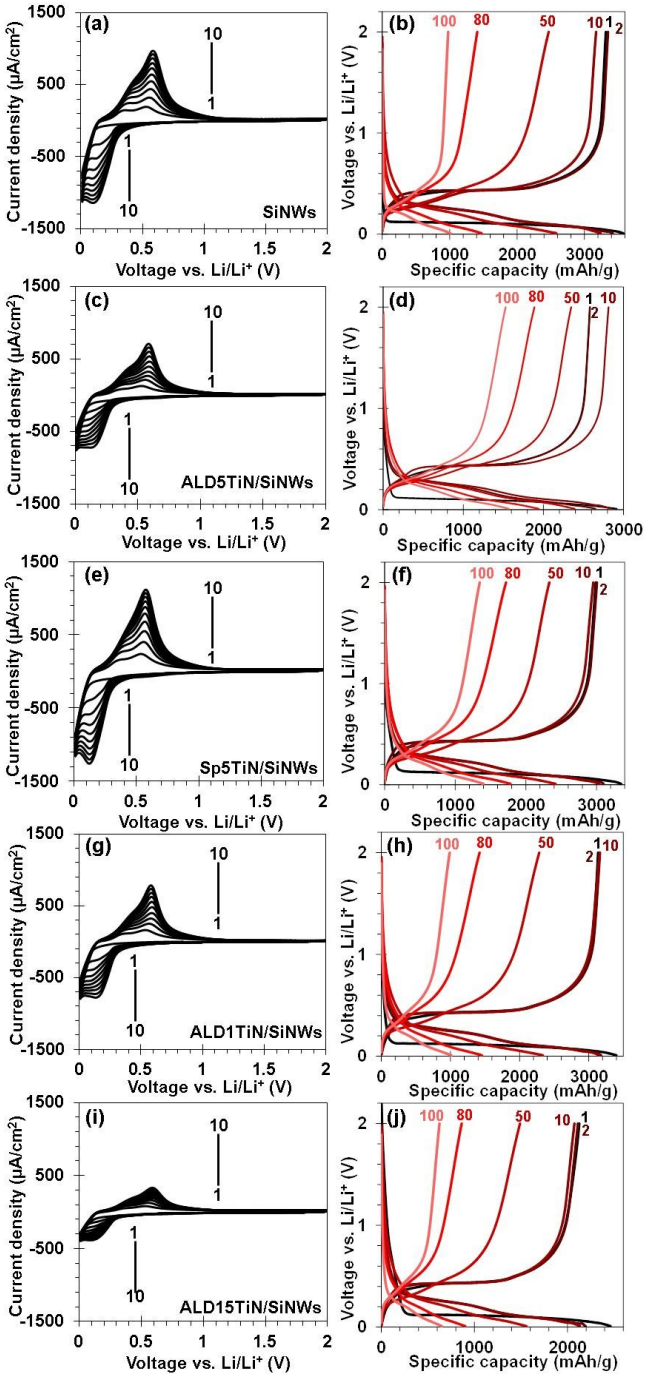

Figure 3-4: Cyclic voltammetry curves (left column) and galvanostatic voltage profiles (right column) of (a-b) SiNWs, (c-d) ALD5TiN/SiNWs, (e-f) Sp5TiN/SiNWs, (g-h) ALD1TiN/SiNWs, and (i-j) ALD15TiN/SiNWs.

The capacity of ALD5TiN/SiNWs increases between cycle 2 and 10 and the plateau in the delithiation voltage profile at ~ 0.4 V is wider in the 10th cycle compared to the first two. A magnification of cycle 1, 2, and 10 is included as Figure 3-5 and shows this more clearly. This is indicative of a clamping effect by the TiN coating for this particular electrode which will be discussed in more detail later.

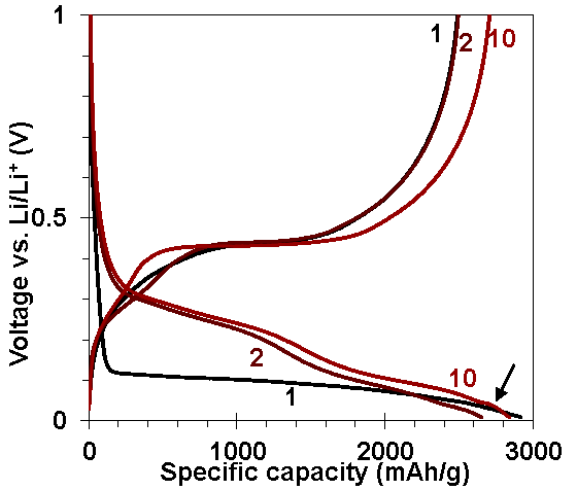

Figure 3-5: Magnification of cycle 1, 2, and 10 CC voltage profiles for ALD5TiN/SiNWs showing the increase in capacity between cycle 2 and 10 and the small plateau at ~ 30 mV vs. Li/Li$^+$ indicated by the arrow, signifying crystallization of $Li_{15}Si_4$

Figure 3-6(a-c) shows the total capacity, the capacity retention in percent, and the coulombic efficiency as a function of cycle number, at a rate of 0.1C for the ALD TiN coated specimens. The same data for sputtered TiN coated SiNWs with different TiN thicknesses are presented in Figure 3-6(d-f). Both results are also presented in Table 3-1 for comparison. Bare SiNWs electrode shows specific capacities of 3576 and 3298 mAh/g upon first lithiation and delithiation, respectively, which are close to the theoretical capacity of Si, based on $Li_{15}Si_4$ formation (3590 mAh/g). Of all the materials tested, ALD5TiN/SiNWs shows the highest capacity retention and best coulombic efficiency. In fact 5 nm is the key thickness to yield significant improvement over bare SiNWs, both for ALD and sputter-deposited coatings. The 1 nm TiN also significantly improves the coulombic efficiency, but is less effective in promoting capacity retention. The

nanowires with the 15 nm coating actually perform slightly worse than the baseline. The difference between the performances of the sputtered versus the ALD deposited films may be explained by the initial film structures: In Si nanowire based anodes, cycling induced failure is caused by the well-known fracture of the individual nanowires due to the severe volume changes incurred by lithiation/delithiation. [33] It is also caused by lithiation-assisted welding of the nanowires and by nanowire agglomeration due to extensive SEI growth, leading to *en-masse* delamination from the current collector. [24,67,68]

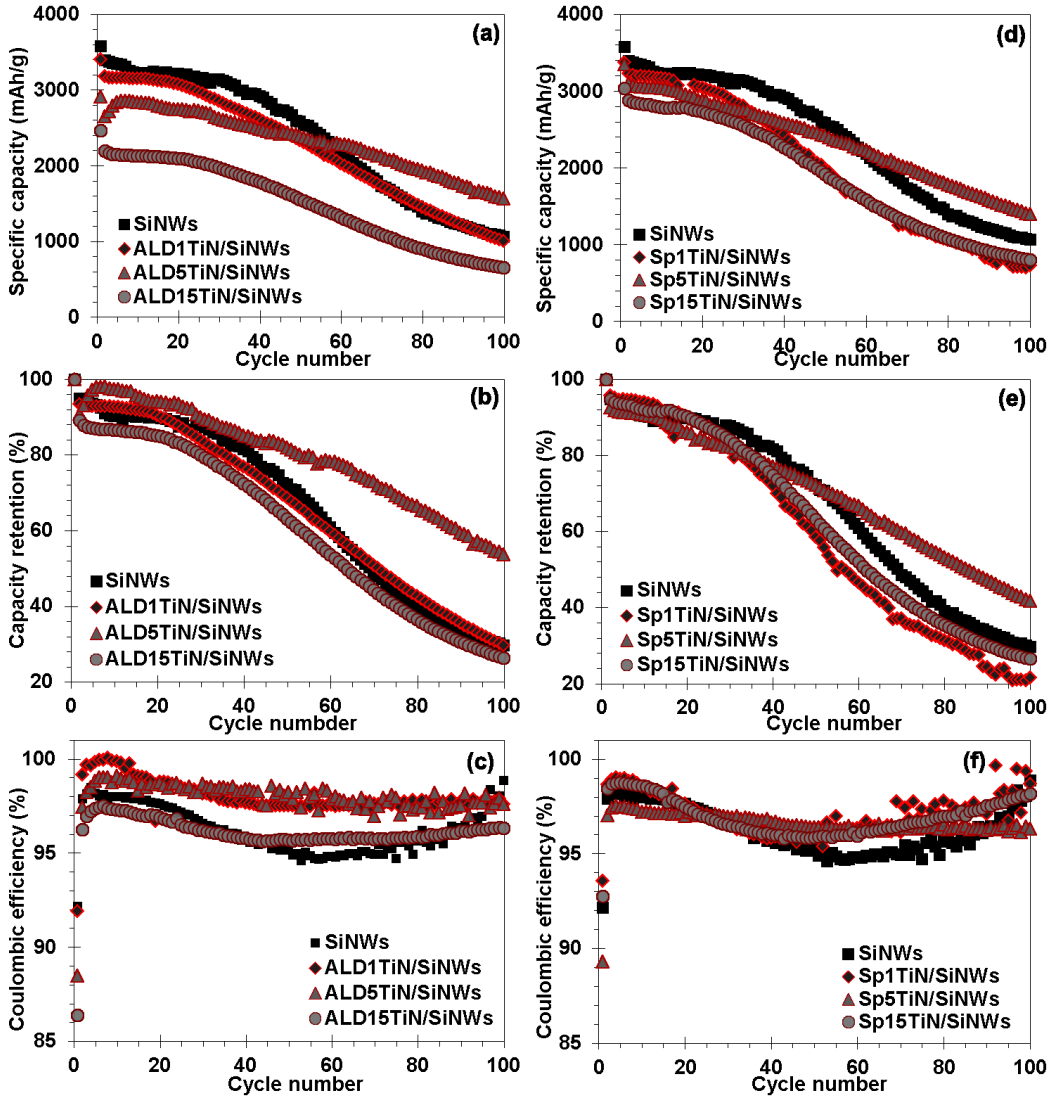

Figure 3-6: Galvanostatic cycling behavior of SiNWs with (a-c) ALD TiN and (d-f) sputtered TiN coatings, tested at a rate of 0.1C. (a,d) Specific capacity retention as a function of cycle number, (b,e) Capacity retention in % of initial value, and (c,f) Coulombic efficiency.

Table 3-1: Galvanostatic cycling results for ALD and sputter coated SiNWs, tested at a rate of 0.1C.

	Specific capacity (mAh/g)		% capacity
Cycle number	**1st**	**100th**	**100th**
SiNWs	3576	1065	29.8
Sp1TiN/SiNWs	3377	732	21.7
Sp5TiN/SiNWs	3348	1408	41.8
Sp15TiN/SiNWs	3035	805	26.5
ALD1TiN/SiNWs	3399	1009	29.7
ALD5TiN/SiNWs	2915	1566	53.7
ALD15TiN/SiNWs	2462	648	26.3

The cycling capacity retention and the coulombic efficiency are also somewhat correlated, since extensive SEI growth will lead to irreversible trapping of Li. As will be demonstrated, TiN coatings of the appropriate geometry and microstructure are effective in reducing the severity of both types (individual and *en-masse*) of failures. The sputtered TiN films are geometrically less uniform and have a coarser grain size than the ALD films. The thickness nonuniformity would give more site-to-site variability in mechanical (fracture) and chemical (SEI growth) protection, with essentially none being imparted in regions where flux shadowing was severe, such as near the nanowire base. We will briefly discuss the thickness dependent performance of TiN later after presenting the post-cycled microstructure.

The electrically conductive TiN coatings also substantially improve the rate-dependent capacity retention of the SiNWs. The results for the ALD coatings are shown in Figure 3-7(a,b), while the sputtered coatings are shown in Figure 3-8(a,b). The electrodes were cycled at 0.1C for 20 cycles, followed by 15 cycles at 0.5, 1, 2, and 5C. The trends in the rate performance are consistent with the rest of the cycling data, with the ALD5TiN/SiNWs being the best. It is worth noting that despite the negative "dead weight" contribution of the TiN layer to the total capacity of the electrode, at high rates the coated SiNWs possess more than twice the capacity of the uncoated baseline (740 mAh/g vs. 330 mAh/g at 5C).

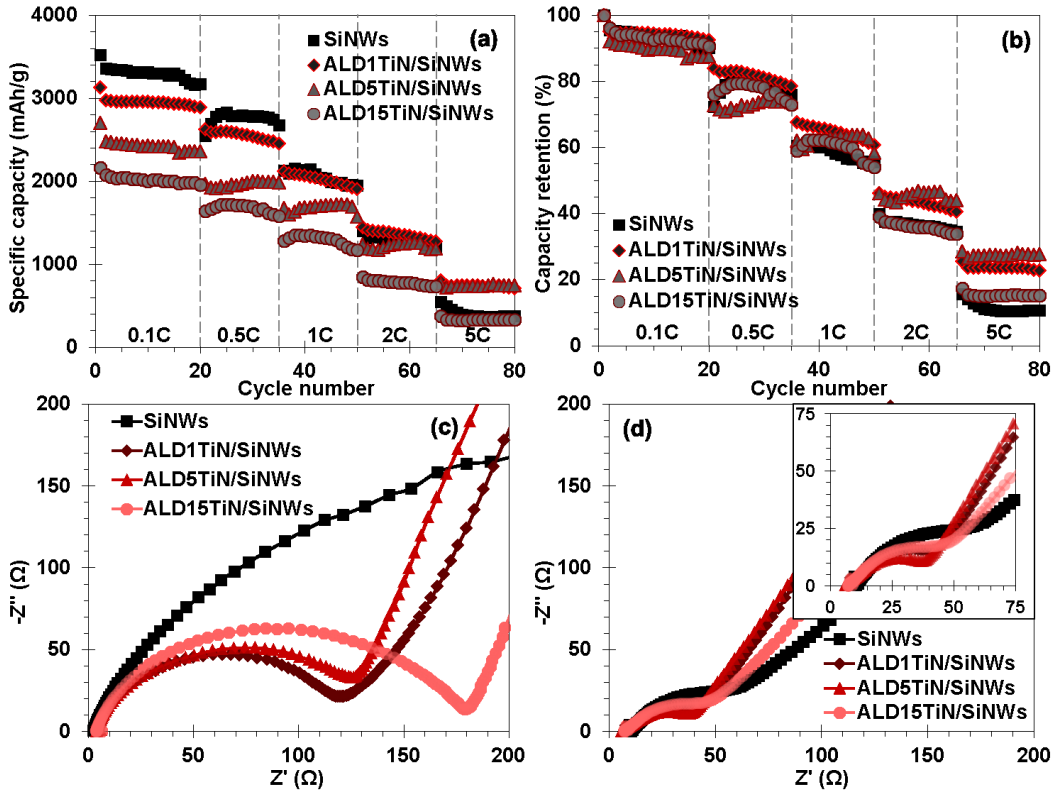

Figure 3-7: (a-b) Galvanostatic cycling behavior of SiNWs with ALD TiN coatings, tested at a rates of 0.1C–5C. (a) Specific capacity retention as a function of cycle number, (b) Capacity retention in % of initial value, (c-d) Electrochemical impedance spectra of SiNWs with ALD coatings, as-synthesized (c) and after 100 cycles at 0.1C (d).

Table 3-2: Conductivity of planar TiN films deposited by ALD and sputtering measured by four-point probe.

Deposition technique	**ALD**		**Sputtering**	
Thickness (nm)	15	15	200	
Deposition temperature (°C)	120	300	250	
Resistivity (μΩ.cm)	6576	2847	4614	170
Sheet resistance (Ω/□)	4384	1898	307	8
Conductivity (S/cm)	152	351	217	5882

Since TiN is highly electrically conductive, for example being 152 S/cm for a 15 nm planar ALD film (see Table 3-2). This is much higher than the 1-10 S/cm reported for lithiated silicon. [69] Therefore a major electrical conductivity enhancement would be expected were the coatings to remain generally intact and connected to the current collector. The sputtered coatings (Figure

3-8) do not provide any capacity retention enhancement at high rates. For example, at 5C the capacity of the Sp5TiN/SiNWs is approximately 290 mAh/g. This is a testament to the much higher effectiveness of the ALD method in penetrating down the nanowire base and hence providing a continuous electrically conductive path.

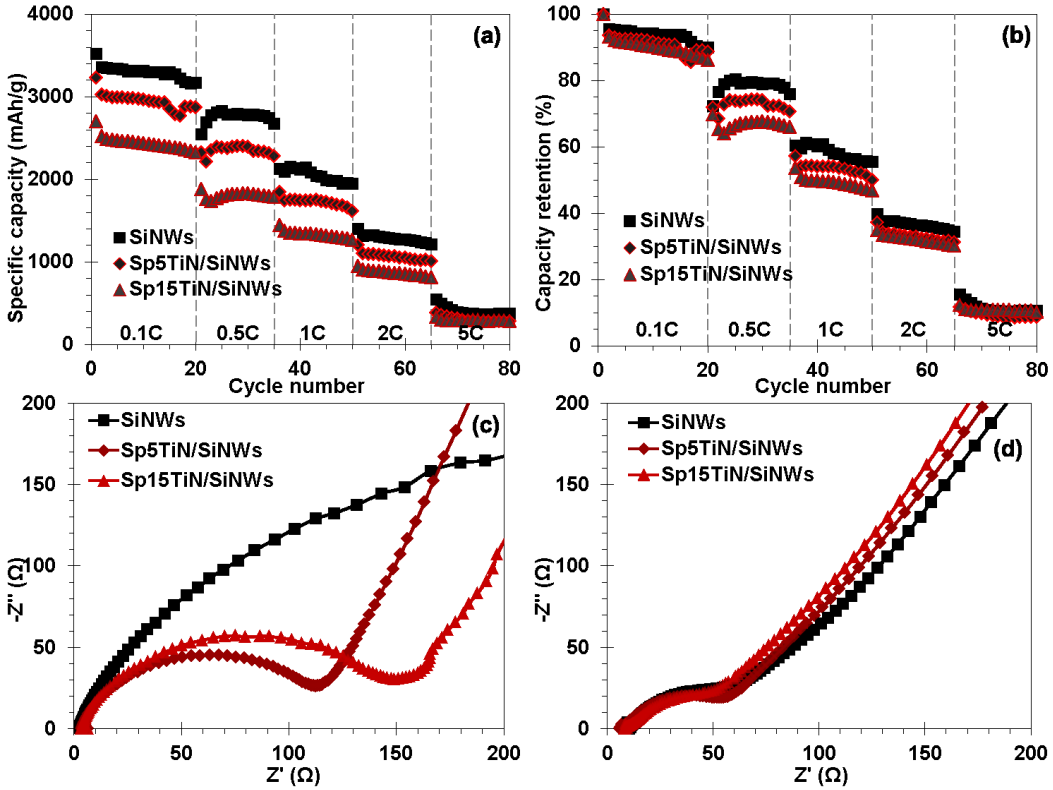

Figure 3-8: (a-b) Galvanostatic cycling behavior of SiNWs with sputtered TiN coatings, tested at a rates of 0.1C–5C. (a) Specific capacity retention as a function of cycle number, (b) Capacity retention in % of initial value, (c-d) Electrochemical impedance spectra of SiNWs with sputtered coatings, as-synthesized (c) and after 100 cycles (d).

Electrochemical impedance spectroscopy (EIS) was employed to further examine the cycling behavior of the TiN coated SiNW's. Figure 3-7(c,d) show the Nyquist plots for the as-synthesized and the post-cycled ALD coated specimens. The same data is shown for the sputter coated nanowires in Figure 3-8(c,d). The impedance spectra of the as-made electrodes were modeled with the equivalent circuit depicted in Figure 3-9(a). R_{el} represents the electrical resistances (contacts, etc.), C_{dl} the electrical double layer capacitance, R_{ct} is the charge transfer resistance and Z_W a Warburg-type element representative of Li diffusion into Si. [70] For the

cycled electrodes an additional parallel combination of a resistor and capacitor are added to represent Li transport through the SEI film denoted as R_f and C_f, respectively. [70-72] Both circuits are depicted in Figure 3-9 and simulated spectra representing the best fit to the data for ALD1TiN/SiNWs are in Figure 3-10. The numerical values obtained from modeling are listed in Table 3-3.

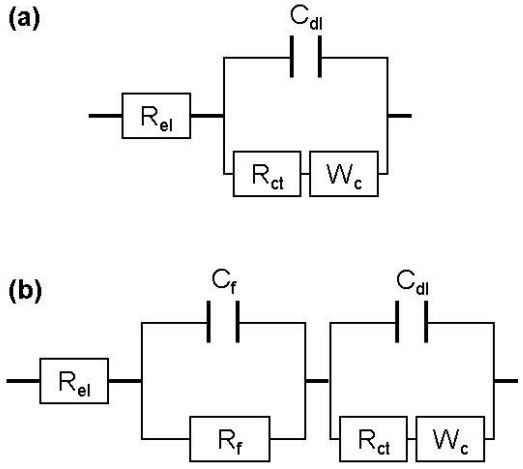

Figure 3-9: Equivalent electronic circuits used to model the impedance data of as-made (a) and cycled (b) electrodes.

The huge charge transfer resistance ($R_{ct} \approx 400\ \Omega$) of the as-grown SiNWs indicates that the surface of the Si electrode is initially covered with a non-conducting native layer of SiO_2. The trend in the charge transfer resistance, which is roughly equal to the diameter of the semicircle in the spectra, indicates that the 15 nm TiN gives much higher charge transfer resistance than the 1 and 5 nm coatings. Lithium ion transfer through the TiN must occur through its grain boundaries, or through geometric defects such as nano-scale cracks and isolated pores (TEM revealed minimal porosity in the ALD layers). Therefore it is reasonable to surmise that the 15 nm TiN layer has properties closer to its "bulk" analogue, blocking or at least impeding Li ion diffusion. Comparing the spectra in Figure 3-7(c) and Figure 3-8(c) and the numerical values for R_{ct} in Table 3-3, we see this is indeed the case. R_{ct} is approximately 120 Ω for ALD1, ALD5, and Sp5TiN/SiNWs and 170 and 150 Ω for ALD15 and Sp15TiN/SiNWs, respectively. The thinner TiN films seem not to possess this problem, with the 5 nm and the 1 nm essentially behaving

nearly identically. The EIS results indicate that the coating process actually has the important effect of negating the impedance contribution due to SiO_2, likely by both reducing the existing oxide and by protecting against additional growth after synthesis.

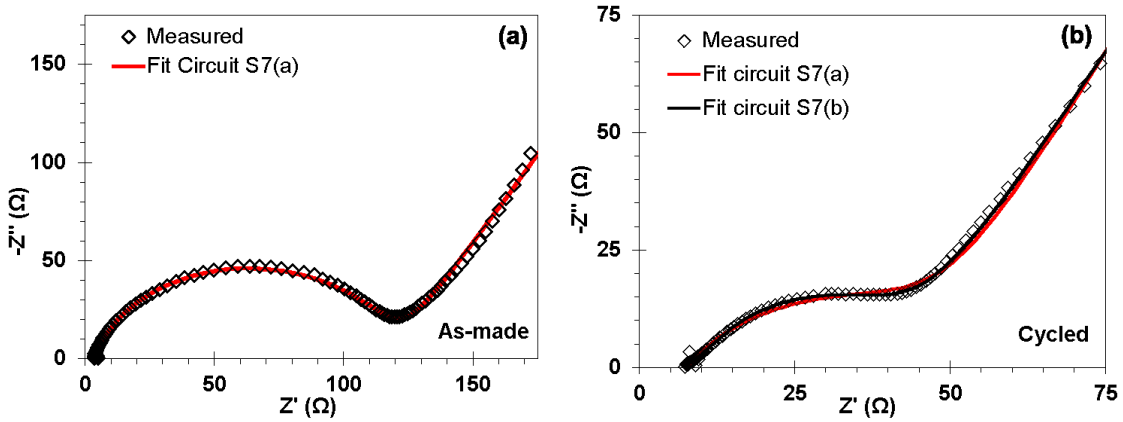

Figure 3-10: Impedance spectra of ALD1TiN/SiNWs in as-made (a) and cycled state (b) together with simulations based on the equivalent circuits shown in Figure 3-9(a) (red line) and Figure 3-9(b) (black line). Note that the fit is slightly better using the circuit with 2 time constants, but it is very hard to resolve them.

Table 3-3: Resistance values obtained from modeling the impedance data in Figure 3-7 and Figure 3-8 with the equivalent circuit in Figure 3-9(a) for as-made and Figure 3-9(b) for cycled electrodes.

	SiNWs	**ALD1TiN /SiNWs**	**ALD5TiN /SiNWs**	**ALD15TiN/SiNWs**	**Sp5TiN /SiNWs**	**Sp15TiN/ SiNWs**
As-made electrodes						
R_{el} (Ω)	2.3	3.5	3.9	3.4	3.5	3.2
R_{ct} (Ω)	403.5	117.3	126.2	172.7	114.3	149.2
Cycled electrodes						
R_{el} (Ω)	8.8	6.9	5.2	6.7	5.6	8.6
R_f (Ω)	13.7	16.3	10.5	21.6	12.1	3.5
R_{ct} (Ω)	39.4	25.5	23.5	24.8	37.9	48.2

After 100 cycles, R_{ct} is substantially lowered for the bare SiNW electrode as compared to the as-synthesized state, going from ~ 400 to ~ 40 Ω. This is attributed to the native SiO_2 layer being reduced by Li. [32] Formation of larger amounts of SEI will increase the total impedance of the electrode and this should be taken into account when modelling the data for the cycled electrodes (see Figure 3-9(b)). [71,72] However, from the spectra in Figure 3-7(d) and Figure 3-8(d) it is obvious that the time-constants of Li migration through the SEI layer and Li transfer into Si

through the TiN coating are comparable, as only one semicircle can be distinguished clearly. The total resistance $R_f + R_{ct}$ associated with transfer of Li from the electrolyte, through the SEI, into the SiNW is clearly larger for bare SiNWs compared to ALD5TiN/SiNWs, 53 vs. 34 Ω, consistent with the observed differences in coulombic efficiency and rate capability.

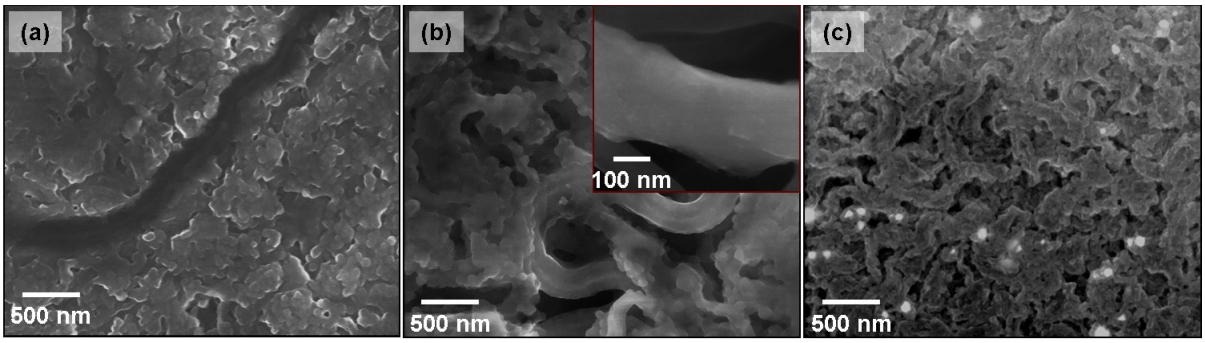

Figure 3-11: Top-down SEM micrographs of post-100 cycles electrodes; (a) bare SiNWs, (b) ALD5TiN/SiNWs, and (c) ALD15TiN/SiNWs.

3.3.3 Post-Cycled Microstructure

Figure 3-11 shows SEM micrographs SiNWs, ALD5TiN/SiNWs, and ALD15TiN/SiNWs electrodes after 100 cycles at 0.1C. Even from this relatively cursory top-down view of the post-cycled microstructures it is evident that the 5 nm ALD TiN coating prevents the nanowires from agglomerating during cycling. The effect of the TiN coating on the structural stability of nanowires is further investigated through TEM analysis. Conventional TEM analysis of cycled ALD1TiN/SiNWs, ALD5TiN/SiNWs, ALD15TiNSiNWs, and Sp5TiN/SiNWs is presented in Figure 3-12. The post-cycled SiNWs are found to be amorphous, which is commonly observed, already after 1 cycle. Deep lithiation, below 50 mV vs. Li/Li^+, results in the formation of crystalline $Li_{15}Si_4$. Upon subsequent delithiation the crystalline $Li_{15}Si_4$ transforms back into the amorphous phase. As no other phase transformation occurs upon further delithiation, silicon is amorphous at the end of the charging step. The nanocrystallites appearing bright in dark field images (e), (h) and (k) are TiN, which was imaged using the crystalline TiN patterns shown and simulated in (d), (g) and (j).

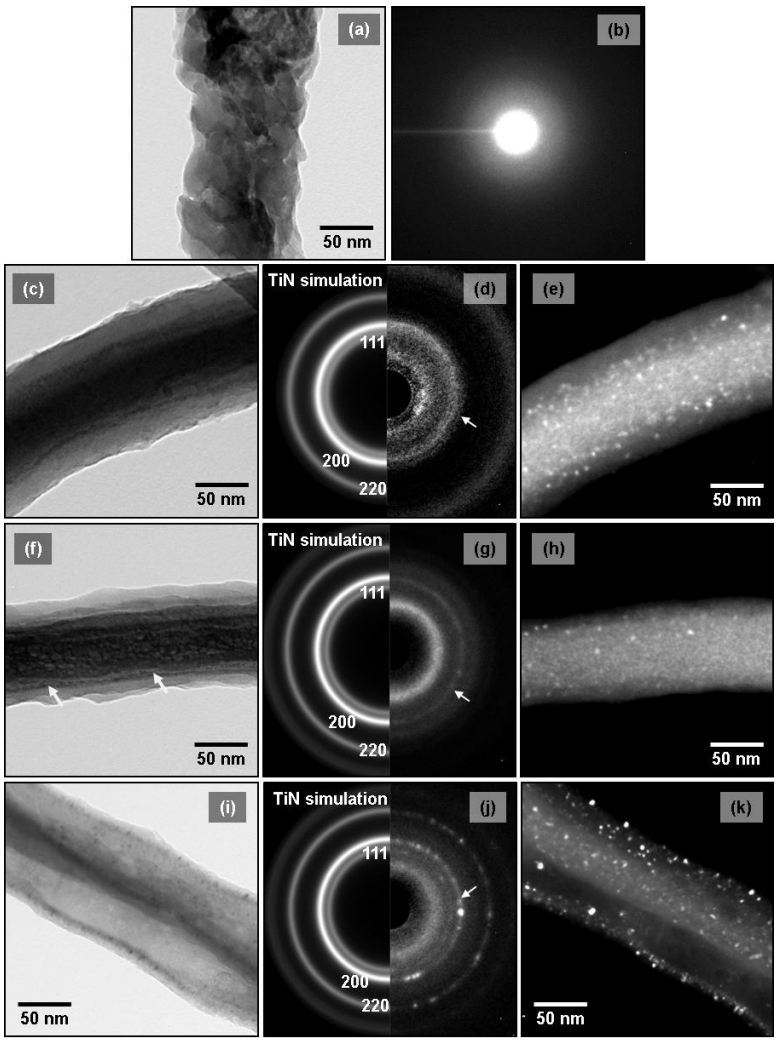

Figure 3-12: Bright-field, SAD, and dark-field TEM micrographs of post-100 cycled (a-b) ALD1TiN/SiNWs, (c-e) ALD5TiN/SiNWs, (f-h) ALD15TiN/SiNWs, (i-k) Sp5TiN/SiNWs. The dark-field micrographs were obtained using the arrowed portion of the TiN ring pattern.

The effectiveness of the TiN coatings in preventing silicon nanowire disintegration and SEI-induced agglomeration may be evaluated from the TEM micrographs of the cycled materials. The ALD1TiN/SiNWs electrodes form a porous network, which is quite similar to is commonly observed for bare nanowires. [24,32,33] Increasing the TiN coating thickness to 5 nm results in much better structural stability of the wire, with much less void formation/disintegration of the Si cores. Moreover, analytical TEM and XPS shown in the subsequent sections will demonstrate that the 5 nm coating is optimum for minimizing SEI formation as well. The bright-field and

dark-field micrographs (Figure 3-12(c) and (e)) confirm that there is minimal detachment between the Si core and the TiN shell. Further increase in ALD TiN thickness to 15 nm causes crack formation at the Si-TiN interface (arrowed in Figure 3-12(f)). Such an unintact interface is not expected to offer any chemical or structural protection to the underlying Si nanowire. As may be seen from Figure 3-12(f), the nanowire consequently develops porosity. The Sp5TiN/SiNWs coating does not seem to separate from the nanowire, but offers less protection than the ALD coating of the same thickness for the reasons previously discussed.

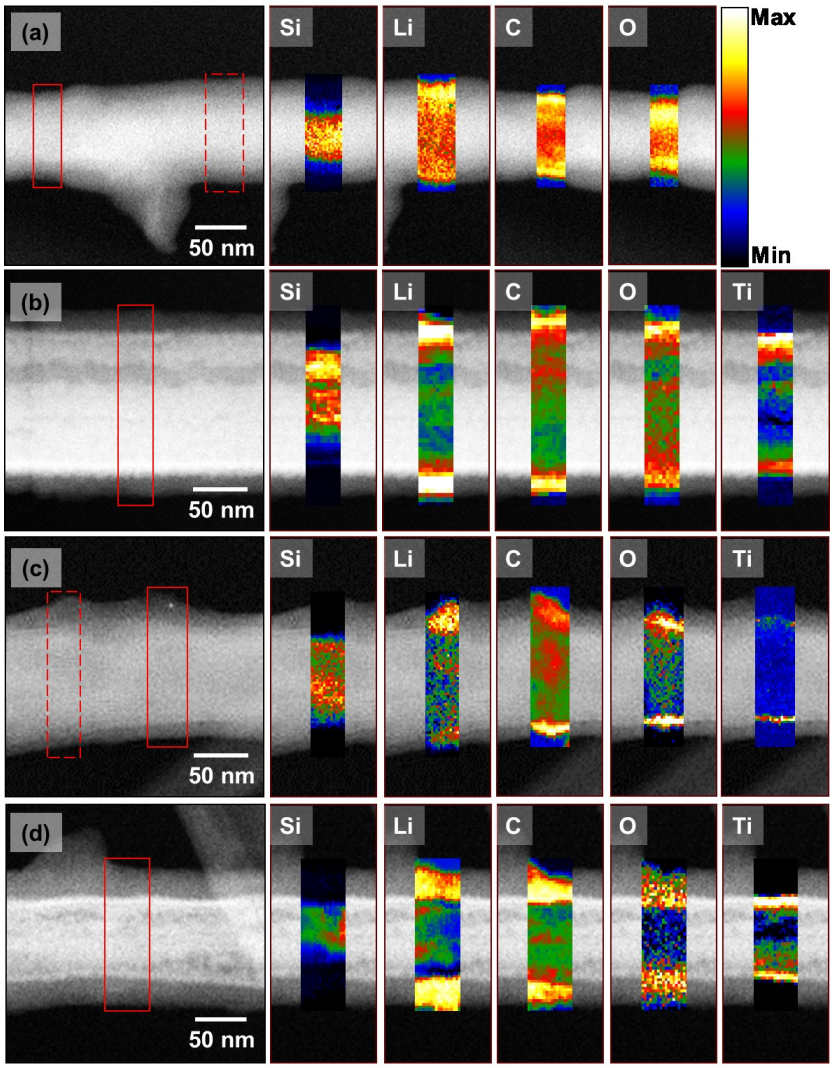

Figure 3-13: HAADF images and EELS elemental maps of Si, Li, C, O, and Ti for (a) SiNWs, (b) Sp5TiN/SiNWs, (c) ALD5TiN/SiNWs, and (d) ALD15TiN/SiNWs electrodes after 100 cycles. In (a) and (c) Si and Li maps were obtained from the region marked by the dashed rectangle, while C and O were obtained from the region marked by the solid rectangle in the HAADF.

Figure 3-13 shows HAADF images and EELS elemental maps of the bare SiNWs and the TiN coated composites after 100 cycles. In the baseline bare SiNW's, the Li, C, and O signals are strong not only near the edge of the wires but though out the entire wire thickness. This indicates that not only are the wires highly porous, but that the SEI layer has grown directly into that porosity, in addition to forming on the original wire surfaces. Conversely the 5 nm TiN samples show much more limited SEI formation, primarily near the original SiNW-electrolyte interface. The specimen displaying the lowest levels of SEI formation is ALD5TiN/SiNWs. Similarly to the uncoated baseline, the ALD15TiN/SiNWs specimen is highly porous with thick and interpenetrating SEI. SEI formation due to the decomposition of conventional LIB electrolyte is known to occur rapidly form on a fresh Si surface below ~ 0.8 V. [32,73,74] The relatively intact 5 nm ALD TiN prevents the Si from "stranding" and hence exposing fresh surfaces during each discharge cycle. This promotes cycling stability and improves coulombic efficiency.

Of course some plastic deformation and/or cracking and/or interfacial slip of the TiN must occur during lithiation, since 280% volume expansion cannot be accommodated purely elastically. Quantitatively explaining the complex role of thickness in the effectiveness of the ALD TiN coating may be beyond the scope of the current study. From the measured Young's modulus of TiN of 450 GPa and the estimated maximum yield strength of 40 GPa, [75] the maximum elastic strain is approximately 9% for the coating, which can accommodate 16% volume expansion of Si. Although coating layers have been found to greatly reduce expansion of small-diameter nanowires, above 50 nm the volume expansion upon full lithiation quickly increases to a factor of 2-2.5. [43] Using our experimental procedures, the average nanowire diameter is usually larger than 100 nm, [24,33] which means the SiNWs will undergo a large volume increase upon full lithiation. Qualitatively we could make general arguments that a thin layer (1 nm) remains adherent on the nanowire surface but is simply not strong enough to provide sufficient mechanical support. That would explain the improved coulombic efficiency (a passivated surface and hence less SEI), but minimal improved cycling lifetime (wires still fracture). The 15 nm film may be too elastically stiff, fracturing and separating from the SiNW's in a manner that you would expect from more "bulk" TiN films that are brittle. Thus, in effect,

the two materials would be "ships passing in the night", having no useful synergy during electrochemical cycling. A coarser grain size of the 15 nm TiN specimen would also reduce its fracture strength. The fact that the 15 nm TiN layer actually makes the cycling capacity retention slightly worse than the baseline is related to the initial capacity loss during cycle 1. According to Figure 3-6(a), the capacity of ALD15TiN/SiNWs quickly drops during the first cycle and then degrades roughly at the same rate as baseline SiNWs.

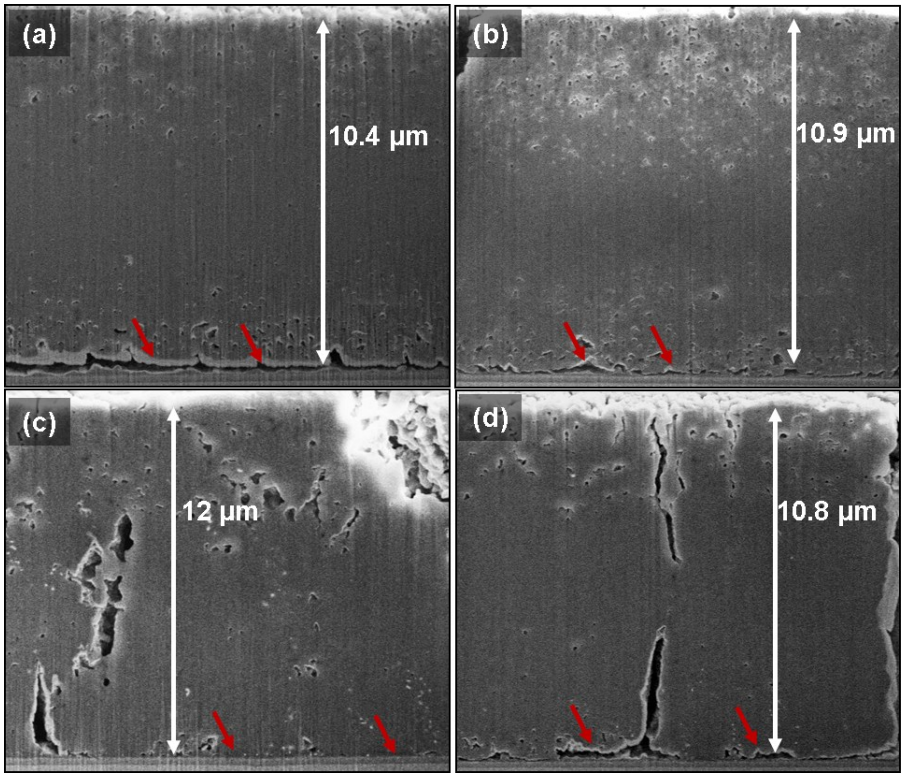

Figure 3-14: Representative FIB cross-sectional SEM micrographs of (a) SiNWs, (b) ALD1TiN/SiNWs, (c) ALD5TiN/SiNWs, and (d) ALD15TiN/SiNWs anode materials after 100 cycles. In (a), (b), and (d) one-way arrows point to the en-masse separation of the SiNWs from the current collector, while in (c) the arrows point to an interface which substantially more intact. Vertical two-way arrow gives the thickness of the agglomerated film and may be used for magnification.

We hypothesize that the thick elastically stiff TiN layer actually interferes with the nanowires during their initial lithiation, and promoting fracture of the brittle partially crystalline silicon. The 5 nm ALD film is an optimum positive compromise of such effects, providing a mechanical support for the Si, while not undergoing catastrophic fracture or not delaminating.

The slightly depressed capacity for ALD5TiN/SiNWs that was observed in the first few CC cycles (see Figure 3-4(d) and Figure 3-5) is further evidence for this. The 5 nm ALD coating appears to be the only one exerting a clamping effect that actually has an effect on the storage capacity of the Si by reducing the expansion [43] over multiple cycles. This shows that 5 nm ALD TiN is indeed the most mechanically robust of all the coatings tested. However, the capacity increases between cycle 2 and 10 towards its theoretical value, which shows that this coating does also fracture to some extent during cycling.

FIB cross sectional SEM micrographs of the cycled materials are shown in Figure 3-14. Since the spaces between the nanowires are filled up with electrolyte decomposition products, the overall electrode morphology resembles that of a porous sponge rather than a nanowire array. However the FIBed ALD5TiN/SiNWs agglomerate was also the most porous, which is consistent with the least electrolyte decomposition products being formed in that specimen. The average height of these agglomerate structures is indicated in each figure, being the highest for ALD5TiN/SiNWs. This indicates that 5 nm ALD TiN is the most effective in providing continued mechanical support to the nanowires during cycling, promoting longitudinal expansion at the expense of radial. Another significant difference between the specimens was the extent of delamination that is observed between the bottom of the cycled nanowire assembly and the current collector. This effect is best observed when contrasting the bare SiNWs and the ALD5TiN/SiNWs. The cross-section of the bare SiNWs shows delamination across the entire image, whereas for ALD5TiN/SiNWs most of the array remained in contact. The ALD1TiN/SiNWs and ALD15TiN/SiNWs show extensive delamination, as indicated by the arrows.

Li 1s, C 1s, O 1s, and F 1s XPS spectra of bare SiNWs, Sp5TiN/SiNWs, ALD1TiN/SiNWs, ALD5TiN/SiNWs, and ALD15TiN/SiNWs are shown in Figure 3-15. Electrolyte decomposition products such as Li_2CO_3, Li alkylcarbonates, and polymeric species are found. In addition to the hydrocarbon signal each C 1s spectrum has a shoulder off the main hydrocarbon peak centered at about 286-287 eV. This broad shoulder indicates the presence of either C-O or C=O bonding and matches with polyethylene oxide; $-(CH_2CH_2O)_n-$. [76] There is also a higher energy signal at ~ 289-290.5 eV, can be related to O-C=O bonding in carboxylic groups. The broad peak at around 290 eV is due to the combination of the Li_2CO_3 with a binding energy of ~ 290.3 eV and semi-

organic lithium alkyl carbonates compounds with a binding energy that is generally slightly lower. [76]

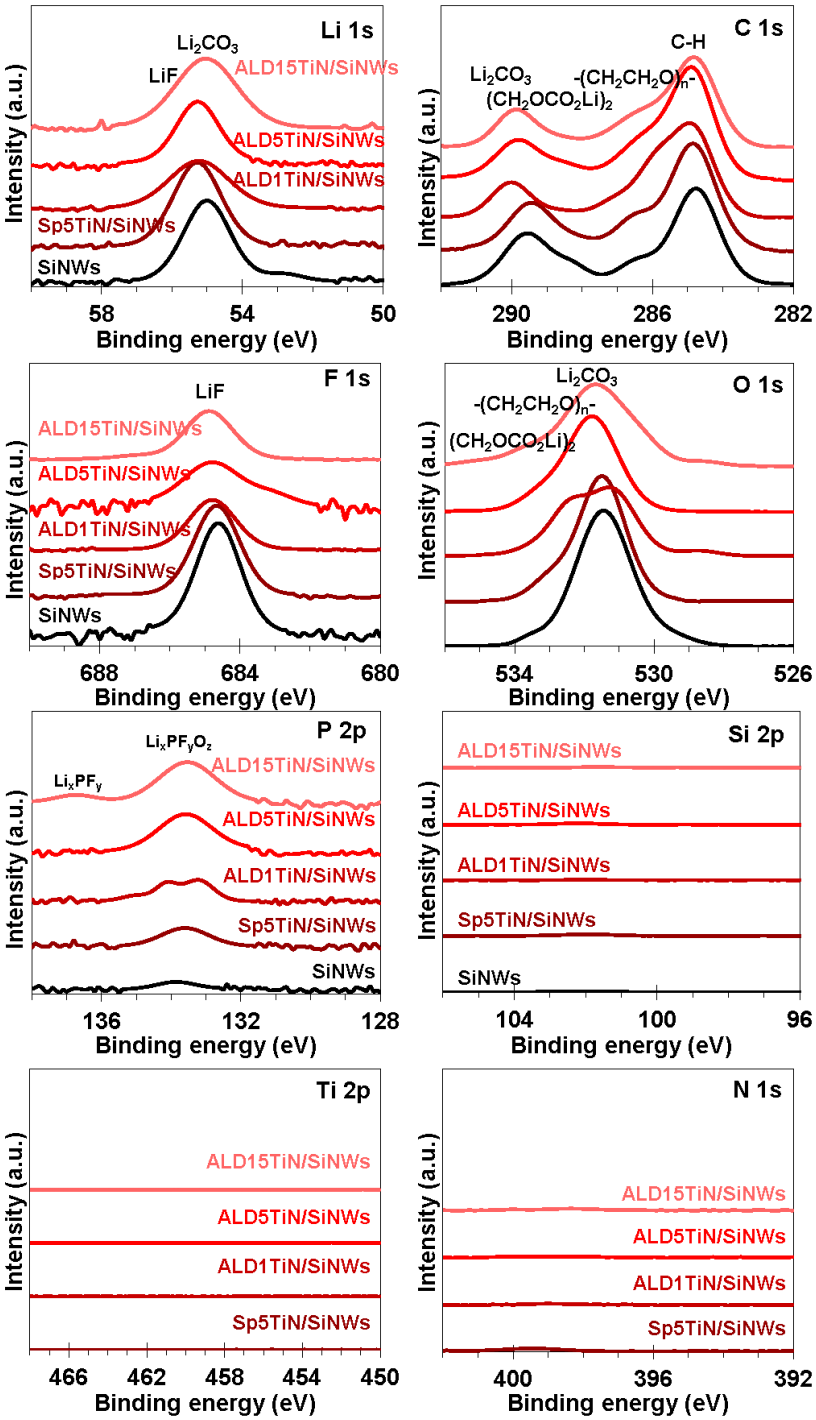

Figure 3-15: Li 1s, C 1s, F 1s, O 1s, P 2p, Si 2p, Ti 2p, and N 1s XPS spectra of SiNWs, Sp5TiN/SiNWs, ALD1TiN/SiNWs, ALD5TiN/SiNWs, and ALD15TiN/SiNWs materials after 100 cycles at 0.1C.

Lithium ethylene dicarbonate $(CH_2OCO_2Li)_2$ is another product of the ethylene carbonate (EC) reduction and has a C 1s binding energy in the same range. In general, organic SEI compounds are produced mostly by the reduction of EC and to less extent diethyl carbonate (DEC) solvent molecules at the electrode/electrolyte interface. [76] There is some variation in the position of the maxima which indicates there are variations in the relative amounts of the different electrolyte reduction products. However, the overall chemical composition, as summarized in Table 3-4, varies very little between the electrodes.

Table 3-4: Atomic composition of SiNWs, Sp5TiN/SiNWs, ALD1TiN/SiNWs, ALD5TiN/SiNWs, and ALD15TiN/SiNWs anode materials in as-synthesized (Figure 3-3) and cycled (Figure 3-15) states in percentage, obtained from XPS measurements.

Material	State	C	O	Si	Li	F	P	Ti	N	Cl	Au
SiNWs	As-grown	12.2	24.1	62.9	-	-	-	-	-	-	0.9
	0.1C	33.7	33.4	-	28.9	3.8	0.1	-	-	-	-
Sp5TiN/SiNWs	As-synthesized	30.3	27.5	6.7	-	-	-	19.7	15.7	-	-
	0.1C	33.6	33.5	-	28.4	3.6	0.9	-	-	-	-
ALD1TiN/SiNWs	As-synthesized	30.3	29.8	26.8	-	-	-	6.9	4.8	0.9	0.4
	0.1C	35.4	33.6	1.3	26.6	2.0	1.0	-	-	-	-
ALD5TiN/SiNWs	As-synthesized	37.2	33.8	10.7	-	-	-	9.8	6.9	1.4	0.1
	0.1C	36.5	32.7	0.2	26.9	2.0	1.6	-	-	-	-
ALD15TiN/SiNWs	As-synthesized	36.7	35.5	-	-	-	-	14.5	10.8	2.4	-
	0.1C	33.7	33.7	-	28.7	2.1	1.6	-	0.2	-	-

XPS spectra of O 1s for cycled materials show characteristic peaks of the same carbonate and polymeric compounds as the C 1s spectra. The Li 1s spectra show one broad peak where both the signal for Li_2CO_3 and LiF are usually found. [77] The signal intensities for Li are similar for each of the electrodes, indicating that the chemical composition of the SEI is similar in each case. The XPS signal only comes from the top 10 nm and is thus not indicative of the total amount of electrolyte decomposition product formed. As a consequence, Ti, N, and Si signals are no longer visible in the XPS spectra of the cycled electrodes (see Figure 3-15). From the data in Table 3-4 it can be seen that the overall chemical composition of the cycled electrodes is indeed very similar. The only difference between the electrodes, judging from the coulombic efficiency

data and the FIB cross-sections is the total amount of SEI formed, the reason for which is improved mechanical stability for ALD5TiN/SiNWs as we discussed earlier.

3.4 Conclusions

Nanoscale coatings of electrically conductive titanium nitride (TiN), deposited by atomic layer deposition (ALD) and by magnetron sputtering, resulted in improvements in the electrochemical performance of silicon nanowires (SiNWs) lithium-ion battery anode. The conformal and uniform ALD-deposited TiN with an optimum thickness of 5 nm achieves the best cycling capacity retention at 55% vs. 30% for bare SiNWs after 100 cycles at 0.1C. Furthermore, the ALD coatings substantially improved the electrode rate performance; 740 mAh/g vs. 330 mAh/g at 5C. Sputtered TiN resulted in a lower performance enhancement, most likely due to the processes' intrinsically directional deposition flux, preventing the coating material from penetrating all the way to the substrate. Combined EELS, TEM, FIB-SEM, and XPS analysis of the cycled electrodes demonstrated that for the optimized coating thickness (5 nm deposited with ALD), the nanowires remain largely intact, reducing SEI formation and nanowire disintegration associated with characteristic 'stranding'. Furthermore, the FIB cross-sections provided additional evidence for improved mechanical stability as the post-cycled ALD5TiN/SiNWs, demonstrating much less cycling-induced delamination from the current collector. This overlayer actually influences the ratio of longitudinal vs. radial lithiation-induced volume expansion in the wires, with the coated cycled arrays being 15% taller than the uncoated ones despite having an identical initial height.

3.5 References

1 N. S. Choi, Z. Chen, S. A. Freunberger, X. Ji, Y. K. Sun, K. Amine, G. Yushin, L. F. Nazar, J. Cho and P. G. Bruce, Angew. Chem. Int. Ed., 2012, 51, 9994.

2 M. Armand and J. M. Tarascon, Nature, 2008, 451, 652.

3 B. Dunn, H. Kamath and J. M. Tarascon, Science, 2011, 334, 928.

4 H. J. Kim, Z. H. Wen, K. H. Yu, O. Mao and J. H. Chen, J. Mater. Chem., 2012, 22, 15514.

5 S. Mao, Z. H. Wen, Haejune Kim, G. H. Lu, P. Hurley and J. H. Chen, ACS Nano, 2012, 6, 7505.

6 H. Okamoto, "Phase Diagrams for Binary Alloys", ASM International, 2000, ISBN 0-87170-682-2.

7 Z. H. Wen, S. M. Cui, H. J. Kim, S. Mao, K. H. Yu, G. H. Lu, H. H. Pu, O. Mao and J. H. Chen, J. Mater. Chem., 2012, 22, 3300.

8 W. Liang, H. Yang, F. Fan, Y. Liu, X. H. Liu, J. Y. Huang, T. Zhu and S. Zhang, ACS Nano, 2013, 7, 3427.

9 C. Wang, Y. S. Chui, R. G. Ma, T. Wong, J. Ren, Q. H. Wu, X. Chen and W. Zhang, J. Mater. Chem. A, 2013, 1, 10092-10098.

10 J. W. Wang, Y. He, F. Fan, X. H. Liu, S. Xia, Y. Liu, C. T. Harris, H. Li, J. Y. Huang and T. Zhu, Nano Lett., 2013, 13, 709.

11 X. Zhou and Y. G. Guo, J. Mater. Chem. A, 2013,1, 9019-9023.

12 J. Li, A. Smith, R. J. Sanderson, T. D. Hatchard, R. A. Dunlap and J. R. Dahn, J. Electrochem. Soc., 2009, 156, A283.

13 M. R. Zamfir, H. T. Nguyen, E. Moyen, Y. H. Lee and D. Pribat, J. Mater. Chem. A, 2013,1, 9566-9586.

14 K. Huang, F. Sun, T. Gao, Y. P. Liu, J. X. Zhong, X. L. Wei and X. Qi, Nanoscale, 2013,5, 8586-8592.

15 R. A. DiLeo, M. J. Ganter, M. N. Thone, M. W. Forney, J. W. Staub, R. E. Rogers and B. J. Landi, Nano Energy, 2013, 2, 268.

16 Y. Oumellal, N. Delpuech, D. Mazouzi, N. Dupre, J. Gaubicher, P. Moreau, P. Soudan, B. Lestriez and D. Guyomard, J. Mater. Chem., 2011, 21, 6201.

17 C. Yue, Y. Yu, J. Yin, T. Wong, Y. Zang, J. Li and J. Kang, J. Mater. Chem. A, 2013, 1, 7896.

18 H. Wu and Y. Cui, Nano Today, 2012, 7, 414.

19 C. K. Chan, H. Peng, G. Liu, K. McIlwrath, X. F. Zhang, R. A. Huggins and Y. Cui, Nature Nanotech., 2008, 3, 31.

20 R. Mukherjee, R. Krishnan, T. M. Lu and N. Koratkar, Nano Energy, 2012, 1, 518.

21 H. C. M. Knoops, M. E. Donders, M. C. M. van de Sanden, P. H. L. Notten and W. M. M. Kessels, J. Vac. Sci. Technol. A, 2012, 30, 010801.

22 H. T. Nguyen, M. R. Zamifir, L. D. Duong, Y. H. Lee, P. Bondavalli and D. Pribat, J. Mater. Chem., 2012, 22, 24618.

23 Y. Hwa, W. S. Kim, B C. Yu, HS. Kim, S. H. Hong and H. J. Sohn, J. Mater. Chem. A, 2013, 1, 3733.

24 E. L. Memarzadeh, W. P. Kalisvaart, A. Kohandehghan, B. Zahiri, C. M. B. Holt and D. Mitlin, J. Mater. Chem., 2012, 22, 6655.

25 N. S. Choi, Y. Yao, Y. Cui and J. Cho, J. Mater. Chem., 2011, 21, 9825.

26 Y. Zhao, X. Liu, H. Li, T. Zhai and H. Zhou, Chem. Commun., 2012, 48, 5079.

27 T. Song, J. Xia, J. H. Lee, D. H. Lee, M. S. Kwon, J. M. Choi, J. Wu, S. K. Doo, H. Chang, W. I. Park, D. S. Zang, H. Kim, Y. Huang, K. C. Hwang, J. A. Rogers and U. Paik, Nano Lett., 2010, 10, 1710.

28 H. Wu, G. Chan, J. W. Choi, I. Ryu, Y. Yao, M. T. McDowell, S. W. Lee, A. Jackson, Y. Yang, L. Hu and Y. Cui, Nature Nanotech., 2012, 7, 310.

29 Y. Yao, M. T. McDowell, I. Ryu, H. Wu, N. Liu, L. Hu, W. D. Nix and Y. Cui, Nano Lett, 2011, 11, 2949.

30 Z. Wen, G. Lu, S. Mao, H. Kim, S. Cui, K. Yu, X. Huang, P. T. Hurley, O. Mao and J. Chen, Electrochem. Comm., 2013, 29, 67.

31 E. Radvanyi, E. De Vito, W. Porcher, J. Danet, P. Desbois, J. F. Colin and S. J. Si Larbi, J. Mater. Chem. A, 2013, 1, 4956.

32 C. K. Chan, R. Ruffo, S. S. Hong and Y. Cui, J. Power Sources, 2009, 189, 1132.

33 A. Kohandehghan, P. Kalisvaart, M. Kupsta, B. Zahiri, B. S. Amirkhiz, Z. Li, E. Memarzadeh, L. A. Bendersky and D. Mitlin, J. Mater. Chem. A, 2013, 1, 1600.

34 Y. Liu, K. Huang, Y. Fan, Q. Zhang, F. Sun, T. Gao, L. Yang and J. Zhong, Electrochimica Acta, 2013, 88, 766.

35 A. M. Chockla, T. D. Bogart, C. M. Hessel, K. C. Klavetter, C. B. Mullins and B. A. Korgel, J. Phys. Chem. C, 2012, 116, 18079.

36 Y. J. Cho, H. S. Kim, H. Im, Y. Myung, G. B. Jung, C. W. Lee, J. Park, M. H. Park, J. Cho and H. S. Kang, J. Phys. Chem. C, 2011, 115, 9451.

37 H. Chen, Y. Xiao, L. Wang and Y. Yang, J. Power Sources, 2011, 196, 6657.

38 Y. Yao, N. Liu, M. T. McDowell, M. Pasta and Y. Cui, Energy Environ. Sci., 2012, 5, 7927.

39 M. T. McDowell, S. W. Lee, C. Wang and Y. Cui, Nano Energy, 2012, 1, 401.

40 X. H. Liu, L. Q. Zhang, L. Zhong, Y. Liu, H. Zheng, J. W. Wang, J. H. Cho, S. A. Dayeh, S. T. Picraux and J. P. Sullivan, Nano Lett, 2011, 11, 2251.

41 W. Wang, M. Tian, Y. Wei, S. H. Lee, Y. C. Lee and R. Yang, Nano Energy, 2013, 2, 943-950.

42 L. Q. Zhang, X. H. Liu, Y. Liu, S. Huang, T. Zhu, L. Gui, S. X. Mao, Z. Z. Ye, C. M. Wang and J. P. Sullivan, ACS Nano, 2011, 5, 4800.

43 M. T. McDowell, S. W. Lee, I. Ryu, H. Wu, W. D. Nix, J. W. Choi and Y. Cui, Nano Lett, 2011, 11, 4018.

44 B. W. Sheldon, S. K. Sony, X. Xiao and Y. Qi, Electrochem. Solid State Lett., 2012, 15, A9.

45 S. M. Dong, X. Chen, X. Y. Zhang, and G. Cui, Coordin. Chem. Rev., 2013, 257, 1946.

46 J. Chen, K. Takanabe, R. Ohnishi, D. Lu, S. Okada, H. Hatasawa, H. Morioka, M. Antonietti, J. Kubota and K. Domen, Chem. Commun., 2010, 46, 7492.

47 P. He, Y. Wang and H. Zhou, Chem. Commun., 2011, 47, 10701.

48 N. Savvides and B. Window, J. Appl. Phys., 1988, 64, 225.

49 P. Han, Y. Yue, X. Wang, W. Ma, S. Dong, K. Zhang, C. Zhang and G. Cui, J. Mater. Chem., 2012, 22, 24918.

50 S. Dong, X. Chen, L. Gu, X. Zhou, L. Li, Z. Liu, P. Han, H. Xu, J. Yao, H. Wang, X. Zhang, C. Shang, G. Cui and L. Chen, Energy Environ. Sci., 2011, 4, 3502.

51 C. W. Liu, J. An, R. S. Guo, Y. Li and L. Liu, J. Alloy. Compd., 2013, 563, 33.

52 G. Xu, L. Zhang, C. Guo, L. Gu, X. Wang, P. Han, K. Zhang, C. Zhang and G. Cui, Electrochim. Acta, 2012, 345.

53 J. Zhang, J. Zhang, W. Cai, F. Zhang, L. Yu, Z. Wu and Z. Zhang, J. Power Sources, 2012, 211, 133.

54 Y. Yue, P. Han, X. He, K. Zhang, Z. Liu, C. Zhang, S. Dong, L. Gu and G. Cui, J. Mater. Chem., 2012, 22, 4938.

55 I. Kim, P. N. Kumta and G. E. Blomgren, Electrochem. Solid State Lett., 2000, 3, 493.

56 J. T. Zhao, L. Hu, S. Jiao, J. Hou and H. Zhu, Phys. Chem. Chem. Phys, 2013, 15, 10472.

57 C. Marichy, M. Bechelany and N. Pinna, Adv. Mater., 2012, 24, 1017.

58 X. Meng, X. Q. Yang and X. Sun, Adv. Mater., 2012, 24, 3589.

59 M. Q. Snyder, S. A. Trebukhova, B. Ravdel, M. C. Wheeler, J. DiCarlo, C. P. Tripp and W. J. DeSisto, J. Power Sources, 2007, 165, 379.

60 H. C. M. Knoops, L. Baggetto, E. Langereis, M. C. M. van de Sanden, J. H. Klootwijk, F. Roozeboom, R. A. H. Niessen, P. H. L. Notten and W. M. M. Kessels, J. Electrochem. Soc., 2008, 155, G287.

61 R. F. Egerton, Electron energy-loss spectroscopy in the electron microscope, Springer, New York, 2011

62 C. Ahn, R. Burgner and O. Krivanek, EELS Atlas: A reference guide of electron energy loss spectra covering all stable elements, Center for Solid State Science, Arizona State Univ., 1983

63 L. Brewer, Chem. Rev., 1953, 52, 1.

64 H. O. Pierson, Handbook of Refractory Carbides and Nitrides, Properties, Characteristics, Processing and Applications, William Andrew, 1996, ISBN 0-8155-1392-5

65 N. C. Saha and H. G. Tompkins, J. Appl. Phys., 1992, 72, 3072.

66 L. Baggetto, R. A. H. Niessen, F. Roozeboom and P. H. L. Notten, Adv. Mater., 2008, 18, 1057.

67 K. Karki, E. Epstein, J.H. Cho, Z. Jia, T. Li, T. Picraux, C. Wang and J. Cumings, Nano Lett., 2012, 12, 1392.

68 E. L. Memarzadeh, W.P. Kalisvaart, K. Cui, A. Kohandehghan, M. Kupsta, B.C. Olsen and D. Mitlin, Phys. Chem. Chem. Phys., 2013, 15, 13646.

69 M. T. McDowell and Y. Cui, Adv. Energy Mater., 2011, 1, 894.

70 R. Ruffo, S. S. Hong, C. K. Chan, R. A. Huggins and Y. Cui, J. Phys. Chem. C, 2009, 113, 11390.

71 M. D. Levi and D. Aurbach, J. Phys. Chem. B, 1997, 101, 4630.

72 V. Etacheri, A. Geiger, Y. Gofer, G. A. Roberts, I. C. Stefan, R. Fasching and D. Aurbach, Langmuir, 2012, 28, 6175.

73 L. Baggetto, J. F. M. Oudenhoven, T. van Dongen, J. H. Klootwijk, M. Mulder, R. A. H. Niessen, M. H. J. M. de Croon and P. H. L. Notten, J. Power Sources, 2009, 189, 402.

74 D. E. A. Salas, A. K. Sra, K. Roodenko, Y. J. Chabal and C. L. Hinkle, J. Phys. Chem. C, 2012, 116, 9072.

75 F. Kauffmann, B. Ji, G. Dehm, H. Gao and E. Arzt, Scripta materialia, 2005, 52, 1269.

76 K. W. Schroder, H. Celio, L. J. Webb and K. J. Stevenson, J. Phys. Chem. C, 2012, 116, 19737.

77 NIST XPS database at http://srdata.nist.gov/xps/Default.aspx.

Chapter 4: Nanometer-scale Sn Coatings Improve the Performance of Silicon Nanowire LIB Anodes

Material in this chapter has been published in:

Kohandehghan, Alireza, Kai Cui, Martin Kupsta, Elmira Memarzadeh, Peter Kalisvaart, and David Mitlin. "Nanometer-scale Sn Coatings Improve the Performance of Silicon Nanowire LIB Anodes." J. Mater. Chem. A 2, (2014): 11261-11279.

4.1 Introduction

Scientific research on improved materials for lithium-ion batteries (LIBs) has been ongoing for at least the last two decades. [1-5] The key advantages of LIBs over other secondary battery chemistries are their substantially higher energy and power densities. The majority of commercial LIBs rely on a graphite anode which lithiates to for LiC_6, and possesses gravimetric and volumetric capacities of 372 mAh/g and 837 mAh/cm^3, respectively. Silicon, with its order of magnitude higher capacity of 3590 mAh/g and 8257 mAh/cm^3 for $Li_{15}Si_4$, is a promising replacement for graphite. [6-10] High power may be achieved through material modification of the Si anodes to enhance the electrical conductivity and/or accelerate the lithiation reaction kinetics, e.g. [11]. While attractive in terms of capacity, Si suffers from cyclability issues associated with the ~ 280% lithiation driven volume change (for $Li_{15}Si_4$). [12-15] This continual volume expansion and contraction causes pulverization of active material in parallel to unstable solid electrolyte interphase (SEI) growth on the freshly exposed Si surfaces. This is why silicon barely retains its large initial capacity over the long course of cycling.

Intense efforts have been directed toward overcoming the pulverization issue, with improvements being achieved through a variety of nanostructuring approaches. [16-25] Attention has been focused on silicon nanowires (SiNWs) as their "1D" morphology shortens Li diffusion distances and also offers strain accommodation. [26,27] However, without additional microstructural engineering to reduce cracking and runaway SEI formation, even these structures are not

sufficiently mechanically robust during extensive cycling. Recent transmission electron microscopy studies revealed the nanometer scale degradation phenomena and structural instabilities of SiNWs during lithiation/delithiation. [28,29] It has been shown that there is a gradual volume expansion/contraction over the lithiation/delithiation time (or as a function of the voltage) depending on the lithiation extent of the Si core. [12,30] Failure processes associated with extensive SEI formation and lithiation accelerated agglomeration of the SiNWs through a lithium-assisted welding process have also been revealed. [31,32] Surface coating of Si anodes with the materials ranging from a polymer, [33] Ge [34] to Cu, [35,36] Al, [37] Ag, [38] Mg [32] and TiO_2, [23,39] TiN, [23,40,41] Al_2O_3, [23,42] SiO_2, [8] Mg_2Si [32] has generally led to cycling and rate performance improvements. A novel shell structure of TiO_{2-x}/C has been also shown to improve the cycling performance of Si anode. [43] The cycling improvement is generally attributed to enhanced structural stability, while the rate performance is associated with the coatings offering a highly electrically conductive path down to the current collector. Proper coatings may induce a compressive stress in the nanowire during lithiation, thereby limiting the initiation of cracks. [37] Evidence for this effect is provided by a measured reduction of the SiNWs radial expansion in favor of longitudinal expansion. [40] Coatings may also make the radial expansion of SiNWs more isotropic, which should also reduce the degree of cracking. [11]

Metallic Sn would be an intriguing choice coating material for SiNWs. Tin is both ductile and electrically conductive, therefore being able to boost both the structural stability of Si and its rate performance. It is also highly electrochemically active towards Li, with a theoretical capacity of 996 mAh/g ($Li_{22}Sn_5$), which corresponds to ~ 260% volume change upon full lithiation. [44,45] Hence a Sn coating is expected to be effective in generating compressive stresses on the Si surface, especially if it lithiated first. The high capacity of Sn also contributes to the overall capacity of the anode, allowing for its inclusion without a significant energy density penalty for the system. Binary Si – Sn nanocomposites with a variety of geometries have exhibited attractive cycling performances in LIBs. [46,47] However a nano-scale Sn coating on SiNWs has not been attempted. In this study we demonstrate that such an architecture, termed Sn/SiNWs, does indeed lead to improve the cycling capacity retention, coulombic efficiency, and rate capability as compared to an electrode based on a generic uncoated SiNWs array. In order to understand the mechanism through which this performance enhancement is achieved, we

analyzed the partially lithiated and delithiated electrodes using analytical and high resolution TEM (EELS TEM and HRTEM), focused ion beam (FIB) analysis, time-of-flight secondary ion mass spectroscopy (TOF-SIMS), and X-ray photoelectron spectroscopy (XPS).

4.2 Experimental procedure

We prepared the SiNW electrodes by using a gold-catalyzed, vapour–liquid–solid (VLS) growth on 316L stainless steel spacers (∅ 15.4 mm, 1.86 cm^2). In order to prevent penetration of Au into stainless steel at elevated temperatures, a Ti/TiN diffusion barrier with layer thicknesses of 50 nm/200 nm was magnetron sputtered (AJA International, ATC Orion 8) onto the polished spacers. The base pressure in the sputtering chamber was always below 5×10^{-8} Torr. For reactive sputtering of TiN, a N_2:Ar ratio of 1:20 was used and the deposition temperature raised to 250 °C. A 10 nm Au catalyst layer was deposited after cooling the substrate down to room temperature. SiNWs were grown in a commercial Tystar CVD furnace using a SiH_4:H_2 ratio of 1:4 at a pressure of 100 Torr. The resulting mass loading of SiNWs grown under these conditions on each electrode is approximately 0.32 mg in average. The average length and diameter of the resulting SiNWs are 12 μm and 114 nm, respectively (see Figure 4-1(a)). [32,37] The surface area enhancement over the geometric surface of the support, due to the nanowires, was approximately 12. [40]

The SiNW electrodes were removed from the CVD furnace, were stored at ambient for approximately 24 – 48 hours and were radio frequency (RF)-magnetron sputter coated with Sn from an elemental high purity target. Depositions were performed with continuous substrate rotation in presence of Ar gas with 5N purity at a sputtering pressure of 4 mTorr, with a maximum base pressure of 5×10^{-8} Torr. The deposition rates were both calibrated in-situ using an in-plane crystal monitor and ex-situ through a series of thickness vs. time, power measurements. A rate of ~ 0.3 Å/s was employed for all three depositions. Both after CVD growth and after sputter coating, the samples were weighed using a high accuracy Mettler Toledo MX5 microbalance (1 μg resolution) to confirm the mass loadings. The planar geometric tin thicknesses were 10, 30, and 50 nm, being equivalent to 4, 11, and 17 wt.% Sn of the total

active electrode mass, respectively. As will be shown, the films were partially dewetted, especially for the case of the 50 nm Sn. However, we will refer to the coating thickness as the geometric thickness/surface area enhancement, i.e. 10/12, 30/12, and 50/12, with the understanding that this is an approximation that is convenient for labeling.

Lithium half-cells were assembled in 2032 button configuration with lithium foil as counter electrode and polyethylene separators (MTI Corporation, porosity of 36 – 44% and average 0.03 μm pore size). The electrolyte employed was 1 M $LiPF_6$ solvated in ethylene carbonate (EC):diethyle carbonate (DEC):dimethyle carbonate (DMC), 1:1:1 volumetric ratio. Assembly was performed in an Ar glovebox with less than 0.2 ppm moisture and oxygen contents. For constant current (CC) experiments, the batteries were galvanostatically cycled within 0.01 − 2 V (vs. Li/Li^+) at various current densities using a computer controlled BT2000 Arbin potentiostat. Specific capacities were calculated based on the combined Si and Sn mass loading, while the C rates were based on the theoretical specific capacity of the electrode as calculated by rule of mixtures (3590 mAh/g for Si and 996 mAh/g for Sn). We employ the usual definition of a reversible capacity being the capacity at first delithiation, i.e. during the first discharge process. [7] Cyclic voltammetry (CV) experiments were conducted on a Solartron 1470 Multistat system with Corrware data acquisition software, with a scan rate of 1 mV/s in a range of 0.01 – 2 V vs. Li/Li^+. Electrochemical impedance spectroscopy (EIS) measurements were performed on Versa STAT3 potentiostat in a frequency range of 1000 Hz – 100 mHz with an AC amplitude of 10 mV. Prior to testing the battery OCP was allowed to stabilize overnight, reaching a voltage of approximately ~ 1.98 V for the as-synthesized specimens and ~ 1.12 V for the post cycled electrodes. All the electrochemical experiments were performed at room temperature. For post-cycling microstructural analysis, the electrodes were disassembled in an Ar glovebox, rinsed in acetonitrile and stored there overnight as to remove any residual electrolyte.

The samples were characterized using transmission electron microscopy (TEM) (JEOL JEM 2100 and JEOL 2200FS, both at 200 kV). TEM micrographs were recorded under similar current density and exposure time. Electron diffraction patterns were simulated using the commercial software Crystal Maker ™ and shareware Diffraction Ring Profiler, [48] with the input of known space group information of the relevant phases. The Diffraction Ring Profiler integrates the SAD ring pattern intensities to accurately calculate the center point of each ring. High resolution TEM

(HRTEM) measurements were conducted using scanning TEM (STEM) (JEOL 2200FS, 200 kV) with a nominal analytical beam size of 0.5 nm. Electron energy loss spectroscopy (EELS) was performed using a JEOL 2200FS with an in-column Ω filter in scanning mode (STEM) with a nominal analytical beam size of 0.5 nm. High angle annular dark-field (HAADF) micrographs were recorded simultaneously with the EELS measurements. Digital Micrograph (Gatan, Inc.) was employed for signal collection and data extraction. The standard procedure of pre-edge background subtraction and integration on the edge was used for the data extraction from the recorded EELS spectra. [49] For each elemental map, a thickness profile was calculated from low-loss EELS spectrum to check for possible artifacts due to large variation in thickness. We acquired O, Si, and Sn maps by integrating over the core-loss edges of O K, Si L, and Sn M– edge, respectively. Low-loss Li K-edge was used for lithium mapping in cycled materials.

Cross sectional SEM images of the bulk cycled materials were acquired by using a Hitachi NB5000 and a Zeiss NVision 40 dual beam FIB/SEM machines. X-ray photoelectron spectroscopy (XPS) measurements of as-synthesized and cycled materials were conducted on ULTRA (Kratos Analytical) spectrometer using Al – K_α radiation ($h\nu$ = 1486.6 eV) run at 210 W. Data collection was conducted in an ultra-high vacuum (10^{-9} Torr) chamber and the X-ray beam was rastered over an area of 300 × 700 μm^2. High resolution spectra were collected with an energy window of 20 eV. Charging effects were compensated by a charge neutralizer. We analyzed the XPS spectra using CasaXPS software and used the universal hydrocarbon contamination at 284.8 eV in C 1s spectra to calibrate the binding energy scale. Background subtraction was done using a non-linear Shirley-type background model. The 100 cycled materials were also depth analyzed using time-of-flight secondary ion mass spectroscopy (TOF-SIMS) instrument, ION-TOF GmbH. The analysis chamber was kept at a pressure of < 5 × 10^{-9} mbar. 2 kV cesium ions with current of ~ 148 nA were used for sputtering over an area of 300 × 300 μm^2 and a 25 kV Bi ion source was used for analysis over an area of 40 × 40 μm^2.

4.3 Results and Discussion

4.3.1 As-synthesized microstructure

As indicated in the experimental, the SiNW electrodes with Sn coating of mean thickness of 1 (~ 10/12), 3 (~ 30/12), and 5 (~ 50/12) nm are labeled 1Sn/SiNWs, 3Sn/SiNWs, and 5Sn/SiNWs, respectively. The films are partially dewetted, so this labeling sequence is employed for convenience without the implication that these thicknesses are locally exact. Figure 4-1 shows the as-synthesized nanowire arrays. Figure 4-1(a) shows a low magnification cross-sectional SEM micrograph of the as-grown uncoated SiNWs. Figure 4-1(b-d) show plan-view SEM images of the as-synthesized nanowires with high magnification inserts, highlighting 1Sn/SiNWs, 3Sn/SiNWs, and 5Sn/SiNWs, respectively.

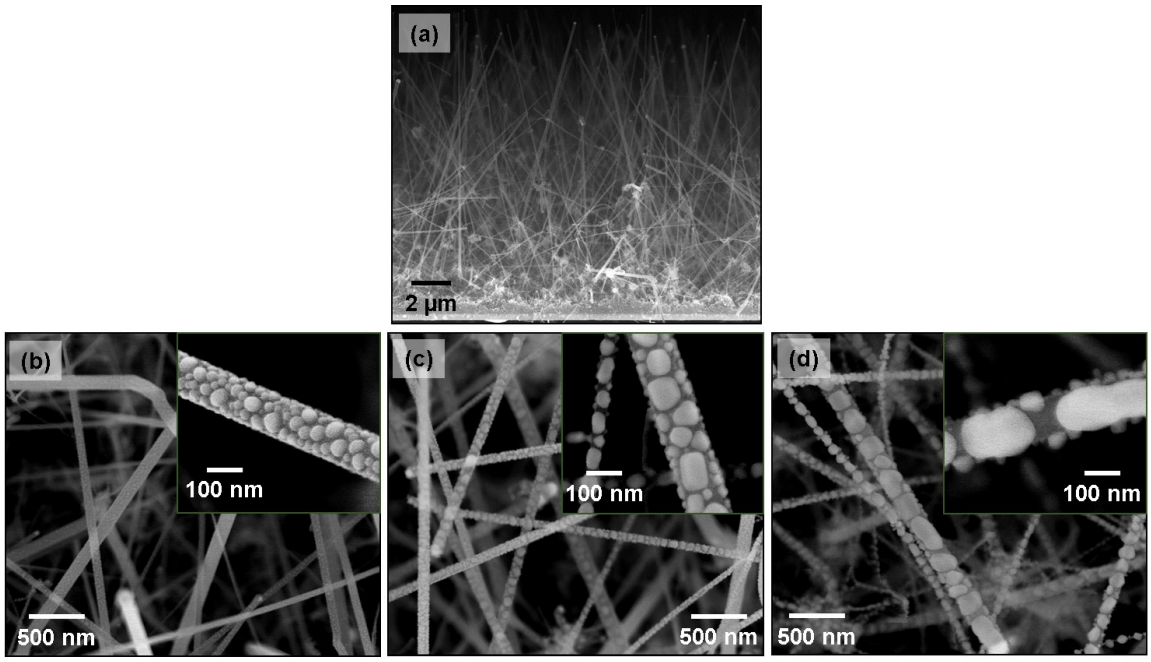

Figure 4-1: (a) Low magnification cross-sectional SEM micrograph of the as-grown uncoated SiNWs. Plan-view SEM images of the as-synthesized nanowires with high magnification inserts. (b) 1Sn/SiNWs, (c) 3Sn/SiNWs, and (d) 5Sn/SiNWs.

Though the nanowires generally grow vertically, there is a good deal of variation in their heights, diameters, and orientations. It may be seen that while a mean value may be assigned nanowire length (12 μm) and diameter (114 nm), it is difficult to assign an exact height to the

array per se due to the significant site-to-site height variation. As will be demonstrated, it is only after extensive cycling (100 cycles) that we may assign a mean height to the electrode.

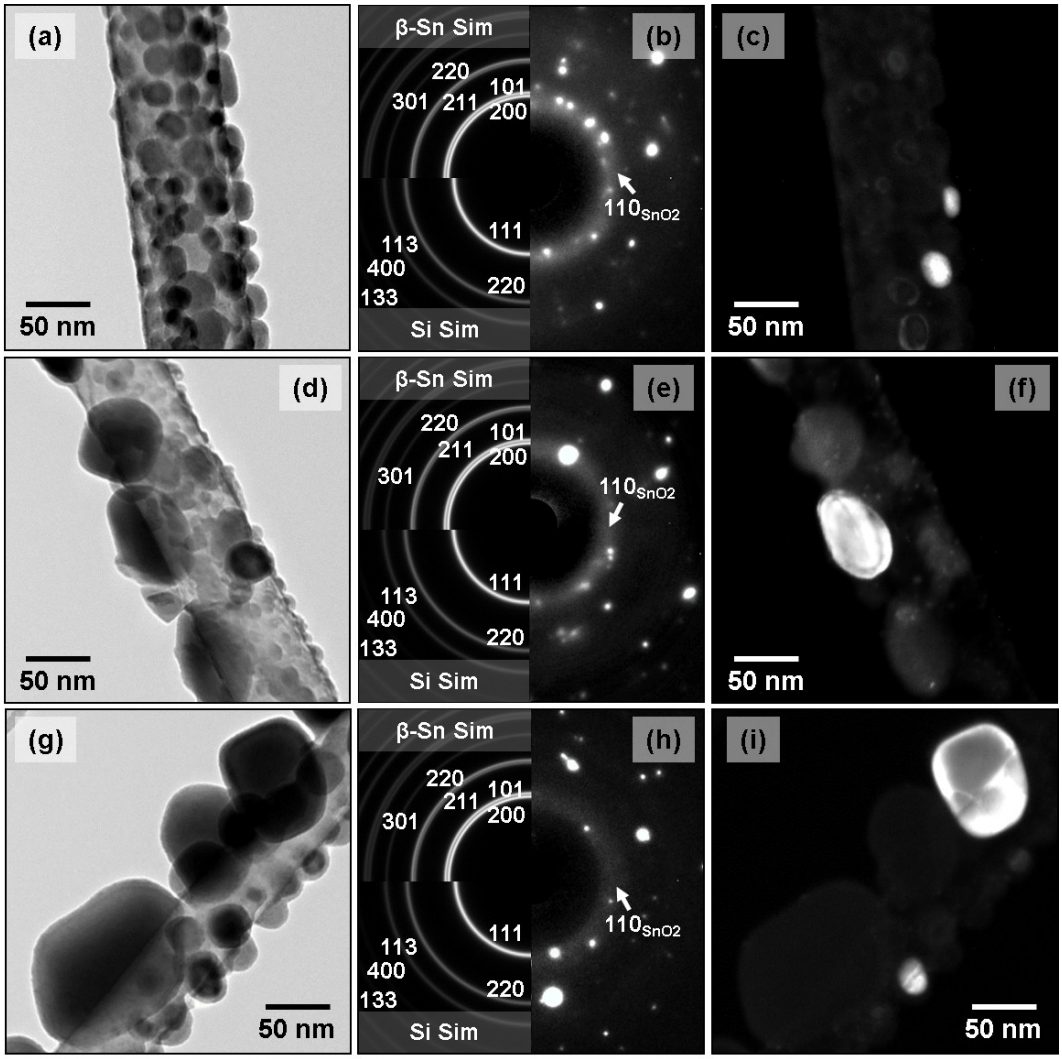

Figure 4-2: TEM micrographs of as-synthesized (a-c) 1Sn/SiNWs; (a) bright-field micrograph, (b) corresponding selected area diffraction (SAD) pattern with β-Sn (top quarter panel) and Si (bottom) simulation, (c) dark-field micrograph obtained using a portion of the 211 Sn ring pattern. (d-f) 3Sn/SiNWs; bright-field micrograph, SAD pattern and dark-field obtained using a portion of the 211 Sn ring pattern. (g-i) 5Sn/SiNWs; bright-field micrograph, SAD pattern, and dark-field micrograph obtained by using a portion of 211 Sn ring.

Figure 4-2 shows TEM micrographs of as-synthesized (a-c) 1Sn/SiNWs, (d-f) 3Sn/SiNWs, and (g-i) 5Sn/SiNWs. The left column shows the bright-field images, the middle column shows

the indexed selected area diffraction (SAD) patterns, while the right column shows dark-field micrographs of the Sn nanocrystals. The β-Sn (space group of $I4_1/amd$, a_0 = 5.8197 Å and c_0 = 3.1749 Å) SAD ring pattern becomes less continuous with increasing film thickness, agreeing with the bright-field and dark-field results that show a coarsening of the particles and a reduction in their number density with increasing film thickness.

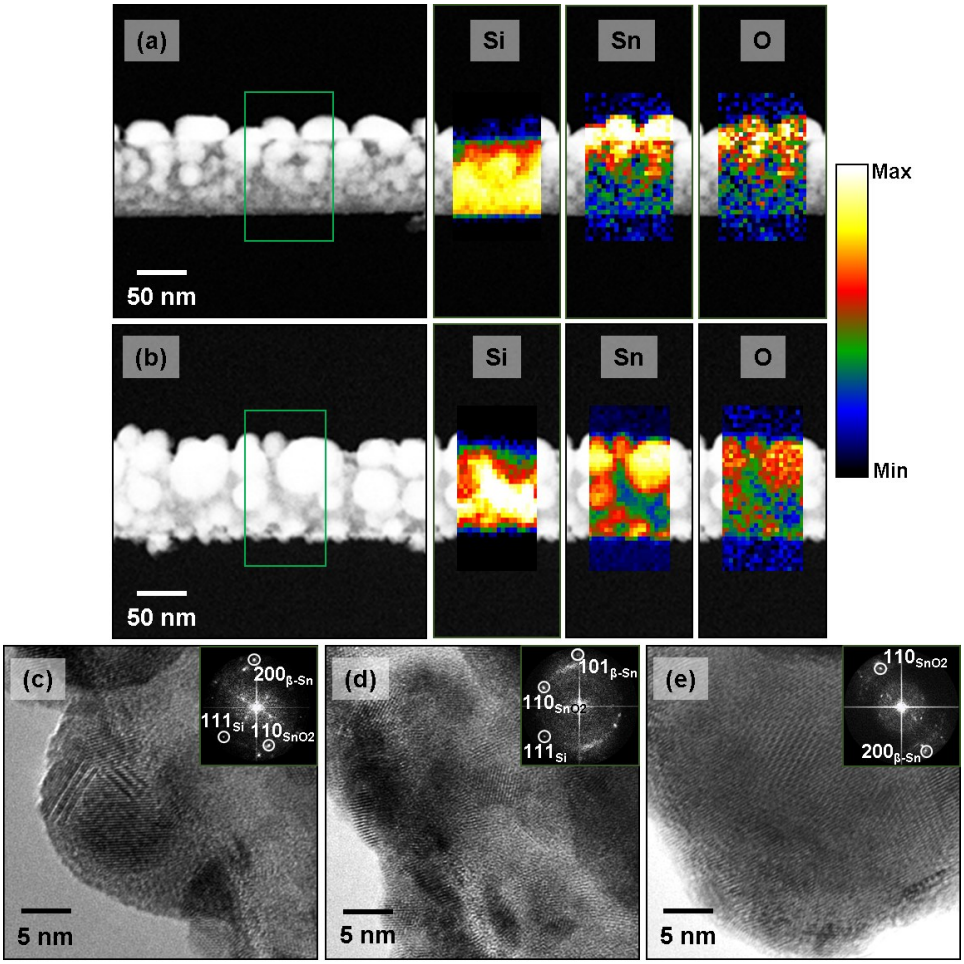

Figure 4-3: High Angle Annular Dark Field (HAADF) micrographs and EELS elemental maps of Si, Sn, and O for (a) 1Sn/SiNWs and (b) 3Sn/SiNWs. High-resolution TEM (HRTEM) micrographs with the corresponding Fast Fourier Transform (FFT) patterns insert for (c) 1Sn/SiNWs, (d) 3Sn/SiNWs, and (e) 5Sn/SiNWs materials.

As expected there is evidence of the Sn nanocrystallites being oxidized in their surface, with a washed-out ring associated with the primary (110) reflection of rutile SnO_2 (space group of

$P4_2/mnm$, a_0 = 4.7370 Å and c_0 = 3.1850 Å). It is important to note that both the bright-field and the dark-field images of the Sn crystallites generally highlight their dimension in the plane of the SiNW surface. The dimensions of the Sn particles normal to the nanowire surface (i.e. the "thickness" of the dewetted Sn film) should be smaller though still substantially thicker than the nominal 1, 3, and 5 nm. Moreover since sputter flux is not conformal and there is shadowing, the Sn films are expected to be thicker near the nanowire surface than near their base.

Figure 4-3 further highlights the as-synthesized microstructures. Figure 4-3(a) and (b) show the High Angle Annular Dark Field (HAADF) micrographs and EELS elemental maps of Si, Sn, and O for 1Sn/SiNWs and 3Sn/SiNWs, respectively. Figure 4-3(c), (d), and (e) show the high-resolution TEM (HRTEM) micrographs with the corresponding Fast Fourier Transform (FFT) patterns insert for 1Sn/SiNWs, 3Sn/SiNWs, and 5Sn/SiNWs, respectively. In the HAADF the Sn nanocrystallites display stronger mass-thickness contrast and appear bright. The O map around the Sn crystallites indicates that the surface is oxidized. The HRTEM images show that the Sn crystallites are multiply twinned, and that some of the particles are actually polycrystalline.

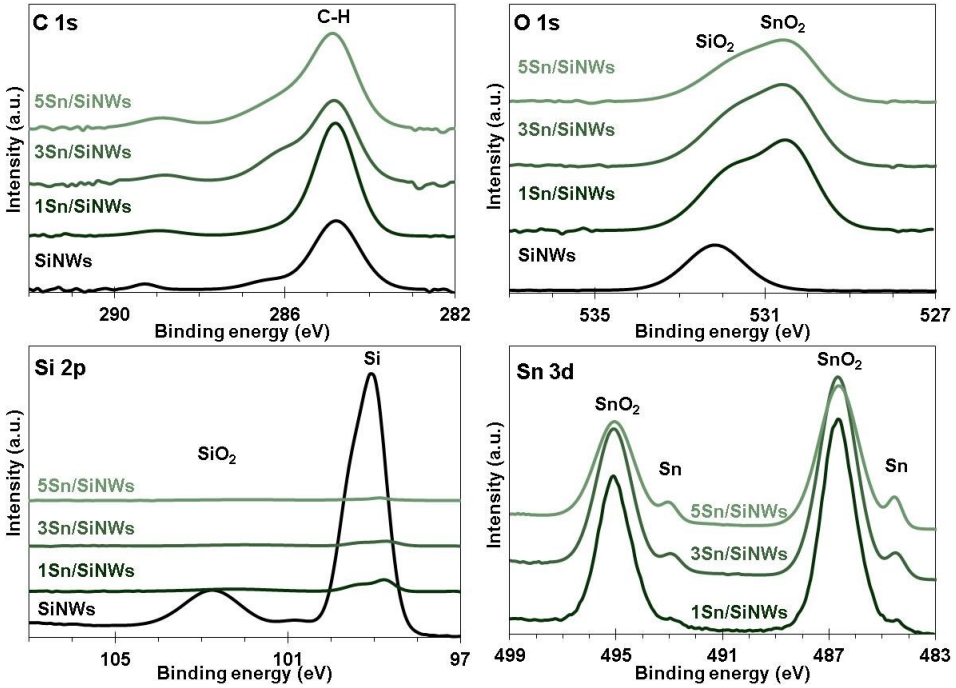

Figure 4-4: C 1s, O 1s ,Si 2p, and Sn 3d XPS spectra for as-prepared SiNWs, 1Sn/SiNWs, 3Sn/SiNWs, and 5Sn/SiNWs.

The near-surface structure of the as-synthesized electrodes was further characterized using XPS (Figure 4-4). Sn 3d and O 1s spectra confirm formation of native SnO_2 upon exposure to air. The Sn 3d spectrum is composed of two minor peaks at binding energies of 484.5 and 493 eV corresponding to Sn $3d_{5/2}$ and Sn $3d_{3/2}$ of Sn^0, respectively. Moreover, there are two major peaks at 486.7 and 495 eV corresponding to SnO_2 $3d_{5/2}$ and SnO_2 $3d_{3/2}$, respectively. Accordingly, a pronounced O 1s peak at 530.5 eV confirms presence of native SnO_2 onto the very top surface of the nanocomposites. The atomic composition of as-prepared materials is listed in Table 4-1.

Table 4-1: Composition (in at.%) of as-prepared materials, obtained from XPS spectra shown in Figure 4-4.

Material	C	O	Si	Sn
SiNWs	12.18	24.08	63.74	-
1Sn/SiNWs	23.01	42.51	17.52	16.96
3Sn/SiNWs	20.87	44.57	8.49	26.07
5Sn/SiNWs	27.55	38.70	5.35	28.40

For all three electrodes the Sn phase is partially dewetted from the Si surface, agreeing with bulk thermodynamics of a positive heat of mixing between the two elements, no intermediate phases and negligible room temperature solubility. [50] Importantly, the degree of dewetting increases with film thickness. In the case of 1 and 3 nm Sn films the structure consists of interconnected Sn nanocrystallites with a percolated structure being largely maintained across the majority nanowire surfaces. However in the 5 nm film, the coarser and more sparsely distributed Sn nanoparticles are primarily (not entirely, since size and position are statistically distributed) isolated. The kinetics of thin film dewetting and breakup on a weakly chemically interacting support have been recently detailed by several groups, e.g. [51,52]. In the sub-10 nm regime dewetting occurs through grain growth and grain-boundary grooving, and is highly time dependent. As explained by ref. [52], grain-boundary grooving is mediated by surface diffusion and is a result of the interface evolving toward a constant curvature surface, constrained by an equilibrium dihedral angle at the grain boundary.

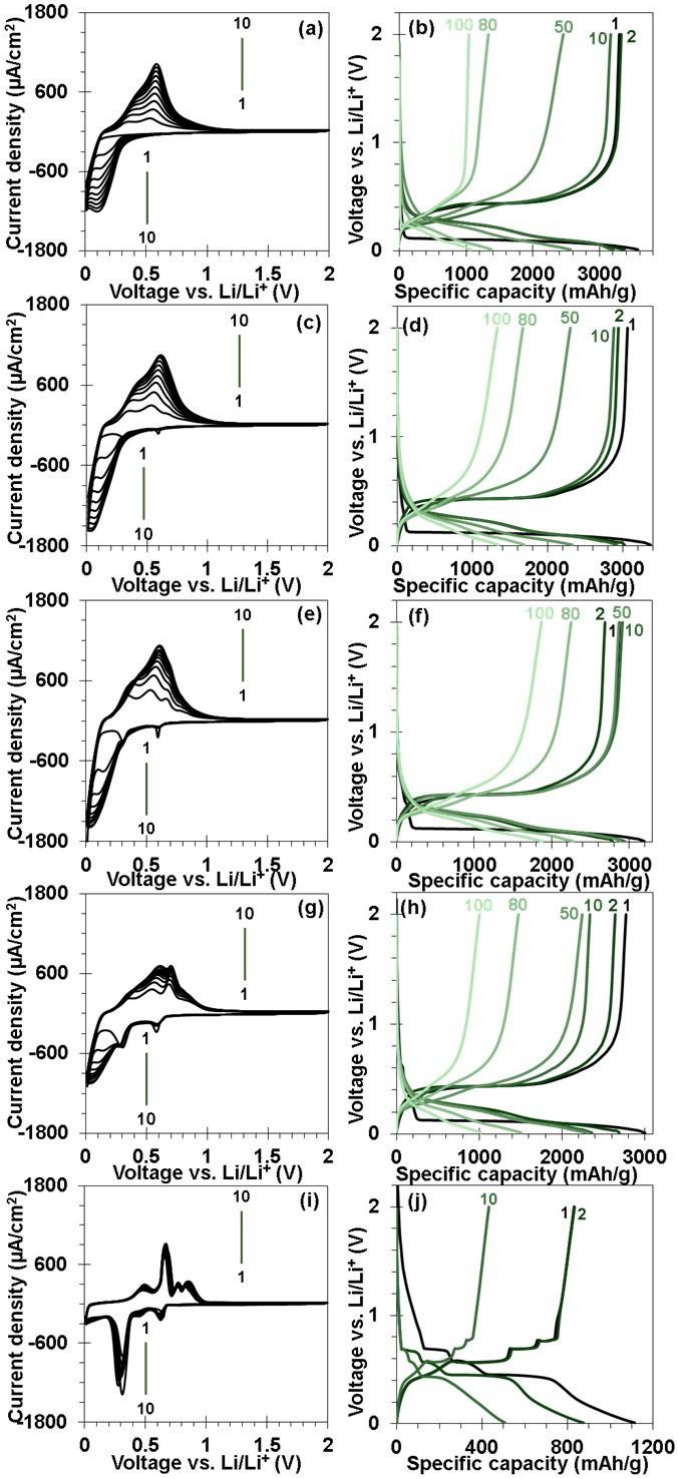

Figure 4-5: Cyclic voltammetry (CV) curves (left column) for cycles 1 – 10 and galvanostatic voltage profiles (right column) for cycles 1 – 100. CV data was collected at 1 mV/s, the constant-current (CC) measurements were conducted at 0.1C. (a,b) bare SiNWs, (c,d) 1Sn/SiNWs, (e,f) 3Sn/SiNWs, (g,h) 5Sn/SiNWs, and (i,j) 100 nm blanket Sn film.

During ambient temperature sputter deposition, which is actually quite a high homologous temperature for Sn (T_m = 232 °C), the adatoms are expected to be very mobile on the Si surfaces. Given the deposition rate of 0.3 Å/s and that the films are 10, 30, and 50 nm in geometrical thickness, it is expected that the thicker films will undergo more dewetting in-situ during the deposition process. At Sn real (not geometrical) thickness much beyond the ones explored in this study, there will be enough material to form continuous blanket films. However rapidly diffusing pure metals on weakly chemically interacting surfaces, such thicknesses may be 50 nm or even higher. [53] For instance, for the case of Cu being deposited at a similar homologous temperature on a non-wetting support, the film needs to be nearly 100 nm before it is fully continuous. [54] As we will demonstrate in the electrochemical section, whether the Sn nanocrystallites are interconnected across the nanowires in effect forming a structural mesh, or are primarily isolated, will profoundly influence the coating's efficacy.

4.3.2 Electrochemical Performance and Cycled Microstructure

Figure 4-5 shows CV curves (left column) and galvanostatic voltage versus specific capacity profiles (right column) of SiNWs, 1Sn/SiNWs, 3Sn/SiNWs, 5Sn/SiWs, and a blanket 100 nm Sn film. The CV data is shown for cycles 1 – 10, while the constant current (CC) data is shown for cycles 1, 2, 10, 50, 80, and 100. The CV tests were performed at 1 mV/s, while the CC data was collected at 0.1C (359 mA/g - 314 mA/g). The CV profiles show three significant broadened redox peaks: The main reduction peak occurs between 0 – 0.2 V. The overlapping peaks in the oxidation profile are at 0.3 – 0.4 V and 0.45 – 0.55 V. These peaks correspond to the multiple stages of lithium alloying and dealloying with Si, consistent with the previous SiNWs studies. [32,37,39,40] The current associated with Si being lithiated to below 0.05 V is associated with the formation of crystalline $Li_{15}Si_4$ phase from the amorphous Li_xSi. This phase transformation has been recently shown to occur congruently, without long distance displacement and diffusion of the atoms. [55] However, the portion of the total capacity that is gained below 0.05 V decreases with increasing cycle number, potentially indicating that with cycling a progressively higher fraction of the total electrode active mass remains amorphous.

The CV profiles of the nanocomposites represent an overlap of the CV curves for Sn and SiNWs, with no additional redox reactions being detected. The most distinct case is for the highest mass loaded Sn specimen (17 wt.% Sn), 5Sn/SiNWs, where the Sn peaks at the described positions are well discerned for both the anodic and the cathodic portions of the CV. During the first lithiation, the surface SnO_2 converts to electrochemically active Sn and an inactive Li_2O, [56,57] the latter being similarly present upon the reduction of surface SiO_2 by Li. [14] This reaction would initiate at an analogous voltage as the formation of the SEI layer (roughly below 0.75 V), the two being indistinguishable on the experimental CV. From the CV profile of 100 nm Sn film plotted in Figure 4-5(i), a reduction peak centered near 0.6 V corresponds to Li_2Sn_5 formation, followed by a peak at 0.45 V associated with appearance of LiSn. The large and broadened peak that is centered near 0.3 V is associated with the progressive formation of the Li_7Sn_3, Li_5Sn_2, $Li_{13}Sn_5$, Li_7Sn_2 and finally the terminal $Li_{22}Sn_5$ (theoretical capacity 991 mAh/g). These phases are known to be difficult to deconvolute both electrochemically and through X-ray crystallography, since they are all based on the bcc unit cell of Li with a varying arrangement of Li and Sn atoms on the individual unit sites. [56,58,59] Similar to the original reports of delithiation of $Li_{22}Sn_5$, the anodic portion of the CV contains four distinct oxidation peaks, centered at ~ 0.52, 0.7, 0.77, and 0.85 V. [56,58-60]

The cycling performance of the electrodes is displayed in Figure 4-6(a-c), the total specific capacity of each electrode, the capacity retention in percentage of cycle 1 capacity, and the coulombic efficiency as a function of cycle number. The first lithiation capacities of the nanocomposites are lower than that of the bare SiNWs due to extra weight of the Sn coating, which has a lower specific capacity than Si (996 mAh/g vs. 3590 mAh/g). However with cycling the 1Sn/SiNWs and the 3Sn/SiNWs electrodes overtake the baseline SiNWs electrode both in terms of % capacity retention (this occurs by cycle 8 for 3Sn/SiNWs) and in terms of the overall capacity retention (this occurs by cycle 33 for 3Sn/SiNWs). This may be attributed to the partially dewetted yet still continuous nano-scale coating of Sn that structurally stabilizes the Si nanowires during lithiation and delithiation. Even the 5Sn/SiNWs electrode, where it was shown that the Sn coating is largely discontinuous, offers an improvement (though not as pronounced) in the % of the cycling capacity retention. The 5Sn/SiNWs electrode starts at a significantly

lower specific capacity due to the 17 wt.% Sn (cycle 1 capacity of 3006 mAh/g vs. 3576 mAh/g), but finishes the 100 cycles at a nearly exact capacity as the baseline (~ 1040 mAh/g).

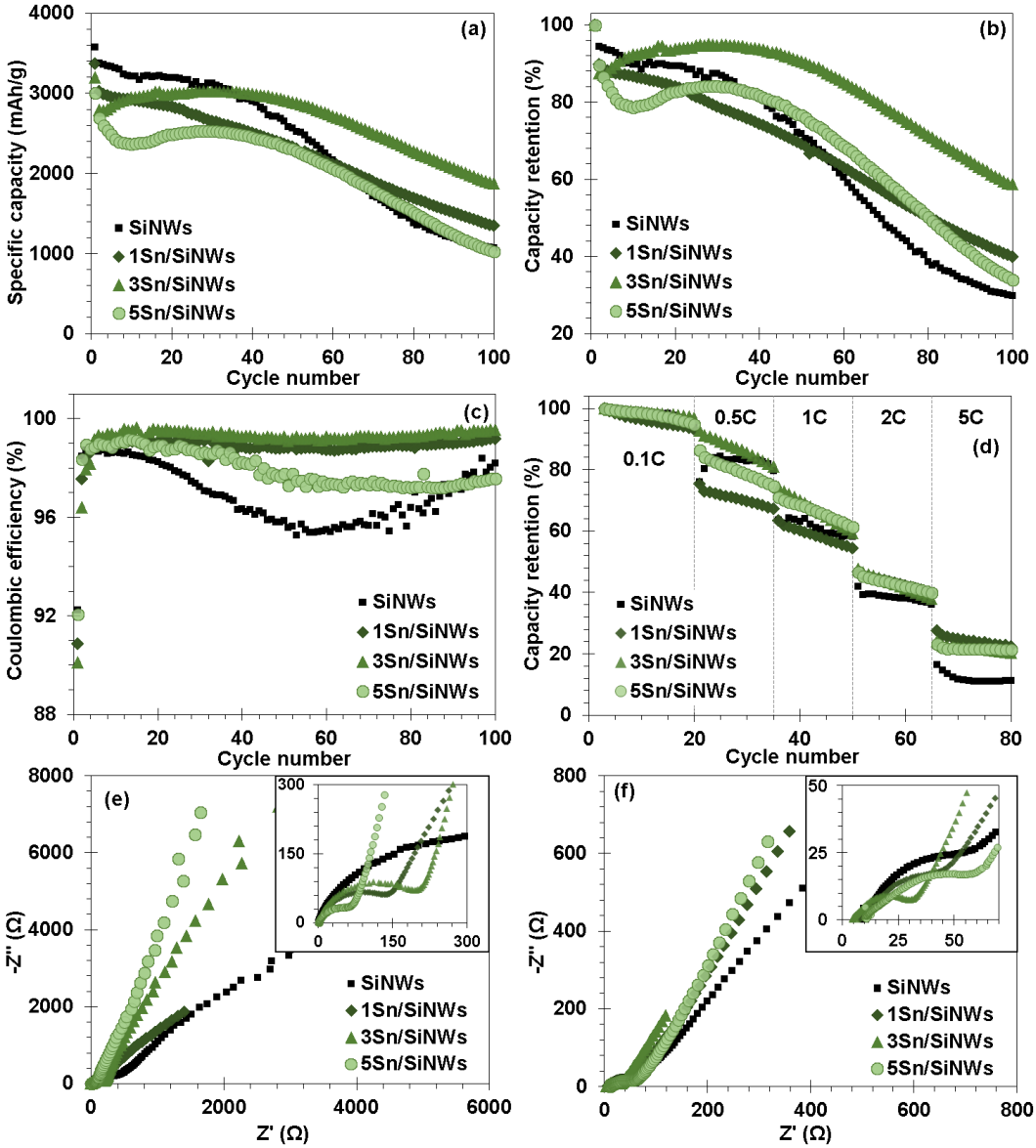

Figure 4-6: Constant-current cycling behavior of SiNWs, 1Sn/SiNWs, 3Sn/SiNWs, and 5Sn/SiNWs electrodes, tested at a rate of 0.1C. (a) Specific capacity as a function of cycle number, (b) capacity retention vs. cycle number, defined as a percentage of the first cycle capacity, and (c) corresponding coulombic efficiency. (d) Rate performance, percent capacity retained normalized to cycle 3 at 0.1C. (e,f) Electrochemical impedance spectroscopy (EIS) of SiNWs, 1Sn/SiNWs, 3Sn/SiNWs, and 5Sn/SiNWs in as-synthesized and after 100 cycles at 0.1C, respectively.

The cycle 1 coulombic efficiency (CE) for the SiNWs, 1Sn/SiNWs, 3Sn/SiNWs, and 5Sn/SiNWs electrodes are all analogous; 92, 91, 90, and 91%. The minor degradation of cycle 1 CE for the 1Sn/SiNWs and 3Sn/SiNWs electrodes is likely related to the irreversible conversion of SnO_2 to Li_2O, with the more continuous coatings offering more surface area and hence more surface oxide for this reaction. Since the underlying Si is still covered by a SiO_2 layer that would be permanently reduced to Li_2O at cycle 1 (the nanowires were exposed to ambient prior to Sn deposition), the irreversible capacity loss is cumulative. As may be observed in Figure 4-6(c), a clear and substantial difference emerges in the cycling CEs of the materials. By cycle 3, the electrodes 1Sn/SiNWs and 3Sn/SiNWs have a CE of upwards of 99%. The CE of 5Sn/SiNWs is intermediate, ranging from 99% to 97% between cycles 2 and 100. The CE of the baseline SiNWs is the lowest, finishing at 97.5% at cycle 100. As will be highlighted by the post-cycled microstructural analysis, this improvement in cycling CE is due to the more continuous 1Sn and 3Sn coatings being effective in reducing the levels of SEI formation.

Considering the CV and CC data for pure Sn and for the nanocomposites, Sn lithiates first (starting at ~ 0.78 V) and fully delithiates last (completes at ~ 0.83 V). Conversely, Si begins substantial lithiation starting at 0.35 V, and finishes delithiation at ~ 0.6 V. This means that during lithiation/delithiation of core SiNWs the Sn coating is always at least partially lithiated. Given the volume expansion of the Li_xSn phases ($0.2 < x < 4.4$), ranging from 23 to 259%, [56] the core Si is always under compressive stress from the Li_xSn shell. It is expected that this relatively ductile compressive sheath will reduce the magnitude of the cracking, disintegration, and consequent electrical contact separation of the nanowires from the current collector in the course of cycling. [37,40] The reduced effectiveness of the 5Sn/SiNWs is expected since the much of the coating is present as isolated Sn particles that cannot provide such a support. As has been shown by several stress modeling studies, thicker coatings are expected to be more effective in supporting the nanowires and preventing fracture. [13,61,62] Thus the 3Sn/SiNWs represents the best compromise of the negative influence of Sn dewetting at higher film thicknesses and the positive influence of a thicker and hence stronger supporting shell. Upon reduction by Li, SnO_2 transforms into Sn nanoparticles surrounded by an amorphous Li_2O matrix. [63] The amorphous Li_2O, which has been shown to be ductile near room temperature and can sustain large mechanical stress, [64] should also impart some structural support to the inner SiNWs.

High rate capacity retention performance (normalized to cycle 3 at 0.1C) is presented in Figure 4-6(d). The anodes were cycled at 0.1C (359-314 mA/g) for 20 cycles and then at 0.5C (1795-1572 mA/g), 1C (3590-3143 mA/g), 2C (7180-6286 mA/g), and 5C (17950-15720 mA/g) each for 15 cycles. All materials perform identically at 0.1C for 20 cycles, but a difference emerges at 0.5C, where the Sn coated electrodes are markedly superior. As the charging rate increases, Sn coated electrodes show progressively better performance as compared to the uncoated baseline. The improvement in the cycling performance at high rates, due to the Sn coatings, stems from their role in providing a highly electrically conductive path down to the current collector. The electrical conductivity of Sn is 10^5 S/cm, which is markedly higher than that for silicon (1.6×10^{-3} S/cm) or even Li doped Si (~ 10 S/cm at most). [65] All the coatings appear to be analogously effective in improving the rate performance, which differs from the cycling capacity retention results. This may be explained by a hypothesis that even for the thickest coating there is always some continuous percolated electron path down to the current collector, i.e. some Sn nanocrystallites touch each other all the way down to the base. For electron conductance a fully interconnected mesh across the entire area of the nanowire is not essential as it is for mechanical stabilization.

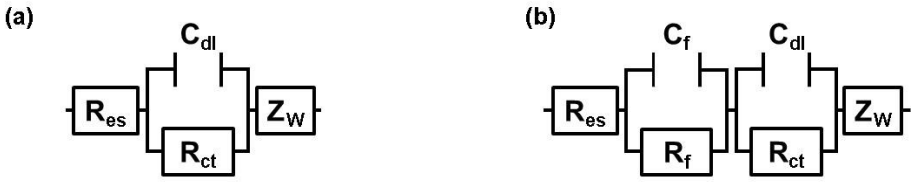

Figure 4-7: Equivalent circuits used for fitting impedance spectra of (a) as-synthesized bare and coated SiNWs, and (b) post-100 cycles (at 0.1C) bare and coated SiNWs.

Electrochemical impedance spectroscopy (EIS) further confirms the favorable impact of the nanoscale Sn coatings. The Nyquist plots in Figure 4-6(e,f) are for the as-synthesized and the post-100 cycles electrodes. The Nyquist plots exhibit well-defined features including a high-frequency depressed semi-circle followed by a 45° sloped line in the low-frequency region of the spectra. The intercept of the spectra with the real part of the impedance axis shows equivalent series resistance (R_{es}) of the half-cell. The diameter of the high frequency semi-circle represents

the interfacial charge transfer resistance (R_{ct}). [66] We modeled the impedance spectra of as-prepared and cycled materials with the equivalent circuits shown in Figure 4-7(a,b), respectively. The values and the associated errors obtained from the model fit are listed in Table 4-2. The simulated and the measured EIS spectra for all the anode materials in as-synthesized and cycled states are presented in Figure 4-8.

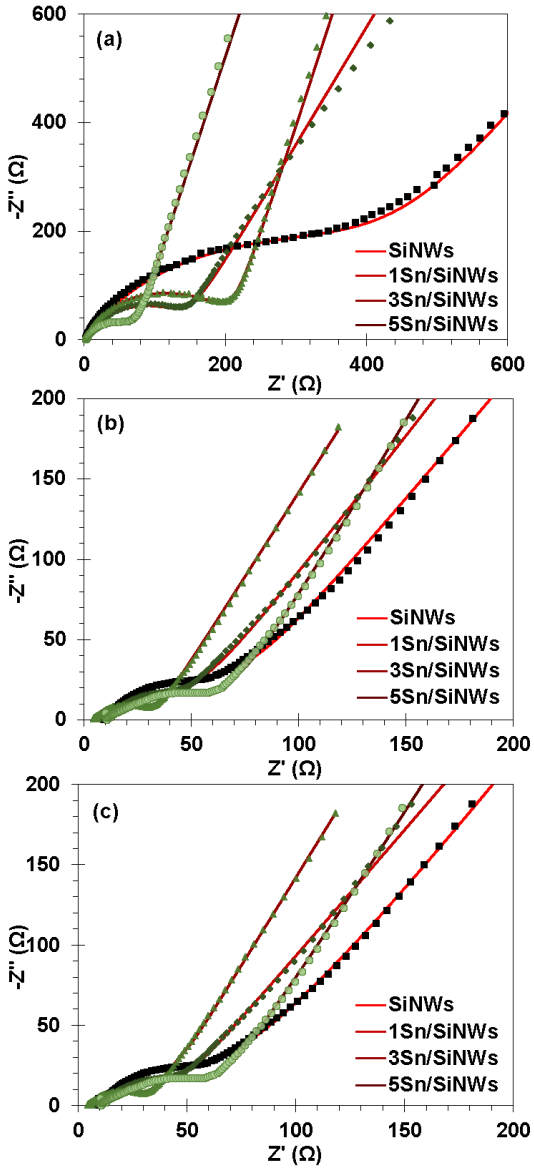

Figure 4-8: The measured and modeled EIS plots for (a) as-synthesized and (b,c) post 100 cycles at 0.1C anode materials. Modeled data obtained from using the equivalent circuit shown in (a,b) Figure 4-7(a) and (c) Figure 4-7(b).

Table 4-2: Resistance values obtained from fitting the EIS results presented in Figure 4-6(e) and (f) using the equivalent circuits shown in Figure 4-7(a) and (b) for as-synthesized and cycled data, respectively.

	SiNWs	1Sn/SiNWs	3Sn/SiNWs	5Sn/SiNWs
As-synthesized electrodes				
R_{es} (Ω)	2.2 ± 0.69%	3.9 ± 1.07%	2.8 ± 0.73%	2.6 ± 0.39%
R_{ct} (Ω)	396.4 ± 0.91%	131.7 ± 1.37%	201.3 ± 0.35%	66.7 ± 0.34%
Post-100 cycles electrodes (equivalent circuit shown in Figure 4-7(a))				
R_{es} (Ω)	9.7 ± 0.49%	8.6 ± 2.1%	5.0 ± 1.95%	9.5 ± 1.90%
R_{ct} (Ω)	62.6 ± 1.64%	40.7 ± 1.86%	27.9 ± 0.77%	59.0 ± 1.02%
Post-100 cycles electrodes (equivalent circuit shown in Figure 4-7(b))				
R_{es} (Ω)	9.0 ± 0.66%	7.3 ± 0.32%	4.9 ± 1.24%	8.9 ± 0.28%
R_f (Ω)	22.9 ± 6.96%	26.6 ± 1.51%	27.8 ± 0.52%	11.4 ± 6.19%
R_{ct} (Ω)	59.7 ± 5.78%	7.8 ± 3.36%	2.9 ± 7.96%	47.0 ± 2.45%

In as-synthesized state R_{ct} is consistently lower for the Sn/SiNWs (132, 201, and 67 Ω) composites than for the uncoated baseline (396 Ω). Prior to the first lithiation there should be minimal SEI formed on the nanowire surfaces. At this stage the electrode's R_{ct} may be correlated primarily to the difficulty in Li ion transfer from the electrolyte into the native oxide that covers the materials. We therefore attribute the difference in the initial charge transfer resistances between the uncoated and the Sn coated specimens to the nature of the oxides initially present on their surfaces. A thin amorphous layer of SiO_2 will instantaneously form on the silicon nanowires' surface upon exposure to air. As our XPS and TEM confirm, for the case of Sn/SiNWs the surface oxide is SnO_2. SnO_2 is known as an n-type semiconductor with an electrical resistivity of ~ 200 Ω.cm, while SiO_2 resistivity is known to be 10^{14} – 10^{16} Ω.cm. Moreover while both oxides are irreversibly reduced by Li ions, SiO_2 is expected to be more tenacious judging by its higher standard enthalpy of formation (-911 kJ/mol vs. -581 kJ/mol). One can therefore put forth a qualitative argument that these two factors, worse electrical conductivity and enhanced stability of SiO_2, will lead to a higher charge transfer resistance of the as-synthesized uncoated SiNW electrodes.

The inset in Figure 4-6(f) and the values reported in Table 4-2 demonstrate that the post-100 cycle total charge transfer resistance (R_{ct} + R_f) for bare SiNWs is substantially larger than that

for the Sn coated SiNWs. This is attributable to the difference in the extent of SEI formation for each of the specimens during cycling. The SEI is an electrically insulating - Li ion conducting multilayer composite, with both organic (e.g. alkyl carbonates, and polyethylene oxide) and inorganic (LiF and Li_2O) phases. [67,68] During cycling, as the SEI builds up in thickness, there is a concomitant increase in the number of interfaces, all which contributing to the charge transfer resistance. [66,68] Poor coulombic efficiency is typically associated with the irreversible and continuous formation of SEI. Both the solvent and salt of the electrolyte solution are thermodynamically unstable and undergo reduction on the anode roughly at 0.7 V vs. Li/Li^+ during the first lithiation cycle. [67,69] These surface films passivate the anode surface and prevent further decomposition of the electrolyte solution. However, high volume changes experienced by silicon during electrochemical cycling can continuously weaken and fracture the SEI layer, exposing fresh silicon to the electrolyte with each cycle. This will form a new SEI layer mostly composed of electrolyte reduction products such as Li_2CO_3 and increase the amount of SEI with each cycle. The instability of the SEI can eventually lead to overall capacity loss, poor coulombic efficiency, and subsequent failure of the battery due to one or a combination of a loss of active material and a depletion of Li. [39,70-72] Besides solvent reduction products such as Li_2CO_3 and alkyl carbonates, SEI also partially consists of LiF which is a (electroless) decomposition product of the $LiPF_6$ salt but can also be formed through reaction with trace amounts of water to HF and eventually LiF. [73,74] The post-100 cycles EIS data are in an excellent accord with the coulombic efficiency of the anodes, presented in Figure 4-6(c). Moreover the charge transfer resistances scale as 3Sn/SiNWs < 1Sn/SiNWs < 5Sn/SiNWs < uncoated SiNWs, which is exactly the reverse order of these electrodes' coulombic efficiencies. This supports our argument that a lower cycling CE is well-correlated with higher levels of SEI formation, since the formation of reduction products such as lithium carbonate and lithium alkyl carbonate will irreversible consume electrons and Li ions.

In Si nanowire based anodes, cycling induced failure is caused by fracture of the individual nanowires due to the severe volume changes incurred by lithiation/delithiation. [32] It is also caused by lithiation-assisted welding of the nanowires and by nanowire agglomeration due to extensive SEI growth, leading to *en-masse* delamination from the current collector. [31,32,72,73] For the case of Si coated with a secondary phase (carbon), several additional phenomena are

observed from in-situ experiments. Si particles embedded in a carbon nanofiber matrix will actually show delayed cycle-1 lithiation. [75] In addition, depending on the strength of the carbon matrix, lithiation of the embedded silicon nanoparticles actually resulted in fracture of the carbon fibers. For the case of a carbon nanotube core and an amorphous Si shell the authors demonstrated a relatively weak interfacial bonding between the two materials, which may be improved by surface functionalization of the CNTs. [76]

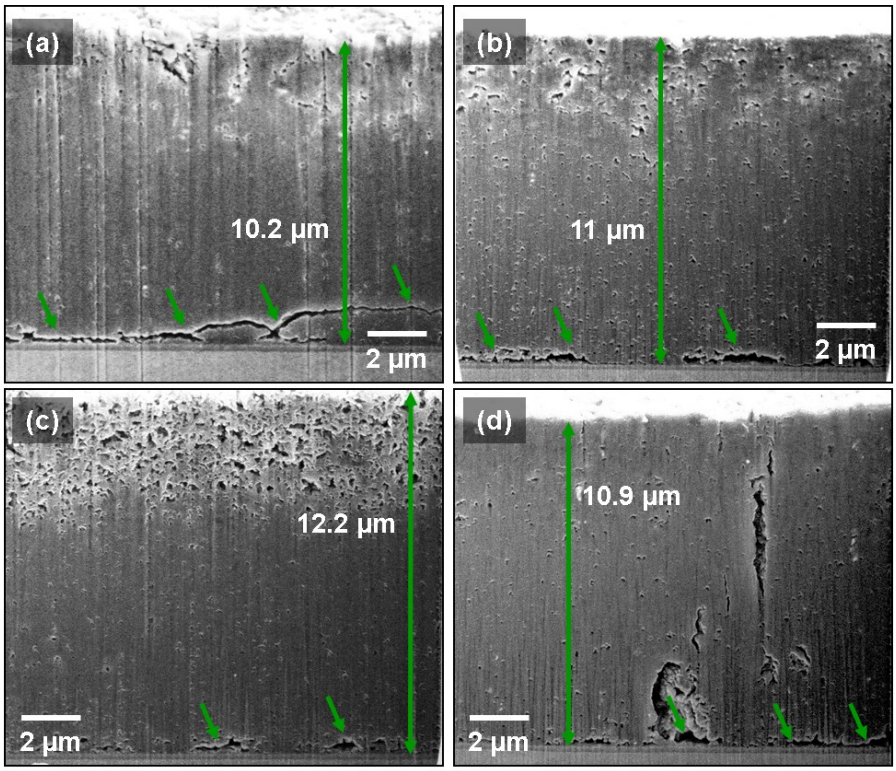

Figure 4-9: FIB cross-sectional SEM images of post 100 cycled (a) bare SiNWs, (b) 1Sn/SiNWs, (c) 3Sn/SiNWs, and (d) 5Sn/SiNWs electrodes.

These and similar in-situ studies demonstrate that coatings are not a 100% satisfactory solution for eliminating the problem of lithiation-induced fracture in silicon. However, they do help in reducing the *extent* of fracture, thus promoting enhanced cycling life. In our case the Sn coatings resulted in 78% improvement in capacity retention after 100 cycles (1865 mAh/g vs. 1046 mAh/g), which is respectable. Moreover the TEM results that will be shown in Figures 8 and 9 fairly conclusively demonstrate that the Sn shell (which is not continuous) does help to

stabilize the Si nanowire structure preventing it from stranding, i.e. fracturing longitudinally. As the FIB results shown in Figure 5 indicate, a major mode of failure of nanowire arrays is their SEI - induced agglomeration and large-scale separation from the current collector. The coatings clearly help in this respect too. As will be demonstrated, the cross-sectional FIB/SEM micrographs, the top-view SEM images, and the XPS results all reveal that there is less SEI formed on the Sn coated SiNWs.

FIB cross-section SEM micrographs of a representative region in each of the post 100-cycled electrodes are shown in Figure 4-9. Rather than being a clearly discernable array of individual nanowires, the electrodes are an agglomerated composite of Si, pores, and SEI. For all specimens, some cracks appear both through the nanowire agglomerates and at the porous film – current collector interface. Such coordinated large-scale separation from the current collector is major source of overall capacity decay in Si nanowire and nanotube architectures. [23,39,40] The associated cause of this failure is the cycling-induced overgrowth of SEI on each nanowire, ultimately fusing them together to make a compressively stressed semi-porous film from what was initially an array of individual non-contacting structures. The overall extent of interfacial cracking was most in the case of the bare SiNWs and the best with the 3Sn/SiNWs electrodes, agreeing with the cycling capacity retention results.

The FIB cross-sections also display well discernable differences in the height of the post-cycled films. As shown by the length of the vertical arrows in Figure 4-9, which are obtained from a Gwyddion 2.31 software analysis of the SEM images, the average height of the post-cycled SiNWs, 1Sn/SiNWs, 3Sn/SiNWs, and 5Sn/SiNWs electrodes is 10.2 μm, 11 μm, 12.2 μm, and 10.9 μm. As discussed in [77], coatings effective for reducing cycling-induced fracture of 1D Si nanostructures will promote anisotropic volume changes upon lithiation/delithiation, favoring longitudinal rather than radial expansion/contraction. The protective shell will still have to locally fracture as to allow the inevitable lengthwise expansion of the nanostructure to accommodate the inserting Li (in alloying reactions the total volume expansion due to lithiation invariably scales with Li content [56]). Such cycling induced changes in the nanowire lengths versus their diameters may be taken as a de-facto measure of the protective shell quality. As less damage is incurred at each cycle, there is less SEI growth on the freshly exposed Si surfaces.

Since growth of SEI on pre-existing SEI is relatively slow, [78,79] the 3Sn/SiNWs are the least agglomerated, have optimum CE, the least amount of SEI, and the least delamination. Figure 4-10 shows the plan-view SEM micrographs of (a) SiNWs, (b) 1Sn/SiNWs, (c) 3Sn/SiNWs, and (d) 5Sn/SiNWs anodes after 100 cycles. The results agree with the cross-sectional data with the 3Sn/SiNWs electrodes being the least agglomerated with SEI while the bare SiNWs being the most.

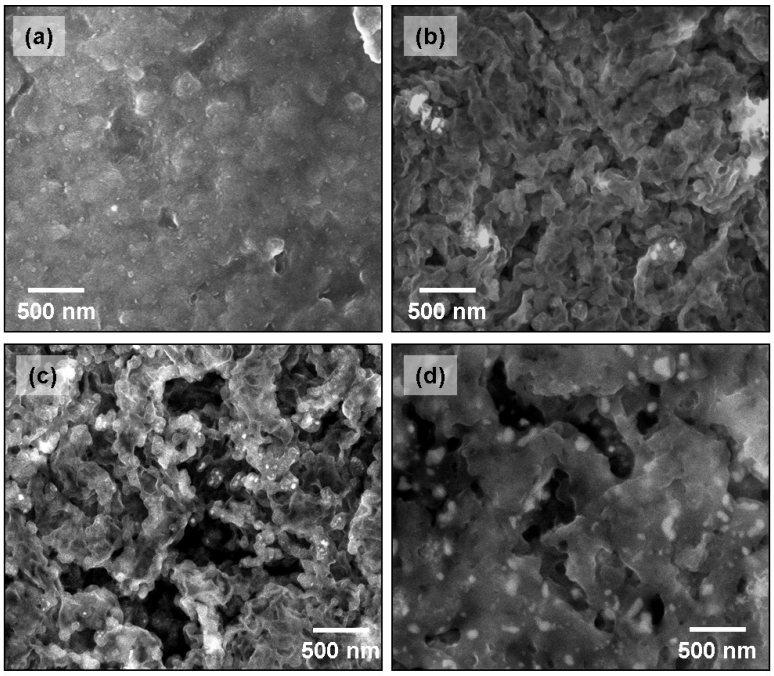

Figure 4-10: Plan-view SEM micrographs of (a) SiNWs, (b) 1Sn/SiNWs, (c) 3Sn/SiNWs, and (d) 5Sn/SiNWs anode materials after 100 cycles at 0.1C.

Figure 4-11 shows TOF-SIMS depth profiles of Li and Ti concentration through the thickness of the post-cycled (100 cycles at 0.1C) bare SiNWs and 3Sn/SiNWs, analyzed in their delithiated state. Since the samples were fully charged, any remnant Li must originate from the SEI layer rather than from the bulk of the Si. The Ti signal originates from the TiN diffusion barrier and marks the current collector – active electrode interface. For the case of bare SiNWs there is an enhanced Li signal at this interface. In fact, the actual Li segregation profile is actually sharper than what the TOF-SIMS results indicate since the current collector's inherent roughness will smear the measured through-thickness Ti and Li distributions. Notably the Li

profile in the Sn-coated specimens is much more uniform. We argue that accumulation of SEI (which is mostly composed of Li-containing compounds) near the interface is the major contributor to the *en-masse* delamination of the nanowire assembly from the underlying current collector. The TOF-SIMS results are in good agreement with this hypothesis and with the FIB observations. Moreover Li segregation Si has been demonstrated both experimentally and from theoretical studies. [80-82] Our group has also recently reported early (after 2 cycles) interfacial segregation of Na in the *bulk* of Sn thin films sitting on stainless steel current collectors. [83] The two phenomena - early segregation of Li and cycling-induced preferential SEI formation at the interface - may in fact be interrelated. Li (and Na) segregation is known to both elastically and plastically soften the material. This may result in more localized deformation during charging/discharging, and would potentially lead to more fresh Si being exposed to the electrolyte per cycle.

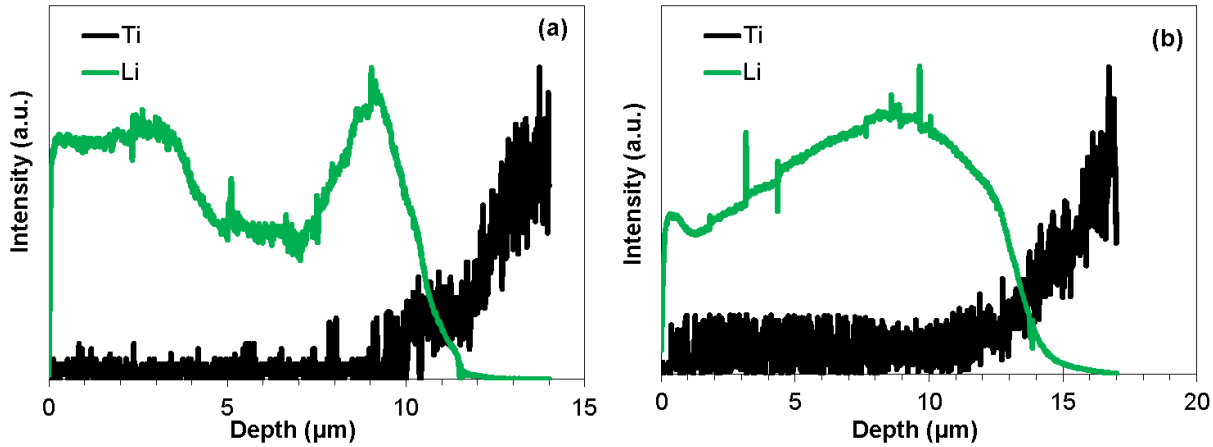

Figure 4-11: TOF-SIMS depth profiles of Li and Ti concentration through the thickness of delithiated (a) bare SiNWs and (b) 3Sn/SiNWs, after 100 cycles at 0.1C. The Ti signal originates from the TiN diffusion barrier and demarcates the active electrode – current collector interface.

The high-resolution XPS spectra of the post 100 cycles electrodes are shown in Figure 4-12. The individual panels show C 1s, O 1s, Li 1s, F 1s, Si 2p, Sn 3d, and P 2p spectra. The near-surface atomic composition (at.%) of each cycled electrode is shown in Table 4-3. These XPS results provide insight into the composition of the SEI layer that has built on the materials'

surface upon cycling, as a result of decomposition of the lithium salt and the reduction of organic solvents.

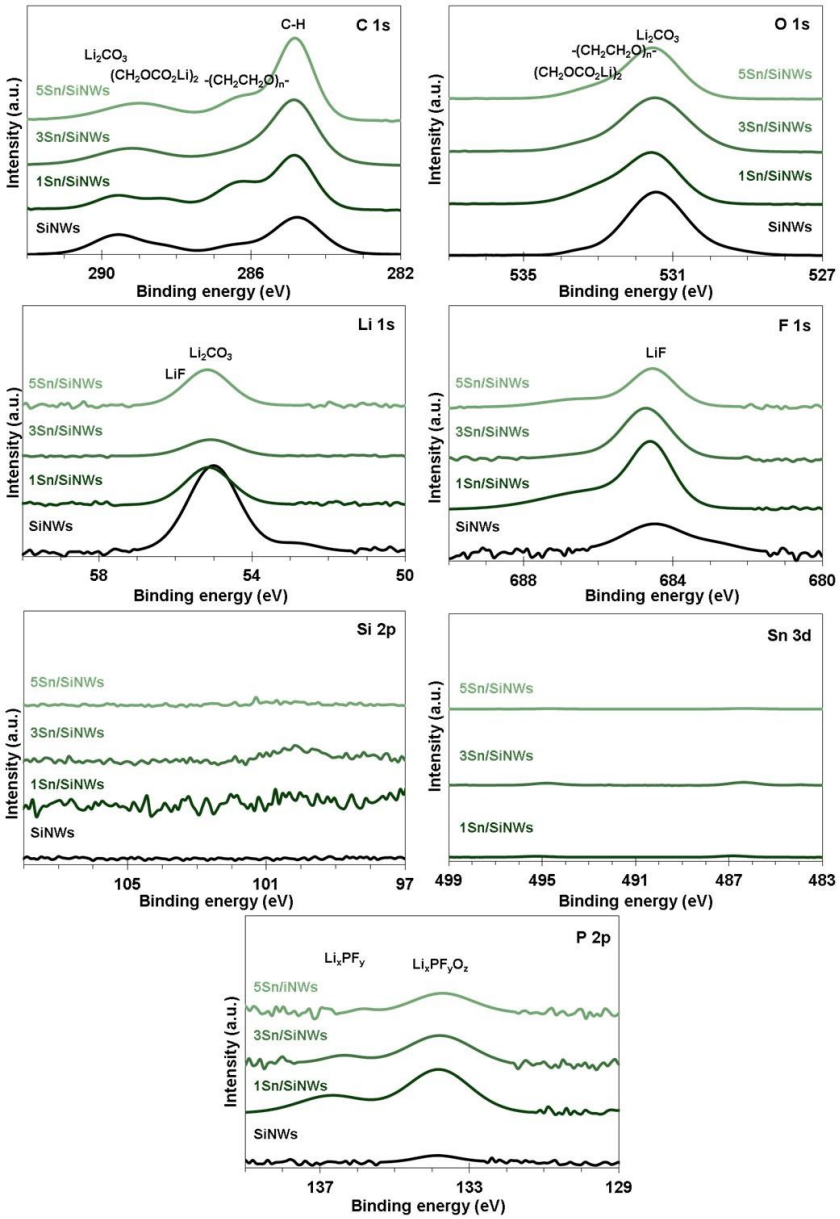

Figure 4-12: XPS spectra of the post 100 cycles electrodes, panels show C 1s, O 1s, Li 1s, F 1s, Si 2p, Sn 3d, and P 2p.

Table 4-3: The near-surface atomic composition (at.%) of each electrode after 100 cycles, analyzed in delithiated state.

Material	C	O	Si	Sn	Li	F	P
SiNWs	33.74	33.41	-	-	28.96	3.76	0.13
1Sn/SiNWs	34.94	34.83	0.05	0.12	21.73	4.85	3.48
3Sn/SiNWs	34.48	38.85	0.36	0.39	19.47	4.29	2.16
5Sn/SiNWs	34.91	33.89	-	-	25.46	3.83	1.91

The 1Sn/SiNWs and 3Sn/SiNWs electrodes still show both a Si and a Sn signal, indicating that the SEI layer in these structures is thinner than in baseline SiNWs and in 5Sn/SiNWs. In particular, the 3Sn/SiNWs shows the highest Si and Sn intensity, indicating that it has the thinnest SEI of all, which is in agreement with the FIB/SEM images, Figure 4-9 and Figure 4-10, and the charge transfer resistance values from the EIS plots, Figure 4-6(f). The higher amounts of C and O compared with F and P in all the materials indicates that the SEI layer formed chiefly through the reduction of solvent molecules, particularly EC. Lithium carbonate, Li_2CO_3, and lithium ethylene dicarbonate, $(CH_2OCO_2Li)_2$, are produced upon the electrochemical reduction of EC solvent. Polyethylene oxide (PEO), $-(CH_2CH_2O)_n-$, is another product of EC degradation. [84]

In C 1s spectra, the shoulder off the main hydrocarbon signal at about 286 – 287 eV is attributed to PEO. Lithium ethylene dicarbonate peak in C 1s appears at the binding energy of 288 – 289 eV. The peak associated with the Li_2CO_3 is located at about 290 eV. The O 1s spectra confirm the assignments made for C 1s spectra. The maximum intensity has a binding energy of around 531 – 532 eV for all the materials with a broad shoulder at higher binding energy of 532 – 534 eV. The main peak at ~ 531.5 eV represents Li_2CO_3 compound and the signals approximately located at 532.5 and 533.5 eV are associated with the PEO-like polymers and lithium ethylene dicarbonate, respectively. Presence of fluorine and phosphorous in the SEI film suggests that degradation of $LiPF_6$ salt occurred during cycling. LiF is the main compound formed upon degradation of $LiPF_6$ through either a chemical decomposition or a reaction in presence of water. Li 1s spectra also have a broad peak with the onset binding energy of 51.5 eV extended to 57 eV. This consists of a main peak at approximately 55.2 eV, corresponding to Li_2CO_3, and another peak at about 56 eV, for LiF. Correspondingly, the main peak in F 1s spectra at ~ 684.5 eV is assigned to LiF. [84] The main signal in P 2p is from $Li_xPF_yO_z$, produced

from the reaction of PF_5, formed upon chemical decomposition of $LiPF_6$ salt, with the contaminations and compounds in the cell. The XPS measurements indicate that the SEI layer consists mostly of Li_2CO_3 and LiF compounds. A CasaXPS software analysis of the Li 1s spectra reveals that the SEI would consist of 98, 89, 83, and 92% of Li_2CO_3, when we assumed that Li_2CO_3 and LiF are the only compounds appearing in the Li 1s spectra.

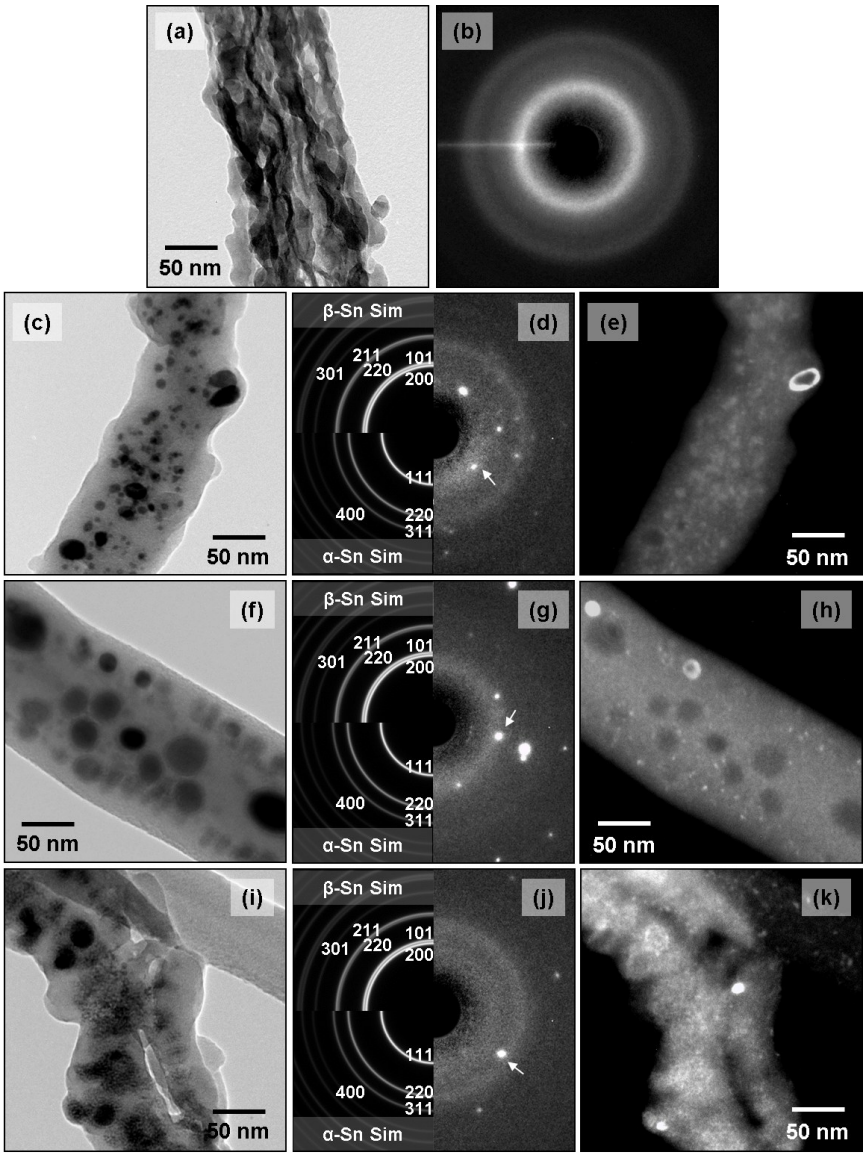

Figure 4-13: TEM micrographs of the post cycled electrodes: (a,b) SiNWs, (c-e) 1Sn/SiNWs, (f-h) 3Sn/SiNWs, and (i-k) 5Sn/SiNWs. The SAD patterns include the ring simulations for both α- and β-Sn. The dark-field images obtained from the arrowed part of the corresponding SAD patterns.

Figure 4-13 shows conventional TEM micrographs for the electrodes after 100 cycles of testing in delithiated charge state. As is well known the Si is amorphized after the first delithiation cycle. The structure of the post-cycled Sn, however, is ambiguous. While the interconnected Sn nanoparticles do retain their general morphology, it is difficult to conclude the degree of amorphization that has occurred as a result of cycling. It is known that delithiation converts the Li_xSn phases back to a mixture of α-Sn (space group of *Fd3m*, a_0 = 6.4912 Å) and β-Sn (both structures are simulated in the SAD overlay). [44,85] However these coatings are thinner than even the "nanostructures" reported in literature and are also mechanically stressed by the underlying Si during cycling. Thus in our opinion it is not possible to conclusively state from the electron diffraction patterns whether the majority final Sn sheath is amorphous, nanocrystalline, or a combination of the both. Moreover even if the Sn particles were 100% nanocrystalline, below a certain crystallite size they would appear "X-ray amorphous" in the SAD, displaying only continuous washed out rings. There are isolated spots in all the recorded SAD patterns that are indexable as either β-Sn or α-Sn. The Sn crystallites associated with the arrowed β-Sn or α-Sn spots are imaged in dark-field in the leftmost panels in the Figure.

The key observation from the above series of images is that the baseline SiNWs and the 5Sn/SiNWs have disintegrated into strands that run parallel to the nanowire axis. This failure mode has been shown to occur initially along [110] directions parallel to the nanowire length and along twin interfaces. [28,29] As the subsequently amorphous Si is additionally lithiation cycled, damage accumulates in the form of progressive crack growth, development of new pores, and SEI formation on fresh Si surfaces. [28,32,70] After cycling, the 1Sn/SiNWs and the 3Sn/SiNWs are much more intact, retaining close to their original geometry and showing minimal intra-wire porosity. This agrees with the cycling lifetime data and supports the argument for the effectiveness of Sn coatings with an optimum thickness. Overall the TEM-observed degree of damage (Figure 4-13) in the post cycled nanowires scales well with the cycling stability results: SiNWs > 5Sn/SiNWs > 1Sn/SiNWs > 3Sn/SiNWs. Although there is a concern regarding the mechanical integrity of the interface of heterogeneous structures, [75,76] our conventional post 100 cycle TEM analysis demonstrated that the dewetted Sn coating is still attached to the surface of the SiNWs. Moreover Sn experiences less drastic mechanical degradation in the course of Li alloying in comparison with Si. [86]

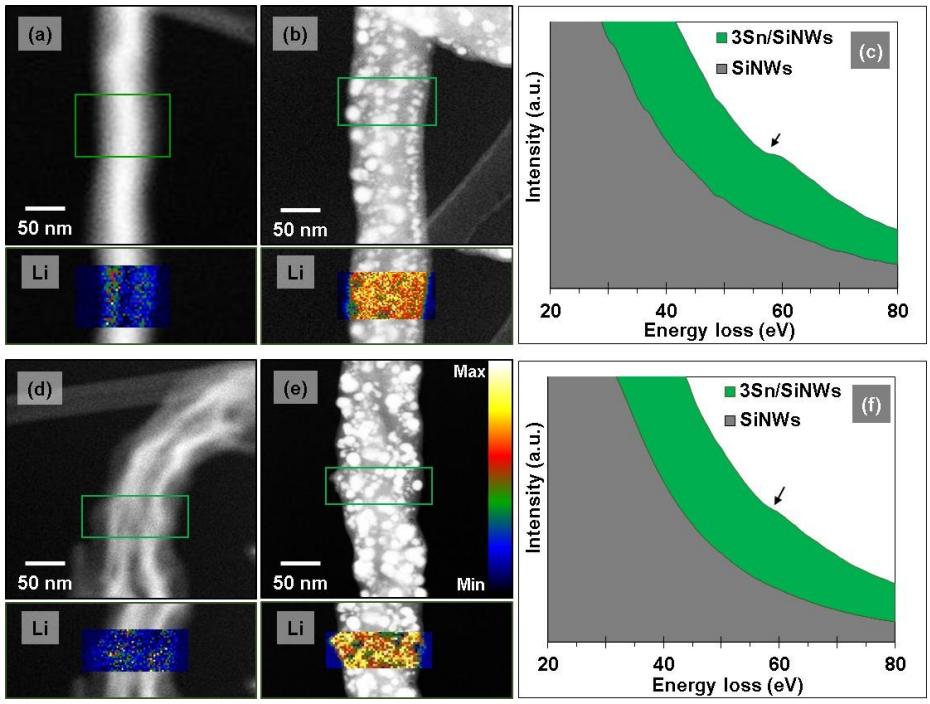

Figure 4-14: HAADF micrographs, EELS elemental maps of Li and corresponding low-loss EELS spectra obtained from the rectangular areas marked in the HAADF images for SiNWs and 3Sn/SiNWs at (a-c) 0.35 V during lithiation and (d-f) 0.52 V during delithiation.

We performed EELS analysis on partially lithiated and partially delithiated baseline SiNWs and 3Sn/SiNWs. The samples were analyzed after 10 cycles at 0.1C. A terminal voltage of 0.35 V was employed for partial lithiation, and 0.52 V for partial delithiation. The HAADF micrographs with the corresponding Li EELS maps are presented in Figure 4-14. Even after 10 cycles, some of the bare nanowires show evidence of lengthwise fragmentation (Figure 4-14(d)). A comparison between the Li maps for SiNWs and 3Sn/SiNWs at 0.35 V during lithiation shows that the nanocomposite holds significantly more Li than the bare SiNWs. This is further illustrated by the corresponding magnified low-loss spectra of the anodes, obtained from the green rectangular areas of the nanowires. The Li K-edge is more apparent in the 3Sn/SiNWs' spectra than that in the baseline SiNWs'. This is also evident by the ratio of Li concentration per unit volume in 3Sn/SiNWs to that in bare SiNWs, estimated from the low-loss spectra using the quantification approach presented in [87], which is 1.75 in average for partially lithiated specimens. Likewise, the EELS Li maps of SiNWs and 3Sn/SiNWs at 0.52 V during delithiation show a higher Li content in the coated nanowire. The Li K-edge in the low-loss spectra of the partially

delithiated specimens also highlight this distinction. The average ratio of Li concentration in partially delithiated 3Sn/SiNWs to that in SiNWs is 2.48.

Combining these EELS observations with the CV and CC data shown in Figure 4-5, one can conclude that upon discharge the Sn coating will lithiate first, i.e. at a higher voltage. Moreover, the CV and CC results show that upon charging Sn layer will remain lithiated up to higher voltages than Si, with the last plateau for Sn being near 0.8 V vs. about 0.4 V for Si. Thus Sn coating expands first upon lithium insertion, applying a compressive stress to the SiNWs. As the lithiation reaction proceeds the increasing Li content in the Li_xSn phases gives larger volume expansion to the Sn shell.

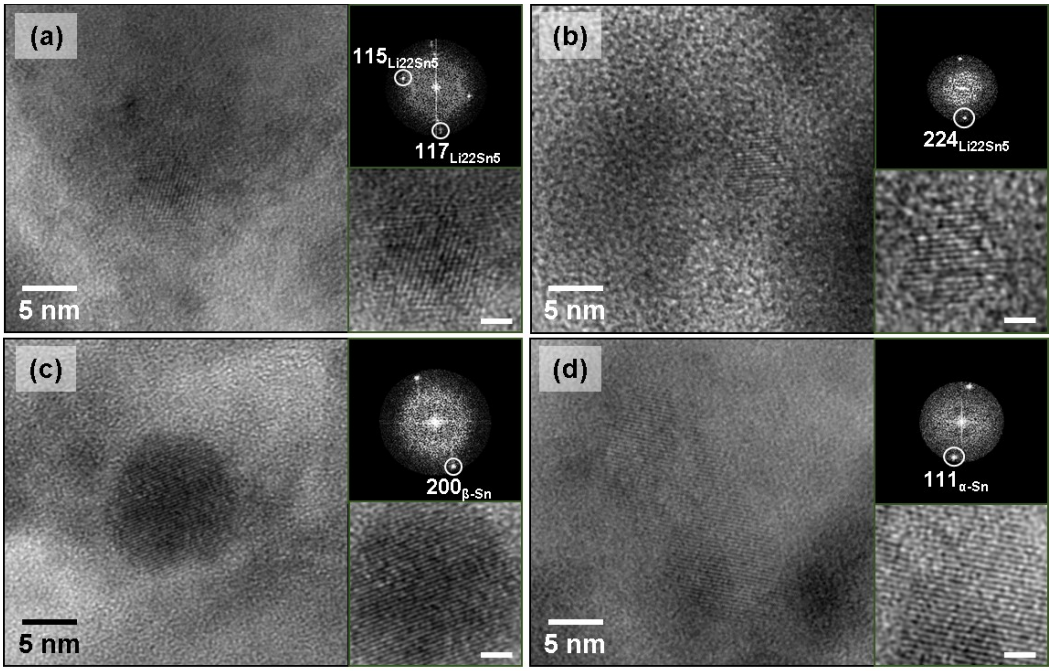

Figure 4-15: HRTEM micrographs of 3Sn/SiNWs with the corresponding FFT patterns after 10 cycles at 0.1C. (a,b) fully lithiated at 0.01 V and (c,d) fully delithated at 2 V vs. Li/Li^+. Magnified images of the fringes in the HRTEM micrographs are shown in the inset of each micrograph. The scale bar in the high magnification insets is 2 nm.

Figure 4-15 shows HRTEM micrographs of 3Sn/SiNWs in fully lithiated and fully delithiated state. The FFT patterns of the fully lithiated electrode shows the presence of fringes associated with the $Li_{22}Sn_5$ phase (space group of *F23*, a_0 = 19.214 Å). This indicates that the

fully lithiated $Li_{15}Si_4$ (volume expansion ~ 280% relative to pure Si) is surrounded by a $Li_{22}Sn_5$ shell (volume expansion of ~ 260% relative to Sn). As such differential volume expansions may not be accommodated purely elastically, there should be a substantial plastic flow in both phases. Moreover recent modeling and experimental work has demonstrated that substantial elastic softening will occur in both Sn and Si upon lithiation, [88,89] which would influence both the elastic response and plastic flow. The HRTEM images of the fully delithiated electrode demonstrate a mix of α-Sn and β-Sn, consistent with the conventional TEM micrographs of the post 100 cycles specimens (Figure 4-13).

It is instructive to compare the performance of our Sn/SiNWs electrodes with other composite SiNWs-based anode systems reported in scientific literature. Table 4-4 displays the electrochemical performance of our best performing electrode material (3Sn/SiNWs) along with previously reported results for core-shell architectures including SiNWs coated by Al, [37] Mg and Mg_2Si, [32] ALD TiO_2, [39] ALD TiN, [40] carbon, [90-92] copper, [90] conductive polymer (PEDOT), [93] silicon nanoparticles, [94] nitrogen-doped graphite, [95] and amorphous silicon. [96] These studies all aimed to improve the long-term galvanostatic cycling performance of SiNWs LIB anodes by some form of a surface coating strategy. From the listed data, it can be concluded that the nanometer-scale Sn coatings represent a highly effective approach for both improving the cycling capacity retention and the coulombic efficiency, the improvement in the CE being especially noteworthy.

Finally, we believe that ductile electrically conductive mesh coatings are an effective strategy for improving the performance of a range of powder-like active materials, which could be scaled for commercial applications. Batch magnetron sputter coating of powders is feasible given a system with a sputter-down configuration and a vibrating powder hopper as a sample holder. Moreover, the coating strategy may not necessarily involve magnetron sputtering. Approaches such as chemical vapor deposition, atomic layer deposition, electrochemical and electroless plating, are all scalable for coating relatively large quantities of powders. Early work by researchers like Dahn et al. have demonstrated the feasibility of these methods for improving the cycling lifetime of both anode and cathode materials, many of which have approached commercial viability. [97,98]

Table 4-4: Comparison of capacity and coulombic efficiency of our best performing anode with previously published different coated SiNWs anode materials at different rates.

SiNWs synthesis method	Average nanowire diameter (length)	Coating material	Potential window (V) vs. Li/Li^+	Cycling rate	Cycle number	Specific capacity (mAh/g)	Coulombic efficiency (%)	Rate capability in mAh/g (cycling rate)	Ref.
Au catalyzed VLS[a]-CVD	114 nm (12 μm)	*Sn*	0.01 – 2	0.1C	*1* *100*	*3192* *1874*	*90.1* *99.5*	*850 (5C)*	*This work*
		Al			1 100	3347 1300	92.8 ~ 99	N/A[b]	37
		Mg			1 100	3209 ~ 980	95.8 ~ 99.2	229 (5C)	32
		Mg_2Si			1 100	3089 ~ 844	93.1 ~ 97.7	144 (5C)	
		ALD TiO_2			1 100	~ 3000 1600	~ 90 ~ 99.5	1020 (5C)	39
		ALD TiN			1 100	2915 1566	89 97.6	740 (5C)	40
	100 nm (N/A)	Carbon	0.02 – 2	0.05C (210 mA/g)	1 15	3702 2776	83.2 N/A	3201 (0.5C)	90
		Copper			1 15	2967 2561	90.3 N/A	3061 (0.5C)	
	200 nm (N/A)	Conductive polymer (PEDOT)	0.01 – 1	0.2C (840 mA/g)	2 100	3263 2510	N/A N/A	N/A	93
	100 nm (10 μm)	Si nanoparticles	0.05 – 1	0.2C (800 mA/g)	1 30	~ 1670 1600	81 ~ 99	N/A	94
Metal-assisted chemical etching	20 – 300 nm (90 μm)	Carbon	0.02 – 2	~ 0.04C (150 mA/g)	1 40	3344 1326	84 ~ 95	~ 2100 (0.07C or 300 mA/g)	91
	80 nm (7 μm)	N-doped graphite	0.01 – 1	~ 0.14C (600 mA/g)	1 45	2140 1260	92 > 99	N/A	95
VS[c]-CVD	N/A (N/A)	Amorphous silicon	0.01 – 2	0.2C (850 mA/g)	1 30	2500 1975	80.4 98	N/A	96
			0.15 – 2		1 100	1060 901	86.2 ~ 98.5	~ 800 (1.6C or 6800 mA/g)	
SBA-15 template	6.5 nm (20 nm)	Carbon	0 – 1.5	0.2C (600 mA/g)	1 80	3161 2750	86 98	2466 (2C)	92

[a] Vapor-Liquid-Solid, [b] Not available, [c] Vapor-Solid

4.4 Conclusions

Silicon nanowire - based lithium ion battery anodes suffer from cyclability issues associated with the ~ 280% lithiation driven volume change. Here we demonstrate that a thin partially dewetted surface film of physical vapor deposited lithium-active Sn will significantly improve

their performance. The optimum architecture employed Sn coating with an average thickness of 3 nm. This electrode maintained a reversible capacity of 1865 mAh/g after 100 cycles at 0.1C, almost double that of the bare SiNWs that degraded to 1046 mAh/g. Furthermore, these nanocomposites offered 2X the capacity retention of bare SiNWs at a high current density of 5C, and demonstrated a cycling coulombic efficiency of > 99.3% vs. 94 - 98% for the baseline. Using HRTEM combined with EELS TEM, FIB SEM, and TOF-SIMS analysis we elucidate the phenomenology by which the Sn boosts cycling performance. The electrochemical data combined with EELS maps of partially lithiated/delithiated bare and Sn-coated SiNWs show that the Sn coating lithiates first during discharge. Moreover, CV and CC results show that Sn will fully delithiate at a higher voltage than Si upon charging. The compressive stress induced by the Li_xSn quasi-shell then confines the radial expansion of the core nanowire in favor of longitudinal expansion, reducing the concomitant mechanical failure and SEI growth associated with the well-known stranding phenomena of 1D Si nanostructures. The findings of our study should provide a broadly applicable design methodology for nanoscale coatings employed to improve the cycling performance of a variety of LIB anode materials.

4.5 References

1 B. Dunn, H. Kamath, and J. –M. Tarascon. Science, 2011, 334, 928-935.

2 V. Etacheri, R. Marom, R. Elazari, G. Salitra, and D. Aurbach. Energy Environ. Sci., 2011,4, 3243-3262

3 J. Liu. Adv. Funct. Mater., 2013, 23, 924-928.

4 Q. Gao, G. Meng, A. Nie, F. Mashayek, C. Wang, G. M. Odegard, and R. S. Yassar. Chem. Mater., 2014, 26, 1660–1669.

5 A. Mauger, and C. Julien. Ionics, 2014, 20, 751-787.

6 M. R. Zamfir, H. T. Nguyen, E. Moyen, Y. H. Lee, and D. Pribat. J. Mater. Chem. A, 2013, 1, 9566-9586.

7 U. Kasavajjula, C. Wang, and A. J. Appleby. J. Power Sources, 2007, 163, 1003-1039.

8 S. Sim, P. Oh, S. Park, and J. Cho. Adv. Mater., 2013, 25, 4498-4503.

9 Y. Liu, X. Guo, J. Li, Q. Lv, T. Ma, W. Zhu, and X. Qiu. J. Mater. Chem. A, 2013, 1, 14075-14079.

10 X. Huang, H. Pu, J. Chang, S. Cui, P. B. Hallac, J. Jiang, P. T. Hurley, and J. Chen. ACS Appl. Mater. Interfaces, 2013, 5, 11965-11970.

11 X. H. Liu, L. Q. Zhang, L. Zhong, Y. Liu, H. Zheng, J. W. Wang, J. –H. Cho, S. A. Dayeh, S. T. Picraux, J. P. Sullivan, S. X. Mao, Z. Z. Ye, and J. Y. Huang. Nano Lett., 2011, 11, 2251-2258.

12 C. R. Becker, K. E. Strawhecker, Q. P. McAllister, and C. A. Lundgren. ACS Nano, 2013, 7, 9173-9182.

13 X. Su, Q. Wu, J. Li, X. Xiao, A. Lott, W. Lu, B. W. Sheldon, and J. Wu. Adv. Energy Mater., 2014, 4, 1-23.

14 X. H. Liu, J. W. Wang, S. Huang, F. Fan, X. Huang, Y. Liu, S. Krylyuk, J. Yoo, S. A. Dayeh, A. V. Davydov, S. X. Mao, S. T. Picraux, S. Zhang, J. Li, T. Zhu, and J. Yu Huang. Nat. Nanotechnol., 2012, 7, 749-756.

15 H. Ghassemi, M. Au, N. Chen, P. A. Heiden, and R. S. Yassar. ACS Nano, 2011, 5, 7805–7811.

16 N. Li, S. Jin, Q. Liao, H. Cui, and C. X. Wang. Nano Energy, 2014, 5, 105-115.

17 N. Liu, W. Li, M. Pasta, and Y. Cui. Front. Phys., 2014, 9, 323-350.

18 S. A. Klankowski, R. A. Rojeski, B. A. Cruden, J. Liu, J. Wu, and J. Li. J. Mater. Chem. A, 2013, 1, 1055-1064.

19 M. W. Forney, R. A. DiLeo, A. Raisanen, M. J. Ganter, J. W. Staub, R. E. Rogers, R. D. Ridgley, and B. J. Landi. J. Power Sources, 2013, 228, 270-280.

20 J. Wan, A. F. Kaplan, J. Zheng, X. Han, Y. Chen, N. J. Weadock, N. Faenza, S. Lacey, T. Li, J. Guo, and L. Hu. J. Mater. Chem. A, 2014, 2, 6051-6057.

21 S. Choi, J. C. Lee, O. Park, M. J. Chun, N. S. Choi, and S. Park. J. Mater. Chem. A, 2013, 1, 10617-10621.

22 P. R. Abel, A. M. Chockla, Y. M. Lin, V. C. Holmberg, J. T. Harris, B. A. Korgel, A. Heller, and C. B. Mullins. ACS Nano, 2013, 7, 2249-2257.

23 E. Memarzadeh Lotfabad, P. Kalisvaart, A. Kohandehghan, K. Cui, M. Kupsta, B. Farbod, and D. Mitlin. J. Mater. Chem. A, 2014, 2, 2504-2516.

24 J. Guo, Z. Yang, and L. A. Archer. J. Mater. Chem. A, 2013, 1, 5709-5714.

25 M. W. Forney, M. J. Ganter, J. W. Staub, R. D. Ridgley, and B. J. Landi. Nano Lett., 2013, 13, 4158–4163.

26 J. H. Cho, and S. T. Picraux. Nano Lett., 2013, 13, 5740–5747.

27 J. H. Cho, X. Li, and S. T. Picraux. J. Power Sources, 2012, 205, 467-473.

28 X. H. Liu, H. Zheng, L. Zhong, S. Huang, K. Karki, L. Q. Zhang, Y. Liu, A. Kushima, W. T. Liang, J. W. Wang, J. H. Cho, E. Epstein, S. A. Dayeh, S. T. Picraux, T. Zhu, J. Li, J. P. Sullivan, J. Cumings, C. Wang, S. X. Mao, Z. Z. Ye, S. Zhang, and J. Y. Huang. Nano Lett., 2011, 11, 3312–3318.

29 H. Yang, S. Huang, X. Huang, F. Fan, W. Liang, X. H. Liu, L. Q. Chen, J. Y. Huang, J. Li, T. Zhu, and S. Zhang. Nano Lett., 2012, 12, 1953–1958.

30 P. Johari, Y. Qi, and V. B. Shenoy. Nano Lett., 2011, 11, 5494–5500.

31 K. Karki, E. Epstein, J. H. Cho, Z. Jia, T. Li, S. T. Picraux, C. Wang, and J. Cumings. Nano Lett., 2012, 12, 1392–1397.

32 A. Kohandehghan, P. Kalisvaart, M. Kupsta, B. Zahiri, B. Shalchi Amirkhiz, Z. Li, E L. Memarzadeh, L. A. Bendersky, and D. Mitlin. J. Mater. Chem. A, 2013, 1, 1600-1612.

33 H. Wu, G. Yu, L. Pan, N. Liu, M. T. McDowell, Z. Bao, and Y. Cui. Nat. Commun., 2013, 4, 1-6.

34 J. Li, C. Yue, Y. Yu, Y. S. Chui, J. Yin, Z. Wu, C. Wang, Y. Zang, W. Lin, J. Li, S. Wu, and Q. Wu. J. Mater. Chem. A, 2013, 1, 14344-14349.

35 M. T. McDowell, S. W. Lee, C. Wang, and Y. Cui. Nano Energy, 2012, 1, 401-410.

36 S. Murugesan, J. T. Harris, B. A. Korgel, and K. J. Stevenson. Chem. Mater., 2012, 24, 1306–1315.

37 E. L. Memarzadeh, W. P. Kalisvaart, A. Kohandehghan, B. Zahiri, C. M. Holt, and D. Mitlin. J. Mater. Chem., 2012, 22, 6655-6668.

38 Y. Yu, L. Gu, C. Zhu, S. Tsukimoto, P. A. van Aken, and J. Maier. Adv. Mater., 2010, 22, 2247-2250.

39 E. Memarzadeh Lotfabad, P. Kalisvaart, K. Cui, A. Kohandehghan, M. Kupsta, B. Olsen, and D. Mitlin. Phys. Chem. Chem. Phys., 2013, 15, 13646-13657.

40 A. Kohandehghan, P. Kalisvaart, K. Cui, M. Kupsta, E. Memarzadeh, and D. Mitlin. J. Mater. Chem. A, 2013, 1, 12850-12861.

41 D. Tang, R. Yi, M. L. Gordin, M. Melnyk, F. Dai, S. Chen, J. Song, and D. Wang. J. Mater. Chem. A, 2014, 2, 10375-10378.

42 H. T. Nguyen, M. R. Zamfir, L. D. Duong, Y. H. Lee, P. Bondavalli, and D. Pribat. J. Mater. Chem., 2012, 22, 24618-24626.

43 G. Jeong, J. G. Kim, M. S. Park, M. Seo, S. M. Hwang, Y. U. Kim, Y. J. Kim, J. H. Kim, and S. X. Dou. ACS Nano, 2014, 8, 2977–2985.

44 L. Xu, C. Kim, A. K. Shukla, A. Dong, T. M. Mattox, D. J. Milliron, and J. Cabana. Nano Lett., 2013, 13, 1800–1805.

45 J. Guo, Z. Yang, and L. A. Archer. J. Mater. Chem. A, 2013, 1, 8710-8715.

46 C. Yue, Y. Yu, J. Yin, T. Wong, Y. Zang, J. Li, and J. Kang. J. Mater. Chem. A, 2013, 1, 7896-7904.

47 W. Ren, C. Wang, L. Lu, D. Li, C. Cheng and J. Liu. J. Mater. Chem. A, 2013, 1, 13433-13438.

48 L. Zhang, C. M. Holt, E. J. Luber, B. C. Olsen, H. Wang, M. Danaie, X. Cui, X. Tan, V. W. Lui, W. P. Kalisvaart, and D. Mitlin. J. Phys. Chem. C, 2011, 115, 24381–24393.

49 R. F. Egerton, Electron energy-loss spectroscopy in the electron microscope, Springer, New York, 3rd edition, 2011.

50 Tadeusz Bronislaw Massalski, Hiroaki Okamoto, Linda Kacprzak, and P.R. Subramanian, Binary Alloy Phase Diagrams, American society for metals, 2nd edition, 1990.

51 E. J. Luber, B. C. Olsen, C. Ophus, and D. Mitlin. Phys. Rev. B, 2010, 82, 085407.

52 W. W. Mullins. J. Appl. Phys., 1957, 28, 333-339.

53 C. Ophus, T. Ewalds, E. J. Luber, and D. Mitlin. Acta Materialia, 2010, 58, 5150-5159.

54 D. Mitlin, A. Misra, V. Radmilovic, M. Nastasi, R. Hoagland, D. J. Embury, J. P. Hirth, and T. E. Mitchell. Philosophical Magazine, 2004, 84, 719-736.

55 M. Gu, Z. Wang, J. G. Connell, D. E. Perea, L. J. Lauhon, F. Gao, and C. Wang. ACS Nano, 2013, 7, 6303-6309.

56 I. A. Courtney, and J. R. Dahn. J. Electrochem. Soc., 1997, 144, 2045-2052.

57 D. Wang, J. Yang, J. Liu, X. Li, R. Li, M. Cai, T. K. Sham, and X. Sun. J. Mater. Chem. A, 2014, 2, 2306-2312.

58 X. Li, X. Meng, J. Liu, D. Geng, Y. Zhang, M. N. Banis, Y. Li, J. Yang, R. Li, X. Sun, M. Cai, M. W. Verbrugge. Adv. Funct. Mater., 2012, 22, 1647–1654.

59 I. A. Courtney, and J. R. Dahn. J. Electrochem. Soc., 1997, 144, 2943-2948.

60 D. Wang, X. Li, J. Yang, J. Wang, D. Geng, R. Li, M. Cai, T.-K. Sham, and X. Sun. Phys. Chem. Chem. Phys., 2013, 15, 3535-3542.

61 S. K. Soni, B. W. Sheldon, X. Xiao, and A. Tokranov. Scripta Materialia, 2011, 64, 307-310.

62 S. K. Soni, B. W. Sheldon, X. Xiao, A. F. Bower, and M. W. Verbrugge. J. Electrochem. Soc., 2012, 159, A1520-A1527.

63 A. Nie, L. Y. Gan, Y. Cheng, H. A. Ardakani, Q. Li, C. Dong, R. Tao, F. Mashayek, H. T. Wang, U. Schwingenschlögl, R. F. Klie, and R. S. Yassar. ACS Nano, 2013, 7, 6203-6211.

64 H. Zheng, Y. Liu, S. X. Mao, J. Wang, and J. Y. Huang. Sci. Rep., 2012, 2, 1-4.

65 M. T. McDowell, and Y. Cui. Adv. Energy Mater., 2011, 1, 894-900.

66 M. D. Levi, and D. Aurbach. J. Phys. Chem. B, 1997, 101, 4630–4640.

67 D. Aurbach, B. Markovsky, M. D. Levi, E. Levi, A. Schechter, M. Moshkovich, and Y. Cohen. J. power sources, 1999, 81-82, 95-111.

68 D. Aurbach. J. Power Sources, 2000, 89, 206-218.

69 V. Etacheri, U. Geiger, Y. Gofer, G. A. Roberts, I. C. Stefan, R. Fasching, and D. Aurbach. Langmuir, 2012, 28, 6175–6184.

70 K. Xu, and A. V. Cresce. J. Mater. Chem., 2011, 21, 9849-9864.

71 D. Liu, and G. Cao. Energy Environ. Sci., 2010, 3, 1218-1237.

72 K. Karki, Y. Zhu, Y. Liu, C. F. Sun, L. Hu, Y. Wang, C. Wang, and J. Cumings. ACS Nano, 2013, 7, 8295–8302.

73 C. K. Chan, R. Ruffo, S. S. Hong, and Y. Cui. J. Power Sources, 2009, 189, 1132-1140.

74 X. Xiao, P. Lu, and D. Ahn. Adv. Mater., 2011, 23, 3911-3915.

75 M. Gu, Y. Li, X. Li, S. Hu, X. Zhang, W. Xu, S. Thevuthasan, D. R. Baer, J. G. Zhang, J. Liu, and C. Wang. ACS Nano, 2012, 6, 8439–8447.

76 H. Liao, K. Karki, Y. Zhang, J. Cumings, and Y. Wang. Adv. Mater., 2011, 23, 4318-4322.

77 L. Q. Zhang, X. H. Liu, Y. Liu, S. Huang, T. Zhu, L. Gui, S. X. Mao, Z. Z. Ye, C. M. Wang, J. P. Sullivan, and J. Y. Huang. ACS Nano, 2011, 5, 4800-4809.

78 V. Etacheri, O. Haik, Y. Goffer, G. A. Roberts, I. C. Stefan, R. Fasching, and D. Aurbach. Langmuir, 2012, 28, 965–976.

79 R. Elazari, G. Salitra, G. Gershinsky, A. Garsuch, A. Panchenko, and D. Aurbach. J. Electrochem. Soc., 2012, 159, A1440-A1445.

80 D. Santhanagopalan, D. Qian, T. McGilvray, Z. Wang, F. Wang, F. Camino, J. Graetz, N. J. Dudney, and Y. S. Meng. J. Phys. Chem. Lett., 2014, 5, 298–303.

81 M. E. Stournara, X. Xiao, Y. Qi, P. Johari, P. Lu, B. W. Sheldon, H. Gao, and V. B. Shenoy. Nano Lett., 2013, 13, 4759–4768.

82 M. Mortazavi, J. Deng, V. B. Shenoy, and N. V. Medhekar. J. Power Sources, 2013, 225, 207-214.

83 B. Farbod, K. Cui, W. P. Kalisvaart, M. Kupsta, B. Zahiri, A. Kohandehghan, E. Memarzadeh, Z. Li, E. J. Luber, and D. Mitlin. ACS Nano, 2014, 8, 4415–4429.

84 B. Philippe, R. Dedryvère, M. Gorgoi, H. Rensmo, D. Gonbeau, and K. Edström. Chem. Mater., 2013, 25, 394–404.

85 H. S. Im, Y. J. Cho, Y. R. Lim, C. S. Jung, D. M. Jang, J. Park, F. Shojaei, and H. S. Kang. ACS Nano, 2013, 7, 11103–11111.

86 K. Li, H. Xie, J. Liu, Z. Ma, Y. Zhou, and D. Xue. Phys. Chem. Chem. Phys., 2013, 15, 17658-17663.

87 P. J. Thomas, and P. A. Midgley. Top. Catal., 2002, 21, 109-138.

88 V. B. Shenoy, P. Johari, and Y. Qi. J. Power Sources, 2010, 195, 6825–6830.

89 M. E. Stournara, P. R. Guduru, and V. B. Shenoy. J. Power Sources, 2012, 208, 165–169.

90 H. Chen, Y. Xiao, L. Wang, and Y. Yang. J. Power Sources, 2011, 196, 6657-6662.

91 R. Huang, X. Fan, W. Shen, and J. Zhu. Appl. Phys. Lett., 2009, 95, 133119-133119.

92 H. Kim, and J. Cho. Nano Lett., 2008, 8, 3688-3691.

93 Y. Yao, N. Liu, M. T. McDowell, M. Pasta, and Y. Cui. Energy Environ. Sci., 2012, 5, 7927-7930.

94 L. Hu, H. Wu, S. S. Hong, L. Cui, J. R. McDonough, S. Bohy, and Y. Cui. Chem. Commun., 2011, 47, 367-369.

95 Y. J. Cho, H. S. Kim, H. Im, Y. Myung, G. B. Jung, C. W. Lee, J. Park, M. H. Park, J. Cho, and H. S. Kang. J. Phys. Chem. C, 2011, 115, 9451-9457.

96 L. F. Cui, R. Ruffo, C. K. Chan, H. Peng, and Y. Cui. Nano Lett., 2008, 9, 491-495.

97 Z. Chen, and J. R. Dahn. Electrochem. Solid-State Lett., 2003, 6, A221-A224.

98 S. D. Beattie, and J. R. Dahn. J. Electrochem. Soc., 2003, 150, A894-A898.

Chapter 5: Activation with Li Enables Facile Sodium Storage in Germanium

Material in this chapter has been published in:

Kohandehghan, Alireza, Kai Cui, Martin Kupsta, Jia Ding, Elmira Memarzadeh, Peter Kalisvaart, and David Mitlin. "Activation with Li Enables Facile Sodium Storage in Germanium." Nano Lett., 2014, 14 (10), pp 5873–5882

5.1 Abstract

Germanium is a promising sodium ion battery anode material that is held back by its extremely sluggish kinetics and poor cyclability. We are the first to demonstrate that activation by a single lithiation - delithiation cycle leads to a dramatic improvement in the practically achievable capacity, in rate capability, and in cycling stability of Ge nanowires (GeNWs) and Ge thin film (GeTF). TEM and TOF-SIMS analysis shows that without activation, the initially single crystal GeNWs are effectively Na inactive, while the 100 nm amorphous GeTF sodiates only partially and inhomogeneously. Activation with Li induces amorphization in GeNWs reducing the barrier for nucleation of the Na_xGe phase(s), and accelerates solid-state diffusion that aids the performance of both GeNWs and GeTF. Low rate (0.1C) Li activation also introduces a dense distribution of nanopores that lead to further improvements in the rate capability, which is ascribed to the lowered solid-state diffusion distances caused by the effective thinning of the Ge walls and by an additional Na diffusion path via the pore surfaces. The resultant kinetics are promising: Tested at 0.15C (1C = 369 mA/g, i.e. Na:Ge 1:1) for 50 cycles the GeNWs and GeTF maintain a reversible (desodiation) capacity of 346 mAh/g and 418 mAh/g, respectively. They also demonstrate a capacity of 355 and 360 mAh/g at 1C and 284 and 310 mAh/g at 4C. Even at a very high rate of 10C the GeTF delivers 169 mAh/g. Preliminary results demonstrate that Li activation is also effective in promoting cycling stability of Sb blanket films.

5.2 Introduction

Sodium ion batteries (NIBs) are an intriguing alternative to LIBs because of sodium's lower cost, as well as its geographically wider spread terrestrial reserves with overall much higher natural abundance. [1,2,3] Since graphite can't intercalate Na (but can Li), scientific attention is often directed to various non-graphitic carbons. [4,5,6,7,8,9,10,11] Potential non-carbon NIB anode materials include amorphous, anatase, and hollandaite TiO_2, [12,13,14,15] $Na_2Ti_3O_7$, [16] $Li_4Ti_5O_{12}$, [17] Sn and Sb - based nanocomposites, [18,19] mesoporous $FePO_4$, [20] and Ti_3C_2. [21] Sodium can alloy with several metallic elements including Sn, Sb, Pb, P, and Bi with theoretical specific capacities of 847 ($Na_{15}Sn_4$), 660 (Na_3Sb), 484 ($Na_{15}Pb_4$), 2596 (Na_3P), and 385 mAh/g (Na_3Bi), respectively. [22,23,24] However, there is a large volume change (250 - 410%) associated with the Na alloying/dealloying reaction in these materials. The volume change upon sodiation, and the concomitant elastic softening of the matrix material, [25] leads to mechanical damage of the electrode and a relatively rapid cycling-induced capacity fade.

One approach for reducing the extent of the rapid capacity fade problem is to employ composite nanostructures that buffer the volume change by introducing a secondary active or inactive matrix. Examples include employing natural wood fiber as a mechanical buffer for Sn, [26] FeS_2 conversion electrodes, [27] Sn_4P_3 - carbon nanocomposites, [28] monodisperse Sb nanocrystals, [29] Sn nanoparticles with conductive polymer binder, [30] nano-Se-impregnated mesoporous carbons, [31] Fe_2O_3 nanocrystals anchored onto graphene nanosheets, [32] SnO_2@MWCNT nanocomposites, [33] layered SnS_2-reduced graphene oxide, [34] commercial microsized red phosphorous and CNTs composite, [35] amorphous phosphorous/carbon nanocomposite, [36] Sb nanoparticles embedded in the carbon nanofibers, [37] Sb_2S_3 coated graphene, [38] microstructure engineered alloys such as Mo_3Sb_7, Sn-Ge, and Sn-Ge-Sb, [39,40,41] and MoS_2. [42] Another methodology involves creating 1D nanostructures with empty space that similarly buffers the volumetric expansion. Materials in this class include hollow carbon nanowires, [43] 3D nanoforests of C/Sn/Ni/TMV1cys, [44] and $Na_4Mn_9O_{18}$ nanowires. [45]

Germanium is a promising NIB anode material, having been experimentally demonstrated to electrochemically react with Na to slightly beyond a 1:1 atomic ratio (NaGe, 369 mAh/g) for pure Ge, [46,47,48] as well as substantially above 1:1 for alloyed Ge. [40] However cycling and rate

capability of Ge with Na remains limited, being effectively negligible for coarser structures such as powders. [49] Delithiation is well known to introduce nanoporosity into a range of insertion and conversion anode materials, including Si and Ge - based films, nanowires, nanotubes, nanoparticulates, etc. [50,51] Our original hypothesis was that by a single round of lithiation/delithiation prior to Na testing, we could drastically modify germanium's NIB performance in a positive manner. This could be achieved by reducing the Na solid-state diffusion distance via the introduction of nanopores that would be wetted by the electrolyte. Sluggish solid-state diffusion of Na is known to plague NIB anodes and generally makes them inferior to their LIB counterparts. [52] What we discovered was that a secondary essential feature necessary for successful Na storage is that the Ge electrode is fully amorphous. This conclusion was reached by considering the complete inability to sodiate the pristine single crystal Ge nanowires, which possessed dimensions that were finer than the amorphous as-deposited Ge films that did charge albeit poorly.

5.3 Experimental section

GeNWs arrays were synthesized in a low-pressure CVD tube furnace (Tystar, Inc.). The arrays were grown directly onto mirrored-finished (polished down to 1 μm) 316L stainless steel spacers (MTI Corporation) with diameter of 15.4 mm covered with 50 nm Ti adhesion and 100 nm TiN diffusion barrier layers. Prior to nanowire growth, in order to de-wet the 10 nm Au catalyst film the samples were annealed at 320 ºC under vacuum for one hour. A 1:4 mixture of GeH_4: H_2 was utilized as the working gas with the total pressure of 100 Torr, with growth being done at 320 ºC for 2 minutes. The average GeNWs mass loading was 0.2212 mg, measured with a Mettler Toledo MX5 microbalance (0.1 μg resolution). A series of 100 nm thick Ge films (0.0865 mg average mass loading) were deposited at nominally ambient temperature onto polished (P-4000 SiC) stainless steel spacers using RF-magnetron sputtering (max. base pressure of 5×10^{-8} Torr).

We employed 2032 button half-cells versus Li or Na metal (MTI). Li activation was done with 1 M $LiPF_6$ in EC:DEC:DMC 1:1:1 by volume (MTI and Alfa Aesar). Li activated electrodes were disassembled, rinsed in acetonitrile (Fisher Scientific) and dried in a glovebox (<

0.2 ppm H_2O and O_2 content) overnight. They were then reassembled in the same glovebox for NIB testing, employing 1 M $NaClO_4$ (Alfa Aesar, 98-102% purity) EC:DEC 1:1 by volume. Polyethylene separators (MTI Corporation) with 36 − 44% porosity and 0.03 mm pore size (Ø 19 mm) were used for both LIB and NIB assemblies. Electrochemical impedance spectroscopy (EIS) measurements were performed on Versa STAT3 potentiostat (Princeton Applied Research) in a frequency range of 1000 kHz – 1 mHz with an AC amplitude of 10 mV. All the electrochemical experiments were performed at room temperature.

Electron energy loss spectroscopy (EELS) and energy-dispersive X-ray (EDX) spectroscopy were performed using a JEOL 2200FS (200 kV) with an in-column Ω filter in scanning mode (STEM) with a nominal analytical beam size of 0.5 nm. The standard procedure of pre-edge background subtraction and integration on the edge was used for the data extraction from the recorded EELS spectra. [53] For each elemental map, a thickness profile was calculated from low-loss EELS spectrum to check for possible artifacts due to large variation in thickness. Ge-*M*, Li-*K*, C-*K*, and Na-*L* edges were used for elemental mapping in cycled materials. We used multiple linear least squares (MLLS) fitting of EELS spectra for separating Ge-*M* and Na-*L* edges.

5.4 Results and discussions

Plan-view and cross-sectional SEM micrographs of the as-grown germanium nanowires (GeNWs) arrays are shown in Figure 5-1(a) and (b). The wires possess relatively uniform diameters, with the catalytic gold particles being primarily at their top. The projected diameter and length distribution histograms, shown in Figure 5-1(c) and (d), demonstrate that the nanowires are on average 48 nm thick and 3 μm long. TEM analysis of as-grown GeNWs is presented in Figure 5-1(e-h). The selected area diffraction (SAD) pattern, the dark-field image ($g = 022_{Ge}$), and the HRTEM image all indicate that the examined nanowire is single crystal (space group of *Fd3m*, a_0 = 5.6578 Å), though other nanowires were twinned. According to the HRTEM micrograph the nanowire is covered with ~ 2 nm layer of amorphous germanium oxide, although there is some error associated with this estimate due to carbon contaminants. The pronounced O 1s and Ge 3d peaks at about 532 eV and 32.9 eV in the high resolution XPS

spectra for the as-grown GeNWs (Figure 5-2) shows that the oxide is GeO_2, being formed upon exposure to air after the growth.

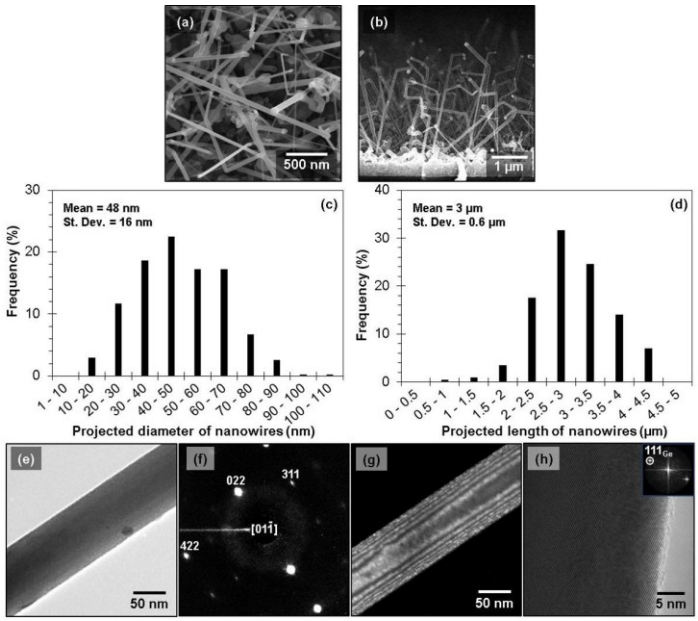

Figure 5-1: (a) Top-view SEM micrograph and (b) cross sectional SEM image of as-grown GeNWs array at 320 °C for 2 minutes. (c,d) Histogram diagram of projected diameter and length of the nanowires, respectively. (e-h) TEM micrographs of as-grown GeNWs: (e) bright-field, (f) corresponding indexed selected area diffraction (SAD) pattern of the nanowire oriented near the [01-1] zone axis, (g) dark-field micrograph obtained using $g = 022_{Ge}$ reflection, and (h) HRTEM micrograph with the corresponding Fast Fourier Transform (FFT) pattern insert.

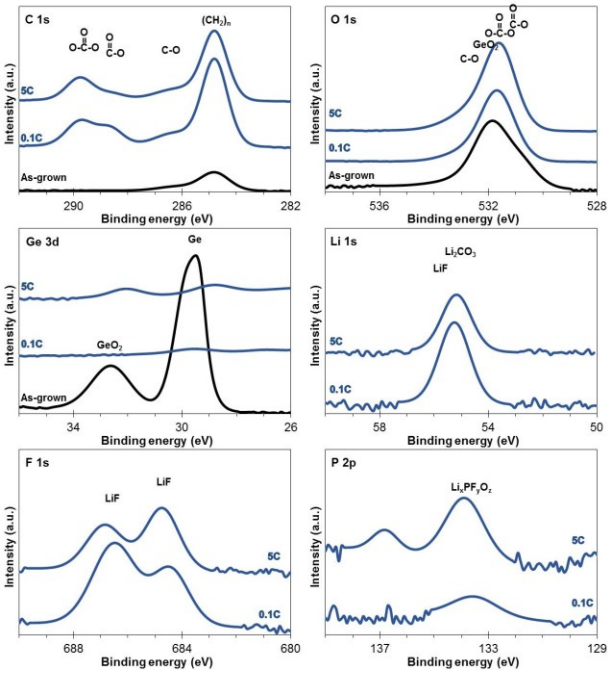

Figure 5-2: XPS spectra of as-grown GeNWs and GeNWs after first delithiation (2 V vs. Li/Li^+) at 0.1C and 5C. Panels present C 1s, O 1s, Ge 3d, Li 1s, F 1s, and P 2p.

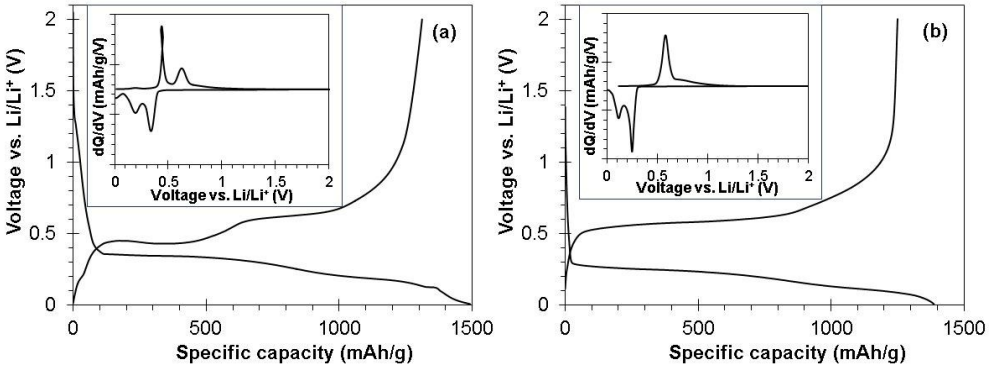

Figure 5-3: CC voltage profile for cycle 1 and corresponding dQ/dV plot insert for GeNWs at (a) 0.1C and (b) 5C with 0.01 – 2 V vs. Li/Li^+ window.

The GeNWs arrays were activated through a single lithiation - delithiation cycle between 0.01 and 2 V vs. Li/Li^{+}. The rate was kept at 160 mA/g, which may be approximated as 0.1C. Those arrays were labeled GeNWs-A-0.1C. Additionally, some high rate Li activation was performed at a rate of 5C (8000 mA/g), with those specimens being labeled GeNWs-A-5C. Both Li activation constant-current (CC) voltage profiles, with the differential capacity inserts, are shown in Figure 5-3. Li activated at 0.1C the nanowires display a lithiation/delithiation capacity of 1491/1311 mAh/g, with corresponding coulombic efficiency of 87% (Figure 5-3(a)).

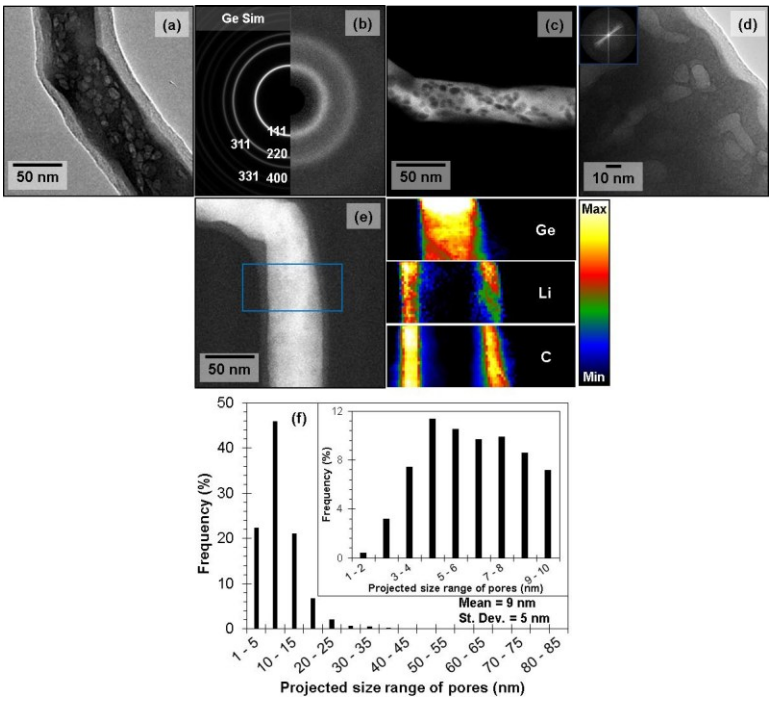

Figure 5-4: TEM analysis of GeNWs activation (full lithiation, full delithiation) with Li at a rate of 0.1C; (a) Bright-field TEM micrograph, (b) Selected area diffraction (SAD) pattern with ring simulation for Ge, (c) High Angle Annular Dark Field (HAADF) micrograph, (d) High resolution TEM (HRTEM) micrograph with corresponding FFT insert, and (e) HAADF micrograph and EELS elemental maps of Ge, Li, and C. (f) Histogram of the projected pore sizes generated within the GeNWs as a result of activation.

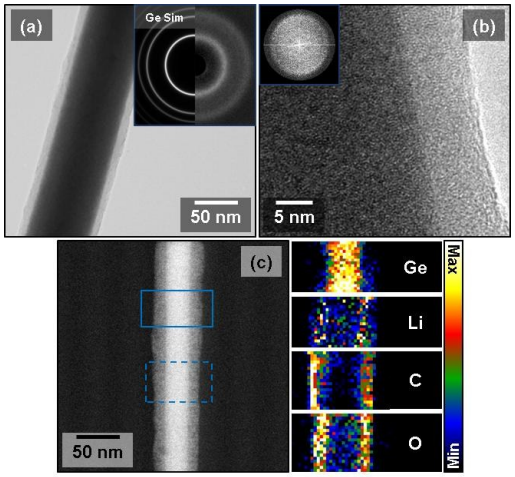

Figure 5-5: TEM analysis of GeNWs after one lithiation – delithiation at 5C. (a) Bright-field micrograph with the corresponding indexed simulated and experimental SAD patterns, inserted. (b) HRTEM micrograph with the corresponding FFT pattern insert. (c) HAADF micrograph and EELS elemental maps of Ge, Li, C, and O. The Ge and Li maps are obtained from the solid rectangular, while the C and O maps are recorded from dashed rectangular.

The long plateau at 0.35 V corresponds to the alloying of initially crystalline Ge with Li to form an amorphous Li_xGe phase. [54] This is followed by a sloping plateau centered at about 0.2 V, which is attributed to the formation of amorphous $Li_{15}Ge_4$. [55] While there is some evidence of a short crystallization plateau at a lower potential (e.g. 0.1 V), the subsequent fully delithiated structure will be fully amorphous, e.g. [54,56] and related citations. Li activated at 5C the nanowires show a lithiation/delithiation capacity of 1389/1250 mAh/g, with corresponding coulombic efficiency of 90.2% (Figure 5-3(b)). Lithiation and expansion of Ge nanowires has been reported to proceed isotropically, [57,58] contrary to the dumbbell-shapes that develop in SiNWs which cause them to split apart. [59,60,61] This implies that our Li activation process will not impart substantial macroscopic mechanical damage to the structures.

The microstructure of GeNWs after the 0.1C activation is characterized in Figure 5-4, while the microstructure at 5C is shown in Figure 5-5. The bright-field TEM micrograph in Figure 5-4(a) reveals the presence of nanopores within the amorphous nanowires. In the bright-field image the pores appear as brighter areas within the darker nanowire structure. In the high angle annular dark field (HAADF) image shown in Figure 5-4(c) the pores appear dark. While a single nanowire is shown in each image, their microstructure is general, being observed in all the wires examined. Beyond the washing/drying procedure described in the experimental section, the nanowires did not receive any additional sample preparation, which means that there is no possibility of the porosity being introduced by anything other than the lithiation/delithiation. We also did not observe a change of the number and size of pores under 200 kV electron beam, i.e. the pores are not created through electron beam damage. As expected and demonstrated in SAD pattern in Figure 5-4(b) and the HRTEM micrograph shown in Figure 5-4(d), the activated GeNWs are amorphous.

Software analysis (Gwyddion 2.31 TM) of more than 130 TEM images (about 4500 nanopores) led us to obtain reliable statistical information regarding the pore size distribution (PSD) for delithiated GeNWs at 0.1C. The PSD, plotted in Figure 5-4(f) demonstrates that projected pore size is in the range of 1 to 73 nm, with an average being 9 nm. Nanopore formation in delithiated Ge anodes has been observed previously [55,62,63] and there is good evidence that nanoporosity promotes rapid lithiation kinetics, e.g. [64,65]. As discussed in ref. [66], it may be a result of local clustering of the vacancies introduced by the Li flux during delithiation.

This occurs because of the high mobility of the vacancies in the amorphous Li_xGe and also fast rate of long-range transport of Li ions. Assuming that they are wetted by the electrolyte, these pores are expected to effectively reduce the Ge wall thickness (hence the solid-state diffusion distance) and provide additional active surfaces for sodiation/desodiation. Moreover pore surfaces should act as fast paths for Na diffusion.

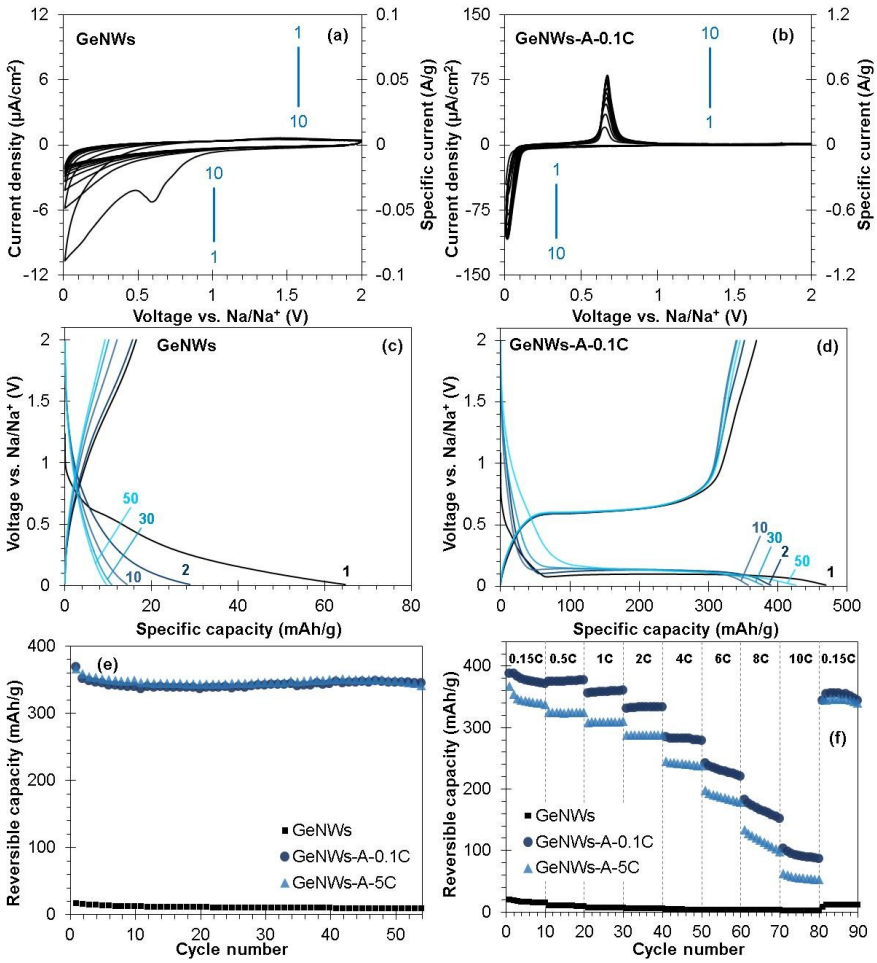

Figure 5-6: (a,b) Cyclic voltammetry (CV) curves for cycles 1 – 10 of GeNWs and GeNWs-A-0.1C electrode materials, respectively, conducted at 0.1 mV/s. (c,d) Galvanostatic voltage profiles for cycles 1, 2, 10, 30, and 50 for GeNWs and GeNWs-A-0.1C anodes, respectively. The constant-current (CC) profiles were collected at 0.15C, both against Na and in 0.01 – 2 V vs. Na/Na^+ voltage window. (e) Reversible capacity as a function of cycle number for GeNWs, GeNWs-A-0.1C, and GeNWs-A-5C anodes at 0.15C. (f) Rate performance of anode materials, reversible capacity vs. cycle number.

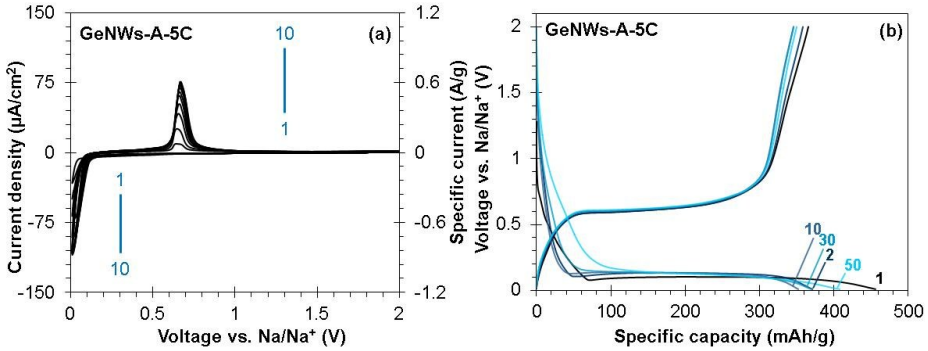

Figure 5-7: (a) Cyclic voltammetry (CV) curves for cycles 1 – 10 at the rate of 0.1 mV/s and (b) galvanostatic voltage profiles of GeNWs-A-5C at cycle 1, 2, 10, 30, and 50 at charging rate of 0.15C. Both CV and CC measurements were conducted within 0.01 – 2 V vs. Na/Na^+ window.

Figure 5-5 shows the detailed TEM analysis of GeNWs after one lithiation – delithiation at 5C. The corresponding SAD pattern and also the FFT pattern show that the nanowires after delithiation at 5C are amorphous, similar to what is observed for the 0.1C. A key difference is that nanopores are not observed at this higher activation rate. We argue that at 5C there is insufficient time for vacancy clustering to lead to pore formation. It is improbable that the nanopores exist but that they are below the practical resolution of the TEM employed for the analysis (nominal beam size ~ 0.5 nm in STEM mode with the sub-nanometer practical resolution, and TEM resolution of 0.2 nm in parallel illumination mode). This will be supported by the electrochemical impedance spectroscopy results presented later in the paper. The porosity findings are in qualitative agreement with the recent work by Chen and Sieradzki. [67]

Table 5-1: Composition (in at.%) of delithiated GeNWs after first cycle at 0.1C and 5C, obtained from the XPS spectra shown in Figure 5-2.

	C	O	Ge	Li	F	P
0.1C	43.51	27.85	0.61	24.63	3.04	0.36
5C	41.11	32.90	3.02	20.14	2.28	0.55

The authors delithiated Sn and observed a reduction of the mean pore size with higher charging rates. For the case of Ge, however, the 5C rate is apparently so high that the pores do not have time to form at all. This is in turn consistent with ~ 20 °C being a much lower

homologous temperature for Ge than for Sn, with a resultant much reduced equilibrium vacancy concentration and mobility in the former. According to Figures 1 and S5 the thickness and morphology of the Li-induced SEI is comparable in both 5C and 0.1C specimens, with the 5C actually having a somewhat thinner SEI layer (8 - 10 nm vs. 10 - 16 nm).

The XPS spectra of delithiated GeNWs at 0.1C and 5C are included in Figure 5-2. According to the XPS analysis shown in Table 5-1 the composition of the SEI in both specimens is generally similar, except for a the relative concentration of Li contained in the SEI (24.63 at.% for 0.1C vs. 20.14 at.% for 5C). Peak analysis of the spectra suggests that the SEI layer largely consists of Li_2CO_3, $(CH_2OCO_2Li)_2$, and $–(CH_2CH_2O)_n–$. Besides these compounds, the peaks associated with LiF and $Li_xPF_yO_z$ also appear in the Li 1s, F 1s, and P 2p spectra of the delithiated GeNWs. The presence of Ge signal and absence of GeO_2 signal in the Ge 3d spectra after 1st delithiation shows that as expected the native oxide is reduced by Li. According to XPS on the 5C specimen there is a slightly stronger Ge signal from the underlying nanowire, which also indicates that the SEI is thinner on the average.

Figure 5-6 and Figure 5-7 compare the NIB anode electrochemical performance of the activated versus the unactivated nanowires. Results are shown for both the 0.1C and 5C Li activation. Figure 5-6(a) and (b) contrast the cyclic voltammetry (CV) curves for cycles 1 – 10 of GeNWs vs. GeNWs-A-0.1C. Figure 5-6(c) and (d) contrast the galvanostatic voltage profiles for cycles 1, 2, 10, 30, and 50 for GeNWs vs. GeNWs-A-0.1C. Figure 5-7(a) and (b) show the CV and galvanostatic results for GeNWs-A-5C, respectively. Cyclic voltammetry was performed at 0.1 mV/s scan rate, while galvanostatic charge-discharge voltage profiles were performed at 55 mA/g (~ 0.15C), both tested with a 0.01 – 2 V vs. Na/Na^+ window. The CV curves of GeNWs show no well-defined redox peaks on either the anodic or the cathodic sweep, while the total current decreases quickly with cycle number. This is an indication that only SEI is being built up, as the current is only on the reduction branch. Conversely the CV curves for GeNWs-A-0.1C show a well-defined single cathodic peak centered at about 0.03 V, and a distinct anodic peak centered at ~ 0.66 V. The increase in the peak currents is a result of more material becoming activated in the course of potentiodynamic CV cycling, and does not occur during the galvanostatic tests. Similar behavior is observed for CV's silicon nanowire (SiNWs) LIB anodes, e.g. refs. [50,68-71]. The galvanostatic profiles show that activation with Li results in flat rather than

sloping plateaus, and much-improved capacity retention. At cycle 2 onwards the sodiation plateaus in GeNWs-A-0.1C remain consistently centered near 0.09 V. The long plateau indicates a two-phase region, corresponding to the transformation of amorphous Ge to a single amorphous Na_xGe phase or to a series of thermodynamically similar amorphous Na_xGe structures with different near-neighbor configurations.

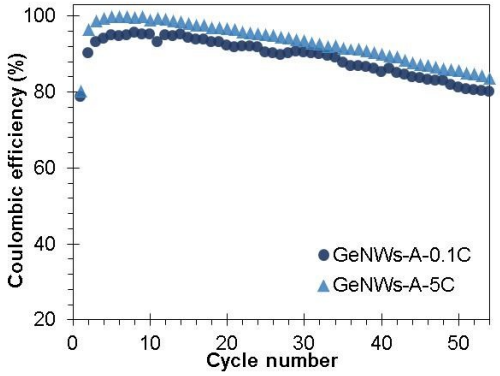

Figure 5-8: Coulombic efficiency (%) of GeNWs-A-0.1C and GeNWs-A-5C anodes at 0.15C.

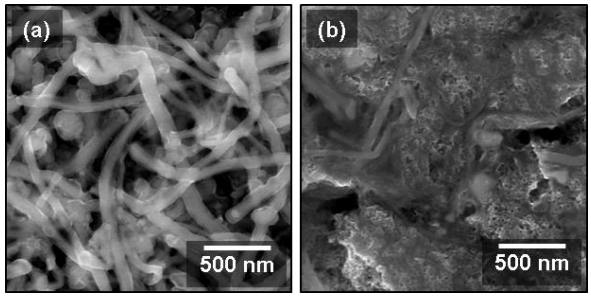

Figure 5-9: Plan-view SEM micrographs of GeNWs-A-0.1C after (a) first and (b) 55 cycles in desodiation state cycled at 0.15C.

The overall capacity for GeNWs vs. GeNWs-A-0.1C/GeNWs-A-5C is hugely different. GeNWs shows an initial reversible capacity (capacity at desodiation) of 16.3 mAh/g and a coulombic efficiency (CE) of 25%. By contrast, GeNWs-A-0.1C and GeNWs-A-5C demonstrate an initial reversible capacity of 367 and 366 mAh/g with a CE of 79% and 80%, respectively. The reversible capacity obtained in the first cycle for GeNWs-A agrees well with the terminal composition NaGe (369 mAh/g). A recent simulation study concluded that the most energetically favorable phase for sodiation of amorphous Ge is $Na_{1.56}Ge$ (576 mAh/g). [72] Thus further sodiation beyond 1:1 may be kinetically rather than thermodynamically limited. The initially low CE of GeNWs-A is primarily attributed to the irreversible formation of an SEI layer, which has been reported to start at about 0.9 V vs. Na/Na^+. [146] A contributor to cycle 1 CE loss in GeNWs is the irreversible reduction of surface GeO_2 by Na, i.e. $GeO_2 + 4Na^+ + 4\bar{e} \Rightarrow Ge + 2Na_2O$. GeNWs-A-0.1C and GeNWs-A-5C would have GeO_2 already irreversibly reduced by Li during the activation process. For the case of GeNWs, the extremely low initial CE occurs because so

little of the bulk GeNWs sodiates, despite the entire electrode surface still becoming reduced from GeO_2 and covered over by SEI.

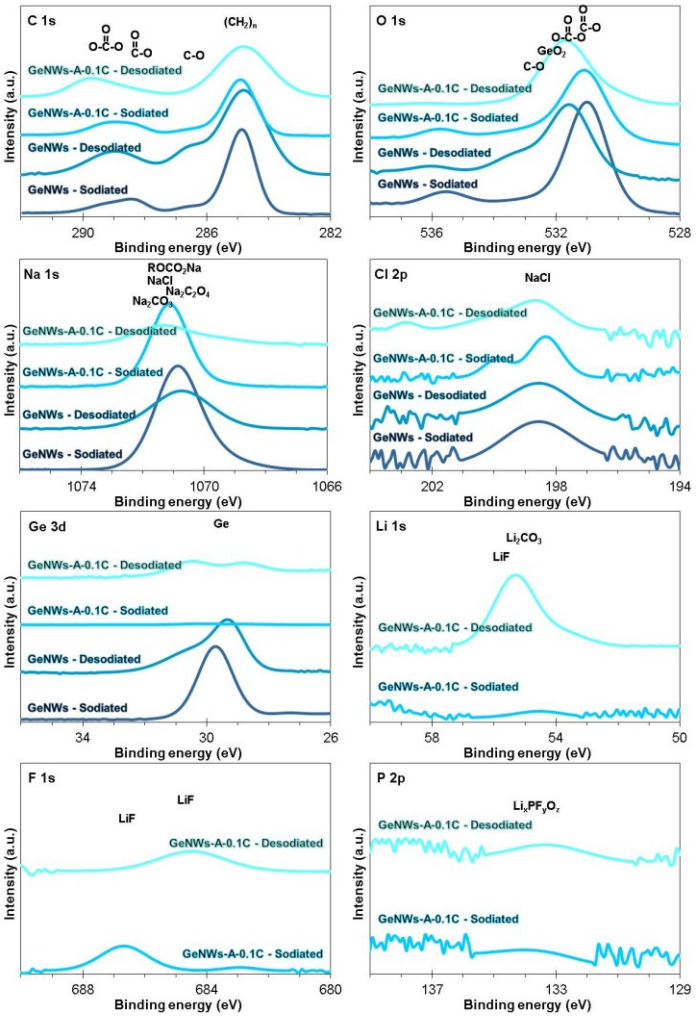

Figure 5-10: XPS spectra of GeNWs and GeNWs-A-0.1C after first sodiation (0.01 V vs. Na/Na^+) and desodiation (2 V vs. Na/Na^+). Panels present C 1s, O 1s, Na 1s, Cl 2p, Ge 3d, Li 1s, F 1s, and P 2p.

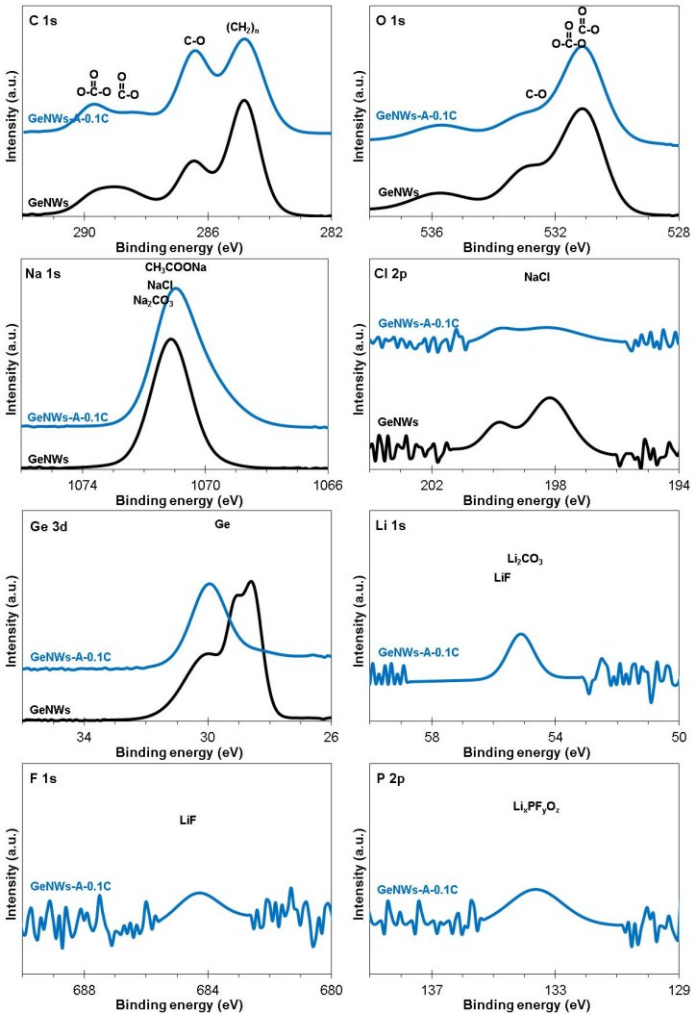

Figure 5-11: C 1s, O 1s, Na 1s, Cl 2p, Ge 3d, Li 1s, F 1s, and P 2p high resolution XPS spectra for GeNWs and GeNWs-A-0.1C anode materials cycled against Na after 55 cycles at 0.15C.

Figure 5-8 shows the cycling CE of the GeNWs-A-0.1C and GeNWs-A-5C at 0.15C, with values (80% - 95% for GeNWs-A-0.1C and 80% – 99% for GeNWs-A-5C) that are on par with what has been previously reported for Ge films and related nanostructures when tested against Na. [146,147] Low cycling CE is well-correlated with high level of SEI formation. The decrease in the efficiency of GeNWs-A is attributed to irreversible and continuous new SEI formation on

freshly exposed material surfaces during each cycle, leading to SEI thickening with each cycle (see SEM micrographs in Figure 5-9).

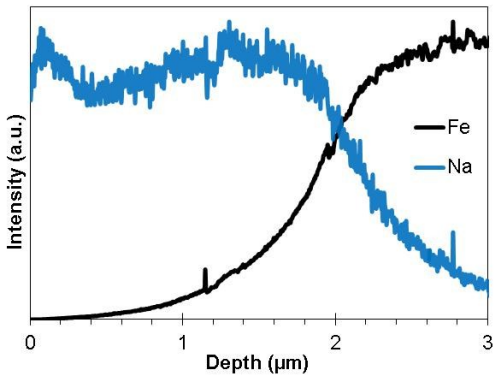

Figure 5-12: TOF-SIMS depth profiles of Na and Fe concentration for GeNWs-A-0.1C anode after 55 cycles in desodiation state.

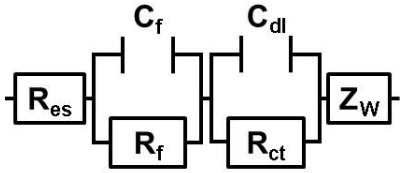

Figure 5-13: Equivalent circuit used for fitting electrochemical impedance spectra.

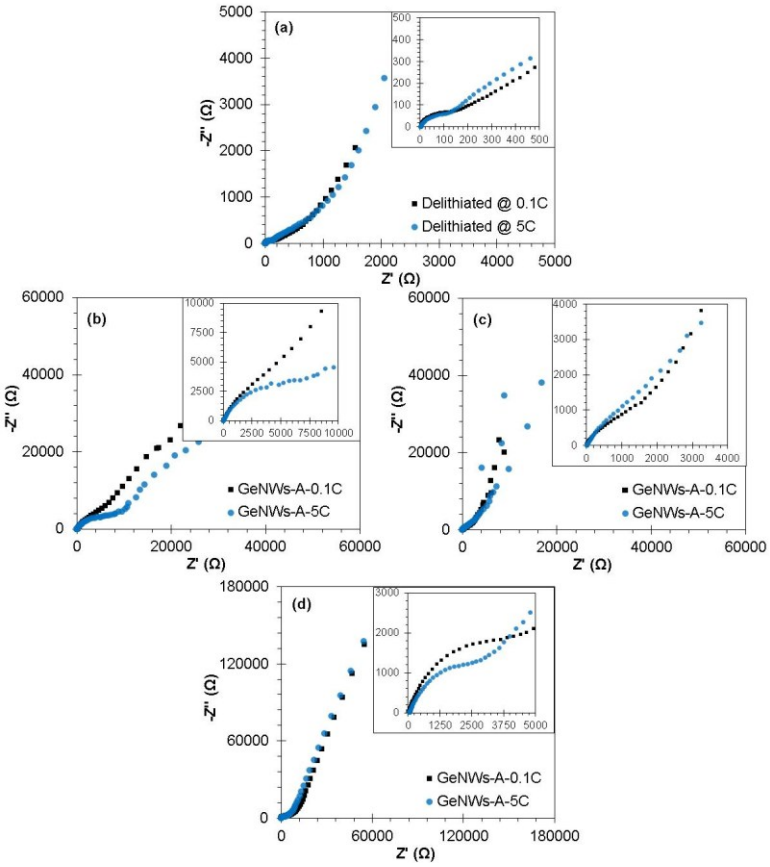

Figure 5-14: (a) Electrochemical impedance spectroscopy (EIS) spectra for GeNWs after first delithiation (2 V vs. Li/Li^+) at 0.1C and 5C. EIS spectra for GeNWs-A-0.1C and GeNWs-A-5C anodes after (b) initial sodiation (0.01 V vs. Na/Na^+), (c) first desodiation (2 V vs. Na/Na^+), and (d) 55 cycles at 0.15C in desodiated state with the high frequency portion of the spectra inserts.

XPS spectra for GeNWs-A-0.1C after cycle 1 (Figure 5-10) and cycle 55 (Figure 5-11), and corresponding atomic composition of GeNWs-A-0.1C in Table S2, demonstrate buildup a thicker and Na richer (3.61 vs. 13.10 at.%) SEI onto the material with cycling. Time-of-flight secondary ion mass spectrometry (TOF-SIMS) depth profile of Na concentration for GeNWs-A-0.1C after 55 cycles in desodiation, shown in Figure 5-12, indicates significant SEI formation at

the interface of active material and substrate, similar to our previous observation for SiNWs LIB anodes. [71]

Table 5-2: Composition (in at.%) of GeNWs-A-0.1C after first and 55 cycles in desodiated state, obtained from the XPS spectra shown in Figure 5-10 and Figure 5-11.

	C	O	Ge	Au	Na	Cl	Li	F	P
Cycle 1	43.44	28.21	1.58	0.02	3.61	0.49	21.61	0.80	0.24
Cycle 55	51.46	32.32	0.37	0.03	13.10	1.21	1.03	0.28	0.20

Figure 5-6(e) contrasts the cycling performance of the GeNWs, GeNWs-A-0.1C, and GeNWs-A-5C, tested at 0.15C. GeNWs-A-0.1C demonstrate much improved cycling capacity retention, with their reversible capacity degrading by only 2.4% going from cycle 2 to 55. From cycle 1 to 11 the capacity of GeNWs-A-0.1C decreases by 9%. Capacity is then stable up to cycle 27, and increasing very slightly (2%) by cycle 47. High rate cycling performance is another challenge for Na-ion batteries due to slow diffusivity of Na ions in the solid-state. [73] The rate capability of the three materials is shown in Figure 5-6(f). Cycling was performed at 0.15C (55 mA/g), 0.5C (185 mA/g), 1C (369 mA/g), 2C (738 mA/g), 4C (1476 mA/g), 6C (2214 mA/g), 8C (2952 mA/g), and 10C (3690 mA/g), each for 10 cycles, then returning to 0.15C for the final 10 cycles. As expected the baseline GeNWs did not sodiate at any of the rates. GeNWs-A-0.1C however exhibited a reversible capacity of 375 at 0.5C, 355 at 1C, 284 at 4C, and 103 mAh/g at 10C, the latter being considered quite a high rate for battery electrodes. The electrode also recovered 88% of its capacity (344 mAh/g) when the cycling rate was finally reverted back to 0.15C.

The 5C activation still improves the sodiation performance although no nanopores are present in the structure. Both the 0.1C and 5C activated GeNWs show a very comparable cycling performance of 343 mAh/g and 339 mAh/g after 55 cycles. Thus pore formation is not a contributor improved cycling stability. However the nanopores do affect the rate performance. The GeNWs-A activated at 0.1C, which contains nanopores within its structure, shows more promising high rate performance, e.g. 284 vs. 245 mAh/g at 4C or 182 vs. 133 mAh/g at 8C.

Thus the pores do not help cycling stability but do improve rate capability; which is ascribed to the lowered solid-state diffusion distances caused by the effective thinning of the Ge walls. However even if not all the pores are fully wetted by the electrolyte, the additional surface created by the activation process will provide a secondary short circuit diffusional path for the Na. The sodium ion diffusion coefficient in Ge was estimated to be about 10^{-13} cm^2/s, being faster in the near surface layers than in the bulk. [147]

An essential point in considering the role of activation is that of Li - induced amorphization. Amorphizing of initially highly crystalline nanowires should both accelerate sodium bulk diffusion and reduce the energetic barrier for nucleation of the Ge-Na phases. The presence of well-defined sodiation plateaus in the case of GeNWs-A, and their complete absence in the baseline GeNWs, supports the argument that two-phase formation is easier in the former. Improved reversible Li alloying/dealloying was reported for amorphous material versus their crystalline counterparts. [74] Moreover, the amorphous Li anode materials have demonstrated higher capacities. [75] Higher ion mobility in amorphous structures in comparison with the crystalline materials is also established. [76,77] For instance, Li ion diffusion in amorphous Si is estimated to be one to three orders of magnitude larger than that through crystalline Si. [78] Lithiation of GeNWs is known to be relatively straight forward, [55,56,62] explaining why the initial Li activation process does not suffer from the same severe kinetic limitations as sodiation of pristine GeNWs. The diffusivity of Na in Ge is markedly slower than that of Li in Ge, with activation energies for Na migration being 1.5 eV vs. 0.5 eV for Li migration. [147]

The XPS spectra for GeNWs and GeNWs-A-0.1C, after 1 and 55 cycles, are shown in Figure 5-10 and Figure 5-11. Surface atomic composition of GeNWs-A-0.1C anode after cycle 1 and 55 are listed in Table 5-2. Presence of Li_2CO_3 and LiF in the SEI in GeNWs-A-0.1C confirms the presence of the initial lithiation induced SEI even after cycling. During each cycle new SEI is known to preferentially form on freshly exposed active material surfaces (e.g. on graphite, Si, Ge), rather than on preexisting SEI, which is electrically insulating. [79,80] It is therefore not surprising that the Li activation - related SEI would still be detectable by XPS, since the Na-containing SEI would not form directly on top of it but rather in regions where it was no longer in contact with Ge. Overall the SEI developed in Na electrolyte ($NaClO_4$ in EC:DEC) upon cycling is primarily composed of Na_2CO_3, Na alkyl carbonates, PEO, and NaCl.

For instance, a common SEI compound for the electrodes cycled in EC-based electrolytes (either vs. Li or Na) is PEO, which shows a signal at energy values around 286 – 287 eV in the C 1s spectrum as a shoulder to the main hydrocarbon peak. [22] The peak at about 288 – 289 eV is for the CO_2 environment, corresponding to esters or oxalate compounds such as sodium oxalate ($Na_2C_2O_4$). [81] The broad peak at binding energies 289 – 290 eV is from compounds containing CO_3^{-2}, such as sodium carbonate, Na_2CO_3, and sodium alkyl carbonates, $ROCO_2Na$. Same conclusions were drawn from analyzing the O 1s spectra. The peaks related to Na carbonates and PEO compounds enlarge with cycling, as may be seen for instance in the C 1s spectra.

Table 5-3: Modeling results for EIS spectra of GeNWs anodes, shown in Figure 5-14.

Material	State	R_{es} (Ω)	$R_{ct} + R_f$ (Ω)	C_{dl} (μF)
GeNWs	1 Delithiation @ 0.1C	3.8	286.2	137
	1 Delithiation @ 5C	2.7	244.9	84
GeNWs-A-0.1C	1 Sodiation	52.8	10832	-
	1 Desodiation	6.2	2854	45
	55 Desodiation	9.5	7469	61
GeNWs-A-5C	1 Sodiation	45.1	12887	-
	1 Desodiation	6.7	2381	39
	55 Desodiation	11.1	5293	67

Electrochemical impedance spectroscopy (EIS) analysis for GeNWs specimens is presented in Figure 5-14. EIS spectra for GeNWs after first delithiation at 0.1C and 5C is shown in Figure Figure 5-14(a). Figure 5-14(b), (c), and (d) show EIS for GeNWs-A-0.1C and GeNWs-A-5C after 1st sodiation, subsequent desodiation, and 55th desodiation, respectively. We used the equivalent circuit shown in Figure 5-13 to model the measured EIS data. The modeling results for GeNWs anodes are listed in Table 5-3. The equivalent series resistance (R_{es}), which is a real axis (Z') intercept, is a combination of ionic resistance of the electrolyte, electrical resistance of the active material, and contact resistance at the interface of anode material and current collector. Similar R_{es} values for GeNWs-A-0.1C and GeNWs-A-5C anodes indicate that Li activation rate has a trivial effect on the conductivity of the active material throughout the Na cycling. The total charge transfer resistance is considered to be the sum of the charge transfer resistance at the original electrode surface (R_{ct}) and through the multiple interfaces within the SEI film (R_f).

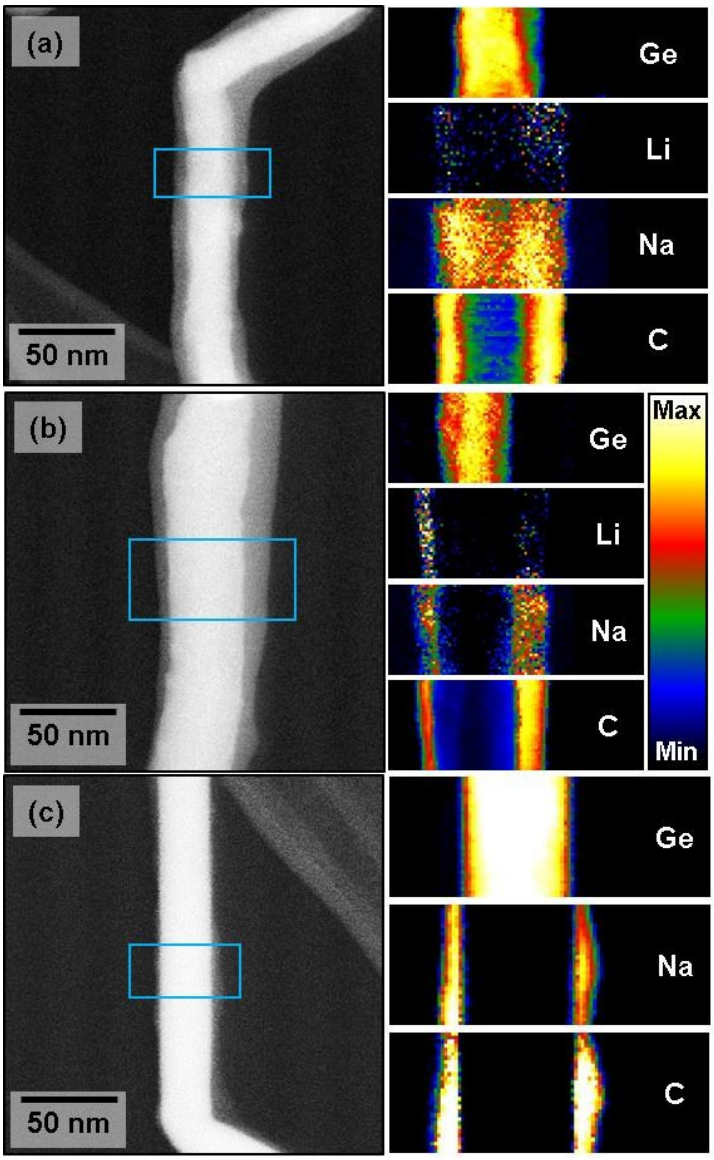

Figure 5-15: (a,b) TEM analysis of GeNWs-A-0.1C after initial sodiation and desodiation, respectively. (c) TEM analysis of baseline GeNWs, after attempted sodiating once at 0.1C. HAADF micrograph and EELS elemental maps of Ge, Na, Li, and C.

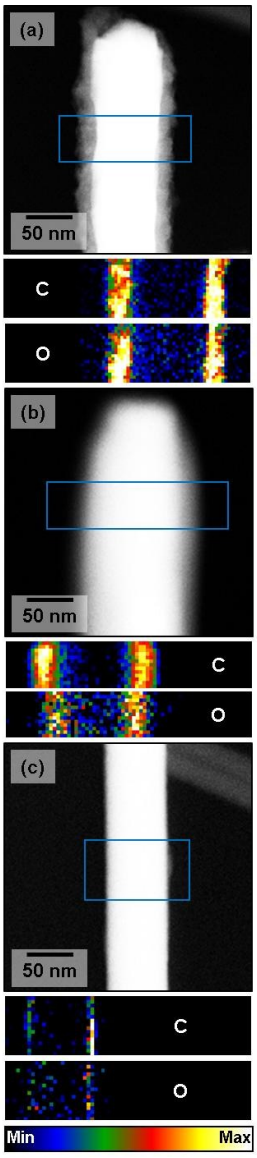

Figure 5-16: HAADF images and corresponding EELS elemental maps of C and O for (a) GeNWs-A-0.1C after first sodiation, (b) GeNWs-A-0.1C after initial desodiation, and (c) GeNWs after first sodiation.

During cycling as more SEI layers grow on the Ge surfaces the total charge transfer resistance is expected to increase. Since formation of SEI irreversibly consumes charge, higher charge transfer resistances may also be qualitatively linked to lower CE values. The relative

differences in the charge transfer resistance of delithiated GeNWs at 0.1C vs. at 5C is in agreement with their coulombic efficiency (87% vs. 90.2%). As expected from the lower CE values and the higher SEI thickness in GeNWs-A-0.1C vs. GeNWs-A-5C (10 - 16 nm vs. 8 - 10 nm by TEM), for at all charge states its (R_{ct} + R_f) is higher.

The Warburg-type line (45° sloped) in the low frequency region is attributed to the ion diffusion limitations within the bulk of the active material (Z_W). In a typical frequency window (1000 kHz – 1 mHz) the charge carrier ions will not have enough time to fully diffuse through the structure for thicker material cross sections. The length of the Warburg-type line (45° portion of the Nyquist plot) can be employed to characterize the Na ion diffusion process, with the shorter Warburg-type line being indicative of faster Na motion in the bulk. There is a shorter Warburg line for GeNWs-A-0.1C in comparison to GeNWs-A-5C (Figure 5-14(a)). Reduced diffusion distance due to nanopores results in shorter 45° line in the Nyquist plot. The onset frequency is defined as the highest frequency where the Nyquist plot starts to go vertical (the impedance of material starts to be dominated by capacitive behavior). Reducing the Li activation rate from 5C to 0.1C raises the onset frequency from 0.3 Hz to 0.6 Hz. With shrinking solid-state diffusion distances the transition to a capacitive type behavior is expected to occur at higher frequencies. [82,83] The double layer capacitance of the electrode C_{dl} is associated with the active material surface area in contact with the electrolyte. We measured a marked difference in C_{dl} of the delithiated GeNWs at 0.1C vs. 5C (137 vs. 84 μF). This effect originates from a larger surface area of the former, and is at least in part due to the nanopores.

Figure 5-15(a) and (b) show TEM analysis of GeNWs-A-0.1C, after first sodiation and desodiation at 0.1C. The panels show a HAADF micrograph and associated EELS elemental maps of Ge, Li, Na, and C. Figure 5-16 shows HAADF and corresponding EELS elemental map of C and O for GeNWs-A-0.1C after first sodiation, GeNWs-A-0.1C after initial desodiation, and GeNWs after first sodiation. These images were obtained from a different set of nanowires than Figure 5-15(a) and (b). The essence of the TEM findings, which agrees well with the electrochemical results, is that GeNWs-A-0.1C are largely sodiated, whereas the baseline GeNWs are effectively pristine. However it is difficult to tell from EELS TEM whether the GeNWs-A-0.1C nanowire is 100% sodiated (from a terminal thermodynamic viewpoint) through its thickness. Judging from the less intense Na contrast towards its core (Figure 5-15(a)), we

would argue that sodiation is not fully complete. Since in the activated Ge thin films (discussed next) it is possible to go beyond 1:1 Na:Ge, one can argue that GeNWs-A may be further sodiated. For the case of unactivated GeNWs (Figure 5-15(c)) the Na is primarily present on its surface, being associated with both the SEI layer and the irreversibly formed sodium oxide.

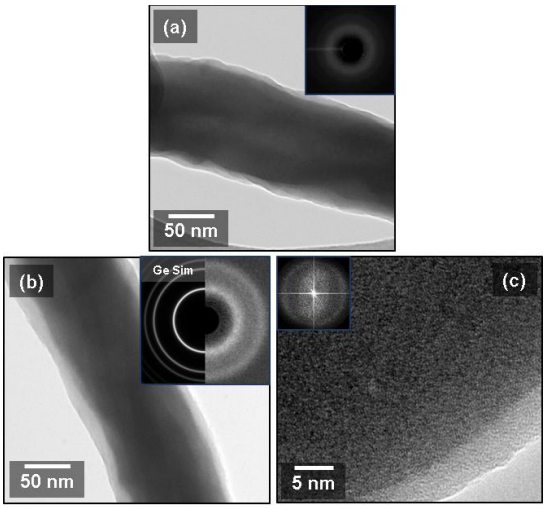

Figure 5-17: (a) Conventional TEM analysis of GeNWs-A-0.1C, after sodiating once at 0.1C. Bright-field micrograph and SAD insert. TEM analysis of GeNWs-A-0.1C, after a single sodiation – desodiation cycle at 0.1C; (b) Bright-field micrograph and SAD insert. (c) HRTEM image highlighting the amorphous structure of de-sodiated Ge.

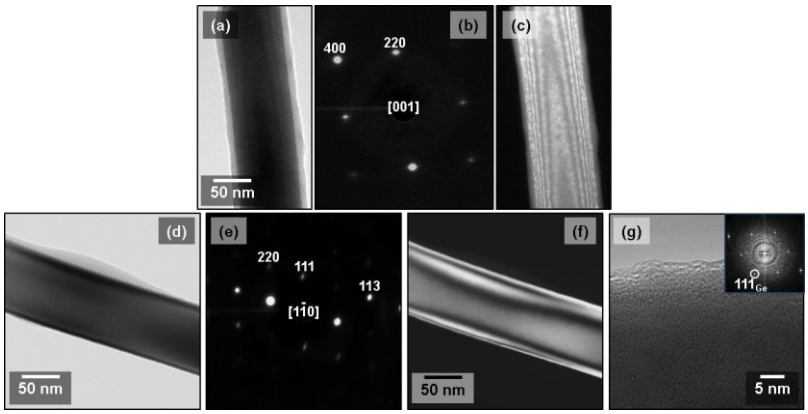

Figure 5-18: TEM analysis of GeNWs after first attempted sodiation (a-c) and after first sodiation – desodiation (d-g). (a) Bright-field micrograph, (b) corresponding SAD pattern, the nanowire is oriented near [001] zone axis, (c) dark-field micrograph, taken using $g = 220_{Ge}$ reflection. (d) bright-field, (e) SAD pattern of the GeNW oriented near the [1-10] zone axis, (f) dark-field image, obtained using $g = 111_{Ge}$, and (g) HRTEM micrograph with the partially indexed FFT pattern insert.

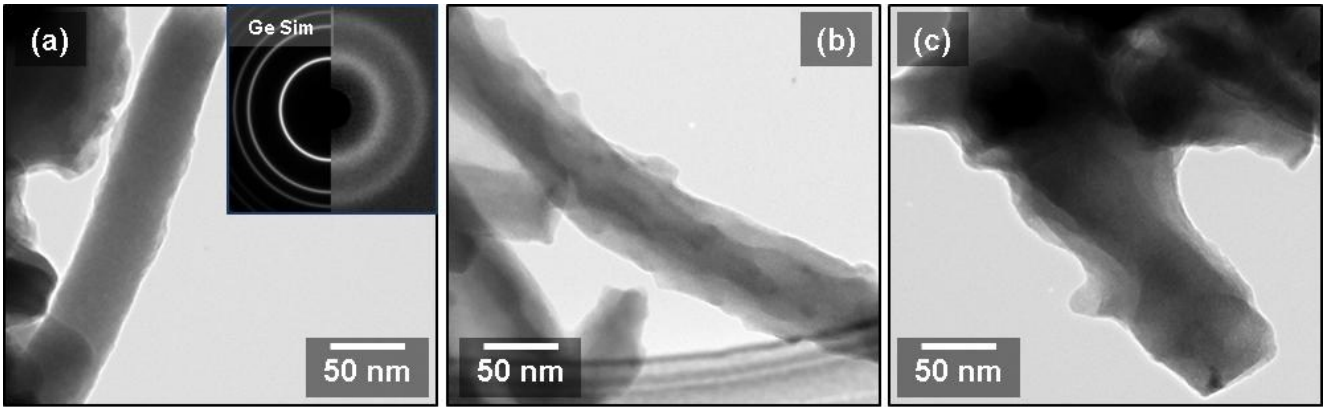

Figure 5-19: TEM micrographs of GeNWs-A-0.1C after 5 cycles at 0.1C in desodiation state: (a-c) bright-field micrographs. The inserts in panel (a) are the simulated and experimental SAD patterns.

Interestingly, we could not image nanoporosity in the sodiated GeNWs-A-0.1C specimens, either at cycle 1 (additional results are shown in Figure 5-17 and Figure 5-18) or at cycle 5 (Figure 5-19). One possibility is that the Ge may become sufficiently soft that it will flow and self-heal during Na insertion/extraction. [25]

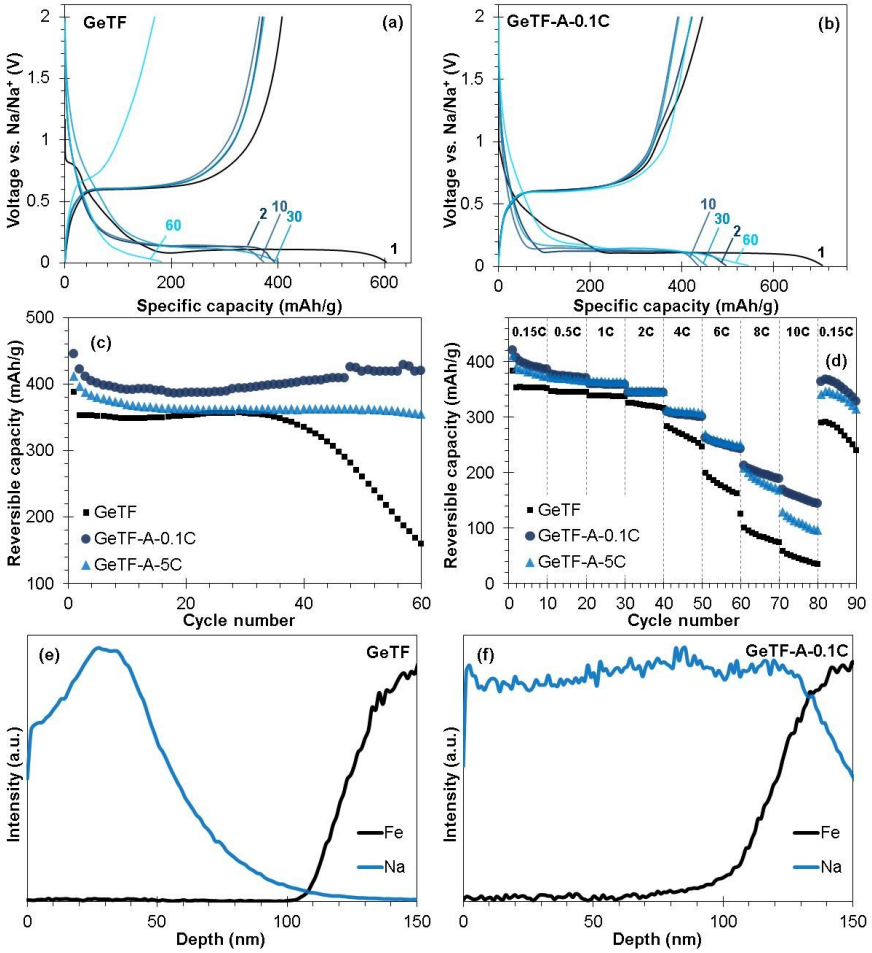

Figure 5-20: (a,b) Constant current profiles at cycle 1, 2, 10, 30, and 60 for GeTF and GeTF-A-0.1C, respectively. (c) Cycling performance of GeTF, GeTF-A-0.1C, and GeTF-A-5C at 0.15C. (d) Rate capability of GeTF, GeTF-A-0.1C, and GeTF-A-5C. (e,f) TOF-SIMS depth profile Na and Fe (support) concentration through the thickness for GeTF and GeTF-A-0.1C after the first sodiation at 0.1C.

The EIS results support this conclusion since the Na cycling values of C_{dl} in both activated materials are in the same range (Table 5-3). However some remnant useful defects should remain in GeNWs-A-0.1C specimen, imbuing it with improved high rate performance over the GeNWs-

A-5C sample. Additional analytical work beyond the scope of this manuscript would be necessary to fully understand this effect. Conventional TEM analysis of the sodiated and desodiated GeNWs-A-0.1C, and of attempted sodiated and desodiated GeNWs are shown in Figure 5-17 and Figure 5-18. The bright-field micrographs, SAD's, dark-field and HRTEM images all demonstrate that the GeNWs take up so little Na that they maintain their as-synthesized single crystal structure.

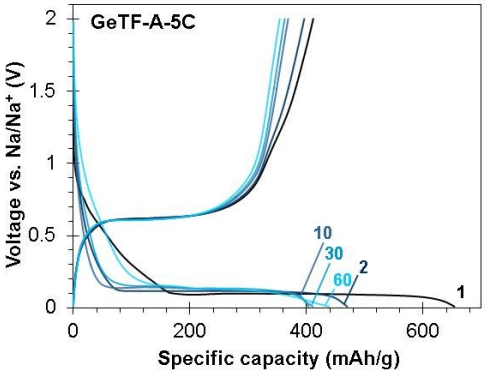

Figure 5-21: CC voltage profiles of GeTF-A-5C at cycle 1, 2, 10, 30, and 60 at charging rate of 0.15C.

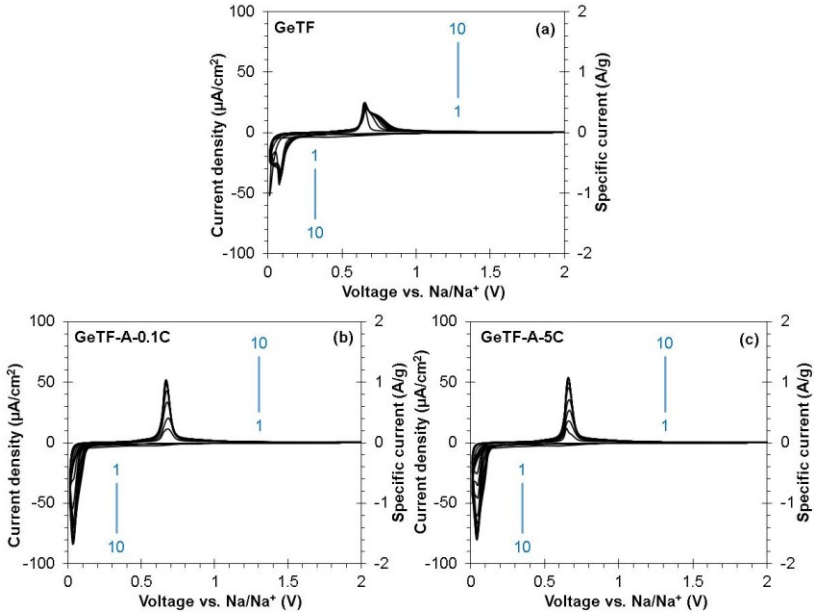

Figure 5-22: CV curves for cycles 1 – 10 of (a) GeTF, (b) GeTF-A-0.1C, and (c) GeTF-A-5C. CV measurements were conducted at 0.1 mV/s.

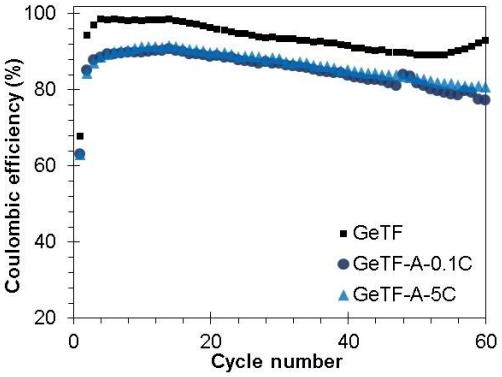

Figure 5-23: Coulombic efficiency (%) of GeTF, GeTF-A-0.1C, and GeTF-A-5C anodes at 0.15C.

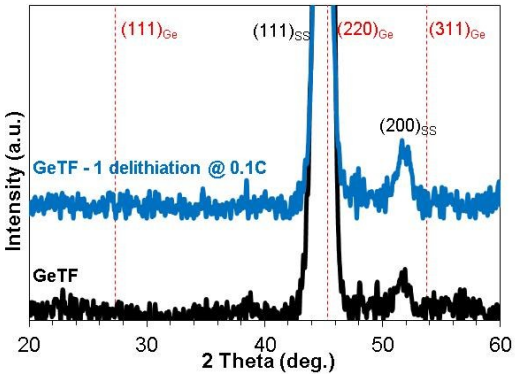

Figure 5-24: Indexed XRD patterns of as-deposited and delithiated (at 0.1C) Ge thin film.

We also explored the role of Li activation on 100 nm thick Ge thin films, labeled GeTF, GeTF-A-0.1C, and GeTF-A-5C. Figure 5-20(a) and (b) show the constant current profiles at cycle 1, 2, 10, 30, and 60 for GeTF and GeTF-A-0.1C, respectively. The voltage profiles for GeTF-A-5C are shown in Figure 5-21. Figure 5-22 shows the CV curves at cycles 1 – 10 for GeTF, GeTF-A-0.1C, and GeTF-A-5C. The cycle 1 reversible capacity of GeTF-A-0.1C and GeTF-A-5C is 450 and 412 mAh/g, for GeTF it is 355 mAh/g. A reversible capacity of 450 mAh/g indicates that it is indeed possible achieve a Na:Ge ratio higher than 1:1, in this case being ~ 1.2:1. Since the reversible capacity is reported at charging (desodiation), differences in coulombic efficiency will not obscure this difference. The CE of GeTF, GeTF-A-0.1C, and GeTF-A-5C anodes at 0.15C are displayed in Figure 5-23. The CE of GeTF is actually higher than that of GeTF-A materials, which we attribute to its lower active surface area and hence less cycling-induced SEI formation. It is feasible that the decreasing trend in the CE after cycle 15 is due to accelerated SEI formation on the active surfaces.

Table 5-4: Modeling data for EIS spectra of GeTF anodes, shown in Figure 5-25.

Material	State	R_{es} (Ω)	$R_{ct} + R_f$ (Ω)	C_{dl} (μF)
GeTF	1 Lithiation @ 0.1C	32.9	1827	2.6
	1 Delithiated @ 0.1C	5.4	238.4	107
	1 Lithiation @ 5C	15.9	1692	3.1
	1 Delithiation @ 5C	3.2	191.5	73
GeTF	1 Sodiation	25.9	3412	-
	1 Desodiation	6.9	456.2	5.9
	60 Desodiation	20.5	2965	8.1
GeTF-A-0.1C	1 Sodiation	12.9	5704	-
	1 Desodiation	3.2	528.3	31
	60 Desodiation	7.3	3543	54
GeTF-A-5C	1 Sodiation	19.8	4391	-
	1 Desodiation	3.7	499.6	27
	60 Desodiation	7.9	3389	56

As indicated in Figure 5-20(d), at higher charging rates the capacity of GeTF-A-0.1C is essentially on-par with the activated nanowires. Meanwhile the GeTF far outperforms the

unactivated nanowires, which are basically inactive. The room temperature magnetron sputtered films are amorphous in their as-synthesized condition (Figure 5-24). [138] This supports our argument that a key impediment towards sodiation of GeNWs is their high degree of crystallinity, and that Li - induced amorphization is an essential feature of the activation process. Comparing the cycling capacity retention of GeTF-A-0.1C and GeTF-A-5C versus GeTF (Figure 5-20(c)), it is evident that the two activated electrodes are substantially more stable.

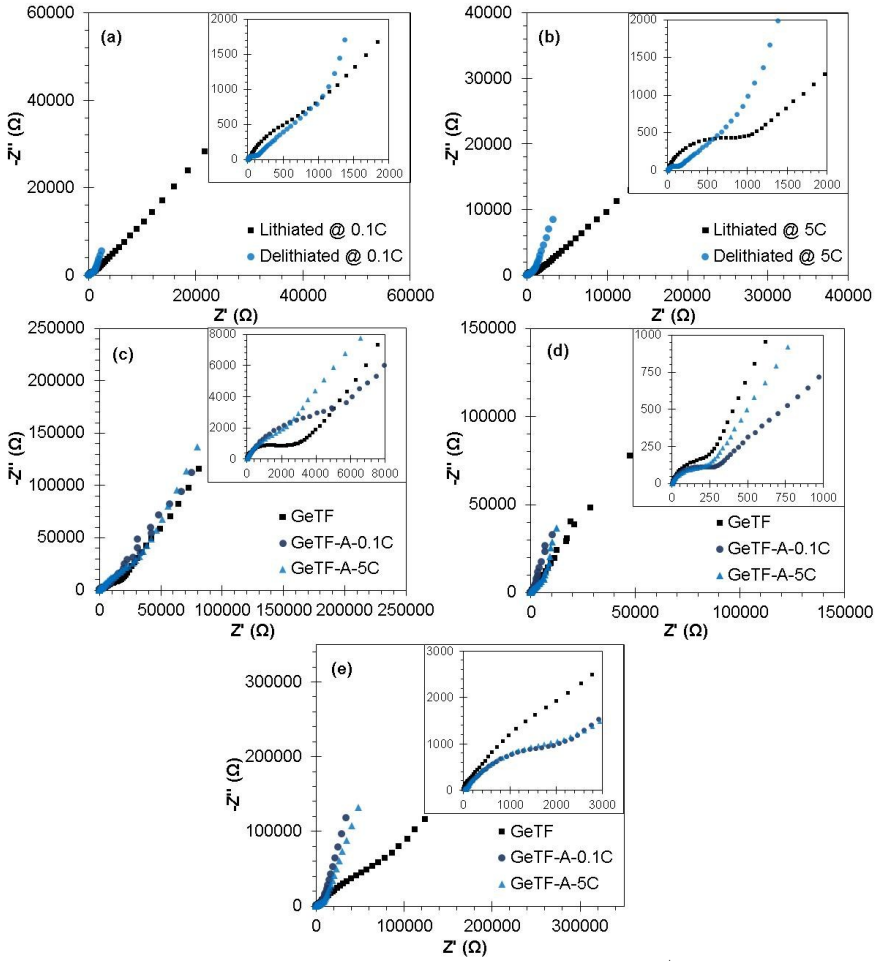

Figure 5-25: EIS spectra for GeTF after first lithiation (0.01 V vs. Li/Li^+) and delithiation (2 V vs. Li/Li^+) at (a) 0.1C and (b) 5C. EIS spectra for GeTF, GeTF-A-0.1C, and GeTF-A-5C anodes after (c) initial sodiation (0.01 V vs. Na/Na^+), (d) first desodiation (2 V vs. Na/Na^+), and (e) 60 cycles at 0.15C in desodiated state with the high frequency portion of the spectra inserts.

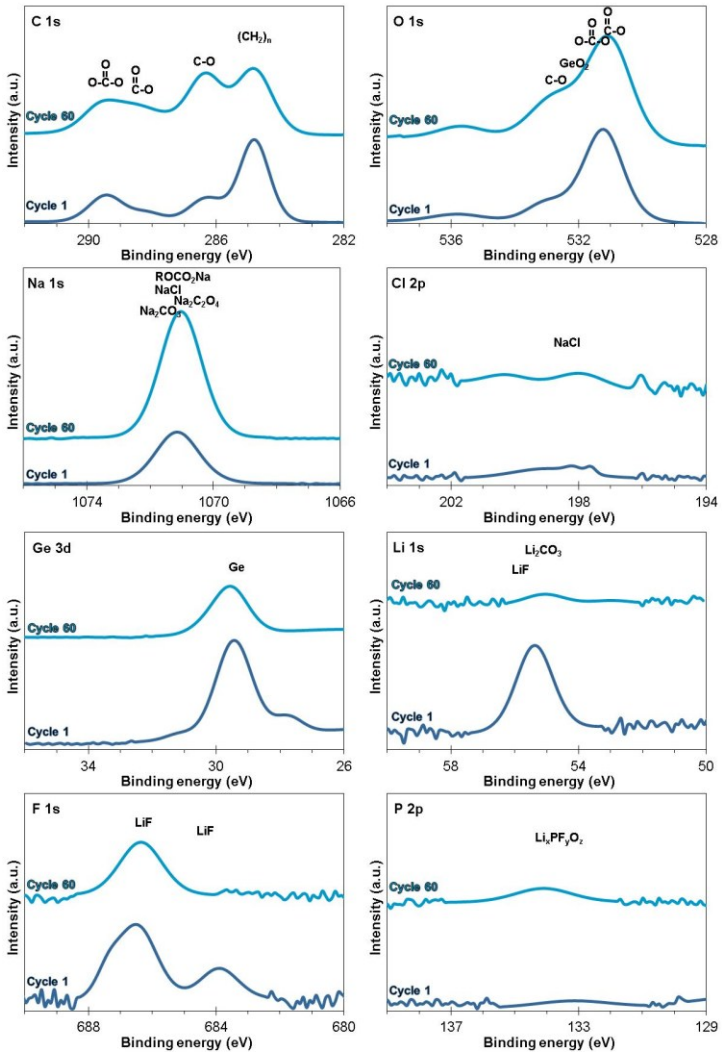

Figure 5-26: C 1s, O 1s, Na 1s, Cl 2p, Ge 3d, Li 1s, F 1s, and P 2p high resolution XPS spectra for desodiated GeTF-A-0.1C after cycle 1 and cycle 60 at 0.15C.

As will be shown in the TOF-SIMS results, the GeTF-A-0.1C sodiate much more uniformly, which is expected to result in lower differential stresses during each charge-discharge cycle. EIS measurements were employed to compare the activated (at 0.1C and 5C) and the non-activated Ge films. EIS spectra of GeTF after initial lithiation and delithiation at 0.1C and 5C is included in Figure 5-25(a) and (b). Figure 5-25(c), (d), and (e) show the EIS spectra for GeTF, GeTF-A-0.1C, and GeTF-A-5C after the first sodiation, the first desodiation, and after the 60th desodiation, respectively. The modeling data, obtained using equivalent circuit shown in Figure 5-13, are provided in Table 5-4. The same trends already discussed in detail for GeNWs are

observed for the thin films, including almost a doubling of the electrolyte contacting double layer capacitance at the slower activation (0.1C vs. 5C).

The XPS spectra of GeTF-A-0.1C after cycle 1 and after cycle 60 desodiation are displayed in Figure 5-26, while the atomic composition of the SEI is listed in Table 5-5. As expected the results are analogous to the GeNWs-A-0.1C case; with cycling the SEI becomes thicker and with more Na becoming incorporated. In case of GeTF, reduced CE values are associated with accelerated capacity decay that occurs near cycle 30. This may be understood as Na being irreversibly trapped within the Ge that is fracturing, pulverizing, and loosing electrical contact. [50,51,68-71]

Table 5-5: Composition (in at.%) of GeTF-A-0.1C after first and 60 cycles in desodiated state, obtained from the XPS spectra shown in Figure 5-26.

	C	O	Ge	Na	Cl	Li	F	P
Cycle 1	39.80	32.64	3.91	4.96	0.15	17.86	0.53	0.15
Cycle 60	44.78	38.72	2.14	11.84	0.16	2.01	0.20	0.15

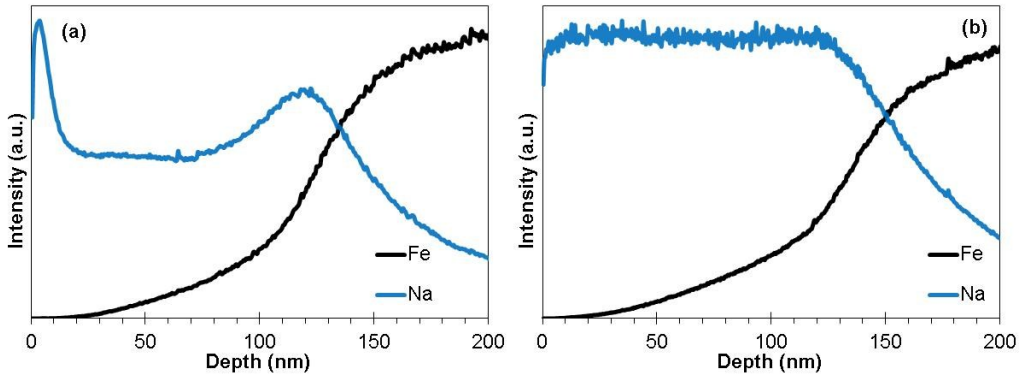

Figure 5-27: TOF-SIMS depth profiles of Na and Fe concentration for (a) GeTF and (b) GeTF-A-0.1C anodes after 60 cycles in desodiation state.

We performed TOF-SIMS depth profiling of the Na and Fe (from stainless steel support) concentrations through the thickness for GeTF and GeTF-A-0.1C, after the first *sodiation* at 0.1C. The results for GeTF and GeTF-A-0.1C are shown in Figure 5-20(e) and (f), respectively. For the case of GeTF, the film is incompletely sodiated through its thickness. The Na

concentration profile appears quite non-uniform, being peaked near the film electrolyte interface and with a lower intensity Na signal "tail" stretching into the last 50 nm of the film. Conversely the GeTF-A-0.1C electrode shows a uniform Na distribution throughout its thickness. The kinetic difficulty of fully sodiating amorphous GeTF film further underscores the beneficial role of Li activation. Finally, it is important to point out that the TOF-SIMS technique employed here does not provide a quantitative measure of the absolute or of the relative film composition. Thus it is not expected that the Na depth profile differences could be directly correlated with the measured differences in the charge storage capacities.

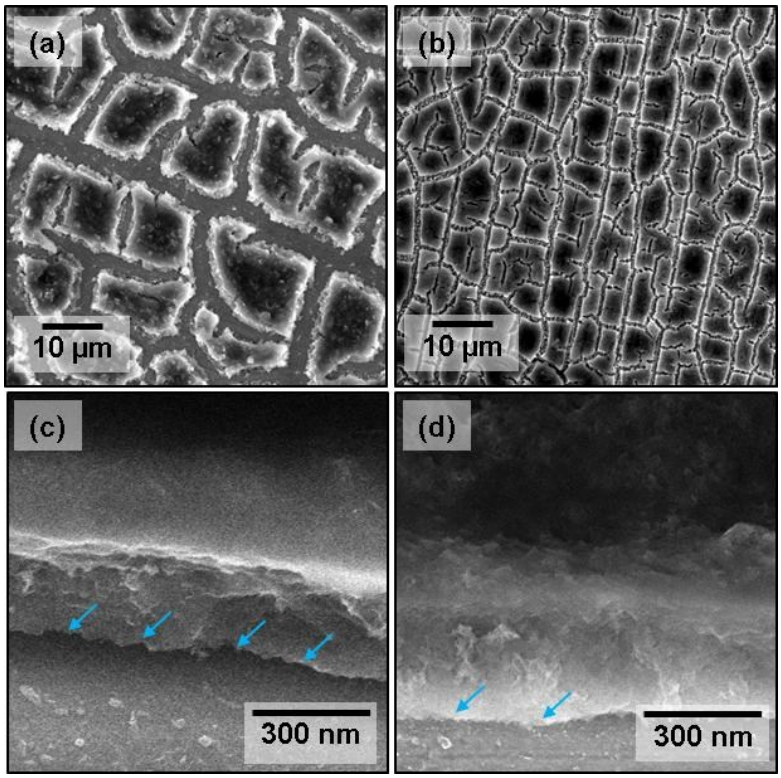

Figure 5-28: (a,b) Plan-view and (c,d) cross sectional SEM micrographs of (a,c) GeTF and (b,d) GeTF-A-0.1C anodes after 60 cycles at 0.15C.

TOF-SIMS Na depth profiles for GeTF and GeTF-A-0.1 after 60 cycles in their *desodiated* state are displayed in Figure 5-27. Sharp peak in Na concentration profile of GeTF at the interface with the substrate indicates accumulation of SEI, which is the major contributor to the delamination of active material from the underlying substrate. [40,68,71] For GeTF-A-0.1C, the Na depth profile through the thickness of film is more uniform, indicating that SEI forms throughout

the film rather than preferentially at the Ge/stainless steel interface. Plan view SEM micrographs (Figure 5-28) of both materials after 60 cycles shows stress-induced breakup of the film into smaller islands. However the GeTF-A-0.1C separates into much smaller grains, consistent with more homogenous stress distribution. They also demonstrate that active material delamination from stainless steel support occurs over larger areas for GeTF.

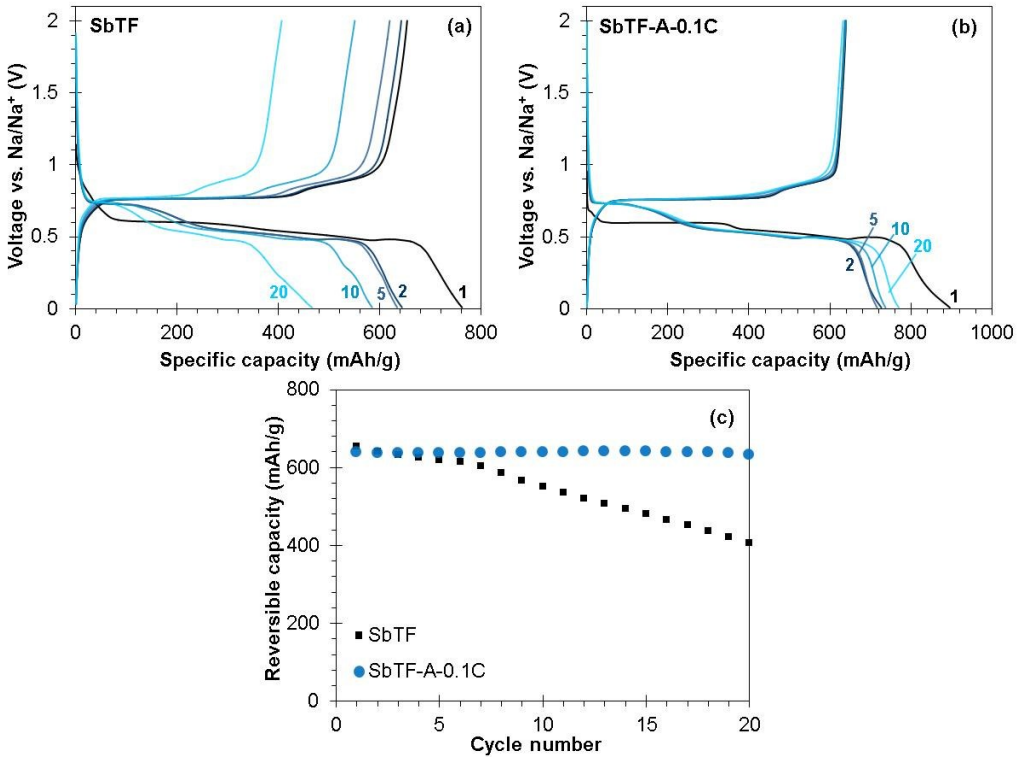

Figure 5-29: Galvanostatic voltage profiles of (a) SbTF and (b) SbTF-A-0.1C anodes at cycle 1, 2, 5, 10, and 20 at 0.1C within 0.01 – 2 V vs. Na/Na^+ window. (c) Constant current cycling performance of SbTF and SbTF-A-0.1C anodes at 0.1C.

Finally, to examine the potential of the Li activation technique in improving the electrochemical performance of other Na materials we performed limited tests on antimony thin film (SbTF) with the same 0.1C activation procedure. These results are shown in Figure 5-29. SbTF and SbTF-A-0.1C display an on par initial reversible capacity: 654 and 639 mAh/g However SbTF retains only 62% of its initial capacity by cycle 20 (406 mAh/g), while SbTF-A-0.1C holds 632 mAh/g capacity at cycle 20 (about 1% capacity loss).

5.5 Conclusion

To summarize we are the first to demonstrate that a single lithiation - delithiation cycle leads to a dramatic improvement in the sodiation kinetics of Ge nanowires and of blanket Ge thin films.

5.6 References

1 M. D. Slater, D. Kim, E. Lee, and C. S. Johnson, Adv. Funct. Mater., 2013, 23, 947-958.

2 S. W. Kim, D. H. Seo, X. Ma, G. Ceder, and K. Kang, Adv. Energy Mater., 2012, 2, 710-721.

3 H. L. Pan, Y. S. Hu, and L. Q. Chen, Energy Environ. Sci., 2013, 6, 2338-2360.

4 A. Metrot, D. Guérard, D. Billaud, and A. Hérold, Synth. Met., 1980, 1, 363-369.

5 Y. Shao, J. Xiao, W. Wang, M. Engelhard, X. Chen, Z. Nie, M. Gu, L. V. Saraf, G. Exarhos, J. G. Zhang, and J. Liu, Nano Lett., 2013, 13, 3909-3914.

6 D. A. Stevens, and J. R. Dahn, J. Electrochem. Soc., 2000, 147, 1271-1273.

7 D. Datta, J. Li, and V. B. Shenoy, ACS Appl. Mater. Interfaces, 2014, 6, 1788-1795.

8 E. Memarzadeh Lotfabad, J. Ding, K. Cui, A. Kohandehghan, W. P. Kalisvaart, M. Hazelton, and D. Mitlin, ACS Nano, 2014, 8, 7115-7129.

9 J. Ding, H. Wang, Z. Li, A. Kohandehghan, K. Cui, Z. Xu, B. Zahiri, X. Tan, E. M. Lotfabad, B. C. Olsen, and D. Mitlin, ACS Nano, 2013, 7, 11004-11015.

10 Y. Yan, Y. X. Yin, Y. G. Guo, and L. J. Wan, Adv. Energy Mater., 2014, 4, 1-5.

11 Y. Liu, F. Fan, J. Wang, Y. Liu, H. Chen, K. Jungjohann, Y. Xu, Y. Zhu, D. Bigio, T. Zhu, and C. Wang, Nano Lett., 2014, 14, 3445-3452.

12 H. Xiong, M. D. Slater, M. Balasubramanian, C. S. Johnson, and T. Rajh, J. Phys. Chem. Lett., 2011, 2, 2560-2565.

13 Y. Xu, E. M. Lotfabad, H. Wang, B. Farbod, Z. Xu, A. Kohandehghan, and D. Mitlin, Chem. Commun., 2013, 49, 8973-8975.

14 K. T. Kim, G. Ali, K. Y. Chung, C. S. Yoon, H. Yashiro, Y. K. Sun, J. Lu, K. Amine, and S. T. Myung, Nano Lett., 2014, 14, 416–422.

15 J. C. P. Flores, C. Baehtz, A. Kuhn, and F. G. Alvarado, J. Mater. Chem. A, 2014, 2, 1825-1833.

16 G. Rousse, M. E. A. Dompablo, P. Senguttuvan, A. Ponrouch, J. M. Tarascon, and M. R. Palacín, Chem. Mater., 2013, 25, 4946-4956.

17 X. Yu, H. Pan, W. Wan, C. Ma, J. Bai, Q. Meng, S. N. Ehrlich, Y. S. Hu, and X. Q. Yang, Nano Lett., 2013, 13, 4721-4727.

18 Y. J. Zhu, X. G. Han, Y. H. Xu, Y. H. Liu, S. Y. Zheng, K. Xu, L. B. Hu, and C. S. Wang, ACS Nano, 2013, 7, 6378-6386.

19 X. Han, Y. Liu, Z. Jia, Y. C. Chen, J. Wan, N. Weadock, K. J. Gaskell, T. Li, and L. Hu, Nano Lett., 2014, 14, 139-147.

20 Y. Fang, L. Xiao, J. Qian, X. Ai, H. Yang, and Y. Cao, Nano Lett., 2014, 14, 3539-3543.

21 D. Er, J. Li, M. Naguib, Y. Gogotsi, and V. B. Shenoy, ACS Appl. Mater. Interfaces, 2014, 6, 11173-11179.

22 L. Baggetto, P. Ganesh, C. N. Sun, R. A. Meisner, T. A. Zawodzinski, and G. M. Veith, J. Mat. Chem. A, 2013, 1, 7985-7994.

23 L. Baggetto, P. Ganesh, R. P. Meisner, R. R. Unocic, J. C. Jumas, C. A. Bridges, and G. M. Veith, J. Power Sources, 2013, 234, 48-59.

24 J. W. Wang, X. H. Liu, S. X. Mao, and J. Y. Huang, Nano Lett., 2012, 12, 5897-5902.

25 M. Mortazavi, J. K. Deng, V. B. Shenoy, and N. V. Medhekar, J. Power Sources, 2013, 225, 207-214.

26 H. L. Zhu, Z. Jia, Y. C. Chen, N. Weadock, J. Y. Wan, O. Vaaland, X. G. Han, T. Li, and L. B. Hu, Nano Lett., 2013, 13, 3093-3100.

27 L. Baggetto, H. Y. Hah, C. E. Johnson, C. A. Bridges, J. A. Johnson, G. M. Veith, Phys. Chem. Chem. Phys., 2014, 16, 9538-9545.

28 J. Qian, Y. Xiong, Y. Cao, X. Ai, and H. Yang, Nano Lett. 2014, 14, 1865-1869.

29 M. He, K. Kravchyk, M. Walter, and M. V. Kovalenko, Nano Lett., 2014, 14, 1255-1262.

30 K. Dai, H. Zhao, Z. Wang, X. Song, V. Battaglia, and G. Liu, J. Power Sources, 2014, 263, 276-279.

31 C. Luo, Y. Xu, Y. Zhu, Y. Liu, S. Zheng, Y. Liu, A. Langrock, and C. Wang, ACS Nano, 2013, 9, 8003-8010.

32 Z. Jian, B. Zhao, P. Liu, F. Li, M. Zheng, M. Chen, Y. Shi, and H. Zhou, Chem. Commun., 2014, 50, 1215-1217.

33 Y. Wang, D. Su, C. Wang, and G. Wang, Electrochem. Commun., 2013, 29, 8-11.

34 B. Qu, C. Ma, G. Ji, C. Xu, J. Xu, Y. S. Meng, T. Wang, and J. Y. Lee, Adv. Mater., 2014, 26, 3854-3859.

35 W. J. Li, S. L. Chou, J. Z. Wang, H. K. Liu, and S. X. Dou, Nano Lett., 2013, 13, 5480-5484.

36 J. Qian, X. Wu, Y. Cao, X. Ai, and H. Yang, Angew. Chem., 2013, 125, 4731-4734.

37 L. Wu, X. Hu, J. Qian, F. Pei, F. Wu, R. Mao, X. Ai, H. Yang, and Y. Cao, Energy Environ. Sci., 2014, 7, 323-328.

38 Y. W. Denis, P. V. Prikhodchenko, C. W. Mason, S. K. Batabyal, J. Gun, S. Sladkevich, A. G. Medvedev, and O. Lev, Nat. Commun., 2013, 4, 1-7.

39 L. Baggetto, E. Allcorn, R. R. Unocic, A. Manthiram, and G. M. Veith, J. Mater. Chem. A, 2013, 1, 11163-11169.

40 B. Farbod, K. Cui, W. P. Kalisvaart, M. Kupsta, B. Zahiri, A. Kohandehghan, E. Memarzadeh, Z. Li, E. J. Luber, and D. Mitlin, ACS Nano, 2014, 8, 4415-4429.

41 P. R. Abel, M. G. Fields, A. Heller, and C. B. Mullins, ACS Appl. Mater. Interfaces, 2014, 6, 15860-15867.

42 L. David, R. Bhandavat, and G. Singh, ACS Nano 2014, 8, 1759-1770.

43 Y. Cao, L. Xiao, M. L. Sushko, W. Wang, B. Schwenzer, J. Xiao, Z. Nie, L. V. Saraf, Z. Yang, and J. Liu, Nano Lett., 2012, 12, 3783-3787.

44 Y. Liu, Y. Xu, Y. Zhu, J. N. Culver, C. A. Lundgren, K. Xu, and C. Wang, ACS Nano, 2013, 7, 3627-3634.

45 Y. Cao, L. Xiao, W. Wang, D. Choi, Z. Nie, J. Yu, L. V. Saraf, Z. Yang, and J. Liu, Adv. Mater., 2011, 23, 3155-3160.

46 V. L. Chevrier, and G. Ceder, J. Electrochem. Soc., 2011, 158, A1011-A1014.

47 L. Baggetto, J. K. Keum, J. F. Browning, and G. M. Veith, Electrochem. Commun., 2013, 34, 41-44.

48 P. R. Abel, Y. M. Lin, T. de Souza, C. Y. Chou, A. Gupta, J. B. Goodenough, G. S. Hwang, A. Heller, and C. B. Mullins, J. Phys. Chem. C, 2013, 117, 18885-18890.

49 S. Komaba, Y. Matsuura, T. Ishikawa, N. Yabuuchi, W. Murata, and S. Kuze, Electrochem. Commun., 2012, 21, 65-68.

50 E. L. Memarzadeh, W. P. Kalisvaart, A. Kohandehghan, B. Zahiri, C. M. Holt, and D. Mitlin, J. Mater. Chem., 2012, 22, 6655-6668.

51 E. M. Lotfabad, P. Kalisvaart, A. Kohandehghan, K. Cui, M. Kupsta, B. Farbod, and D. Mitlin, J. Mater. Chem. A, 2014, 2, 2504-2516.

52 S. P. Ong, V. L. Chevrier, G. Hautier, A. Jain, C. Moore, S. Kim, X. Ma, and G. Ceder, Energy Environ. Sci., 2011, 4, 3680-3688.

53 R. F. Egerton, Electron energy-loss spectroscopy in the electron microscope, Springer, New York, 3rd edition, 2011.

54 L. Baggetto, and P. H. Notten, J. Electrochem. Soc., 2009, 156, A169-A175.

55 T. Kennedy, E. Mullane, H. Geaney, M. Osiak, C. O'Dwyer, and K. M. Ryan, Nano Lett., 2014, 14, 716-723.

56 B. Farbod, K. Cui, M. Kupsta, P. Kalisvaart, E. Memarzadeh, A. Kohandehghan, B. Zahiri, and D. Mitlin, J. Mater. Chem. A, 2014, 2, 16770-16785.

57 Y. Liu, X. H. Liu, B. M. Nguyen, J. Yoo, J. P. Sullivan, S. T. Picraux, J. Y. Huang, and S. A. Dayeh, Nano Lett., 2013, 13, 4876-4883.

58 X. H. Liu, Y. Liu, A. Kushima, S. Zhang, T. Zhu, J. Li, and J. Y. Huang, Adv. Energy Mater., 2012, 2, 722-741.

59 H. Wu, G. Chan, J. W. Choi, Y. Yao, M. T. McDowell, S. W. Lee, A. Jackson, Y. Yang, L. Hu, Y. Cui, Nat. Nanotechnol., 2012, 7, 310-315.

60 X. H. Liu, and J. Y. Huang, Energy Environ. Sci., 2011, 4, 3844-3860.

61 X. H. Liu, H. Zheng, L. Zhong, S. Huan, K. Karki, L. Q. Zhang, Y. Liu, A. Kushima, W. T. Liang, J. W. Wang, J. H. Cho, E. Epstein, S. A. Dayeh, S. T. Picraux, T. Zhu, J. Li, J. P. Sullivan, J. Cumings, C. S. Wang, S. X. Mao, Z. Z. Ye, S. L. Zhang, and J. Y. Huang, Nano Lett., 2011, 11, 3312-3318.

62 X. H. Liu, S. Huang, S. T. Picraux, J. Li, T. Zhu, and J. Y. Huang, Nano Lett., 2011, 11, 3991-3997.

63 F. W. Yuan, H. J. Yang, and H. Y. Tuan, ACS Nano, 2012, 6, 9932-9942.

64 J. H. Pikul, H. G. Zhang, J. Cho, P. V. Braun, and W. P. King, Nat. Commun., 2013, 4, 1-5.

65 H. Zhang, and P. V. Braun, Nano Lett., 2012, 12, 2778-2783.

66 M. Gu, Y. Li, X. Li, S. Hu, X. Zhang, W. Xu, S. Thevuthasan, D. R. Baer, J. G. Zhang, J. Liu, and C. Wang, ACS Nano, 2012, 6, 8439-8447.

67 Q. Chen, and K. Sieradzki, Nat. Mater., 2013, 12, 1102-1106.

68 A. Kohandehghan, P. Kalisvaart, M. Kupsta, B. Zahiri, B. S. Amirkhiz, Z. Li, E. L. Memarzadeh, L. A. Bendersky, and D. Mitlin, J. Mater. Chem. A, 2013, 1, 1600-1612.

69 E. M. Lotfabad, P. Kalisvaart, K. Cui, A. Kohandehghan, M. Kupsta, B. Olsen, and D. Mitlin, Phys. Chem. Chem. Phys., 2013, 15, 13646-13657.

70 A. Kohandehghan, P. Kalisvaart, K. Cui, M. Kupsta, E. Memarzadeh, and D. Mitlin, J. Mater. Chem. A, 2013, 1, 12850-12861.

71 A. Kohandehghan, K. Cui, M. Kupsta, E. Memarzadeh, P. Kalisvaart, and D. Mitlin, J. Mater. Chem. A, 2014, 2, 11261-11279.

72 S. C. Jung, D. S. Jung, J. W. Choi, and Y. K. Han, J. Phys. Chem. Lett., 2014, 5, 1283-1288.

73 O. Malyi, V. V. Kulish, T. L. Tan, and S. Manzhos, Nano Energy, 2013, 2, 1149-1157.

74 Y. W. Xiao, J. Y. Lee, A. S. Yu, and Z. L. Liu, J. Electrochem. Soc., 1999, 146, 3623-3629.

75 J. Graetz, C. C. Ahn, R. Yazami, and B. Fultz, Electrochem. Solid-State Lett., 2003, 6, A194-A197.

76 J. R. Szczech, and S. Jin, Energy Environ. Sci., 2011, 4, 56-72.

77 M. Green, E. Fielder, B. Scrosati, M. Wachtler, and J. S. Moreno, Electrochem. Solid-State Lett., 2003, 6, A75-A79.

78 A. S. Fedorov, Z. I. Popov, A. A. Kuzubov, and S. G. E. Ovchinnikov, JETP Lett., 2012, 95, 143-147.

79 V. Etacheri, O. Haik, Y. Goffer, G. A. Roberts, I. C. Stefan, R. Fasching, and D. Aurbach, Langmuir, 2011, 28, 965-976.

80 R. Elazari, G. Salitra, G. Gershinsky, A. Garsuch, A. Panchenko, and D. Aurbach, J. Electrochem. Soc., 2012, 159, A1440-A1445.

81 A. Ponrouch, R. Dedryvère, D. Monti, A. E. Demet, J. M. A. Mba, L. Croguennec, C. Masquelier, P. Johansson, and M. R. Palacín, Energy Environ. Sci., 2013, 6, 2361-2369.

82 M. D. Levi, and D. Aurbach, J. Phys. Chem. B, 1997, 101, 4630-4640.

83 R. Ruffo, S. S. Hong, C. K. Chan, R. A. Huggins, and Y. Cui, J. Phys. Chem. C, 2009, 113, 11390-

11398.

Chapter 6: Concluding remarks

In this thesis we investigated the effects of three different coating materials on the electrochemical performance of Si nanowires lithium-ion battery anode. We also study the effect of deposition technique for coating materials (sputtering and ALD) on the cycling results of SiNWs. Moreover, we proposed an activation methodology for enabling Na storage in CVD-grown Ge nanowires. This method was also demonstrated to positively affect the cycling results of Na anode materials.

Chapter 2 was mainly focused on investigation of the degradation mechanisms of SiNWs electrodes for lithium ion batteries during prolonged cycling using a wide variety of techniques. Our findings indicate that contact loss between the nanowires and the current collector is possibly the most important degradation mechanism. Using FIB cross-sectioning, formation of large voids between the substrate and nanowire assembly were found. From EDX elemental maps, large deposits of electrolyte decomposition products were found near these voids. Using XPS analysis, we identified some important differences in the composition of the SEI. On Mg and Mg_2Si coated nanowires, a passivating layer of polyethylene oxide (PEO) was found and a relatively lower amount of carbonate species resulting from electrolyte reduction. These differences in SEI composition were correlated to improved coulombic efficiency, 95 vs. 98% for bare and Mg-coated SiNWs, respectively, which is an important finding with regard to practical applications, as the total amount of Li in a battery is limited by the $LiCoO_2$ cathode and any irreversible consumption of Li ions will deteriorate the useful capacity.

Mg and Mg_2Si coatings might be suitable coating materials for SiNWs, but the deposition technique used for these coating materials (magnetron sputtering) may not be effective as they may not cover SiNWs uniformly or in a conformal manner from top all the way down to the base at the interface with substrate. In chapter 3, we demonstrated that nanometer-scale TiN coatings will actually significantly improve the electrochemical cycling performance of SiNWs based LIB anodes. For example, 5 nm thick TiN (deposited by via atomic layer deposition) coated SiNWs possessed an excellent coulombic efficiency of 98% throughout cycling, whereas the same nanowires without the coating were less than 95% efficient. Furthermore, the coated nanowires demonstrated nearly 2X the cycling capacity retention and more than 2X high rate capacity

retention, as compared to the baseline. We employed a variety of analytical techniques to elucidate the origin of these effects. It was demonstrated that at an optimum thickness (5 nm), the TiN layer remained largely intact and limited the growth of the SEI. This in turn both improved the overall coulombic efficiency and reduced the life-ending delamination of the nanowire assemblies from the underlying current collector. The findings of this chapter should provide a broadly applicable design methodology for nanoscale coatings employed to improve the cycling performance of a variety of nanostructured LIB anode materials where SEI growth is universally detrimental.

TiN coated SiNWs nanocomposite was indeed an instance of active-inactive nanocomposite, where the inactive component is supposed to accommodates the volume change in the SiNWs active material, thereby preventing pulverization and disintegration of SiNWs. We also studied an active-active nanocomposite as LIB anode, where both components are active towards Li with different onset and completeion potentials for alloying/dealloying with Li. We demonstrated in chapter 4 that a thin partially dewetted surface film of physical vapor deposited lithium-active Sn will significantly improved the performance of SiNWs anodes. The anode with an optimized Sn coating (3 nm) showed nearly 2X the cycling capacity retention and high-rate capability as compared to the baseline uncoated nanowires. The coulombic efficiency was also improved from as low as 94% to over 99%. We employed a variety of analytical techniques to explain the origin of such a dramatic enhancement. It was shown that Sn coating is first to lithiate, which generates a compressive stress around the nanowire. This confines the radial expansion of the core nanowire in favor of axial expansion, and reduces failure. TOF-SIMS analysis demonstrated that during cycling there is preferential growth of Li - containing SEI at the Si nanowire - current collector interface. We showed that an optimized 3 nm Sn coating substantially reduces this effect, promoting both enhanced cycling life and higher coulombic efficiency. The optimum Sn coating (3 nm) was the most effective in promoting longitudinal lithiation-induced expansion of the nanowires at the expense of their radial expansion. The post-cycled 3 nm Sn coated SiNWs arrays are in-fact longer than their uncoated counterparts, and also contain markedly less SEI.

Finally in chapter 5, we revealed that activation by a single lithiation - delithiation cycle leads to a dramatic improvement in practically achievable capacity, in rate capability, and in cycling stability of Ge nanowires (GeNWs) and Ge thin films (GeTF). TEM and TOF-SIMS

analysis showed that without Li activation, the initially crystalline GeNWs are not electrocehmically active towards Na, while the 100 nm amorphous GeTF sodiates only partially. Activation with Li induced amorphization (in GeNWs), reducing the barrier for nucleation of the Na_xGe phase(s), while introducing a dense distribution of nanopores that shorten the Na solid-state diffusion length, and buffer the sodiation stresses. We conclusively demonstrated that only the low rate (0.1C) Li activation introduces a dense distribution of nanopores, which lead to further improvements in the rate capability but not the cycling capacity retention. Nanopores don't help cycling stability but do improve rate capability; which is ascribed to the shortened solid-state diffusion distances caused by the effective thinning of the Ge walls and by an additional Na diffusion path via the pore surfaces. The EIS spectra and corresponding modeling data also showed that Li - induced activation at low rates results in higher surface area and faster Na diffusion in the bulk due to nanopore formation. At 0.15C (1C = 369 mA/g, i.e. Na:Ge 1:1), the GeNWs and GeTF maintained a reversible (desodiation) capacity of 346 mAh/g and 418 mAh/g for 55 cycles and 60 cycles, respectively. They also showed a capacity of 355 and 360 mAh/g at 1C and 284 and 310 mAh/g at 4C. GeTF delivered capacity of 169 mAh/g even at a very high rate of 10C. TOF-SIMS Na depth profiles for thin films demonstrated that accumulation of SEI at the interface with support is the major contributor to the active material delamination form the substrate.

Bibliography

1. J. M. Tarascon, and M. Armand, Nature, 2001, 414, 359-367.
2. W. J. Zhang, J. Power Sources, 2011, 196, 877-885.
3. A. Anani, and R. A. Huggins, J. Power Sources, 1992, 38, 351-362.
4. U. Kasavajjula, C. Wang, and A. J. Appleby, J. Power Sources, 2007, 163, 1003-1039.
5. M. Winter, and R. J. Brodd, Chem. Rev., 2004, 104, 4245-4270.
6. D. Linden, and T. B. Reddy, Handbook of Batteries, 3rd Ed., McGraw-Hill, New York, 2002.
7. M. R. Palacín, Chem. Soc. Rev., 2009, 38, 2565-2575.
8. A. Manthiram, J. Phys. Chem. Lett., 2011, 2, 176-184.
9. R. Teki, M. K. Datta, R. Krishnan, T. C. Parker, T.-M. Lu, P. N. Kumta, and N. Koratkar, Small, 2009, 5, 2236-2242.
10. W. Xu, Silicon Nanowire Anode for Lithium-Ion Batteries: Fabrication, Characterization and Solid Electrolyte Interphase, PhD thesis, Louisiana State University, 2011.
11. J. Wen, Y. Yu, and C. Chen, Mater. Express, 2012, 2, 197-212.
12. J. M. Tarascon, and M. Armand, Nature, 2001, 414, 359-367.
13. C. A. Vincent, and B. Scrosati, Modern Batteries: An Introduction to Electrochemical Power Sources. E. Arnold, 1997, Ed. 2.
14. M. M. Thackeray, C. Wolverton, and E. D. Isaacs, Energy Environ. Sci., 2012, 5, 7854-7863.
15. B. Scrosati, Electrochim. Acta, 2000, 45, 2461-2466.
16. E. Peled, C. Menachem, D. Bar-Tow, and A. Melman, J. Electrochem. Soc., 1996, 143, L4-L7.
17. M. Yoshio, H. Wang, and K. Fukuda, Angew. Chem., 2003, 115, 4335-4338.

18. M. Yoshio, H. Wang, K. Fukuda, Y. Hara, and Y. Adachi, J. Electrochem. Soc., 2000, 147, 1245-1250.

19. Q. Wang, P. Ping, X. Zhao, G. Chu, J. Sun, and C. Chen, J. Power Sources, 2012, 208, 210-224.

20. Y. Chen, and J. W. Evans, J. Electrochem. Soc., 1996, 143, 2708-2712.

21. W. J. Zhang, J. Power Sources, 2011, 196, 13-24.

22. H. Wu, and Y. Cui, Nano Today, 2012, 7, 414-429.

23. M. R. Zamfir, H. T. Nguyen, E. Moyen, Y. H. Lee, and D. Pribat, J. Mater. Chem. A, 2013, 1, 9566-9586.

24. J. YangáLee, J. Mater. Chem., 2011, 21, 9819-9824.

25. Y. Oumellal, N. Delpuech, D. Mazouzi, N. Dupre, J. Gaubicher, P. Moreau, P. Soudan, B. Lestriez, and D. Guyomard, J. Mater. Chem., 2011, 21, 6201-6208.

26. C. R. Becker, K. E. Strawhecker, Q. P. McAllister, and C. A. Lundgren, ACS Nano, 2013, 7, 9173-9182.

27. M. N. Obrovac, and L. Christensen, Electrochem. Solid-State Lett., 2004, 7, A93-A96.

28. C. K. Chan, H. Peng, G. Liu, K. McIlwrath, X. F. Zhang, R. A. Huggins, and Y. Cui, Nat. Nanotechnol., 2007, 3, 31-35.

29. P. G. Bruce, B. Scrosati, and J. -M. Tarascon, Angew. Chem., Int. Ed., 2008, 47, 2930-2946.

30. M. K. Datta, J. Maranchi, S. J. Chung, R. Epur, K. Kadakia, P. Jampani, P. N. Kumta, Electrochim. Acta, 2011, 56, 4717-4723.

31. P. R. Abel, Y. M. Lin, H. Celio, A. Heller, and C. B. Mullins, ACS Nano, 2012, 6, 2506-2516.

32. H. C. Liu, and S. K. Yen, J. Power Sources, 2007, 166, 478-484.

33. J. P. Maranchi, A. F. Hepp, and P. N. Kumta, Electrochem. Solid-State Lett., 2003, 6, A198-A201.

34. Z. S. Wu, W. Ren, L. Wen, L. Gao, J. Zhao, Z. Chen, G. Zhou, F. Li, and H. M. Cheng, ACS Nano, 2010, 4, 3187-3194.

35. J. Z. Wang, C. Zhong, D. Wexler, N. H. Idris, Z. X. Wang, L. Q. Chen, and H. K. Liu, Chemistry-A European Journal, 2011, 17, 661-667.

36. C. He, S. Wu, N. Zhao, C. Shi, E. Liu, and J. Li, ACS Nano, 2013, 7, 4459-4469.

37. J. Luo, X. Zhao, J. Wu, H. D. Jang, H. H. Kung, J. Huang, J. Phys. Chem. Lett., 2012, 3, 1824-1829.

38. H. Wu, G. Zheng, N. Liu, T. J. Carney, Y. Yang, and Y. Cui, Nano letters, 2012, 12, 904-909.

39. A. Xing, S. Tian, H. Tang, D. Losic, and Z. Bao, RSC Adv., 2012, 3, 10145-10149.

40. J. Li, S. Xiong, Y. Liu, Z. Ju, and Y. Qian, ACS Appl. Mater. Interfaces, 2013, 5, 981-988.

41. J. Li, P. Wu, F. Lou, P. Zhang, Y. Tang, Y. Zhou, and T. Lu, Electrochim. Acta, 2013, 111, 862-868.

42. E. Kim, D. Son, T. G. Kim, J. Cho, B. Park, K. S. Ryu, and S. H. Chang, Angew. Chem., 2004, 116, 6113-6116.

43. Z. Wen, Q. Wang, Q. Zhang, and J. Li, Adv. Funct. Mater., 2007, 17, 2772-2778.

44. T. Song, J. Xia, J. H. Lee, D. H. Lee, M. S. Kwon, J. M. Choi, J. Wu, S. K. Doo, H. Chang, W. I. Park, D. S. Zang, H. Kim, Y. Huang, K. C. Hwang, J. A. Rogers, and U. Paik, Nano Lett., 2010, 10, 1710–1716.

45. Z. Wen, G. Lu, S. Mao, H. Kim, S. Cui, K. Yu, X. Huang, P. T. Hurley, O. Mao, and J. Chen, Electrochem. Commun., 2013, 29 67-70.

46. J. Wang, N. Du, H. Zhang, J. Yu, and D. Yang, J. Phys. Chem. C, 2011, 115, 11302-11305.

47. H. Wu, G. Chan, J. W. Choi, Y. Yao, M. T. McDowell, S. W. Lee, A. Jackson, Y. Yang, L. Hu, Y. Cui, Nat. Nanotechnol., 2012, 7, 310-315.

48. C. de las Casas, and W. Li, J. Power Sources, 2012, 208, 74-85.

49. H. Wu, M. Xu, Y. Wang, and G. Zheng, Nano Res., 2013, 6, 167-173.

50. L. P. Tan, Z. Lu, H. T. Tan, J. Zhu, X. Rui, Q. Yan, and H. H. Hng, J. Power Sources, 2012, 206, 253-258.

51. J. Chen, X. H. Xia, J. P. Tu, Q. Q. Xiong, Y. X. Yu, X. L. Wang, and C. D. Gu, J. Mater. Chem., 2012, 22, 15056-15061.

52. J. Y. Huang, L. Zhong, C. M. Wang, J. P. Sullivan, W. Xu, L. Q. Zhang, S. X. Mao, N. S. Hudak, X. H. Liu, A. Subramanian, H. Fan, L. Qi, A. Kushima, and J. Li, Science, 2010, 330, 1515-1520.

53. P. Meduri, E. Clark, J. H. Kim, E. Dayalan, G. U. Sumanasekera, M. K. Sunkara, Nano Lett., 2012, 12, 1784-1788.

54. N. Liu, L. Hu, M. T. McDowell, A. Jackson, and Y. Cui, Y. ACS Nano, 2011, 5, 6487-6493.

55. B. Liu, J. Zhang, X. Wang, G. Chen, D. Chen, C. Zhou, and G. Shen, Nano Lett., 2012, 12, 3005-3011.

56. H. Kim, and J. Cho, Nano Lett., 2008, 8, 3688-3691.

57. K. T. Nam, D. W. Kim, P. J. Yoo, C. Y. Chiang, N. Meethong, P. T. Hammond, Y. M. Chiang, and A. M. Belcher, Science, 2006, 312, 885-888.

58. M. S. Park, G. X. Wang, Y. M. Kang, D. Wexler, S. X. Dou, and H. K. Liu, Angew. Chem., 2007, 119, 764-767.

59. H. Ma, S. Zhang, W. Ji, Z. Tao, and J. Chen, J. Am. Chem. Soc., 2008, 130, 5361-5367.

60. A. Débart, A. J. Paterson, J. Bao, and P. G. Bruce, Angew. Chem., 2008, 120, 4597-4600.

61. Y. Li, B. Tan, and Y. Wu, Nano Lett., 2008, 8, 265-270.

62. K. Peng, J. Jie, W. Zhang, and S. T. Lee, Appl. Phys. Lett., 2008, 93, 033105.

63. L. F. Cui, Y. Yang, C. M. Hsu, and Y. Cui, Nano Lett., 2009, 9, 3370-3374.

64. H. Kim, and J. Cho, J. Mater. Chem., 2008, 18, 771-775.

65. E. M. Lotfabad, P. Kalisvaart, A. Kohandehghan, K. Cui, M. Kupsta, B. Farbod, and D. Mitlin. J. Mater. Chem. A, 2014, 2, 2504-2516.

66. M. H. Park, M. G. Kim, J. Joo, K. Kim, J. Kim, S. Ahn, Y. Cui, and J. Cho, Nano Lett., 2009, 9, 3844-3847.

67. J. Xu, C. Jia, B. Cao, and W. F. Zhang, Electrochim. Acta, 2007, 52, 8044-8047.

68. X. W. Lou, D. Deng, J. Y. Lee, J. Feng, and L. A. Archer, Adv. Mater., 2008, 20, 258-262.

69. A. L. M. Reddy, M. M. Shaijumon, S. R. Gowda, and P. M. Ajayan, Nano Lett., 2009, 9, 1002-1006.

70. J. H. Ryu, J. W. Kim, Y. E. Sung, and S. M. Oh, Electrochem. Solid-State Lett., 2004, 7, A306-A309.

71. E. L. Memarzadeh, W. P. Kalisvaart, A. Kohandehghan, B. Zahiri, C. M. Holt, and D. Mitlin, J. Mater. Chem., 2012, 22, 6655-6668.

72. I. S. Kim, G. E. Blomgren, and P. N. Kumta, Electrochem. Solid-State Lett., 2003, 6, A157-A161.

73. I. S. Kim, G. E. Blomgren, and P. N. Kumta, J. Power Sources, 2004, 130, 275-280.

74. Z. Y. Zeng, J. P. Tu, Y. Z. Yang, J. Y. Xiang, X. H. Huang, F. Mao, and M. Ma, Electrochim. Acta, 2008, 53, 2724-2728.

75. Y. Liu, K. Hanai, T. Matsumura, N. Imanishi, A. Hirano, and Y. Takeda, Electrochem. Solid-State Lett., 2004, 7, A492-A495.

76. K. Hanai, Y. Liu, N. Imanishi, A. Hirano, M. Matsumura, T. Ichikawa, and Y. Takeda, J. Power Sources, 2005, 146, 156-160.

77. H. Mukaibo, T. Osaka, P. Reale, S. Panero, B. Scrosati, and M. Wachtler, J. Power Sources, 2004, 132, 225-228.

78. H. Kim, J. Choi, H. J. Sohn, and T. Kang, J. Electrochem. Soc., 1999, 146, 4401-4405.

79. M. Stjerndahl, H. Bryngelsson, T. Gustafsson, J. T. Vaughey, M. M. Thackeray, and K. Edström, Electrochim. Acta, 2007, 52, 4947-4955.

80. J. Yin, M. Wada, S. Yoshida, K. Ishihara, S. Tanase, and T. Sakai, J. Electrochem. Soc., 2003, 150, A1129-A1135.

81. T. L. Kulova, A. M. Skundin, Y. V. Pleskov, E. I. Terukov, and O. I. Kon'Kov, J. Electroanal. Chem., 2007, 600, 217-225.

82. T. Takamura, S. Ohara, M. Uehara, J. Suzuki, and K. Sekine, J. Power Sources, 2004, 129, 96-100.

83. C. Yu, X. Li, T. Ma, J. Rong, R. Zhang, J. Shaffer, Y. An, Q. Liu, B. Wei, and H. Jiang, Adv. Energy Mater., 2012, 2, 68-73.

84. P. R. Abel, A. M. Chockla, Y.-M. Lin, V. C. Holmberg, J. T. Harris, B. A. Korgel, A. Heller, and C. B. Mullins, ACS Nano, 2013, 7, 2249-2257.

85. Y. Yao, M. T. McDowell, I. Ryu, H. Wu, N. Liu, L. Hu, W. D. Nix, and Y. Cui, Nano Lett., 2011, 11, 2949-2954.

86. B. L. Ellis, and L. F. Nazar, Curr. Opin. Solid State Mater. Sci., 2012, 16, 168-177.

87. V. Palomares, P. Serras, I. Villaluenga, K. B. Hueso, J. Carretero-González, and T. Rojo, Energy Environ. Sci., 2012, 5, 5884-5901.

88. K. B. Hueso, M. Armand, and T. Rojo, Energy Environ. Sci., 2013, 6, 734-749.

89. J. M. Tarascon, Phil. Trans. R. Soc. A, 2010, 368, 3227-3241.

90. M. D. Slater, D. Kim, E. Lee, and C. S. Johnson, Adv. Funct. Mater., 2013, 23, 947-958.

91. D. Buchholz, A. Moretti, R. Kloepsch, S. Nowak, V. Siozios, M. Winter, and S. Passerini, Chem. Mater., 2013, 25, 142-148.

92. S. W. Kim, D.-H. Seo, X. Ma, G. Ceder, and K. Kang, Adv. Energy Mater., 2012, 2, 710-721.

93. J. L. Murray, Bull. Alloy Phase Diagrams, 1983, 4, 407-410.

94. C. Y. Chen, K. Matsumoto, T. Nohira, C. Ding, T. Yamamoto, and R. Hagiwara, Electrochim. Acta, 2014, 133, 583-588.

95. X. Xia, and J. R. Dahn, Electrochem. Solid-State Lett., 2012, 15, A1-A4.

96. S. M. Oh, S. T. Myung, C. S. Yoon, J. Lu, J. Hassoun, B. Scrosati, K. Amine, and Y. K. Sun, Nano Lett., 2014, 14, 1620-1626.

97. J. Billaud, G. Singh, A. R. Armstrong, E. Gonzalo, V. Roddatis, M. Armand, T. Rojo, and P. G. Bruce. Energy Environ. Sci., 2014, 7, 1387-1391.

98. L. Wang, Y. Lu, J. Liu, M. Xu, J. Cheng, D. Zhang, and J. B. Goodenough, Angew. Chem., Int. Ed., 2013, 52, 1964 –1967.

99. C. Zhu, K. Song, P. A. van Aken, Y. Yu, and J. Maier, Nano Lett., 2014, 14, 2175–2180.

100. H. Kim, Y. U. Park, K. Y. Park, H. D. Lim, J. Hong, and K. Kang, Nano Energy, 2014, 4, 97-104.

101. M. Yao, K. Kuratani, T. Kojima, N. Takeichi, H. Senoh, and T. Kiyobayashi, Sci. Rep., 2014, 4.

102. T. R. Jow, and L. W. Shacklette, J. Electrochem. Soc., 1989, 136, 1-6.

103. S. Y. Hong, Y. Kim, Y. Park, A. Choi, N. S. Choi, and K. T. Lee, Energy Environ. Sci., 2013, 6, 2067-2081.

104. Y. Shao, J. Xiao, W. Wang, M. Engelhard, X. Chen, Z. Nie, M. Gu, L. V. Saraf, G. Exarhos, J. G. Zhang, and J. Liu, Nano Lett., 2013, 13, 3909–3914.

105. T. T. Tran, and M. N. Obrovac, J. Electrochem. Soc., 2011, 158, A1411-A1416.

106. A. Metrot, D. Guérard, D. Billaud, and A. Hérold, Synth. Met., 1980, 1, 363-369.

107. D. A. Stevens, and J. R. Dahn, J. Electrochem. Soc., 2000, 147, 1271-1273.

108. S. Komaba, W. Murata, T. Ishikawa, N. Yabuuchi, T. Ozeki, T. Nakayama, A. Ogata, K. Gotoh, and K. Fujiwara, Adv. Funct. Mater., 2011, 21, 3859-3867.

109. X. Zhou, and Y.-G. Guo, ChemElectroChem, 2014, 1, 83-86.

110. W. Luo, J. Schardt, C. Bommier, B. Wang, J. Razink, J. Simonsen, and X. Ji, J. Mater. Chem. A, 2013, 1, 10662-10666.

111. K. Tang, L. Fu, R. J. White, L. Yu, M.-M. Titirici, M. Antonietti, and J. Maier, Adv, Energy Mater., 2012, 2, 873–877.

112. J. Ding, H. Wang, Z. Li, A. Kohandehghan, K. Cui, Z. Xu, B. Zahiri, X. Tan, E. Memarzadeh Lotfabad, B. C. Olsen, and D. Mitlin, ACS Nano, 2013, 7, 11004-11015.

113. E. Memarzadeh Lotfabad, J. Ding, K. Cui, A. Kohandehghan, W. P. Kalisvaart, M. Hazelton, and D. Mitlin, ACS Nano, 2014, 8, 7115–7129.

114. Y. Xu, E. Memarzadeh Lotfabad, H. Wang, B. Farbod, Z. Xu, A. Kohandehghan, and D. Mitlin, Chem. Commun., 2013, 49, 8973-8975.

115. L. Wu, D. Buchholz, D. Bresser, L. G. Chagas, and S. Passerini, J. Power Sources, 2014, 251, 379-385.

116. K. T. Kim, G. Ali, K. Y. Chung, H. Yashiro, Y. K. Sun, J. Lu, K. Amine, and S. T. Myung, Nano Lett., 2014, 14, 416–422.

117. J. C. P. Flores, C. Baehtz, A. Kuhn, and F. G. Alvarado, J. Mater. Chem. A, 2014, 2, 1825-1833.

118. G. Rousse, M. E. A. Y. De Dompablo, P. Senguttuvan, A. Ponrouch, J. M. Tarascon, and M. R. Palacín, Chem. Mater., 2013, 25, 4946-4956.

119. X. Yu, H. Pan, W. Wan, C. Ma, J. Bai, Q. Meng, S. N. Ehrlich, Y. S. Hu, and X. Q. Yang, Nano Lett., 2013, 13, 4721-4727.

120. Y. Yan, Y. X. Yin, Y. G. Guo, and L. J. Wan, Adv. Energy Mater., 2014.

121. L. David, R. Bhandavat, and G. Singh, ACS Nano, 2014, 8, 1759–1770.

122. Y. Liu, B. H. Zhang, S. Y. Xiao, L. L. Liu, Z. B. Wen, and Y. P. Wu, Electrochi. Acta, 2014, 116, 512–517.

123. C. Luo, Y. Xu, Y. Zhu, Y. Liu, S. Zheng, Y. Liu, A. Langrock, and C. Wang, ACS Nano, 2013, 9, 8003–8010.

124. Z. Jian, B. Zhao, P. Liu, F. Li, M. Zheng, M. Chen, Y. Shi, and H. Zhou, Chem. Commun., 2014, 50, 1215-1217.

125. H. Zhu, Z. Jia, Y. Chen, N. Weadock, J. Wan, O. Vaaland, X. Han, T. Li, and L. Hu, Nano Lett., 2013, 13, 3093–3100.

126. K. Dai, H. Zhao, Z. Wang, V. Battaglia, and G. Liu, J. Power Sources, 2014, 263, 276-279.

127. L. Baggetto, H. Y. Hah, C. E. Johnson, C. A. Bridges, J. A. Johnson, and G. M. Veith, Phys. Chem. Chem. Phys., 2014, 16, 9538-9545.

128. M. He, K. V. Kravchyk, M. Walter, and M. V. Kovalenko, Nano Lett., 2014, 14, 1255–1262.

129. L. D. Ellis, B. N. Wilkes, T. D. Hatchard, and M. N. Obrovac, J. Electrochem. Soc., 2014, 161, A416-A421.

130. Y. Kim, Y. Park, A. Choi, N.-S. Choi, J. Kim, J. Lee, J. H. Ryu, S. M. Oh, and K. T. Lee, Adv. Mater., 2013, 25, 3045-3049.

131. Y. Wang, D. Su, C. Wang, and G. Wang, Electrochem. Commun., 2013, 29, 8-11.

132. B. Qu, C. Ma, G. Ji, C. Xu, J. Xu, Y. S. Meng, T. Wang, and J. Y. Lee, Adv. Mater., 2014.

133. J. Qian, Y. Xiong, Y. Cao, X. Ai, and H. Yang, Nano Lett., 2014, 14, 1865–1869.

134. W. J. Li, S. L. Chou, J. Z. Wang, H. K. Liu, and S. X. Dou, Nano Lett., 2013, 13, 5480-5484.

135. J. Qian, X. Wu, Y. Cao, X. Ai, and H. Yang, Angew. Chem., 2013, 125, 4731-4734.

136. L. Wu, X. Hu, J. Qian, F. Pei, F. Wu, R. Mao, X. Ai, H. Yang, and Y. Cao, Energy Environ. Sci., 2014, 7, 323-328.

137. Y. W. Denis, P. V. Prikhodchenko, C. W. Mason, S. K. Batabyal, J. Gun, S. Sladkevich, A. G. Medvedev, and O. Lev, Nat. Commun., 2013, 4.

138. B. Farbod, K. Cui, W. P. Kalisvaart, M. Kupsta, B. Zahiri, A. Kohandehghan, E. Memarzadeh, Z. Li, E. J. Luber, and D. Mitlin, ACS Nano, 2014, 8, 4415–4429.

139. M. H. Seo, M. Park, K. T. Lee, K. Kim, J. Kim, and J. Cho. Energy Environ. Sci., 2011, 4, 425-428.

140. C. K. Chan, X. F. Zhang, and Y. Cui, Nano Lett., 2008, 8, 307–309.

141. T. Kennedy, E. Mullane, H. Geaney, M. Osiak, C. O'Dwyer, and K. M. Ryan, Nano Lett., 2014, 14, 716–723.

142. Y. Cao, L. Xiao, M. L. Sushko, W. Wang, B. Schwenzer, J. Xiao, Z. Nie, L. V. Saraf, Z. Yang, and J. Liu, Nano Lett., 2012, 12, 3783-3787.

143. Y. Liu, Y. Xu, Y. Zhu, J. N. Culver, C. A. Lundgren, K. Xu, and C. Wang, ACS Nano, 2013, 7, 3627-3634.

144. Y. Cao, L. Xiao, W. Wang, D. Choi, Z. Nie, J. Yu, L. V. Saraf, Z. Yang, and J. Liu, Adv. Mater., 2011, 23, 3155-3160.

145. V. L. Chevrier, and G. Ceder, J. Electrochem. Soc., 2011, 158, A1011-A1014.

146. L. Baggetto, J. K. Keum, J. F. Browning, and G. M. Veith, Electrochem. Commun., 2013, 34, 41-44.

147. P. R. Abel, Y. M. Lin, T. de Souza, C. Y. Chou, A. Gupta, J. B. Goodenough, G. S. Hwang, A. Heller, and C. B. Mullins, J. Phys. Chem. C, 2013, 117, 18885-18890.

148. J. Sangster, and A. D. Pelton, J. Phase Equilib., 1997, 18, 295-297.

149. S. Komaba, Y. Matsuura, T. Ishikawa, N. Yabuuchi, W. Murata, and S. Kuze, Electrochem. Commun., 2012, 21, 65-68.

150. J. Graetz, C. C. Ahn, R. Yazami, and B. Fultz, J. Electrochem. Soc., 2004, 151, A698-A702.

151. M. Roberts, P. Johns, J. Owen, D. Brandell, K. Edstrom, G. El Enany, C. Guery, D. Golodnitsky, M. Lacey, C. Lecoeur, H. Mazor, E. Peled, E. Perre, M. M. Shaijumon, P. Simon, and P. L. Taberna, J. Mater. Chem., 2011, 21, 9876.

152. R. Marom, S. F. Amalraj, N. Leifer, D. Jacob, and D. Aurbach, J. Mater. Chem., 2011, 21, 9938.

153. M. R. Palacin, Chem. Soc. Rev., 2009, 38, 2565.

154. M. Liang, and L. Zhi, J. Mater. Chem., 2009, 19, 5871.

155. H. K. Liu, Z. P. Guo, J. Z. Wang, and K. Konstantinov, J. Mater. Chem., 2010, 20, 10055.

156. V. L. Chevrier, J. W. Zwanziger, and J. R. Dahn, Can. J. Phys., 2009, 87, 625.

157. J. Li, and J. R. Dahn, J. Electrochem. Soc., 2007, 154, A156.

158. S. D. Beattie, D. Larcher, M. Morcrette, B. Simon, and J. M. Tarascon, J. Electrochem. Soc., 2008, 155, A158.

159. T. D. Hatchard, and J. R. Dahn, J. Electrochem. Soc., 2004, 151, A838.

160. V. L. Chevrier, and J. R. Dahn, J. Electrochem. Soc., 2010, 157, A392.

161. J. L. G. Cámer, J. Morales, and L. Sánchez, J. Mater. Chem., 2011, 21, 811.

162. M. Gu, Y. Li, X. Li, S. Hu, X. Zhang, W. Xu, S. Thevuthasan, D. R. Baer, J. G. Zhang, J. Liu, and C. Wang, ACS Nano, 2012, 6, 8439.

163. Y. Oumellal, N. Delpuech, D. Mazouzi, N. Dupre, J. Gaubicher, P. Moreau, P. Soudan, B. Lestriez, and D. Guyomard, J. Mater. Chem., 2011, 21, 6201.

164. L. Y. Beaulieu, T. D. Hatchard, A. Bonakdarpour, M. D. Fleischauer, and J. R. Dahn, J. Electrochem. Soc., 2003, 150, A1457.

165. H. Haftbaradaran, and H. Gao, Appl. Phys. Lett., 2012, 100, 121907.

166. U. Kasavajjula, C. Wang, and A.J. Appleby, J. Power Sources, 2007, 163, 1003.

167. J. Cho, J. Mater. Chem., 2010, 20, 4009.

168. A. Gohier, B. Laïk, K. H. Kim, J. L. Maurice, J. P. Pereira-Ramos, C. S. Cojocaru, and P. T. Van, Adv. Mater., 2012, 24, 2592.

169. C. K. Chan, H. Peng, J. Liu, K. McIlwrath, X. F. Zhang, R. A. Huggins, and Y. Cui, Nat. Nanotechnol., 2008, 3, 31.

170. C. K. Chan, R. Ruffo, S. S. Hong, R. A. Huggins, and Y. Cui, J. Power Sources, 2009, 189, 34.

171. X. H. Liu, H. Zheng, L. Zhong, S. Huang, K. Karki, L. Q. Zhang, Y. Liu, A. Kushima, W. T. Liang, J. W. Wang, J. H. Cho, E. Epstein, S. A. Dayeh, S. T. Picraux, T. Zhu, J. Li, J. P. Sullivan, J. Cumings, C. Wang, S. X. Mao, Z. Z. Ye, S. Zhang, and J. Y. Huang, Nano Lett., 2011, 11, 3312.

172. J. W. Choi, J. McDonough, S. Jeong, J. S. Yoo, C. K. Chan, and Y. Cui, Nano Lett., 2010, 10, 1409.

173. G. P. Yin, Y. H. Xu, Y. L. Ma, P. J. Zuo, and X. Q. Cheng, J. Mater. Chem., 2010, 20, 3216.

174. H. Jung, Y. U. Kim, M. S. Sung, Y. Hwa, G. Jeong, G. B. Kim, and H. J. Sohn, J. Mater. Chem., 2011, 21, 11213.

175. C. Du, M. Chen, L. Wang, and G. Yin, J. Mater. Chem., 2011, 21, 15692.

176. Z. Chen, Y. Qin, K. Amine, and Y. K. Sun, J. Mater. Chem., 2010, 20, 7606.

177. L. Q. Zhang, X. H. Liu, Y. Liu, S. Huang, T. Zhu, L. Gui, S. X. Mao, Z. Z. Ye, C. M. Wang, J. P. Sullivan, and J. Y. Huang, ACS Nano, 2011, 5, 4800 and references therein.

178. E. L. Memarzadeh, W. P. Kalisvaart, A. Kohandehghan, B. Zahiri, C. M. B. Holt, and D. Mitlin, J. Mater. Chem., 2012, 22, 6655.

179. H. Chen, Y. Xiao, L. Wang, and Y. Yang, , J. Power Sources, 2011, 196, 6657.

180. I. Ryu, J. W. Choi, Y. Cui and W. D. Nix, J. Mech. Phys. Solid, 2011, 59, 1717.

181. H. Okamoto, Desk Handbook "Phase Diagrams for Binary Alloys", ASM International, 2000, p. 527.

182. H. Kim, J. Choi, H. J. Sohn, and T. Kang, J. Electrochem. Soc., 1999, 146, 4401.

183. T. Moriga, J. Solid State Chem., 2000, 153, 386.

184. G. A. Roberts, E. J. Cairns, and J. A. Reimer, J. Power Sources, 2002, 110, 424.

185. S. W. Song, K. A. Striebel, X. Song, and E. J. Cairns, J. Power Sources, 2003, 119-121, 110.

186. G. Ji, Y. Ma, and J. Y. Lee, J. Mater. Chem., 2011, 21, 9819.

187. K. Xu, and A. von Cresce, J. Mater. Chem., 2011, 21, 9849.

188. A. J. Smith, J. C. Burns, X. Zhao, D. Xiong, and J. R. Dahn, J. Electrochem. Soc., 2011, 158, A447.

189. C. K. Chan, R. Ruffo, S. S. Hong, and Y. Cui, J. Power Sources, 2009, 189, 1132.

190. Y. C. Yen, S. C. Chao, H. C. Wu, and N. L. Wu, J. Electrochem. Soc., 2009, 156, A95.

191. W. Xu, S. S. S. Vegunta, and J. C. Flake, ECS Transactions, 2011, 33, 55.

192. http://www.mtixtl.com/ElectrolyteLiPF6forLiCoO2Lithium-ionbatteryRandD1KginaSafeStainle.aspx

193. G. S. Doerk, N. Ferralis, C. Carraro, and R. Maboudian, J. Mater. Chem., 2008, 18, 5376.

194. L. Brewer, Chem. Rev., 1953, 52, 1.

195. B. Key, R. Bhattacharyya, M. Morcrette, V. Seznec, J. M. Tarascon, and C. P. Grey, J. Am. Chem. Soc., 2009, 131, 9239.

196. V. L. Chevrier, J. W. Zwanziger, and J. R. Dahn, J. Alloy Compd., 2010, 496, 25.

197. H. C. M. Knoops, L. Baggetto, E. Langereis, M. C. M. van de Sanden, J. H. Klottwijk, F. Roozeboom, R. A. H. Niessen, P. H. L. Notten, and W. M. M. Kessels, J. Electrochem. Soc., 2008, 155, G287.

198. K. Karki, E. Epstein, J. H. Cho, Z. Jia, T. Li, S. T. Picraux, C. Wang, and J. Cumings, Nano Lett., 2012, 12, 1392.

199. W. J. Zhang, J. Power Sources, 2011, 196, 13.

200. J. Morales, R. Trócoli, and J. Santos-Peña, Electrochem. Solid St. Lett., 2009, 12, A145.

201. S. P. V. Nadimpalli, V. A. Sethuraman, S. Dalave, B. Lucht, M. J. Chon, V. B. Shenoy, and P. R. Guduru, J. Power Sources, 2012, 215, 145.

202. NIST XPS database at http://srdata.nist.gov/xps/Default.aspx

203. K. Xu, Chem. Rev., 2004, 104, 4303.

204. T. Kawamura, A. Kimura, M. Egashira, S. Okada, and J. I. Yamaki, J. Power Sources, 2002, 104, 260.

205. J. C. Lee, and M. H. Litt, Macromolecules, 2000, 33, 1618.

206. A. M. Chockla, T. D. Bogart, C. M. Hessel, K. C. Klavetter, C. B. Mullins, and B. A. Korgel, J. Phys. Chem. C, 2012, 116, 18079.

207. N. S. Choi, Z. Chen, S. A. Freunberger, X. Ji, Y. K. Sun, K. Amine, G. Yushin, L. F. Nazar, J. Cho and P. G. Bruce, Angew. Chem. Int. Ed., 2012, 51, 9994.

208. M. Armand and J. M. Tarascon, Nature, 2008, 451, 652.

209. B. Dunn, H. Kamath and J. M. Tarascon, Science, 2011, 334, 928.

210. H. J. Kim, Z. H. Wen, K. H. Yu, O. Mao and J. H. Chen, J. Mater. Chem., 2012, 22, 15514.

211. S. Mao, Z. H. Wen, Haejune Kim, G. H. Lu, P. Hurley and J. H. Chen, ACS Nano, 2012, 6, 7505.

212. H. Okamoto, "Phase Diagrams for Binary Alloys", ASM International, 2000, ISBN 0-87170-682-2.

213. Z. H. Wen, S. M. Cui, H. J. Kim, S. Mao, K. H. Yu, G. H. Lu, H. H. Pu, O. Mao and J. H. Chen, J. Mater. Chem., 2012, 22, 3300.

214. W. Liang, H. Yang, F. Fan, Y. Liu, X. H. Liu, J. Y. Huang, T. Zhu and S. Zhang, ACS Nano, 2013, 7, 3427.

215. C. Wang, Y. S. Chui, R. G. Ma, T. Wong, J. Ren, Q. H. Wu, X. Chen and W. Zhang, J. Mater. Chem. A, 2013, 1, 10092-10098.

216. J. W. Wang, Y. He, F. Fan, X. H. Liu, S. Xia, Y. Liu, C. T. Harris, H. Li, J. Y. Huang and T. Zhu, Nano Lett., 2013, 13, 709.

217. X. Zhou and Y. G. Guo, J. Mater. Chem. A, 2013,1, 9019-9023.

218. J. Li, A. Smith, R. J. Sanderson, T. D. Hatchard, R. A. Dunlap and J. R. Dahn, J. Electrochem. Soc., 2009, 156, A283.

219. M. R. Zamfir, H. T. Nguyen, E. Moyen, Y. H. Lee and D. Pribat, J. Mater. Chem. A, 2013,1, 9566-9586.

220. K. Huang, F. Sun, T. Gao, Y. P. Liu, J. X. Zhong, X. L. Wei and X. Qi, Nanoscale, 2013,5, 8586-8592.

221. R. A. DiLeo, M. J. Ganter, M. N. Thone, M. W. Forney, J. W. Staub, R. E. Rogers and B. J. Landi, Nano Energy, 2013, 2, 268.

222. Y. Oumellal, N. Delpuech, D. Mazouzi, N. Dupre, J. Gaubicher, P. Moreau, P. Soudan, B. Lestriez and D. Guyomard, J. Mater. Chem., 2011, 21, 6201.

223. C. Yue, Y. Yu, J. Yin, T. Wong, Y. Zang, J. Li and J. Kang, J. Mater. Chem. A, 2013, 1, 7896.

224. H. Wu and Y. Cui, Nano Today, 2012, 7, 414.

225. C. K. Chan, H. Peng, G. Liu, K. McIlwrath, X. F. Zhang, R. A. Huggins and Y. Cui, Nature Nanotech., 2008, 3, 31.

226. R. Mukherjee, R. Krishnan, T. M. Lu and N. Koratkar, Nano Energy, 2012, 1, 518.

227. H. C. M. Knoops, M. E. Donders, M. C. M. van de Sanden, P. H. L. Notten and W. M. M. Kessels, J. Vac. Sci. Technol. A, 2012, 30, 010801.

228. H. T. Nguyen, M. R. Zamifir, L. D. Duong, Y. H. Lee, P. Bondavalli and D. Pribat, J. Mater. Chem., 2012, 22, 24618.

229. Y. Hwa, W. S. Kim, B C. Yu, HS. Kim, S. H. Hong and H. J. Sohn, J. Mater. Chem. A, 2013, 1, 3733.

230. E. L. Memarzadeh, W. P. Kalisvaart, A. Kohandehghan, B. Zahiri, C. M. B. Holt and D. Mitlin, J. Mater. Chem., 2012, 22, 6655.

231. N. S. Choi, Y. Yao, Y. Cui and J. Cho, J. Mater. Chem., 2011, 21, 9825.

232. Y. Zhao, X. Liu, H. Li, T. Zhai and H. Zhou, Chem. Commun., 2012, 48, 5079.

233. T. Song, J. Xia, J. H. Lee, D. H. Lee, M. S. Kwon, J. M. Choi, J. Wu, S. K. Doo, H. Chang, W. I. Park, D. S. Zang, H. Kim, Y. Huang, K. C. Hwang, J. A. Rogers and U. Paik, Nano Lett., 2010, 10, 1710.

234. H. Wu, G. Chan, J. W. Choi, I. Ryu, Y. Yao, M. T. McDowell, S. W. Lee, A. Jackson, Y. Yang, L. Hu and Y. Cui, Nature Nanotech., 2012, 7, 310.

235. Y. Yao, M. T. McDowell, I. Ryu, H. Wu, N. Liu, L. Hu, W. D. Nix and Y. Cui, Nano Lett, 2011, 11, 2949.

236. Z. Wen, G. Lu, S. Mao, H. Kim, S. Cui, K. Yu, X. Huang, P. T. Hurley, O. Mao and J. Chen, Electrochem. Comm., 2013, 29, 67.

237. E. Radvanyi, E. De Vito, W. Porcher, J. Danet, P. Desbois, J. F. Colin and S. J. Si Larbi, J. Mater. Chem. A, 2013, 1, 4956.

238. C. K. Chan, R. Ruffo, S. S. Hong and Y. Cui, J. Power Sources, 2009, 189, 1132.

239. A. Kohandehghan, P. Kalisvaart, M. Kupsta, B. Zahiri, B. S. Amirkhiz, Z. Li, E. Memarzadeh, L. A. Bendersky and D. Mitlin, J. Mater. Chem. A, 2013, 1, 1600.

240. Y. Liu, K. Huang, Y. Fan, Q. Zhang, F. Sun, T. Gao, L. Yang and J. Zhong, Electrochimica Acta, 2013, 88, 766.

241. A. M. Chockla, T. D. Bogart, C. M. Hessel, K. C. Klavetter, C. B. Mullins and B. A. Korgel, J. Phys. Chem. C, 2012, 116, 18079.

242. Y. J. Cho, H. S. Kim, H. Im, Y. Myung, G. B. Jung, C. W. Lee, J. Park, M. H. Park, J. Cho and H. S. Kang, J. Phys. Chem. C, 2011, 115, 9451.

243. H. Chen, Y. Xiao, L. Wang and Y. Yang, J. Power Sources, 2011, 196, 6657.

244. Y. Yao, N. Liu, M. T. McDowell, M. Pasta and Y. Cui, Energy Environ. Sci., 2012, 5, 7927.

245. M. T. McDowell, S. W. Lee, C. Wang and Y. Cui, Nano Energy, 2012, 1, 401.

246. X. H. Liu, L. Q. Zhang, L. Zhong, Y. Liu, H. Zheng, J. W. Wang, J. H. Cho, S. A. Dayeh, S. T. Picraux and J. P. Sullivan, Nano Lett, 2011, 11, 2251.

247. W. Wang, M. Tian, Y. Wei, S. H. Lee, Y. C. Lee and R. Yang, Nano Energy, 2013, 2, 943-950.

248. L. Q. Zhang, X. H. Liu, Y. Liu, S. Huang, T. Zhu, L. Gui, S. X. Mao, Z. Z. Ye, C. M. Wang and J. P. Sullivan, ACS Nano, 2011, 5, 4800.

249. M. T. McDowell, S. W. Lee, I. Ryu, H. Wu, W. D. Nix, J. W. Choi and Y. Cui, Nano Lett, 2011, 11, 4018.

250. B. W. Sheldon, S. K. Sony, X. Xiao and Y. Qi, Electrochem. Solid State Lett., 2012, 15, A9.

251. S. M. Dong, X. Chen, X. Y. Zhang, and G. Cui, Coordin. Chem. Rev., 2013, 257, 1946.

252. J. Chen, K. Takanabe, R. Ohnishi, D. Lu, S. Okada, H. Hatasawa, H. Morioka, M. Antonietti, J. Kubota and K. Domen, Chem. Commun., 2010, 46, 7492.

253. P. He, Y. Wang and H. Zhou, Chem. Commun., 2011, 47, 10701.

254. N. Savvides and B. Window, J. Appl. Phys., 1988, 64, 225.

255. P. Han, Y. Yue, X. Wang, W. Ma, S. Dong, K. Zhang, C. Zhang and G. Cui, J. Mater. Chem., 2012, 22, 24918.

256. S. Dong, X. Chen, L. Gu, X. Zhou, L. Li, Z. Liu, P. Han, H. Xu, J. Yao, H. Wang, X. Zhang, C. Shang, G. Cui and L. Chen, Energy Environ. Sci., 2011, 4, 3502.

257. C. W. Liu, J. An, R. S. Guo, Y. Li and L. Liu, J. Alloy. Compd., 2013, 563, 33.

258. G. Xu, L. Zhang, C. Guo, L. Gu, X. Wang, P. Han, K. Zhang, C. Zhang and G. Cui, Electrochim. Acta, 2012, 345.

259. J. Zhang, J. Zhang, W. Cai, F. Zhang, L. Yu, Z. Wu and Z. Zhang, J. Power Sources, 2012, 211, 133.

260. Y. Yue, P. Han, X. He, K. Zhang, Z. Liu, C. Zhang, S. Dong, L. Gu and G. Cui, J. Mater. Chem., 2012, 22, 4938.

261. I. Kim, P. N. Kumta and G. E. Blomgren, Electrochem. Solid State Lett., 2000, 3, 493.

262. J. T. Zhao, L. Hu, S. Jiao, J. Hou and H. Zhu, Phys. Chem. Chem. Phys, 2013, 15, 10472.

263. C. Marichy, M. Bechelany and N. Pinna, Adv. Mater., 2012, 24, 1017.

264. X. Meng, X. Q. Yang and X. Sun, Adv. Mater., 2012, 24, 3589.

265. M. Q. Snyder, S. A. Trebukhova, B. Ravdel, M. C. Wheeler, J. DiCarlo, C. P. Tripp and W. J. DeSisto, J. Power Sources, 2007, 165, 379.

266. H. C. M. Knoops, L. Baggetto, E. Langereis, M. C. M. van de Sanden, J. H. Klootwijk, F. Roozeboom, R. A. H. Niessen, P. H. L. Notten and W. M. M. Kessels, J. Electrochem. Soc., 2008, 155, G287.

267. R. F. Egerton, Electron energy-loss spectroscopy in the electron microscope, Springer, New York, 2011

268. C. Ahn, R. Burgner and O. Krivanek, EELS Atlas: A reference guide of electron energy loss spectra covering all stable elements, Center for Solid State Science, Arizona State Univ., 1983

269. L. Brewer, Chem. Rev., 1953, 52, 1.

270. H. O. Pierson, Handbook of Refractory Carbides and Nitrides, Properties, Characteristics, Processing and Applications, William Andrew, 1996, ISBN 0-8155-1392-5

271. N. C. Saha and H. G. Tompkins, J. Appl. Phys., 1992, 72, 3072.

272. L. Baggetto, R. A. H. Niessen, F. Roozeboom and P. H. L. Notten, Adv. Mater., 2008, 18, 1057.

273. K. Karki, E. Epstein, J.H. Cho, Z. Jia, T. Li, T. Picraux, C. Wang and J. Cumings, Nano Lett., 2012, 12, 1392.

274. E. L. Memarzadeh, W.P. Kalisvaart, K. Cui, A. Kohandehghan, M. Kupsta, B.C. Olsen and D. Mitlin, Phys. Chem. Chem. Phys., 2013, 15, 13646.

275. M. T. McDowell and Y. Cui, Adv. Energy Mater., 2011, 1, 894.

276. R. Ruffo, S. S. Hong, C. K. Chan, R. A. Huggins and Y. Cui, J. Phys. Chem. C, 2009, 113, 11390.

277. M. D. Levi and D. Aurbach, J. Phys. Chem. B, 1997, 101, 4630.

278. V. Etacheri, A. Geiger, Y. Gofer, G. A. Roberts, I. C. Stefan, R. Fasching and D. Aurbach, Langmuir, 2012, 28, 6175.

279. L. Baggetto, J. F. M. Oudenhoven, T. van Dongen, J. H. Klootwijk, M. Mulder, R. A. H. Niessen, M. H. J. M. de Croon and P. H. L. Notten, J. Power Sources, 2009, 189, 402.

280. D. E. A. Salas, A. K. Sra, K. Roodenko, Y. J. Chabal and C. L. Hinkle, J. Phys. Chem. C, 2012, 116, 9072.

281. F. Kauffmann, B. Ji, G. Dehm, H. Gao and E. Arzt, Scripta materialia, 2005, 52, 1269.

282. K. W. Schroder, H. Celio, L. J. Webb and K. J. Stevenson, J. Phys. Chem. C, 2012, 116, 19737.

283. NIST XPS database at http://srdata.nist.gov/xps/Default.aspx.

284. B. Dunn, H. Kamath, and J. –M. Tarascon. Science, 2011, 334, 928-935.

285. V. Etacheri, R. Marom, R. Elazari, G. Salitra, and D. Aurbach. Energy Environ. Sci., 2011,4, 3243-3262

286. J. Liu. Adv. Funct. Mater., 2013, 23, 924-928.

287. Q. Gao, G. Meng, A. Nie, F. Mashayek, C. Wang, G. M. Odegard, and R. S. Yassar. Chem. Mater., 2014, 26, 1660–1669.

288. A. Mauger, and C. Julien. Ionics, 2014, 20, 751-787.

289. M. R. Zamfir, H. T. Nguyen, E. Moyen, Y. H. Lee, and D. Pribat. J. Mater. Chem. A, 2013, 1, 9566-9586.

290. U. Kasavajjula, C. Wang, and A. J. Appleby. J. Power Sources, 2007, 163, 1003-1039.

291. S. Sim, P. Oh, S. Park, and J. Cho. Adv. Mater., 2013, 25, 4498-4503.

292. Y. Liu, X. Guo, J. Li, Q. Lv, T. Ma, W. Zhu, and X. Qiu. J. Mater. Chem. A, 2013, 1, 14075-14079.

293. X. Huang, H. Pu, J. Chang, S. Cui, P. B. Hallac, J. Jiang, P. T. Hurley, and J. Chen. ACS Appl. Mater. Interfaces, 2013, 5, 11965-11970.

294. X. H. Liu, L. Q. Zhang, L. Zhong, Y. Liu, H. Zheng, J. W. Wang, J. –H. Cho, S. A. Dayeh, S. T. Picraux, J. P. Sullivan, S. X. Mao, Z. Z. Ye, and J. Y. Huang. Nano Lett., 2011, 11, 2251-2258.

295. C. R. Becker, K. E. Strawhecker, Q. P. McAllister, and C. A. Lundgren. ACS Nano, 2013, 7, 9173-9182.

296. X. Su, Q. Wu, J. Li, X. Xiao, A. Lott, W. Lu, B. W. Sheldon, and J. Wu. Adv. Energy Mater., 2014, 4, 1-23.

297. X. H. Liu, J. W. Wang, S. Huang, F. Fan, X. Huang, Y. Liu, S. Krylyuk, J. Yoo, S. A. Dayeh, A. V. Davydov, S. X. Mao, S. T. Picraux, S. Zhang, J. Li, T. Zhu, and J. Yu Huang. Nat. Nanotechnol., 2012, 7, 749-756.

298. H. Ghassemi, M. Au, N. Chen, P. A. Heiden, and R. S. Yassar. ACS Nano, 2011, 5, 7805–7811.

299. N. Li, S. Jin, Q. Liao, H. Cui, and C. X. Wang. Nano Energy, 2014, 5, 105-115.

300. N. Liu, W. Li, M. Pasta, and Y. Cui. Front. Phys., 2014, 9, 323-350.

301. S. A. Klankowski, R. A. Rojeski, B. A. Cruden, J. Liu, J. Wu, and J. Li. J. Mater. Chem. A, 2013, 1, 1055-1064.

302. M. W. Forney, R. A. DiLeo, A. Raisanen, M. J. Ganter, J. W. Staub, R. E. Rogers, R. D. Ridgley, and B. J. Landi. J. Power Sources, 2013, 228, 270-280.

303. J. Wan, A. F. Kaplan, J. Zheng, X. Han, Y. Chen, N. J. Weadock, N. Faenza, S. Lacey, T. Li, J. Guo, and L. Hu. J. Mater. Chem. A, 2014, 2, 6051-6057.

304. S. Choi, J. C. Lee, O. Park, M. J. Chun, N. S. Choi, and S. Park. J. Mater. Chem. A, 2013, 1, 10617-10621.

305. P. R. Abel, A. M. Chockla, Y. M. Lin, V. C. Holmberg, J. T. Harris, B. A. Korgel, A. Heller, and C. B. Mullins. ACS Nano, 2013, 7, 2249-2257.

306. E. Memarzadeh Lotfabad, P. Kalisvaart, A. Kohandehghan, K. Cui, M. Kupsta, B. Farbod, and D. Mitlin. J. Mater. Chem. A, 2014, 2, 2504-2516.

307. J. Guo, Z. Yang, and L. A. Archer. J. Mater. Chem. A, 2013, 1, 5709-5714.

308. M. W. Forney, M. J. Ganter, J. W. Staub, R. D. Ridgley, and B. J. Landi. Nano Lett., 2013, 13, 4158–4163.

309. J. H. Cho, and S. T. Picraux. Nano Lett., 2013, 13, 5740–5747.

310. J. H. Cho, X. Li, and S. T. Picraux. J. Power Sources, 2012, 205, 467-473.

311. X. H. Liu, H. Zheng, L. Zhong, S. Huang, K. Karki, L. Q. Zhang, Y. Liu, A. Kushima, W. T. Liang, J. W. Wang, J. H. Cho, E. Epstein, S. A. Dayeh, S. T. Picraux, T. Zhu, J. Li, J. P. Sullivan, J. Cumings, C. Wang, S. X. Mao, Z. Z. Ye, S. Zhang, and J. Y. Huang. Nano Lett., 2011, 11, 3312–3318.

312. H. Yang, S. Huang, X. Huang, F. Fan, W. Liang, X. H. Liu, L. Q. Chen, J. Y. Huang, J. Li, T. Zhu, and S. Zhang. Nano Lett., 2012, 12, 1953–1958.

313. P. Johari, Y. Qi, and V. B. Shenoy. Nano Lett., 2011, 11, 5494–5500.

314. K. Karki, E. Epstein, J. H. Cho, Z. Jia, T. Li, S. T. Picraux, C. Wang, and J. Cumings. Nano Lett., 2012, 12, 1392–1397.

315. A. Kohandehghan, P. Kalisvaart, M. Kupsta, B. Zahiri, B. Shalchi Amirkhiz, Z. Li, E L. Memarzadeh, L. A. Bendersky, and D. Mitlin. J. Mater. Chem. A, 2013, 1, 1600-1612.

316. H. Wu, G. Yu, L. Pan, N. Liu, M. T. McDowell, Z. Bao, and Y. Cui. Nat. Commun., 2013, 4, 1-6.

317. J. Li, C. Yue, Y. Yu, Y. S. Chui, J. Yin, Z. Wu, C. Wang, Y. Zang, W. Lin, J. Li, S. Wu, and Q. Wu. J. Mater. Chem. A, 2013, 1, 14344-14349.

318. M. T. McDowell, S. W. Lee, C. Wang, and Y. Cui. Nano Energy, 2012, 1, 401-410.

319. S. Murugesan, J. T. Harris, B. A. Korgel, and K. J. Stevenson. Chem. Mater., 2012, 24, 1306–1315.

320. E. L. Memarzadeh, W. P. Kalisvaart, A. Kohandehghan, B. Zahiri, C. M. Holt, and D. Mitlin. J. Mater. Chem., 2012, 22, 6655-6668.

321. Y. Yu, L. Gu, C. Zhu, S. Tsukimoto, P. A. van Aken, and J. Maier. Adv. Mater., 2010, 22, 2247-2250.

322. E. Memarzadeh Lotfabad, P. Kalisvaart, K. Cui, A. Kohandehghan, M. Kupsta, B. Olsen, and D. Mitlin. Phys. Chem. Chem. Phys., 2013, 15, 13646-13657.

323. A. Kohandehghan, P. Kalisvaart, K. Cui, M. Kupsta, E. Memarzadeh, and D. Mitlin. J. Mater. Chem. A, 2013, 1, 12850-12861.

324. D. Tang, R. Yi, M. L. Gordin, M. Melnyk, F. Dai, S. Chen, J. Song, and D. Wang. J. Mater. Chem. A, 2014, 2, 10375-10378.

325. H. T. Nguyen, M. R. Zamfir, L. D. Duong, Y. H. Lee, P. Bondavalli, and D. Pribat. J. Mater. Chem., 2012, 22, 24618-24626.

326. G. Jeong, J. G. Kim, M. S. Park, M. Seo, S. M. Hwang, Y. U. Kim, Y. J. Kim, J. H. Kim, and S. X. Dou. ACS Nano, 2014, 8, 2977–2985.

327. L. Xu, C. Kim, A. K. Shukla, A. Dong, T. M. Mattox, D. J. Milliron, and J. Cabana. Nano Lett., 2013, 13, 1800–1805.

328. J. Guo, Z. Yang, and L. A. Archer. J. Mater. Chem. A, 2013, 1, 8710-8715.

329. C. Yue, Y. Yu, J. Yin, T. Wong, Y. Zang, J. Li, and J. Kang. J. Mater. Chem. A, 2013, 1, 7896-7904.

330. W. Ren, C. Wang, L. Lu, D. Li, C. Cheng and J. Liu. J. Mater. Chem. A, 2013, 1, 13433-13438.

331. L. Zhang, C. M. Holt, E. J. Luber, B. C. Olsen, H. Wang, M. Danaie, X. Cui, X. Tan, V. W. Lui, W. P. Kalisvaart, and D. Mitlin. J. Phys. Chem. C, 2011, 115, 24381–24393.

332. R. F. Egerton, Electron energy-loss spectroscopy in the electron microscope, Springer, New York, 3rd edition, 2011.

333. Tadeusz Bronislaw Massalski, Hiroaki Okamoto, Linda Kacprzak, and P.R. Subramanian, Binary Alloy Phase Diagrams, American society for metals, 2nd edition, 1990.

334. E. J. Luber, B. C. Olsen, C. Ophus, and D. Mitlin. Phys. Rev. B, 2010, 82, 085407.

335. W. W. Mullins. J. Appl. Phys., 1957, 28, 333-339.

336. C. Ophus, T. Ewalds, E. J. Luber, and D. Mitlin. Acta Materialia, 2010, 58, 5150-5159.

337. D. Mitlin, A. Misra, V. Radmilovic, M. Nastasi, R. Hoagland, D. J. Embury, J. P. Hirth, and T. E. Mitchell. Philosophical Magazine, 2004, 84, 719-736.

338. M. Gu, Z. Wang, J. G. Connell, D. E. Perea, L. J. Lauhon, F. Gao, and C. Wang. ACS Nano, 2013, 7, 6303-6309.

339. I. A. Courtney, and J. R. Dahn. J. Electrochem. Soc., 1997, 144, 2045-2052.

340. D. Wang, J. Yang, J. Liu, X. Li, R. Li, M. Cai, T. K. Sham, and X. Sun. J. Mater. Chem. A, 2014, 2, 2306-2312.

341. X. Li, X. Meng, J. Liu, D. Geng, Y. Zhang, M. N. Banis, Y. Li, J. Yang, R. Li, X. Sun, M. Cai, M. W. Verbrugge. Adv. Funct. Mater., 2012, 22, 1647–1654.

342. I. A. Courtney, and J. R. Dahn. J. Electrochem. Soc., 1997, 144, 2943-2948.

343. D. Wang, X. Li, J. Yang, J. Wang, D. Geng, R. Li, M. Cai, T.-K. Sham, and X. Sun. Phys. Chem. Chem. Phys., 2013, 15, 3535-3542.

344. S. K. Soni, B. W. Sheldon, X. Xiao, and A. Tokranov. Scripta Materialia, 2011, 64, 307-310.

345. S. K. Soni, B. W. Sheldon, X. Xiao, A. F. Bower, and M. W. Verbrugge. J. Electrochem. Soc., 2012, 159, A1520-A1527.

346. A. Nie, L. Y. Gan, Y. Cheng, H. A. Ardakani, Q. Li, C. Dong, R. Tao, F. Mashayek, H. T. Wang, U. Schwingenschlögl, R. F. Klie, and R. S. Yassar. ACS Nano, 2013, 7, 6203-6211.

347. H. Zheng, Y. Liu, S. X. Mao, J. Wang, and J. Y. Huang. Sci. Rep., 2012, 2, 1-4.

348. M. T. McDowell, and Y. Cui. Adv. Energy Mater., 2011, 1, 894-900.

349. M. D. Levi, and D. Aurbach. J. Phys. Chem. B, 1997, 101, 4630–4640.

350. D. Aurbach, B. Markovsky, M. D. Levi, E. Levi, A. Schechter, M. Moshkovich, and Y. Cohen. J. power sources, 1999, 81-82, 95-111.

351. D. Aurbach. J. Power Sources, 2000, 89, 206-218.

352. V. Etacheri, U. Geiger, Y. Gofer, G. A. Roberts, I. C. Stefan, R. Fasching, and D. Aurbach. Langmuir, 2012, 28, 6175–6184.

353. K. Xu, and A. V. Cresce. J. Mater. Chem., 2011, 21, 9849-9864.

354. D. Liu, and G. Cao. Energy Environ. Sci., 2010, 3, 1218-1237.

355. K. Karki, Y. Zhu, Y. Liu, C. F. Sun, L. Hu, Y. Wang, C. Wang, and J. Cumings. ACS Nano, 2013, 7, 8295–8302.

356. C. K. Chan, R. Ruffo, S. S. Hong, and Y. Cui. J. Power Sources, 2009, 189, 1132-1140.

357. X. Xiao, P. Lu, and D. Ahn. Adv. Mater., 2011, 23, 3911-3915.

358. M. Gu, Y. Li, X. Li, S. Hu, X. Zhang, W. Xu, S. Thevuthasan, D. R. Baer, J. G. Zhang, J. Liu, and C. Wang. ACS Nano, 2012, 6, 8439–8447.

359. H. Liao, K. Karki, Y. Zhang, J. Cumings, and Y. Wang. Adv. Mater., 2011, 23, 4318-4322.

360. L. Q. Zhang, X. H. Liu, Y. Liu, S. Huang, T. Zhu, L. Gui, S. X. Mao, Z. Z. Ye, C. M. Wang, J. P. Sullivan, and J. Y. Huang. ACS Nano, 2011, 5, 4800-4809.

361. V. Etacheri, O. Haik, Y. Goffer, G. A. Roberts, I. C. Stefan, R. Fasching, and D. Aurbach. Langmuir, 2012, 28, 965–976.

362. R. Elazari, G. Salitra, G. Gershinsky, A. Garsuch, A. Panchenko, and D. Aurbach. J. Electrochem. Soc., 2012, 159, A1440-A1445.

363. D. Santhanagopalan, D. Qian, T. McGilvray, Z. Wang, F. Wang, F. Camino, J. Graetz, N. J. Dudney, and Y. S. Meng. J. Phys. Chem. Lett., 2014, 5, 298–303.

364. M. E. Stournara, X. Xiao, Y. Qi, P. Johari, P. Lu, B. W. Sheldon, H. Gao, and V. B. Shenoy. Nano Lett., 2013, 13, 4759–4768.

365. M. Mortazavi, J. Deng, V. B. Shenoy, and N. V. Medhekar. J. Power Sources, 2013, 225, 207-214.

366. B. Farbod, K. Cui, W. P. Kalisvaart, M. Kupsta, B. Zahiri, A. Kohandehghan, E. Memarzadeh, Z. Li, E. J. Luber, and D. Mitlin. ACS Nano, 2014, 8, 4415–4429.

367. B. Philippe, R. Dedryvère, M. Gorgoi, H. Rensmo, D. Gonbeau, and K. Edström. Chem. Mater., 2013, 25, 394–404.

368. H. S. Im, Y. J. Cho, Y. R. Lim, C. S. Jung, D. M. Jang, J. Park, F. Shojaei, and H. S. Kang. ACS Nano, 2013, 7, 11103–11111.

369. K. Li, H. Xie, J. Liu, Z. Ma, Y. Zhou, and D. Xue. Phys. Chem. Chem. Phys., 2013, 15, 17658-17663.

370. P. J. Thomas, and P. A. Midgley. Top. Catal., 2002, 21, 109-138.

371. V. B. Shenoy, P. Johari, and Y. Qi. J. Power Sources, 2010, 195, 6825–6830.

372. M. E. Stournara, P. R. Guduru, and V. B. Shenoy. J. Power Sources, 2012, 208, 165–169.

373. H. Chen, Y. Xiao, L. Wang, and Y. Yang. J. Power Sources, 2011, 196, 6657-6662.

374. R. Huang, X. Fan, W. Shen, and J. Zhu. Appl. Phys. Lett., 2009, 95, 133119-133119.

375. H. Kim, and J. Cho. Nano Lett., 2008, 8, 3688-3691.

376. Y. Yao, N. Liu, M. T. McDowell, M. Pasta, and Y. Cui. Energy Environ. Sci., 2012, 5, 7927-7930.

377. L. Hu, H. Wu, S. S. Hong, L. Cui, J. R. McDonough, S. Bohy, and Y. Cui. Chem. Commun., 2011, 47, 367-369.

378. Y. J. Cho, H. S. Kim, H. Im, Y. Myung, G. B. Jung, C. W. Lee, J. Park, M. H. Park, J. Cho, and H. S. Kang. J. Phys. Chem. C, 2011, 115, 9451-9457.

379. L. F. Cui, R. Ruffo, C. K. Chan, H. Peng, and Y. Cui. Nano Lett., 2008, 9, 491-495.

380. Z. Chen, and J. R. Dahn. Electrochem. Solid-State Lett., 2003, 6, A221-A224.

381. S. D. Beattie, and J. R. Dahn. J. Electrochem. Soc., 2003, 150, A894-A898.

382. M. D. Slater, D. Kim, E. Lee, and C. S. Johnson, Adv. Funct. Mater., 2013, 23, 947-958.

383. S. W. Kim, D. H. Seo, X. Ma, G. Ceder, and K. Kang, Adv. Energy Mater., 2012, 2, 710-721.

384. H. L. Pan, Y. S. Hu, and L. Q. Chen, Energy Environ. Sci., 2013, 6, 2338-2360.

385. A. Metrot, D. Guérard, D. Billaud, and A. Hérold, Synth. Met., 1980, 1, 363-369.

386. Y. Shao, J. Xiao, W. Wang, M. Engelhard, X. Chen, Z. Nie, M. Gu, L. V. Saraf, G. Exarhos, J. G. Zhang, and J. Liu, Nano Lett., 2013, 13, 3909-3914.

387. D. A. Stevens, and J. R. Dahn, J. Electrochem. Soc., 2000, 147, 1271-1273.

388. D. Datta, J. Li, and V. B. Shenoy, ACS Appl. Mater. Interfaces, 2014, 6, 1788-1795.

389. E. Memarzadeh Lotfabad, J. Ding, K. Cui, A. Kohandehghan, W. P. Kalisvaart, M. Hazelton, and D. Mitlin, ACS Nano, 2014, 8, 7115-7129.

390. J. Ding, H. Wang, Z. Li, A. Kohandehghan, K. Cui, Z. Xu, B. Zahiri, X. Tan, E. M. Lotfabad, B. C. Olsen, and D. Mitlin, ACS Nano, 2013, 7, 11004-11015.

391. Y. Yan, Y. X. Yin, Y. G. Guo, and L. J. Wan, Adv. Energy Mater., 2014, 4, 1-5.

392. Y. Liu, F. Fan, J. Wang, Y. Liu, H. Chen, K. Jungjohann, Y. Xu, Y. Zhu, D. Bigio, T. Zhu, and C. Wang, Nano Lett., 2014, 14, 3445-3452.

393. H. Xiong, M. D. Slater, M. Balasubramanian, C. S. Johnson, and T. Rajh, J. Phys. Chem. Lett., 2011, 2, 2560-2565.

394. Y. Xu, E. M. Lotfabad, H. Wang, B. Farbod, Z. Xu, A. Kohandehghan, and D. Mitlin, Chem. Commun., 2013, 49, 8973-8975.

395. K. T. Kim, G. Ali, K. Y. Chung, C. S. Yoon, H. Yashiro, Y. K. Sun, J. Lu, K. Amine, and S. T. Myung, Nano Lett., 2014, 14, 416–422.

396. J. C. P. Flores, C. Baehtz, A. Kuhn, and F. G. Alvarado, J. Mater. Chem. A, 2014, 2, 1825-1833.

397. G. Rousse, M. E. A. Dompablo, P. Senguttuvan, A. Ponrouch, J. M. Tarascon, and M. R. Palacín, Chem. Mater., 2013, 25, 4946-4956.

398. X. Yu, H. Pan, W. Wan, C. Ma, J. Bai, Q. Meng, S. N. Ehrlich, Y. S. Hu, and X. Q. Yang, Nano Lett., 2013, 13, 4721-4727.

399. Y. J. Zhu, X. G. Han, Y. H. Xu, Y. H. Liu, S. Y. Zheng, K. Xu, L. B. Hu, and C. S. Wang, ACS Nano, 2013, 7, 6378-6386.

400. X. Han, Y. Liu, Z. Jia, Y. C. Chen, J. Wan, N. Weadock, K. J. Gaskell, T. Li, and L. Hu, Nano Lett., 2014, 14, 139-147.

401. Y. Fang, L. Xiao, J. Qian, X. Ai, H. Yang, and Y. Cao, Nano Lett., 2014, 14, 3539-3543.

402. D. Er, J. Li, M. Naguib, Y. Gogotsi, and V. B. Shenoy, ACS Appl. Mater. Interfaces, 2014, 6, 11173-11179.

403. L. Baggetto, P. Ganesh, C. N. Sun, R. A. Meisner, T. A. Zawodzinski, and G. M. Veith, J. Mat. Chem. A, 2013, 1, 7985-7994.

404. L. Baggetto, P. Ganesh, R. P. Meisner, R. R. Unocic, J. C. Jumas, C. A. Bridges, and G. M. Veith, J. Power Sources, 2013, 234, 48-59.

405.J. W. Wang, X. H. Liu, S. X. Mao, and J. Y. Huang, Nano Lett., 2012, 12, 5897-5902.

406.M. Mortazavi, J. K. Deng, V. B. Shenoy, and N. V. Medhekar, J. Power Sources, 2013, 225, 207-214.

407.H. L. Zhu, Z. Jia, Y. C. Chen, N. Weadock, J. Y. Wan, O. Vaaland, X. G. Han, T. Li, and L. B. Hu, Nano Lett., 2013, 13, 3093-3100.

408.L. Baggetto, H. Y. Hah, C. E. Johnson, C. A. Bridges, J. A. Johnson, G. M. Veith, Phys. Chem. Chem. Phys., 2014, 16, 9538-9545.

409.J. Qian, Y. Xiong, Y. Cao, X. Ai, and H. Yang, Nano Lett. 2014, 14, 1865-1869.

410.M. He, K. Kravchyk, M. Walter, and M. V. Kovalenko, Nano Lett., 2014, 14, 1255-1262.

411.K. Dai, H. Zhao, Z. Wang, X. Song, V. Battaglia, and G. Liu, J. Power Sources, 2014, 263, 276-279.

412.C. Luo, Y. Xu, Y. Zhu, Y. Liu, S. Zheng, Y. Liu, A. Langrock, and C. Wang, ACS Nano, 2013, 9, 8003-8010.

413.Z. Jian, B. Zhao, P. Liu, F. Li, M. Zheng, M. Chen, Y. Shi, and H. Zhou, Chem. Commun., 2014, 50, 1215-1217.

414.Y. Wang, D. Su, C. Wang, and G. Wang, Electrochem. Commun., 2013, 29, 8-11.

415.B. Qu, C. Ma, G. Ji, C. Xu, J. Xu, Y. S. Meng, T. Wang, and J. Y. Lee, Adv. Mater., 2014, 26, 3854-3859.

416.W. J. Li, S. L. Chou, J. Z. Wang, H. K. Liu, and S. X. Dou, Nano Lett., 2013, 13, 5480-5484.

417.J. Qian, X. Wu, Y. Cao, X. Ai, and H. Yang, Angew. Chem., 2013, 125, 4731-4734.

418.L. Wu, X. Hu, J. Qian, F. Pei, F. Wu, R. Mao, X. Ai, H. Yang, and Y. Cao, Energy Environ. Sci., 2014, 7, 323-328.

419.Y. W. Denis, P. V. Prikhodchenko, C. W. Mason, S. K. Batabyal, J. Gun, S. Sladkevich, A. G. Medvedev, and O. Lev, Nat. Commun., 2013, 4, 1-7.

420. L. Baggetto, E. Allcorn, R. R. Unocic, A. Manthiram, and G. M. Veith, J. Mater. Chem. A, 2013, 1, 11163-11169.

421. B. Farbod, K. Cui, W. P. Kalisvaart, M. Kupsta, B. Zahiri, A. Kohandehghan, E. Memarzadeh, Z. Li, E. J. Luber, and D. Mitlin, ACS Nano, 2014, 8, 4415-4429.

422. P. R. Abel, M. G. Fields, A. Heller, and C. B. Mullins, ACS Appl. Mater. Interfaces, 2014, 6, 15860-15867.

423. L. David, R. Bhandavat, and G. Singh, ACS Nano 2014, 8, 1759-1770.

424. Y. Cao, L. Xiao, M. L. Sushko, W. Wang, B. Schwenzer, J. Xiao, Z. Nie, L. V. Saraf, Z. Yang, and J. Liu, Nano Lett., 2012, 12, 3783-3787.

425. Y. Liu, Y. Xu, Y. Zhu, J. N. Culver, C. A. Lundgren, K. Xu, and C. Wang, ACS Nano, 2013, 7, 3627-3634.

426. Y. Cao, L. Xiao, W. Wang, D. Choi, Z. Nie, J. Yu, L. V. Saraf, Z. Yang, and J. Liu, Adv. Mater., 2011, 23, 3155-3160.

427. V. L. Chevrier, and G. Ceder, J. Electrochem. Soc., 2011, 158, A1011-A1014.

428. L. Baggetto, J. K. Keum, J. F. Browning, and G. M. Veith, Electrochem. Commun., 2013, 34, 41-44.

429. P. R. Abel, Y. M. Lin, T. de Souza, C. Y. Chou, A. Gupta, J. B. Goodenough, G. S. Hwang, A. Heller, and C. B. Mullins, J. Phys. Chem. C, 2013, 117, 18885-18890.

430. S. Komaba, Y. Matsuura, T. Ishikawa, N. Yabuuchi, W. Murata, and S. Kuze, Electrochem. Commun., 2012, 21, 65-68.

431. E. L. Memarzadeh, W. P. Kalisvaart, A. Kohandehghan, B. Zahiri, C. M. Holt, and D. Mitlin, J. Mater. Chem., 2012, 22, 6655-6668.

432. E. M. Lotfabad, P. Kalisvaart, A. Kohandehghan, K. Cui, M. Kupsta, B. Farbod, and D. Mitlin, J. Mater. Chem. A, 2014, 2, 2504-2516.

433. S. P. Ong, V. L. Chevrier, G. Hautier, A. Jain, C. Moore, S. Kim, X. Ma, and G. Ceder, Energy Environ. Sci., 2011, 4, 3680-3688.

434. R. F. Egerton, Electron energy-loss spectroscopy in the electron microscope, Springer, New York, 3rd edition, 2011.

435. L. Baggetto, and P. H. Notten, J. Electrochem. Soc., 2009, 156, A169-A175.

436. T. Kennedy, E. Mullane, H. Geaney, M. Osiak, C. O'Dwyer, and K. M. Ryan, Nano Lett., 2014, 14, 716-723.

437. B. Farbod, K. Cui, M. Kupsta, P. Kalisvaart, E. Memarzadeh, A. Kohandehghan, B. Zahiri, and D. Mitlin, J. Mater. Chem. A, 2014, 2, 16770-16785.

438. Y. Liu, X. H. Liu, B. M. Nguyen, J. Yoo, J. P. Sullivan, S. T. Picraux, J. Y. Huang, and S. A. Dayeh, Nano Lett., 2013, 13, 4876-4883.

439. X. H. Liu, Y. Liu, A. Kushima, S. Zhang, T. Zhu, J. Li, and J. Y. Huang, Adv. Energy Mater., 2012, 2, 722-741.

440. H. Wu, G. Chan, J. W. Choi, Y. Yao, M. T. McDowell, S. W. Lee, A. Jackson, Y. Yang, L. Hu, Y. Cui, Nat. Nanotechnol., 2012, 7, 310-315.

441. X. H. Liu, and J. Y. Huang, Energy Environ. Sci., 2011, 4, 3844-3860.

442. X. H. Liu, H. Zheng, L. Zhong, S. Huan, K. Karki, L. Q. Zhang, Y. Liu, A. Kushima, W. T. Liang, J. W. Wang, J. H. Cho, E. Epstein, S. A. Dayeh, S. T. Picraux, T. Zhu, J. Li, J. P. Sullivan, J. Cumings, C. S. Wang, S. X. Mao, Z. Z. Ye, S. L. Zhang, and J. Y. Huang, Nano Lett., 2011, 11, 3312-3318.

443. X. H. Liu, S. Huang, S. T. Picraux, J. Li, T. Zhu, and J. Y. Huang, Nano Lett., 2011, 11, 3991-3997.

444. F. W. Yuan, H. J. Yang, and H. Y. Tuan, ACS Nano, 2012, 6, 9932-9942.

445. J. H. Pikul, H. G. Zhang, J. Cho, P. V. Braun, and W. P. King, Nat. Commun., 2013, 4, 1-5.

446. H. Zhang, and P. V. Braun, Nano Lett., 2012, 12, 2778-2783.

447. M. Gu, Y. Li, X. Li, S. Hu, X. Zhang, W. Xu, S. Thevuthasan, D. R. Baer, J. G. Zhang, J. Liu, and C. Wang, ACS Nano, 2012, 6, 8439-8447.

448. Q. Chen, and K. Sieradzki, Nat. Mater., 2013, 12, 1102-1106.

449. A. Kohandehghan, P. Kalisvaart, M. Kupsta, B. Zahiri, B. S. Amirkhiz, Z. Li, E. L. Memarzadeh, L. A. Bendersky, and D. Mitlin, J. Mater. Chem. A, 2013, 1, 1600-1612.

450. E. M. Lotfabad, P. Kalisvaart, K. Cui, A. Kohandehghan, M. Kupsta, B. Olsen, and D. Mitlin, Phys. Chem. Chem. Phys., 2013, 15, 13646-13657.

451. A. Kohandehghan, P. Kalisvaart, K. Cui, M. Kupsta, E. Memarzadeh, and D. Mitlin, J. Mater. Chem. A, 2013, 1, 12850-12861.

452. A. Kohandehghan, K. Cui, M. Kupsta, E. Memarzadeh, P. Kalisvaart, and D. Mitlin, J. Mater. Chem. A, 2014, 2, 11261-11279.

453. S. C. Jung, D. S. Jung, J. W. Choi, and Y. K. Han, J. Phys. Chem. Lett., 2014, 5, 1283-1288.

454. O. Malyi, V. V. Kulish, T. L. Tan, and S. Manzhos, Nano Energy, 2013, 2, 1149-1157.

455. Y. W. Xiao, J. Y. Lee, A. S. Yu, and Z. L. Liu, J. Electrochem. Soc., 1999, 146, 3623-3629.

456. J. Graetz, C. C. Ahn, R. Yazami, and B. Fultz, Electrochem. Solid-State Lett., 2003, 6, A194-A197.

457. J. R. Szczech, and S. Jin, Energy Environ. Sci., 2011, 4, 56-72.

458. M. Green, E. Fielder, B. Scrosati, M. Wachtler, and J. S. Moreno, Electrochem. Solid-State Lett., 2003, 6, A75-A79.

459. A. S. Fedorov, Z. I. Popov, A. A. Kuzubov, and S. G. E. Ovchinnikov, JETP Lett., 2012, 95, 143-147.

460. V. Etacheri, O. Haik, Y. Goffer, G. A. Roberts, I. C. Stefan, R. Fasching, and D. Aurbach, Langmuir, 2011, 28, 965-976.

461. R. Elazari, G. Salitra, G. Gershinsky, A. Garsuch, A. Panchenko, and D. Aurbach, J. Electrochem. Soc., 2012, 159, A1440-A1445.

462. A. Ponrouch, R. Dedryvère, D. Monti, A. E. Demet, J. M. A. Mba, L. Croguennec, C. Masquelier, P. Johansson, and M. R. Palacín, Energy Environ. Sci., 2013, 6, 2361-2369.

463. M. D. Levi, and D. Aurbach, J. Phys. Chem. B, 1997, 101, 4630-4640.

464. R. Ruffo, S. S. Hong, C. K. Chan, R. A. Huggins, and Y. Cui, J. Phys. Chem. C, 2009, 113, 11390-11398.